



# THE INTEGRATION OF INPUT FILTERS IN ELECTRICAL DRIVES

Mohamed Awad S Mohamed

A thesis submitted for the degree of  
Doctor of Philosophy

© Newcastle University 2019  
School of Engineering  
Submitted March 2019

# Abstract

The integration of passive components such as inductors and capacitors has gained significant popularity in integrated drive research, and future power electronics systems will require more integrated and standardised packages. These give rise to better power density and improved performance. However, packaging techniques and passive components have been considered a technological barrier which is limiting advances in power electronics. The focus on size reduction should be turned towards the passive components, such as converter chokes, DC-link capacitors and electromagnetic interference (EMI) filters, and achieving greater power density depends on innovative integration concepts, flexibility in structures and extended operating temperature ranges while system integration and modularity are not mutually exclusive.

This research considers the possibility of integrating input power filter components into electric machines. Particular attention is paid to the integration of electromagnetic line filter inductors to give better utilisation of the motor volume and envelope. This can be achieved by sharing the machine's magnetic circuit. An LCL line filter has been chosen to be integrated with a grid-connected permanent magnet synchronous machine. Machines have been proposed in this study for low speed (3000 RPM) and high speed (25000 RPM) operation. The two machines have similar dimensions, but the low-speed machine is less challenging in terms of losses and filter integration, so attention is directed more to the high-speed machine. Both are supplied with low- and high-power drives at power ratings of 4.5 kW and 38 kW respectively.

Several novel techniques have been investigated to integrate filter inductors into the electrical machines to produce a single mechanically packaged unit without significant increases in size and losses. Different approaches have been simulated using finite element analysis (FEA) to assess the effectiveness of the integration of passives within the machine structure. Each design has been iteratively optimised to determine the best mass of copper and core for the integrated filter inductors, targeting parity in power density when compared to traditional separate packages. The research demonstrates that an approach utilising a double-slot stator machine (named the integrated double slot (IDS) machine) with input filters wound into the outermost slots is the most appropriate choice in terms of achieving higher power density.

The integrated filter inductors mimic the electromagnetic behaviour of the discrete industrially packaged inductors but with a volume reduction of 87.6%. A prototype of the IDS machine design of a 38 kW, 25000 RPM, including filter inductors was manufactured and tested.

**To my parents, Professor Barrie Mecrow and my wife  
for your love and support**

# Acknowledgment

Praise is to Allah by whose grace good deeds are completed. I would like to start by expressing my gratitude to the backers of this research project: the General Electricity Company of Libya (GECOL), the Engineering and Physical Sciences Research Council (EPSRC), and the Engineering Doctorate scheme at Newcastle University.

To my supervisors Professor Barrie Mecrow, Dr Simon Lambert and Dr Dave Atkinson I sincerely thank you so much for your support, advice and guidance over the last four years. Without your experience and knowledge, I have no idea how we would have taken this project from a blank sheet of paper to the final rig. I cannot thank Professor Barrie Mecrow enough for his encouragement and unlimited support in different ways and for having the faith in myself to successfully deliver the integrated prototype of a high-power motor drive which introduces a new approach to integration.

Thanks to the members of the UG lab, past and present, who have provided a friendly, enjoyable and motivating place to work and who accepted, without complaint, the excessive noise generated whilst testing!. Special thanks go to Amanda Lane, Paul Killan, Yang Lu, John Smith, Samuel Burn, Chris Annan, Michael Richardson, Kris Smith, Andy Steven and Yaohui Gai for making each day at work useful and for their enthusiasm in such a dynamic environment. I would like to express my gratitude to Mehmet Kulan, who is always close and showing good character in terms of positive discussions and exemplary behaviour towards others and wishing the best to all.

To the two people closest to my heart, my parents, Awad Elsaadi Mohamed and Kamela Abdel-Rahman, all that I can say at this moment are that hopefully this step forward in my life makes you both proud and happy.

I express my sincere gratitude to my brother Mansour Awad Elsaadi for being one of the key power players. I believe that your words and attitude at the beginning of this journey helped me in achieving the strength of this study.

To my wife and children, Kamela, Saqr and Fatima Elzahra, your love, support, patience and understanding has been unending despite the lost weekends and frequent absences. I will always be grateful for your encouragement when there seemed to be no way forward.





# List of Contents

Abstract.....	i
Acknowledgment.....	iii
List of Contents .....	v
List of Tables .....	x
List of Figures.....	xii
List of Symbols.....	xix
<b>CHAPTER 1 Introduction.....</b>	<b>1</b>
1.1 Thesis overview.....	2
1.2 Objectives and contribution.....	4
1.3 Motivation .....	5
1.4 Published Work .....	6
1.5 The advantages of packaging of electric motors .....	7
1.5.1 Input power filters and associated IMDs.....	9
1.6 Passive components size and cost .....	11
1.7 Methodology.....	12
1.8 Prior work.....	13
1.8.1 Developing integrated passive components .....	15
1.8.2 Integrated passive filter components within the structure of electric machines.....	16
1.8.2.1 Integrated inductors within the stator of the machines .....	17
1.8.2.2 Filter capacitors integrated into the motor structure .....	20
1.9 Outcome of the literature review .....	21
<b>CHAPTER 2 Input Power Filter Design.....</b>	<b>23</b>
2.1 Introduction .....	23
2.2 Regulations .....	23
2.3 Use of an input power filter .....	25

2.4 Specifications of low- and high-power drives .....	27
2.4.1 L type filter.....	27
2.4.1.1 Frequency response of L filter type .....	28
2.4.2 LCL Type Filter .....	29
2.4.2.1 Frequency response of the LCL filter .....	30
2.4.2.2 Constraints on LCL filter parameters .....	32
2.4.2.3 Design methodology for the LCL filter .....	33
2.4.2.4 Calculation of drive-side inductance ( $L_2$ ) .....	34
2.4.2.5 Calculation of filter capacitance ( $C_f$ ) .....	35
2.4.2.6 Calculation of grid side inductance ( $L_1$ ) .....	35
2.4.2.7 Calculation of the damping branch $R_d$ and resonant frequency $f_{res}$ .....	36
2.5 General comparison between the total inductance of L and LCL filters .....	36
2.6 Determination of lumped parameters for low- and high-power LCL filters.....	39
2.6.1 LCL filter parameters for the low-power drive of 4.56 kW at 3000 RPM .....	39
2.6.2 LCL filter parameters for the high-power drive of 38 kW at 25000 RPM .....	41
2.6.3 PLECS Simulation results for low-and high-power LCL filter .....	42
2.7 A conventional inductor design at low- and high-power ratings .....	43
2.7.1 Design of drive-side 3-phase inductors ( $L_2$ ) for the low-power rating at 4.56 kW .....	44
2.7.1.1 FEA simulation results .....	48
2.7.2 Design of drive side 3-phase inductors $L_2$ for the high-power drive at 38 kW .....	48
2.7.3 Manufacturing of LCL filter inductors for the high-power drive at 38kW .....	50
2.8 An overall comparison study of input LCL filters at different power ratings. ....	50
2.9 Conclusion .....	52
<b>CHAPTER 3 High-Speed High-Power (HSHP) Electrical Machine Design.....</b>	<b>53</b>
3.1 Background .....	53
3.2 Permanent magnet machine .....	53
3.3 Materials.....	55

3.3.1 Stator material .....	55
3.3.2 Magnet materials .....	57
3.3.3 Sleeve materials .....	57
3.4 Specifications of low- and high-speed PM machines.....	58
3.5 Design optimisation of the HSHP machine at 25000 RPM.....	58
3.5.1 Parameters and constraints for optimisation.....	59
3.5.2 Unbalanced magnetic pull in rotating electrical machines .....	62
3.5.3 FEA Results .....	62
3.5.3.1 Machine torque prediction and back EMF .....	63
3.5.3.2 Machine inductance.....	65
3.5.4 Rotor stress analysis validation .....	66
3.5.5 Loss estimation .....	68
3.5.5.1 Rotor losses .....	69
3.5.5.2 Stator losses.....	71
3.5.5.2.1 Iron losses .....	71
3.5.5.2.1.1 Prediction of iron losses based on the Steinmetz equation for the HSHP machine .....	74
3.5.5.2.2 Copper losses .....	76
3.5.5.3 Windage losses of a rotating machine.....	81
3.5.6 Axial location of rotor magnets .....	84
3.6 Design of the low speed machine .....	86
3.7 Conclusion.....	88
<b>CHAPTER 4 The Integration of LCL Filter Inductors in Electrical Machines.....</b>	<b>90</b>
4.1 Introduction .....	90
4.2 Study of balanced and unbalanced magnetic pull for integrated machines.....	92
4.2.1 Unbalanced magnetic pull (UMP).....	92
4.2.2 Balanced magnetic pull (BMP) .....	93
4.3 Constraints of preliminary integrated design and fundamental equations .....	95

4.4 Integration of 3-phase filter inductors $L_2$ into the HSHP machine at 25000 RPM .....	98
4.4.1 Method 1: filter inductor windings $L_2$ around the stator core back .....	98
4.4.2 Method 2: inductor windings around stator teeth .....	102
4.4.3 Method 3: additional interior slots forming 3-phase inductors $L_2$ .....	104
4.4.3.1 FE Simulation results for interior extra slot technique .....	108
4.4.3.2 Magnetic cross-coupling between the fields of the filter inductors and the HSHP machine .....	109
4.4.4 Method 4: additional outer slots (double slot machine).....	111
4.4.4.1 FEA results .....	112
4.4.4.2 Modularity option for the IDS machine.....	115
4.4.5 Method 5: corner inductors .....	116
4.4.5.1 FE Results .....	118
4.5 Integration of drive-side filter inductors $L_2$ in a power drive of 4.56 kW at 3000 RPM .....	118
4.6 Discussion .....	120
4.7 Summary of design options.....	124
4.8 Design of integrated magnetic filter (grid-side inductors $L_1$ ) .....	124
4.8.1 Winding configuration of integrated filter inductors .....	125
4.8.2 Verification of mutual coupling for the IDS machine .....	129
4.9 DC loss of integrated 3-phase filter inductors .....	130
4.10 Iron Losses of the IDS machine including the 3-phase filter inductors.....	131
4.11 Conclusion .....	132
<b>CHAPTER 5 Machine and Filter Construction .....</b>	<b>134</b>
5.1 Rotor construction.....	134
5.2 Stator construction of the IDS machine .....	138
5.2.1 Construction of the stator laminations .....	138
5.2.2 Direct On-Tooth compressed coils .....	139
5.3 Interconnection power board for the IDS machine .....	144

5.4 Manufacturing of shunt capacitors of the LCL filter.....	153
5.5 Test stand assembly.....	154
<b>CHAPTER 6 Test Results and Evaluation .....</b>	<b>156</b>
6.1 Measurements of the integrated LCL filter .....	156
6.1.1 Initial experimental results .....	156
6.1.2 Mutual coupling between filter inductors ( $L_1$ and $L_2$ ).....	160
6.1.3 Measurements of filter inductance ( $L_1$ and $L_2$ ).....	161
6.1.4 The measurement of the 3-phase current waveforms of the grid- and drive-side inductors .....	162
6.1.5 Magnetic cross-coupling between the base machine and filter windings .....	164
6.2 HSHP machine measurements .....	165
6.2.1 Open circuit voltages (back-EMF) .....	165
6.2.2 Coil testing (resistance, ground wall insulation and inter-turn) .....	166
6.2.2.1 Balance resistance test.....	166
6.2.2.2 Mega and surge test.....	168
6.3 Conclusion.....	168
<b>CHAPTER 7 Conclusion and Future Work .....</b>	<b>169</b>
8.1 Background.....	169
8.2 Summary of work .....	170
8.3 Future research possibilities and recommendations .....	171
References .....	173
<b>Appendix A – Analytical calculation and further integration method.....</b>	<b>189</b>
<b>Appendix B – 34kW/25000 RPM machine drawings .....</b>	<b>196</b>
<b>Appendix C – Drawings of pressing tools .....</b>	<b>200</b>
<b>Appendix D – 4.56 kW/3000 RPM - FE results .....</b>	<b>203</b>

# List of Tables

Table 2-1 Current distortion limits for systems rated 120 V through 69 kV .....	24
Table 2-2 Specifications of two prototype motor design .....	27
Table 2-3 Specifications of two proposed electric drives .....	39
Table 2-4 LCL filter parameters for input power drive 4.56 KW .....	40
Table 2-5 LCL filter parameters for drive input power 38 kW .....	41
Table 2-6 Inductor dimensions per phase and Table 2-7 Inductor electrical characteristics ...	47
Table 2-8 Inductor dimensions/ phase and Table 2-9 Inductor electrical characteristics .....	49
Table 2-10 Comparison of low-and high-power conventional 3-phase inductors.....	51
Table 3-1 Specifications of low- and high-speed machines .....	58
Table 3-2 Chosen materials for HSHP machine 25000 RPM.....	61
Table 3-3 Validation the HSHP machine inductance (25000 RPM) .....	66
Table 3-4 Material dependent constants for the super-core of 10JNEX-900 .....	74
Table 3-5 Magnet and electrical load flux densities in the stator regions.....	75
Table 3-6 Improvement in AC winding loss conversion power ratio $K_{AC}$ via 2D FEA .....	80
Table 3-7 Results for 12 slot/8 pole PM machine at 25000 RPM .....	83
Table 3-8 Performed results for 12 slot/8 pole PM machine at 3000 RPM.....	88
Table 4-1 A summary of proposed machine specifications .....	91
Table 4-2 Different BMP and UMP cases for different pole numbers of the filter inductor and main machine windings .....	95
Table 4-3 Illustration of the integration of 3-phase filter inductors around the stator core back in a 38 kW drive.....	101
Table 4-4 Illustration of the integration of 3-phase filter inductors around the stator teeth in a 38 kW drive.....	103
Table 4-5 Specifications of a single inductor slot within IDS stator .....	107
Table 4-6 Illustration of the integration of 3-phase filter inductors around the stator core back at 4.56 kW drive: Method 1 .....	119

Table 4-7 Illustration of the integration of 3-phase filter inductors around the stator teeth at 4.56 kW drive: Method 2.....	120
Table 4-8 Different topologies for integrating low and high power electric drives .....	122
Table 4-9 Comparison of integrated and discrete commercial filter inductors .....	123
Table 4-10 Winding configurations for direct on-tooth compressed IDS machine coils .....	128
Table 4-11 Verification of mutual inductance in the design of IDS machine.....	130
Table 5-1 Volume comparison between the integrated and discrete 3-phase LCL filter inductors .....	143
Table 5-2 Parameters of four-layer design .....	145
Table 5-3 Parameters of four-layer busbar design.....	147
Table 6-1 Simulated and measured inductances for the IDS machine filter windings in the stator motorette .....	159
Table 6-2 Measurements of inductance and resistance for the six LCL filter inductors.....	162
Table 6-3 Specifications of the dyno test rig .....	163
Table 6-4 Measured and projected back-EMF at 7000 RPM.....	166
Table 6-5 Measured resistance values for the HSHP machine coils .....	167



# List of Figures

Figure 1-1 Standard cabinet of a variable speed drive with rated current 25 A .....	8
Figure 1-2 Location of 3-phase input filters as an interface between a grid and ASDs system	9
Figure 1-3 Different transformer core types .....	10
Figure 1-4 3-phase input power inductors for rated power 630 kW/1600 A <sub>pk</sub> .....	10
Figure 1-5 Typical material cost and volume distribution in power electronics systems [1] ..	11
Figure 1-6 The development of 4 kW standard adjustable speed drive: a) number of components and functions; b) comparison of size and weight .....	13
Figure 1-7 Different converter topologies suited for integrated motor drives with: a) electronic inductor in dc-link; b) a boost converter; c) two interleaved CCM parallel boost converter; d) three-level CCM boost converter; e) DCM boost converter; f) Vienna rectifier; g) three-level PWM rectifier with RB-IGBTs, h) three-phase buck converter; i) back-to-back VSI, j) matrix converter; k) two-stage DPEC; l) two-stage DPEC with RB-IGBTs .....	14
Figure 1-8 Illustration of process of integrated L-L-C-T a) equivalent lumped parameters model of L-L-C-T, b) exploded view of construction of integrated L-L-C-T .....	16
Figure 1-9 Schematic view of shared stator core carrying integrated filter inductor and main machine windings .....	17
Figure 1-10 Axial presentation of integrated motor-shaped inductor .....	18
Figure 1-11 Integrated motor drive: a) motor housing and power electronics heat sink; b) integrated 50kW, 50krpm PM motor and power electronics concept .....	19
Figure 1-12 Integrated motor-drive system: a) design concept for an integrated segmented inverter-motor drive system; b) integrated modular motor drive .....	21
Figure 2-1 Different topologies of input filters: a) L type; b) LC type; c) LCL type .....	26
Figure 2-2 Schematic of a conventional electric drive system .....	26
Figure 2-3 Schematic of permanent magnet machine ASD circuit including three-phase identical input line inductors (L filter type) .....	28
Figure 2-4 Equivalent circuit of L type filter including only the switching harmonic component .....	28
Figure 2-5 Frequency response of L filter using Bode diagram .....	29
Figure 2-6 Three-phase voltage source rectifier with LCL filter .....	30
Figure 2-7 Equivalent circuit of single-phase of LCL input filter showing switch harmonics and voltage fundamental components .....	30

Figure 2-8 Equivalent circuit of single-phase LCL input filter considering switch harmonics fundamental component .....	30
Figure 2-9 Bode diagram for LCL filter with (blue) and without (green) damping resistor ....	31
Figure 2-10 Illustration of the relationship between AC side vectors of VSR .....	32
Figure 2-11 Phasor diagram at unity power factor .....	32
Figure 2-12 Current waveforms for each filter component .....	33
Figure 2-13 Illustration of a simplified equivalent circuit of single phase of drive-side filter inductor $L_2$ in generating mode .....	34
Figure 2-14 Comparison of L and LCL filters at different switching frequencies.....	37
Figure 2-15 Comparison of L and LCL filter types at different power rating values .....	38
Figure 2-16 Grid-side 3-phase current waveforms: a) and b) unfiltered currents of low- and high power drives of 4.56 kW and 38 kW respectively; c) and d) filtered currents of low- and high power drives of 4.56 kW and 38 kW respectively .....	42
Figure 2-17 Characteristics of AC inductor: a) geometry of single phase inductor; b) magnetic equivalent circuit .....	43
Figure 2-18 Features of conventional 3-phase AC inductors .....	44
Figure 2-19 Optimisation chart loop of conventional inductors design .....	45
Figure 2-20 Optimisation process of the EE 3-phase inductor design for low power drive at 4.56 kW .....	46
Figure 2-21 Total conduction loss of the predicted design of the EE3-phase inductor for the low power drive at 4.56 kW .....	46
Figure 2-22 3D presentation of the predicted design of the 3-phase drive-side inductors $L_2$ for the low power drive of 4.56 kW .....	47
Figure 2-23 3-phase waveforms for $L_2$ for the power drive of 4.56 kW: a) voltage; b) flux linkage .....	48
Figure 2-24 Conventional 3-phase input AC inductor for the high-power drive of 38 kW .....	49
Figure 2-25 Manufactured 3-phase LCL filter inductors for the drive of 38kW: a) drive-side inductors $L_2$ ; b) grid-side inductors $L_1$ .....	50
Figure 3-1 Some rotor possibilities: (a) and (b) surface PM; (c) inset PM; (d), (e), (f) and (g) interior permanent magnet (IPM) .....	54
Figure 3-2 Illustration of enhancement of manufacturing process of siliconizing steel sheets .....	56
Figure 3-3 Magnetic characteristics of super core 10JNEX-900 .....	56
Figure 3-4 Illustration of parameters set for optimisation in 12 slot/8 pole HSHP PM motor	60
Figure 3-5 12 slot - 8 pole HSHP machine windings layout .....	62

Figure 3-6 Illustrates FEA model with the mesh size elements and contour plot at 25000 RPM .....	63
Figure 3-7 3D Magnetic FEA model of the HSHP machine at 25000 RPM .....	64
Figure 3-8 3D torque performance prediction at 25000 RPM .....	64
Figure 3-9 3D Back EMF voltages at 25000 RPM .....	65
Figure 3-10 Harmonic spectrum of Line-Line back EMF at a fundamental frequency of 1.67 kHz .....	65
Figure 3-11 Rotor components including sleeve with mesh overlaid .....	67
Figure 3-12 Rotor structure analysis: a) deformation on sleeve; b) equivalent von-Mises stress on rotor structure .....	68
Figure 3-13 Effect of magnet segmentation on losses at rated current and shaft speed .....	69
Figure 3-14 High rotor speed: a) rotor assembly, showing segmented magnets; b) effect of segmentation on eddy current paths; c) manufactured segmented rotor magnet for one pole; d) representation of the wedge filled by the resin .....	70
Figure 3-15 Eddy current shield applied to the high-speed rotor .....	71
Figure 3-16 Drive phase current with 7.18% THD .....	71
Figure 3-17 Behaviour of domain alignment for an external magnetic field .....	72
Figure 3-18 A comparison of iron loss for different core materials .....	73
Figure 3-19 Different stator components .....	74
Figure 3-20 Composition of full load iron losses for the HSHP machine stator .....	75
Figure 3-21 MMF flow chart within a slot with conductors .....	78
Figure 3-22. Geometry of the proposed machine slot .....	79
Figure 3-23 Field and current contributions of adjacent conductors within the slot .....	81
Figure 3-24 Demagnetisation obtained at full rated current and speed .....	84
Figure 3-25 The effect of front-end rotor collars: a) assembly of rotor; b) contour plot demonstrating the shorting of the end magnets .....	85
Figure 3-26 Effect of collars on torque performance at 25000 RPM .....	85
Figure 3-27 Suitable rotor topologies for low-speed machines: a) SPM rotor with offset; b) inset SPM rotor .....	86
Figure 3-28 FEA model with mesh size elements and contour plot at 3000 RPM .....	87
Figure 4-1 Electrical drive configuration with the highlighted 3-phase inductor in the drive side .....	91

Figure 4-2 Unbalanced total flux density for different machine and filter inductor pole numbers .....	93
Figure 4-3 Balanced total flux density for different machine and filter inductor pole numbers .....	94
Figure 4-4 Stator pole pitch and the effective magnet width .....	96
Figure 4-5 Stator slot pitch definition and tooth width .....	97
Figure 4-6 General schematic of the AC inductors integrated into a motor: a) 2D FEA model; b) 3D representation .....	99
Figure 4-7 Illustration of the effect of integrating AC inductor into the HSHP machine .....	100
Figure 4-8 Layout of auxiliary windings into the PM motor .....	102
Figure 4-9 Geometry of the extra slot forming the 3-phase filter inductors.....	104
Figure 4-10 A single tooth of interior extra slots demonstrating a part of the phase inductor geometry .....	105
Figure 4-11 Flow chart of optimisation process for the integration of 3-phase filter inductors into the machine stator as extra slots .....	106
Figure 4-12 The required masses of copper and steel at different air gap lengths in a power drive of 38 kW .....	107
Figure 4-13 3-phase filter inductors sharing the HSHP machine stator .....	108
Figure 4-14 Magnetic coupling behaviour between the filter inductors and the HSHP machine .....	108
Figure 4-15 Contour plot of integration technique using interior extra slots .....	109
Figure 4-16 Voltage induced in inductor windings due to rotor magnets and armature fields .....	109
Figure 4-17 Voltage induced in armature windings solely due to inductor magnetic field ...	110
Figure 4-18 Magnetic flux cross-coupling between rotor magnets and filter inductor windings .....	110
Figure 4-19 Magnetic flux cross-coupling at full operation condition.....	110
Figure 4-20 Geometry of a half model of double slot machine with the incorporation of 3-phase AC inductors into the HSHP machine at 25000 RPM .....	111
Figure 4-21 Winding layout of the IDS machine .....	111
Figure 4-22 3D representation of integrated double slot (IDS) machine .....	112
Figure 4-23 Contour of dual magnetic flux of 8 pole machine and 10 pole inductors windings .....	112
Figure 4-24 Magnetic flux behaviour within a single inductor slot .....	113

Figure 4-25 FE results for integrated 3-phase filter inductors $L_2$ : a) voltage; b) flux linkage	113
Figure 4-26 Machine rated torque before and after integrating 3-phase AC inductors .....	114
Figure 4-27 Induced voltage in inductor windings due to magnetic field of rotor magnets..	114
Figure 4-28 Voltage induced in armature windings due to energising filter windings only .	114
Figure 4-29 Voltage induced in inductor windings due to magnetic field of armature fields only .....	115
Figure 4-30 Magnetic cross-coupling between integrated filter inductors and the HSHP machine .....	115
Figure 4-31 Integration of 3-phase drive-side inductors with stator modularity option: a) double slot tooth; b) double slot tooth with pressed coils; and c) assembly of stator of integrated double slot (IDS) machine .....	116
Figure 4-32 Utilization of motor corners for integrating AC inductors.....	117
Figure 4-33 A 3D representation of integrated 3-phase filter inductors $L_2$ within motor corners .....	117
Figure 4-34 FE Results for 3-phase filter inductors $L_2$ : a) 3-phase voltages; b) 3-phase flux linkage.....	118
Figure 4-35 Illustration of the final motor profile associated with the 3-phase filter inductor $L_2$ in: a) low-power drive of 4.56 kW; b) high-power drive of 38 kW .....	121
Figure 4-36 3D presentation of the general schematic of the IDS machine .....	125
Figure 4-37 Example of mutual coupling between $L_1$ and $L_2$ located in the same slots .....	126
Figure 4-38 Results of cross-coupling investigation between integrated filter inductors with different numbers of poles in the stator .....	126
Figure 4-39 The original machine back-EMF line voltage before and after integration .....	127
Figure 4-40 24 slots - 8 pole base machine windings and 16 and 10 poles for filter inductors $L_1$ and $L_2$ respectively.....	128
Figure 4-41 Filter winding arrangements in a single inductor slot .....	129
Figure 4-42 Flux linkage in single coil strands: a) grid-side inductor; b) drive-side inductor .....	129
Figure 4-43 Full load flux plot of the double slot machine .....	131
Figure 4-44 The composition of non-load iron Losses for double slot machine .....	131
Figure 4-45 Drawing of full segment tooth .....	133
Figure 5-1 Different components for the high-speed rotor .....	135
Figure 5-2 Assembly of rotor magnets showing the effect of front-end collars .....	135
Figure 5-3 Assembly of the rotor core and collars to the machine shaft .....	136

Figure 5-4 Assembly process of the rotor magnets .....	136
Figure 5-5 Process of filling gaps between the rotor poles.....	137
Figure 5-6 HSHP final rotor assembly .....	137
Figure 5-7 Rotor on balancing machine .....	138
Figure 5-8 pre-assembly of the double slot stator .....	138
Figure 5-9 Single tooth stator segment.....	139
Figure 5-10 The on-tooth pressing method .....	141
Figure 5-11 On-tooth pressed coils with gap to reduce fringing.....	141
Figure 5-12 The full assembly of a compressed coils of double slot tooth.....	142
Figure 5-13 Fully assembled integrated double slot stator.....	142
Figure 5-14 A comparison in volume between the discrete and the integrated AC inductors of the LCL input filter.....	143
Figure 5-15 Layout of windings in the IDS machine .....	144
Figure 5-16 3D presentation of the four-layer busbar design: a) a complete assembly; b) the assembly of the four layers in order .....	145
Figure 5-17 Illustration of clearance and creepage: a) clearance (in air); b) creepage (along a surface) .....	146
Figure 5-18 Specifications of power board design: a) thickness of barrier and copper busbars; b) external connections from different layers.....	147
Figure 5-19 Manufacturing process of power board design.....	148
Figure 5-20 Manufactured copper busbars and the PTEF boards .....	148
Figure 5-21 Arrangement of end terminal .....	149
Figure 5-22 Management of the end terminals of the main machine windings .....	149
Figure 5-23 Board 1: a) front view; b) the neutral ring copper with groove and the process of filling with solder .....	150
Figure 5-24 Board 2: a) soldered busbars of $L_2$ ; b) 3D inventor model (the back side of the second board showing the assembly of the neutral copper ring).....	151
Figure 5-25 Board 3: assembly of busbars and external connections of the LCL filter inductors .....	151
Figure 5-26 Board 4: process of assembly with a single busbar in the last board.....	152
Figure 5-27 The final assembly of the four-layer design associated with external connections .....	152
Figure 5-28 The final assembly of the machine housing.....	153

Figure 5-29 Capacitors and full design: a) 3-phase shunt capacitors of the LCL filter; b) the complete design of the integrated high power drive .....	154
Figure 5-30 High speed no-load test rig.....	155
Figure 6-1 Three-tooth motorette used to test single-tooth inductor coil inductance .....	157
Figure 6-2 Three tooth motorette with test leads .....	157
Figure 6-3 Set up of the test rig.....	158
Figure 6-4 Single tooth inductance measurements of motorette.....	158
Figure 6-5 Three-tooth fully assembled IDS machine motorette .....	159
Figure 6-6 Three-tooth motorette with test leads.....	159
Figure 6-7 Initial examination of mutual coupling between the integrated filter inductors ..	160
Figure 6-8 Final examination of cross-coupling between the integrated filter inductors .....	161
Figure 6-9 Measurement of filter inductance per phase: a) drive-side; b) grid-side.....	161
Figure 6-10 3-phase currents of the integrated LCL input filter at 3000 RPM .....	163
Figure 6-11 3-phase currents of the integrated LCL input filter at 15000 RPM .....	164
Figure 6-12 Examination of magnetic cross-coupling between the base machine and filter windings .....	165
Figure 6-13 Line back-EMF measured and predicted at 7000 RPM .....	165
Figure 6-14 Measurement of resistance for the high-speed machine coils.....	167
Figure 7-1 Illustration of the integration of grid-side inductors using two different methods .....	172

# List of Symbols

Below is a list of symbols used in this thesis. Wherever possible a symbol or subscript which donate to a specific meaning is defined in the main body of the text where used.

$V_L$	Voltage across inductor	$I_{max}$	The maximum current
$L$	Inductance	$f_{sw}$	Switching frequency
$L_1$	Grid-side inductor	$m_a$	Modulation factor
$L_2$	Drive-side inductor	$\omega_{sw}$	Angular switching frequency
$C_f$	Capacitance of the filter	$K_a$	Attenuation factor of the current ripple
$I_{L1}$	Grid-side filter current	$f_{res}$	Resonant frequency
$I$	Input converter current	$\omega_{res}$	Angular resonant frequency
$I_C$	Capacitor current	$R_d$	Damping resistance
$v_c$	Input voltage of the converter	$f_g$	Grid frequency
$v_{sw}$	Switching harmonics voltage	N	Number of turns
$E_m$	Peak phase voltage	$\phi$	Magnetic flux
$V_{dc}$	DC bus voltage	$R_{eq}$	Equivalent reluctance
$\omega$	Angular frequency	$R_C$	Reluctance of the core
$I_m$	Peak value of phase current	$R_g$	Reluctance of the gap
THD	Total harmonic distortion	$A_C$	Cross-sectional area of the core
$Z_b$	Base impedance	$L_M$	Magnetic path length
$C_b$	Base capacitance	$L_g$	Length of the air gap
$E_n$	Line-to-line rms voltage	$\mu_0$	Permeability of free space
$\omega_g$	Grid angular frequency	$\mu_r$	Permeability of the material
$P_n$	Rated power	$\hat{\psi}$	Peak of flux linkage
I	Current	$\hat{\phi}$	Peak of magnetic flux
$\Delta I_{Lmax}$	The maximum current ripple	B	Magnetic flux density
		H	Magnetic field strength



## List of symbols

---

$ff$	Winding fill factor	$l_{sw}$	Slot width
$J$	Current density	$D_c$	Conductor diameter
$P_{Loss}$	Power loss	$l_a$	Conductor axial length
$K_e$	Eddy current loss coefficient	$K_{AC}$	AC loss conversion factor
$K_h$	Hysteresis loss coefficient	$C_d$	Skin friction coefficient
$K_d$	Domain loss coefficient	Re	Reynold number
$R_{DC}$	DC resistance	$W$	Windage power loss
$R_{AC}$	Equivalent AC resistance	$t$	Thickness of lamination
$\rho_c$	Resistivity of copper	$N_{inductor}$	Number of turns per phase inductor
$T_{ref}$	Reference temperature	$SL$	Machine stack length
$\alpha$	Temperature coefficient	$\hat{\Phi}_{armature}$	Magnetic flux due to armature winding
$R_{ref}$	Conductor resistance at the reference temperature	$\hat{\Phi}_{inductor}$	Magnetic flux due to filter inductor winding
$C.S.A$	Cross-sectional area	$A_{core\ back}$	Stator core back area
$\delta$	Skin depth	$A_{pk}$	Peak value of Current
$\sigma$	Copper conductivity	RPM	Rotations Per Minute
$A_{rms}$	Root mean square of current		

# CHAPTER 1

## INTRODUCTION

---

This research forms part of the integrated drives work package of the drive themes of the ‘Underpinning Power Electronics (UPE) project’, which is a programme managed by the Engineering and Physical Sciences Research Council (EPSRC). The project focuses on enhancing the functionality of integrated approach to produce a single packaged unit with high power density, composed of a power electronics converter and controller, passive components (i.e. inductors and capacitors) and an electrical machine. This type of compact system is named an Integrated Motor Drive (IMD). As an IMD is a combination of different components requiring a multidisciplinary approach, the consortium consists of five UK universities searching different aspects to further improve the capability of high power density. In particular, Newcastle University focuses on structural integration, which in turn incorporates input filter components within a structure of an electrical machine and mainly focused on electromagnetic filter components without significant increases in size and losses.

Miniaturisation and system integration in electric drives are mainly required for applications with limited installation space, such as in the automotive, aerospace and robotic fields. In view of a further reduction of costs and volume of the integrated system, the development of standardised power electronics and passive components merged with their mechanical environments is used [1]. An integrated drive may be considered to be a full mechanical integration of the base machine and electric drive components, including passive components, into a single package. This approach is important for applications when the motor and load are intimately connected to each other.

The integrated approach aims to increase the performance of integrated systems and their reliability and manufacturability. It has been established that industrial sectors require improvements in the components of semiconductor devices [2, 3]. The future of power electronics essentially relies upon the use of integrated and standardised packages. These give rise to better power density and improved performance. However, packaging techniques and passive components have been considered a technological barrier which is limiting advances in power electronics [3, 4].

## 1.1 Thesis overview

In this thesis, various integrated motor drives (IMD) are described, with each packaged in a single unit which consists of a power electronics converter, power electronics controller, passive components (i.e. inductors and capacitors), an electrical machine and voltage and current sensing. From chapter four onward the thesis focuses solely on the integration of AC filter inductors located between the utility grid and active rectifier converter (grid-connected drives). To investigate the impact of drive power rating on the integration of passives, two similar base machines have been designed with low- and high-power ratings related to their base speeds. These two machines were taken as foundation motors for the purpose of integrating passive components into the low- and high-power machines which they described as follows:

- Low-speed surface-mounted permanent magnet (PM) motor (3000 RPM / 4.1 kW).
- High-speed surface-mounted PM motor (25000 RPM / 34 kW). This motor has been considered as a baseline with the low-speed machine for comparison. The final integrated high-speed motor, including passive filter components, has been built and tested where it is discussed in chapters five, six and seven.

The structure of the thesis is as follows:

- **Chapter 1** introduces the concept behind integrated motor drives (IMDs) associated with passive components and discusses the varying size of filter inductors with drives of different power ratings. This leads to a description of the core of this research, which concerns integrating filter components into electrical machines. Some relevant technical examples are given of integrated filter inductors and capacitors within the structure of electrical motors.
- **Chapter 2** describes the different types of conventional input power filters and analytical approaches used to determine the parameters of different filter types. The most appropriate filter type is selected for the chosen drive systems. 2D FE models of the discrete low- and high-power inductors have been built and simulated. The optimal total volume achieved for the two sets of inductors was obtained via a simple iterative process. For the purpose of comparison, commercial industrial filter inductors are manufactured, which correspond to those of the chosen type of filter for the 38 kW drive.
- **Chapter 3** describes the design processes for the low- and high-speed machines which are identical but operate at different shaft speeds of 3000 RPM and 25000 RPM

respectively. The selection of advanced materials with different manufacturing techniques are discussed in order to achieve high power density and to enhance machine performance.

- **Chapter 4** describes the research and development of the integration of filter inductors surrounding the low- and high-speed machines. Different integration methods are investigated in order to examine the effectiveness of integrating filter inductors into the proposed machines. Finally, the high-speed specification drive is developed into a working demonstrator.
- **Chapter 5** presents the manufacturing processes utilised for the integrated machine demonstrator, including passive filter components.
- **Chapter 6** presents and discusses the experiments conducted and the test results for the integrated machine demonstrator.
- **Chapter 7** provides the overall conclusions of the study and possible avenues for future work.

## 1.2 Objectives and contribution

The work presented in this thesis focuses on the integration of input filters for AC grid connected integrated drives with a specific focus on the magnetic components.

The objectives of the work are;

- To investigate input filter topologies for grid-connected drives
- To benchmark a traditionally constructed drive and filter arrangement
- To design low- and high-speed machines (taken as base machines for the work) where the underlying machines have similar dimensions, but operate at two different rated speeds.
- To examine various methods of integration of the magnetic components of the input filter and propose solutions which improve power density and minimise the envelope
- To understand the impact of drive power and shaft speed on the relative size of the impact filter and electric machine and recognise the design implications for integrated drives
- To design, simulate, build, test and evaluate an integrated filter demonstrator to be included in a fully functional integrated drive (other drive aspects such as the power electronic converter are beyond the scope of this thesis).

The contributions to previously unpublished knowledge contained within this work are summarised as

- Incorporation of three phase AC input filter inductors into a high-speed high power PM electrical machine to compose a single drive unit
- Significant volume reduction in the integrated filter inductors compared to traditional industrial inductors of the same power rating
- Validation of various integration methods of filter inductors into a base machine with different levels of drive power ratings
- Suitability and determination of 3-phase filter winding configuration with respect to machine winding configuration to avoid magnetic coupling between filter to filter and filter to machine windings in which all share the same magnetic circuit
- Electromagnetically compatible high frequency end windings management and the design of a power circuit embedded into the machine housing

### 1.3 Motivation

The chief motivation of this research is to reduce the size of essential input filters in high-speed drives, where the overall size of these filters would otherwise be larger than the machine itself. This must be achieved without affecting the base machine performance.

In order to meet this requirement, a bespoke, integrated, high-performance machine has to be thoroughly researched and prototyped. The desired shaft speed of the base machine and its full torque capability across the speed range are chosen to be 25,000 RPM and 13 Nm respectively, delivering 34 kW at full speed.

As can be noted from literature, this is the first time that the six, 3-phase inductors of an LCL input filter have been designed to share the machine's magnetic circuit, producing a new topology of integrated machine. This type of passive integration into a machine is named an Integrated High Speed Double Slot (IHSDS) machine. The required performance specifications and the constraints of different winding arrangements present a challenging combination that has not yet been tackled in published literature. One of the key design factors is that the integrated AC filter inductors should share the machine cooling system, and this will help in the concept of compact systems in terms of further reductions in volume. This research into integrated passive components explores the capability of several integration techniques to be used for the construction of the IHSDS machine. Furthermore, this approach enhances the development of standardised filter inductors for use for future product requirements.

## 1.4 Published Work

The following peer-reviewed publications and conference papers have stemmed from this research.

1. M. A. Mohamed, S. M. Lambert, B. M. Mecrow, D. J. Atkinson, A.C. Smith, “An Electrical Machine with Integrated Drive LCL Filter Components”, 8th IET International Conference on Power Electronics, Machines and Drives, pp. 1- 6, 2016.

URL: <http://ieeexplore.ieee.org/stamp/stamp.jsp?arnumber=7739410>

2. M. A. S. Mohamed, S. M. Lambert, B. M. Mecrow, X. Deng, S. Ullah, A.C. Smith, “Integrating the Magnetics of an LCL Filter into a High Speed Machine with Pre-Compressed Coils”, IEEE International Electric Machines and Drive Conference, pp. 1- 6, 2017.

URL: <http://ieeexplore.ieee.org/stamp/stamp.jsp?arnumber=8002292>

3. Mohamed Awad S Mohamed, Xu Deng, Simon Lambert and Barrie Mecrow, *Member, IEEE*, “Development of a High-Speed, Permanent Magnet, SiC-Based Drive with Integrated Input Filters-Part 1: Integration of Magnetic Components”, in preparation for submission to IEEE.

4. X. Deng, S. M. Lambert, B. M. Mecrow, M. A. S. Mohamed, S. Ullah, A.C. Smith, “Winding Connection Solution for an Integrated Synchronous Motor Drive”, IEEE International Electric Machines and Drive Conference, pp. 1- 6, 2017.

URL: <http://ieeexplore.ieee.org/stamp/stamp.jsp?arnumber=8002162>

5. Xu Deng, Mohamed Awad S Mohamed, Simon Lambert and Barrie Mecrow, *Member, IEEE*, “Development of a High-Speed, Permanent Magnet, SiC-Based Drive with Integrated Input Filters-Part 2: Integration of Power Electronics”, in preparation for submission to IEEE.

## 1.5 The advantages of packaging of electric motors

The vast majority of adjustable speed drives (ASDs) treat the various subsystems of the drive (electric machine, power electronics, passive converters etc.) as mechanically isolated entities. As a result of this, the power electronics converter and the motor are commonly packaged and installed separately. Machine drives can be categorised according to their power source: DC or AC grid-connected. In this research, a grid-connected AC power source is used. A conventional grid-connected power drive consists of several separate components such as an input power filter, rectifier, DC-link capacitor and an inverter (more details are in section 1.5.1). It is common practice for all of the drive components to be located in a standardised cabinet. Figure 1-1 shows an example of a conventional cabinet of a variable frequency drive with an electrical machine and associated hardware.

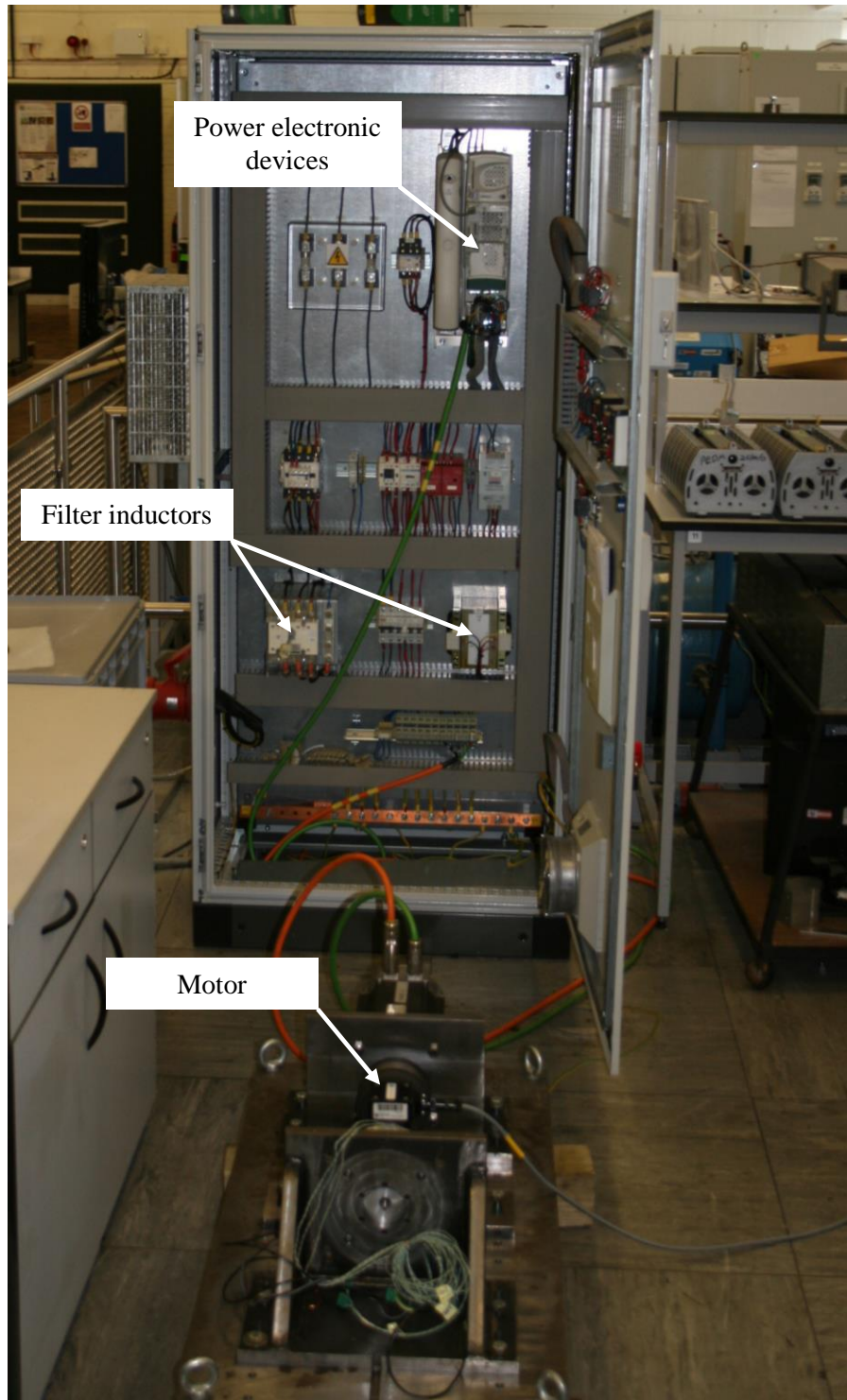
As ASD technology has matured, the trend has been towards the greater mechanical and functional integration of the various subsystems [3]. Vas and Drury in 1996 expected in the future that the power electronics and the motor would be integrated as a single packaged electronic motor unit [5].

The structural integration of all IMDs requires vigilant mechanical and thermal analysis of the machine and converter components collectively as a single unit. This packaged approach offers many advantages, as listed below [4, 6, 7].

- Volume/mass reduction over traditional, separately constructed systems resulting in an increased power density
- Possible EMC reduction/elimination due to the reduced length of cable transferring HF power
- Reduction in cooling system requirements incorporating a shared cooling system which also increases power density
- The ability to replace direct on-line machines with variable speed machines within the same package size
- Reduced installation time and cost due to single package construction

However, there are some challenges with such these compact systems, for example, advanced thermal techniques are needed for the integrated single package unit so as to avoid excessive heat which might damage the whole system. The effect of parasitic capacitance should be avoided between integrated components in high frequency applications.





**Figure 1-1 Standard cabinet of a variable speed drive with rated current 25 A**

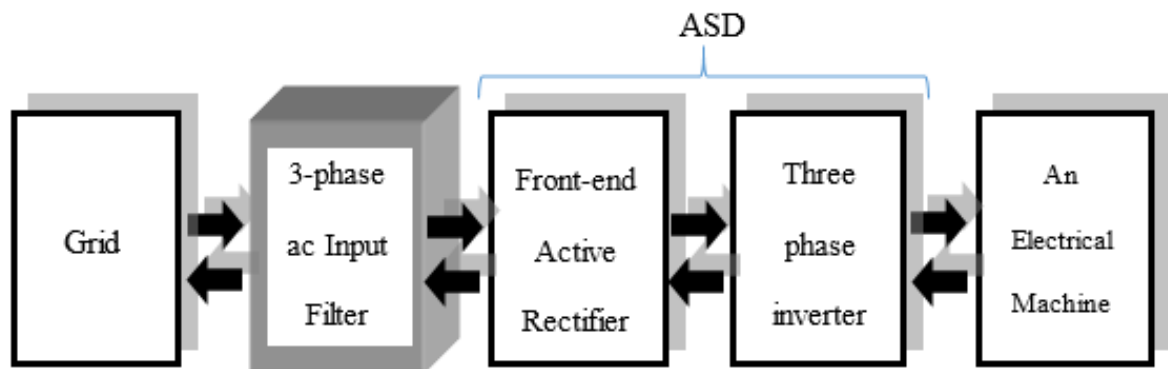
However, the most serious barriers for integrated systems are packaging, system integration issues, thermal management and the lack of standardisation of power electronics devices. This results in a need for better integrated system and design tools [3, 8].

In order to realise these advantages, physical integration of the various structural and functional components of an electric drive should be further investigated.

### 1.5.1 Input power filters and associated IMDs

Grid-connected drives are regulated by grid codes [9] which dictate the levels of total harmonic distortion (THD), power factor and sag sensitivity which the drives produce. In active power converters, supply current filtering is achieved using input filters which are responsible for reducing switching frequency ripple and suppressing voltage transients [2]. If unfiltered these converters would inject harmonic current distortions onto the supply current and hence input AC filters are used to mitigate these harmonics [2, 10]. Thus, an AC current filter is necessary for grid-connected, three-phase active rectifiers supplying ASDs.

In the most basic case, the DC-link inductor is replaced with 3-phase AC inductors at the input of a front-end active rectifier. However, large iron chokes are needed to improve the interaction between the utility grid and active converters [11-13]. A general schematic is presented in figure 1-2 to illustrate the power flow between the grid and an electrical machine via 4-quadrant drives. This diagrammatic presentation shows the location of input AC power filters and their function as an interface between the utility grid and a front-end active rectifier, which is part of the electric drive.



**Figure 1-2 Location of 3-phase input filters as an interface between a grid and ASDs system**

The block highlighted in figure 1-2 represents the 3-phase AC input filter which is the main target of this research for incorporation into an electrical machine.

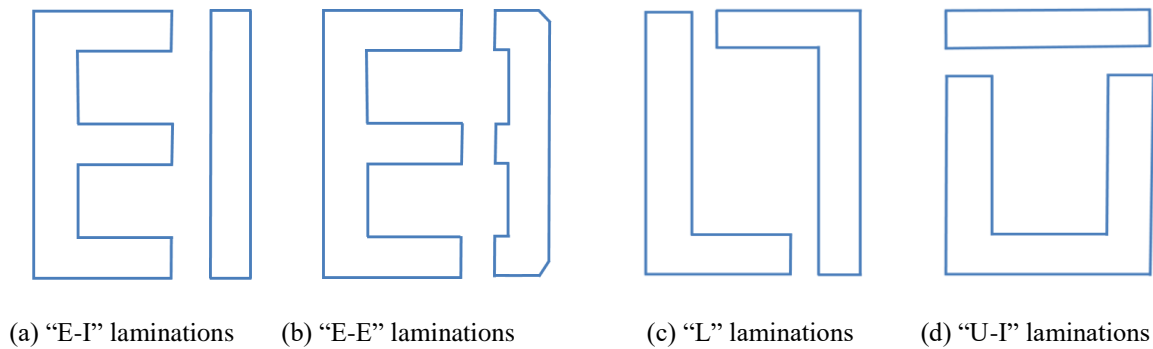
The input inductor is simply a passive two-terminal electrical component which acts as a high impedance to any load harmonics. Current harmonics are therefore attenuated to a level which is required by the regulations.

The voltage at the terminals of the inductor is related to the current flowing as shown below:

$$V_L = \frac{L di(t)}{dt} \rightarrow \frac{1}{L} \propto \frac{di(t)}{dt} \quad (1.2)$$

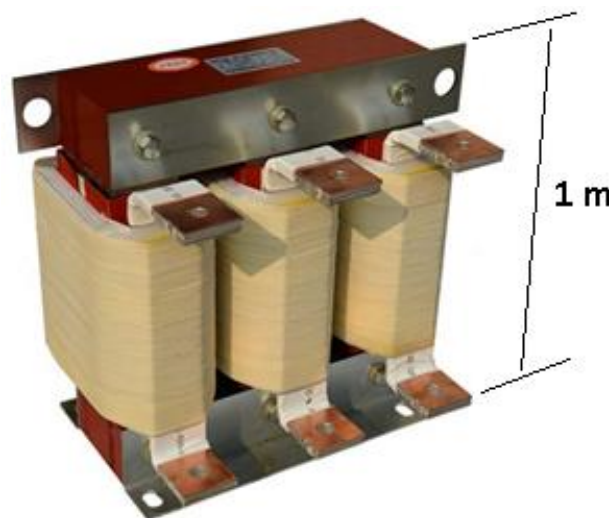
As the power rating of a drive rises then so does the required energy storage of the inductor. Thus the physical size of the inductor will rise approximately linearly with drive power rating.

Laminated iron cores are usually used for low frequency input filter inductors. Laminated cores are composed of punched steel sheets, with the surfaces of the sheets coated with insulating material, resulting in reduced eddy currents between the sheets. In practice, conventional 3-phase filter inductors share the same magnetic core circuitry as EE and EI cores (Figure 1-3 (a and b)). Other shapes of transformer cores can be LL and UI, as presented in figure 1.3 (c and d) [14].



**Figure 1-3 Different transformer core types**

As the size of the inductor is dictated by the demand of storage energy, an example from an industrial application shown in figure 1-4, which illustrates the physical size of a conventional input 3-phase AC reactor power inductor for an output power rating of 630 kW with a rated input current of 1600 A<sub>pk</sub> [15].

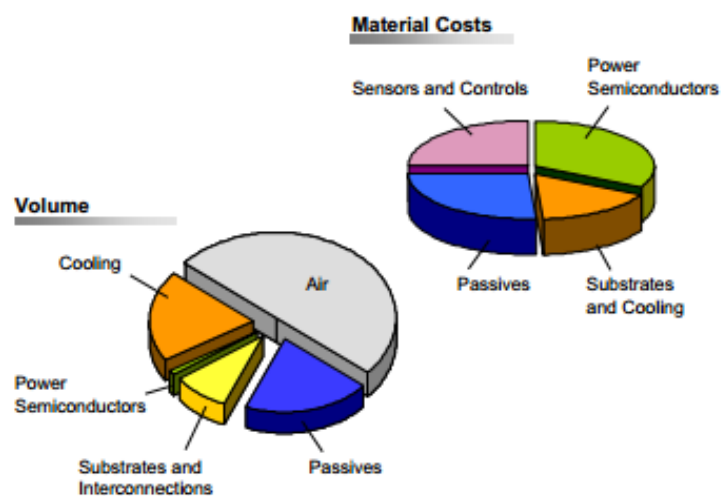


**Figure 1-4 3-phase input power inductors for rated power 630 kW/1600 A<sub>pk</sub> [15]**

Due to the required large size of these line inductors for high power applications and the demand for packaged electrical systems, integrating magnetic filter components into electrical machines is promising and can in turn achieve smaller sizes than with conventional inductors with a separate motor and drive with associated hardware [16, 17]. As a consequence, producing a single packaged unit along with achieving higher power density at low cost and installation time is feasible.

### 1.6 Passive components size and cost

Major challenges regarding the integration of passive components and power electronics often arise from limited installation space along with, most frequently, problems of mechanical stress and high temperature. Passive components (i.e. inductors and capacitors) represent a significant proportion of material costs and volume compared to other components in a power electronics system, as shown graphically in figure 1-5. In addition, the mechanical requirements dictate the installation space without considering the standardisation of power electronics devices and passive components.



**Figure 1-5 Typical material cost and volume distribution in power electronics systems [1]**

The focus on size reduction should be turned towards the passive components, such as converter chokes, DC-link capacitors and electromagnetic interference (EMI) filters. The achievement of high power density depends on innovative integration concepts, the flexibility of the overall structure and extensions to the operating temperature range. Meanwhile, system integration and modularity are not mutually exclusive [1, 3].

## 1.7 Methodology

Integrated drives are defined as the functional and structural integration of the power electronics converter with the machine as a single unit taking into consideration the electrical, thermal and structural impacts both components have on each other and the system as a whole.

For the purposes of this work, low and high drive power ratings are considered to deliver the power from the grid to following proposed machines in which the two machines are identically dimensioned.

- Low-speed surface-mounted permanent magnet synchronous motor (3000 RPM / 4.1kW).
- High-speed surface-mounted permanent magnet synchronous motor (25000 RPM / 34kW). This motor has been considered to be the base machine for the prototype demonstrator since the passive components are much larger and consequently more challenging.

Five different techniques are considered in this research in order to investigate the effectiveness of integrating input filter line inductors into the low- and high-speed machines. These techniques are as follows:

- Inductor windings around the stator teeth
- Inductor windings around the stator core back
- Inner auxiliary slots placed radially outwards from the primary slots
- Auxiliary slots around the outer surface of the stator in a double slot machine
- Inductors placed at the corners of square laminations

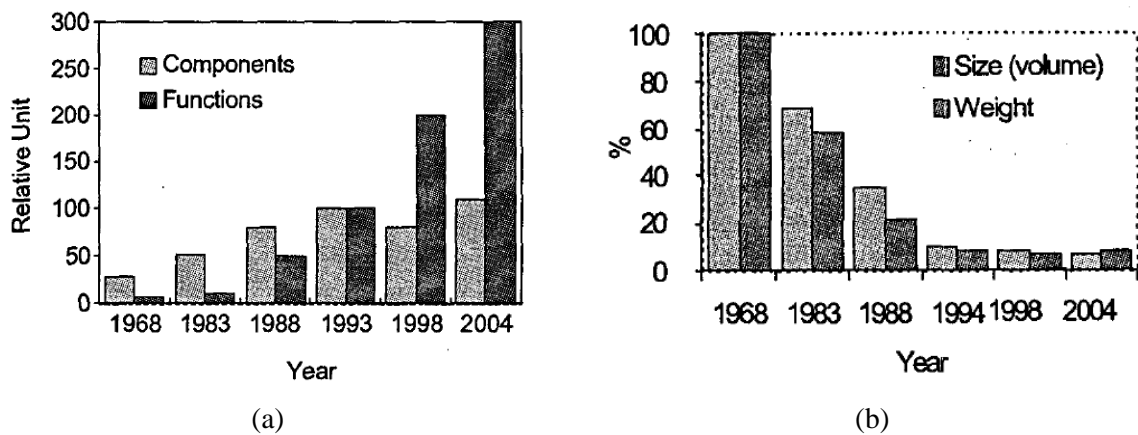
The best integration method would be selected in terms of achieving the smallest volume for the integrated 3-phase filter inductors compared to other suggested techniques.

The proposed integration techniques only take into consideration the input power filter inductors, as the most challenging task in integration is to incorporate filter inductors into a machine without interfering with the electromagnetic characteristics of the original machine. However, advances in technology are required to improve the functionality of integration systems, such as the standardization of parts, increased level of integration and improvements in packaging techniques for enhanced thermal management and electrical performance.

## 1.8 Prior work

Over the last twenty years, fundamental concepts and pioneering solutions have been proposed which strive to accomplish high power densities. The fundamental approach to power conversion has shifted to aim for high switching speeds [3]. This, in turn, results in the reduction in size of passive components and improvements in the efficiency of the converter, volume, weight, and cost. However, this motivation is valid only if adverse thermal effects at these higher frequencies do not negate the benefit of size reduction, indicating the need for the development of materials to meet the functional requirements of integrated systems.

The main trend in the industrial field towards passive elements, power electronics and electrical machines is the production of a single packaged system combining all of these different items of equipment. The efforts of researchers and industry aim to produce more efficient electrical and electronic components along with achieving lower volume and weight, lower installed system costs, and guaranteed electromagnetic compatibility. Figure 1-6 illustrates the development of components and functions and how the pace of progress steadily increased until the publication date of the reference (2004). These trends will have continued through to the present day.

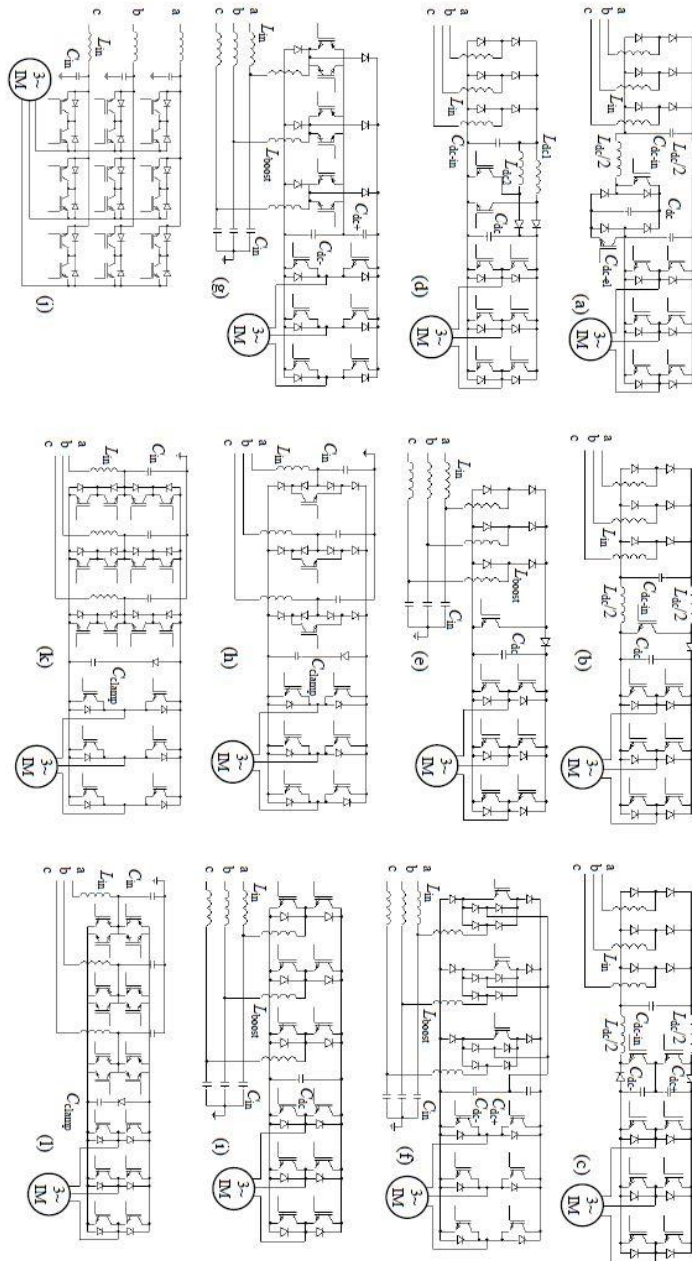


**Figure 1-6 The development of 4 kW standard adjustable speed drive: a) number of components and functions; b) comparison of size and weight [18]**

Figure 1-6 (b) clearly shows that a high level of integration has been achieved with the aim of reducing manufacturing cost while producing the most reliable systems possible. A number of converter topologies, including passive filter elements, are presented in figure 1-7, some of which are attractive for use in integrated motor drives. The range of integrated filter components presented in the literature can be divided into two categories based on their applications as follows:

- Integrating separate passive filter elements
- Integrating passive filter elements within the structure of electrical machines.

The next two sections focus on a comprehensive literature review of different approaches taken to reduce the size of passive filter components, whether separately or by incorporating them into electrical machines.



**Figure 1-7** Different converter topologies suited for integrated motor drives with: a) electronic inductor in dc-link; b) a boost converter; c) two interleaved CCM parallel boost converter; d) three-level CCM boost converter; e) DCM boost converter; f) Vienna rectifier; g) three-level PWM rectifier with RB-IGBTs, h) three-phase buck converter; i) back-to-back VSI, j) matrix converter; k) two-stage DPEC; l) two-stage DPEC with RB-IGBTs [2]



### 1.8.1 Developing integrated passive components

This section focuses on preliminary achievements in the size reduction of individual filter inductors. Three-phase PWM converters are essentially frequency conversion devices, converting input power of one frequency to output power of another frequency. Because this is performed through digital switching, both low and high frequency harmonics are introduced and filters are introduced to comply with electromagnetic compatibility (EMC) requirements [2].

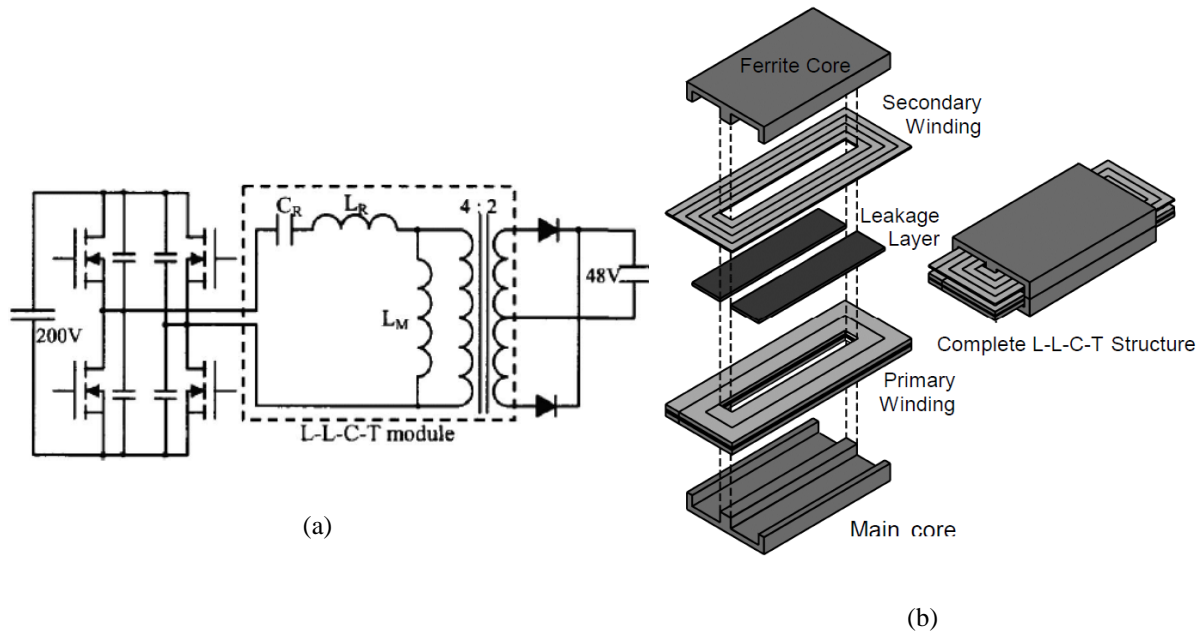
In some cases, the size of the inductor has been reduced through choice of control scheme. For example, the size of an inductor in a boost converter [19] has been significantly reduced by using chopped sinusoidal peak current control schemes. The proposed reference of peak current inductor is a chopped sinusoidal waveform for critical conduction mode in a PFC converter, and so the required inductance and peak current of the inductor can be reduced simultaneously.

Integrated three-phase common mode inductors [20] have been proposed which achieve a reduction to half of the total weight compared to separate reactors. This magnetic core structure design is composed of a peripheral ring and three bridge legs which are evenly distributed within the core structure. Three-phase inductor windings share the same magnetic circumferential magnetic core, whilst the air gaps of the inductors are located in the centre of the circular magnetic core. The material weight savings using this design of copper windings and iron per phase are 40% and 60% respectively. Furthermore, it has been stated [21, 22] that common mode inductors are widely required for ASD, UPS, battery charging for electric vehicles and renewable energy applications and hence further work has been conducted to design a common mode inductor aiming to minimize volume, losses and commissioning cost compared to separate industrial inductors.

For high frequency inductors a spiral integrated power passive structure has been enhanced over a number of years to introduce significant improvements in electromagnetic modelling, design and loss determination [23-26]. This integration approach has led to an integrated structure which can achieve high power densities in excess of  $30 \text{ W/cm}^3$  operated at frequencies up to 1 MHz [27]. The advantages of integrating high-density multi-functionality by using a planar integration technology have been introduced by Jacobus et al. [28]. This approach introduces two layers of simple spiral windings separated by a dielectric material, and this structure results in distributed inductance and capacitance to form a spiral integrated LC structure. This approach can be even more complex when forming an integrated resonant



transformer by adding additional layers of spiral windings. Figure 1-8, shows a converter circuit presents passive components which replaced by LLCT model and a 3D presentation of the construction of an integrated L-L-C-T respectively.



**Figure 1-8 Illustration of process of integrated L-L-C-T a) equivalent lumped parameters model of L-L-C-T, b) exploded view of construction of integrated L-L-C-T [28]**

However, the design of these integrated structures necessitates deliberate increases in and modifications to the existing impedance of the structure to satisfy the equivalent circuit functioning. The concept is applicable to very high frequency systems, but not to mains frequency filters. Where the frequency is 50 or 60Hz, as required in input filters, it is not feasible to introduce enough capacitance in this manner.

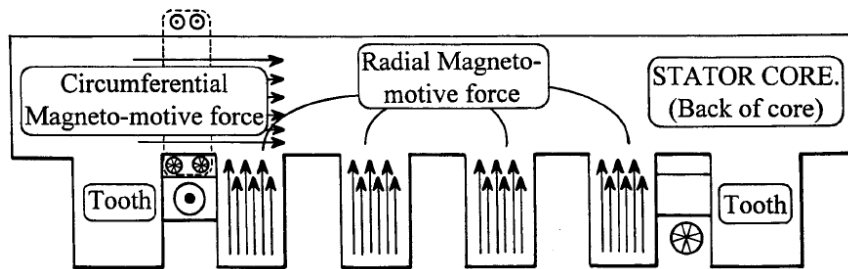
The next section presents a survey concerning how the passive components of filters can be integrated into electrical machines.

### 1.8.2 Integrated passive filter components within the structure of electric machines

The evolution of integrated passive components is still continuing, urged on by the industrial demand for compact systems such as IMDs. As mentioned above, the demand for integrated passive filter components is steadily increasing for some applications where the motor and load are intimately connected to each other along with limited installation space. The following literature survey of integrated filter elements into electrical machines is divided onto two parts: electromagnetic passive filter components and capacitors used in converter modules.

### 1.8.2.1 Integrated inductors within the stator of the machines

Work published by Garvey et al. [29] provides useful insights in to the integration of passive filter elements into an electrical machine. A  $dv/dt$  output filter is sometimes fitted between an inverter and motor so as to avoid sharp transient voltages caused by the speed of power electronics switching in variable-speed drive inverters, which in turn protects both the winding insulation of the motor and its bearings. In [29] the filter inductor windings are wound around the stator core back, returning around the bottoms of slots. The stator core back is utilized as a toroidal magnetic circuit which drives a ring flux and so forms the inductor, as diagrammatically presented in figure 1-9.



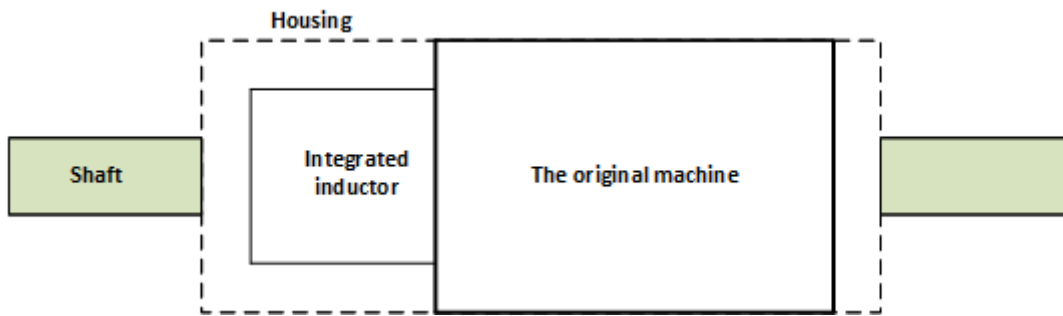
**Figure 1-9 Schematic view of shared stator core carrying integrated filter inductor and main machine windings [29]**

The inductor windings and main machine windings share the same machine stator core back, and so the ring flux caused by the inductor windings travels around the core back in the same direction at any instant. The direction of the main machine flux is dictated by the configuration of the base machine windings, and so at any instant there is as much flux rotating clockwise in the core back as is going counter-clockwise simultaneously. As a result of interaction between the two magnetic fluxes in the shared machine stator, the net magnetic flux at some points is high while at other points it is low. By far the most important constraint for integrating inductors into electrical machines following this type of integration is that the stator core back should not become saturated; in other words, the machine's magnetic circuit should not be too heavily loaded. Because the core back has no gap in it, this above arrangement, in which the inductor creates a circumferentially flowing flux will saturate the core back with low inductor MMFs, which forms a serious drawback.

A theoretical design study has been proposed [30] with the aim of integrating the output filter inductor into a permanent magnet synchronous motor. A part of the inductance of the motor windings is used to form the filter inductance, and thereby the filter capacitor and damping resistor are placed between the machine windings. This proposed integrated motor eliminates

the separate filter inductor, which in turn reduces the overall losses, weight and volume. However, the efficiency of the integrated motor is adversely affected by the integrated filter inductor because of the presence of switching components in the filter branch. In addition, based on the recommendations given to designers for the proposed motor with an integrated inductor, the filter branch should not occupy more than quarter of the entire motor windings, and therefore the remaining portion of the motor windings can carry the filtered current.

A further integration step forward has been accomplished [31] aiming to integrate the passive filter inductor in high-speed AC drives. This work presented two proposed integration methods: a motor-shaped rotational inductor and a motor-shaped rotor-less inductor. The design of the integrated inductors has a stator and rotor similar to those in a conventional motor or generator, but the main machine shaft is used as the inductor's rotor without any magnets, saliency or windings as shown in figure 1-10.

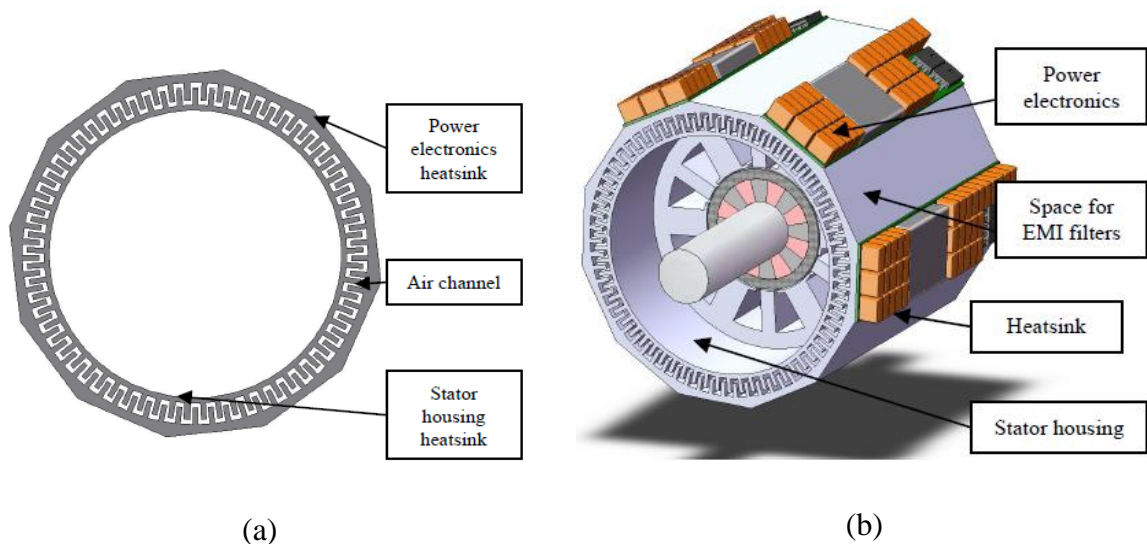


**Figure 1-10 Axial presentation of integrated motor-shaped inductor**

Since the inductor windings are inserted into the slots of an additional motor-shaped stator, slot opening gaps within the stator form the air gap of the integrated inductor. The advantages of this motor-shaped inductor are that it can share the same cooling system as the machine and so can operate at high current densities, in turn achieving lower volume. The other benefit of the proposed inductor shape is that it can share the same motor housing. However, both integration methods presented in this study [31] come at the value of 6.1% increase in weight.

A further integration method has been conducted [32, 33] which is named a compact integral PMS motor. This method has used machine corners to integrate the coils of the input line-filter and that of the DC-link. Two different placements of 4 coils have been designed as either back-to-back or side-by-side integration methods. Although these coils are incorporated into the stator core, they do not affect machine performance since the magnetic fluxes produced by these integrated coils have independent paths. This results in less iron being used, higher inductance

values are obtained, and the procedure for winding the filter coils is easier. Another patent [34] illustrates the possibility of integrating a transformer within the structure of a motor. This combination was utilized in a microwave oven to provide a step-down voltage for a fan. Auxiliary windings are wound around the stator lamination stack to share part of the motor's magnetic circuit. This compact product offers smaller space and lower cost compared to the separate transformers and conventional motors. A 50kW permanent magnet machine with integrated power electronics and fault tolerance has also been presented [35]. This integrated single unit increases power density, where in the aerospace industry weight, volume and reliability are of primary importance. Figure 1-11 illustrates the proposed concept, where the inner ring acts as a motor housing (Figure 1-11 (a)) responsible for cooling the motor stator while the outer ring jacket has been used to mount and cool the power electronics and EMI filter components. Figure 1-11 (b) demonstrates a more complete integrated motor drive.



**Figure 1-11 Integrated motor drive: a) motor housing and power electronics heat sink; b) integrated 50kW, 50krpm PM motor and power electronics concept [35]**

As stated in previous publications [36-40], several integration techniques seek to produce a packaged single unit; for example, power electronics components may be attached in front of a segmented stator in what is known as an integrated modular motor drive. Another example of a compact system is named the integrated segmented inverter-motor for drive traction systems in which the inverter IGBTs, gate driver and control card and bus capacitor are mounted on three separate plates axially positioned with the motor shaft. Modular systems offer many advantages, such as fault tolerance, power rating scalability, and better thermal capability along with potential reductions in the overall size and manufacturing cost. This has led to active research and the development of smaller passive components and advanced power modules.

### 1.8.2.2 Filter capacitors integrated into the motor structure

Capacitors are also used in ASDs as, for example, input/output filters and DC link capacitors. These entities represent a considerable amount of the volume and material cost of a power electronics system. The thermal limits of several common capacitor materials are also a challenge at high operational temperatures as they are typically considerably lower than the thermal limits of the magnetic components. A further issue concerning the operational temperature limits is that, at high temperatures, it is hard for a capacitor to hold charge due to leakage currents [41] effectively reducing the available capacitance at high temperatures. There are four main capacitors technologies available as listed below [1, 6]:

- Multi-layer ceramic capacitors (MLCCs)
- Aluminium electrolytic capacitors
- Polymer film capacitors
- Electro-chemical double layer (ECDL) capacitors

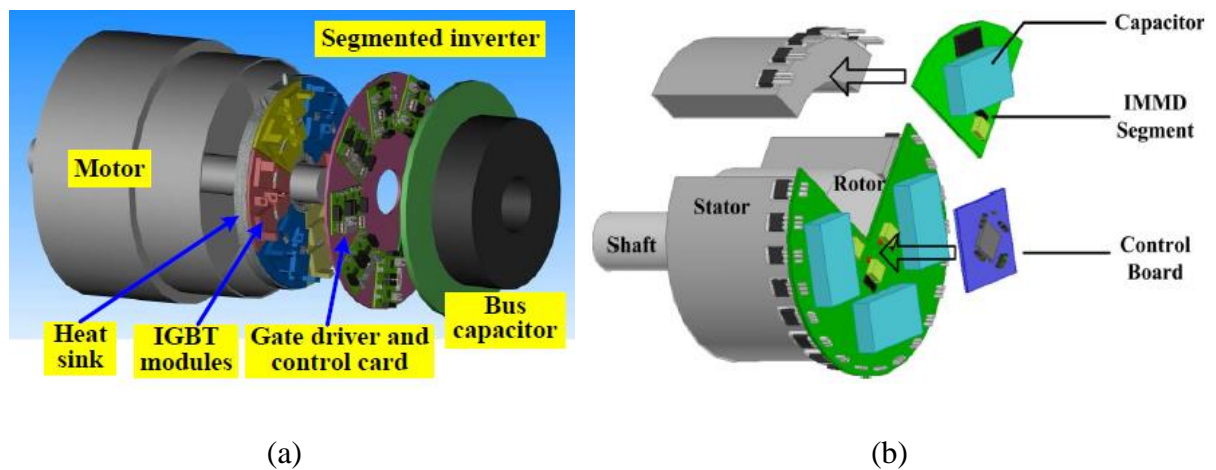
Ceramic capacitors are mostly used for high temperature and high voltage applications. The most important features of MLCCs are their high capacitance along with compactness. High temperature ceramic capacitors can withstand temperatures up to 250 °C along with achieving high energy density. Other types of capacitors are large and furthermore thermal limitations are a significant problem, especially in IMDs where the compact nature of the unit is essential [42]. The key technical advantage in integrating capacitors into the motor structure is to produce a single packaged unit with higher power density compared to separate motor-drive systems. However, the thermal limitations of the devices in conjunction with the restrictions of mechanical installation space are prominent issues. Consequently, the concept of integrating capacitors in IMDs has sparsely been considered in the literature.

It has been shown [43] that it is possible to use stator laminations to form a capacitor. The structure of adjacent laminations with insulation layers between them offers the possibility of creating an integrated capacitor although the capacitance per unit would be relatively small.

Gui-Jia et al. presented an inverter packaging scheme carried out for an integrated segmented traction drive system [38]. The system cost of a segmented traction drive is reduced due to segmenting the voltage source inverter, where the ripple currents and thus the size of the DC bus capacitor are significantly reduced. The ring-shaped segmented inverter design is shown in

figure 1-12 (a). The packaged inverter-motor drive system has six water channels in a toroidal heat exchanger which is capable of operating a single cooling system mainly used for the engine cooling loop.

Due to the restrictions of physical installation space for power electronics and passive components inside or on the motor housing, research into complete structural integration can be divided into three major categories: stator iron mount integration, surface mount integration, and end-plate mount integration. One study [39], an integrated modular motor drive with GaN devices has been presented. A circle-plate shape is used for mounting the DC-link capacitor, while MOSFETs are distributed evenly and circumferentially on the integrated plate and mounted on the stator iron surface as shown in figure 1-12 (b).



**Figure 1-12 Integrated motor-drive system: a) design concept for an integrated segmented inverter-motor drive system [38]; b) integrated modular motor drive [39]**

However, integrating capacitors into the structure of electrical machines is still an embryonic area and is a considerable challenge in order to achieve a smaller volume compared to independent electric drives. It is sufficient here to note that advanced standardised design processes along with new materials are needed to satisfy future demands.

## 1.9 Outcome of the literature review

Increasing demand for distributed power system approaches related to system integration has been demonstrated necessitating a step forward in standardized, decentralized power system components and integrated design technologies. The merits and advantages of new integration concepts compared to traditionally separated systems have been discussed, such as modularity, redundancy, serviceability and fault tolerance. Integrated motor drives or electronic motors designs seek to profit from these advantages in a trade-off with the challenges of mechanical,

electromagnetic and thermal material capabilities. For integrated passive components, several integration methods have been proposed whether separately or within a machine structure. The relative size of the inductor within a drive has been reduced to a certain extent as identified in the literature, however, more advanced integration approaches are still needed to meet future demand for compact systems.

There has been very little research into the integration of the AC input inductors within electrical machines. The author believes that the contribution made in this work has not previously been published by others.

# CHAPTER 2

## Input Power Filter Design

---

**Summary\_** In this chapter conventional input power filters and the principles of different filter designs are discussed. Specifications for low- and high-speed drives are chosen and the total filter inductance is calculated for each filter type. An overall comparison between these filters is conducted in terms of achieving the lowest inductance. The most appropriate type of input power filter is selected for the chosen drive systems. Finite Element Analysis (FEA) is been used to build and simulate the two sets of 3-phase LCL filters inductors for the low- and high-power ratings. The optimal volume achieved for both low- and high-power inductors will then be used as a benchmark throughout this thesis to compare with cases when these inductors are integrated into electrical machines.

### 2.1 Introduction

It is important to consider the effect of harmonic emissions from drives on other equipment, and their possible effect on the drive itself. Even when AC drives use a front-end active rectifier at their input, harmonics are still present in the current drawn from the supply, which need to be filtered. Harmonics currents flowing through the impedance of the supply cause harmonic voltages which can disturb or stress other equipment connected to the same supply point [44].

There are regulations to protect a public power network from excessive harmonics. For installations such as variable-speed drives and uninterruptable power supplies, which contain a large proportion of power electronic equipment, they may have to meet the requirement of the supply authority's guidelines before they have permission to be connected to the public network. For variable-speed drives, the subject of harmonics is generally considered independently from other EMC aspects, which are concerned with the effects of much higher frequencies and are created in a different manner.

### 2.2 Regulations

Regulations exist to control the quality of power that is to be provided at the point of common coupling (PCC) with other power consumers, where the immunity to excessive harmonics is



granted [9, 44]. Detailed regulations may be found in the references: in this section the low- and high-frequency emissions are discussed in brief.

- **Low-frequency emissions**

There are two kinds of regulations, including regulations for installations and regulations and standards for equipment. These regulations tend to be based on achievable voltage distortion that can be tolerated by other equipment. This limitation of distortion can be specified in terms of total harmonic distortion (THD), which is expressed as a percentage of the ratio of harmonic voltage to the fundamental; more details can be found in [9, 44].

The accepted maximum THD in a low voltage system, named the compatibility level, is 8 per cent however, in order to achieve this with a high degree of confidence it preferable to aim for a lower level of typically 5 per cent. It is not recommended to allow the compatibility level of 8 per cent to be exceeded [44], because it is then likely to affect other equipment, which will have been designed according to this standard of harmonic limitation. For example, regulations from the United Kingdom Energy Networks Association recommend clear strategies to permit connection, based on harmonic current data that can be easily obtained from the manufacturer's technical data. The international standard of harmonic control for equipment at less than 16 A is IEC 61000-3-2 as adopted from [44]. The recommended current distortion limits (IEEE Std 519-2014) applies to users connected to systems and is illustrated in table 2-1, where the rated voltage is 120 V to 69 kV at the PCC [9].

**Table 2-1 Current distortion limits for systems rated 120 V through 69 kV**

Maximum harmonic current distortion in per cent of $I_L$						
Individual harmonic order (odd harmonics)						
$I_s/I_L$	$3 \leq h < 11$	$11 \leq h < 17$	$17 \leq h < 23$	$23 \leq h < 35$	$35 \leq h < 50$	TDD
$< 20$	4.0	2.0	1.5	0.6	0.3	0.5
$20 < 50$	7.0	3.5	2.5	1.0	0.5	0.8
$50 < 100$	10.0	4.5	4.0	1.5	0.7	12.0
$< 20$	12.0	5.5	5.0	2.0	1.0	15.0
$> 1000$	15.0	7.0	6.0	2.5	1.4	20.0

$I_s$  = maximum short-circuit current at PCC

$I_L$  = maximum demand load current (fundamental frequency component) at the PCC under normal load operation conditions

TDD= Total demand distortion

- **High-frequency emissions**

The power stage of a variable-speed drive is a potentially powerful source of electromagnetic emission due to the high voltage and current in conjunction with rapid switching. Unwanted electromagnetic coupling is unlikely to occur below about 100 kHz. If the installation guidelines are ignored, interference predominantly occurs in the 100 kHz to 10 MHz range, where harmonic emission is strongest [44].

The most important standards for drive applications are listed below [9, 44, 45].

- IEC Standard 61000-4-7: a general guide on harmonics and inter-harmonics measurement and instrumentation, for power supply systems and equipment connected thereto.
- IEC 61800-3 power drive systems (contains emission and immunity requirements).
- IEC 61000-6-2 generic immunity standard for the industrial environment.
- IEEE Standard 519-2014 recommended practice and requirements for harmonic control in electric power systems.

As a consequence, it is important for users or designers of variable speed drives to know the authority's guidelines in terms of maximum allowable THD and harmonic emissions range, to prevent interference and poor quality of public power network.

### **2.3 Use of an input power filter**

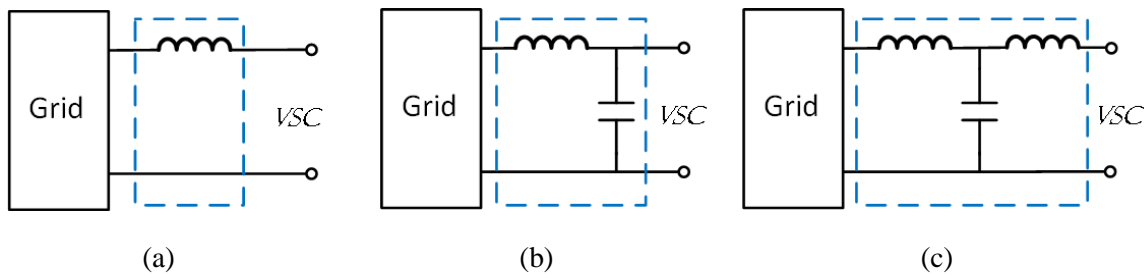
Input power filters are widely used with voltage source converters (VSCs) as this type of converter has well-known advantages in terms of improved energy efficiency and flexibility of control. A sizable proportion of grid-connected drives utilise an active front-end rectifier offering various advantages such as being able to work bi-directional power modes and having the capability to provide a unity power factor load [44, 46]. Voltage source active rectifiers become more attractive in industrial applications, such as the interfacing of power generation systems. Input power filters are generally necessary for all grid-connected drives of rating over 1kW.

A considerable amount of research effort has been devoted to attenuate the switching frequency ripple, using different types of input power filters, such as the L type, LC type and LCL type. As discussed in chapter one, the overarching role of input filters is to mitigate current harmonics distortions and to alleviate the burden upon the utility grid. The resonant frequency of LC filters

changes with varying grid inductance, and hence they are not the optimal choice to act as input power filters, especially for a weak grid [47, 48]. This type of filter is therefore not considered in this study. The European standard frequency range is 2-150 kHz and it might extend in future. Therefore, power grid filters should be designed to operate in this range or even at higher frequencies: as such the recommended interval of total harmonic distortion (THD) is up to 5 % [44, 46]. Capacitors are essential elements of the filters, but there is still a lack of standardisation [49]: less efforts have been paid in this study to integrate them within electrical machines.

Different topologies of input power filter types are identified in figure 2-1.

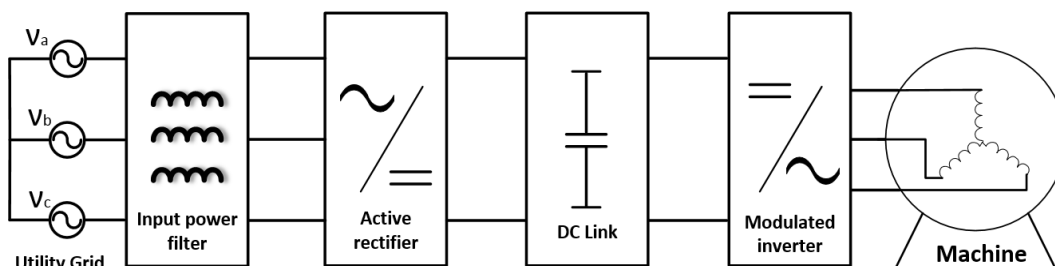
The sizing of input filter inductors is dictated by the rated power of the drive they are connected to. For example, if the rated power drive is increased by a factor of  $\chi$ , the input current of the drive will increase by the same factor of  $\chi$  and hence the storage energy required in the filter will increase by the same factor. Therefore the size of input filter inductors becomes significantly larger for high-power applications.



**Figure 2-1 Different topologies of input filters: a) L type; b) LC type; c) LCL type**

In the literature, it is shown that LCL filters offer optimum results in power ranges up to hundreds of kilovolt-amperes (kVA) [46].

The LCL filter components per phase are the grid-side inductor, boost inductor (drive-side), capacitor and damping resistor. The grid-side inductor and capacitor are physically small compared to the drive-side inductor, which accounts for the largest proportion of volume among the LCL filter components. Figure 2-2 illustrates the schematic of a grid-connected drive with an input power filter to deliver power to an electrical machine.



**Figure 2-2 Schematic of a conventional electric drive system**

## 2.4 Specifications of low- and high-power drives

Two different speed drives have been chosen with specific power ratings, driving two machines of similar dimensions and torque capability, operating at different speeds for comparison purposes. High and low power ratings result in very different filter sizes, despite the electrical machine sizes being effectively the same and due to the purpose of this research only winding/number of turns is adjusted for operation at different speeds. The two machine ratings are given in Table 2-2: one of 4.5 kW drive is operating at 3000 RPM, whilst the other is 38 kW at 25000 RPM.

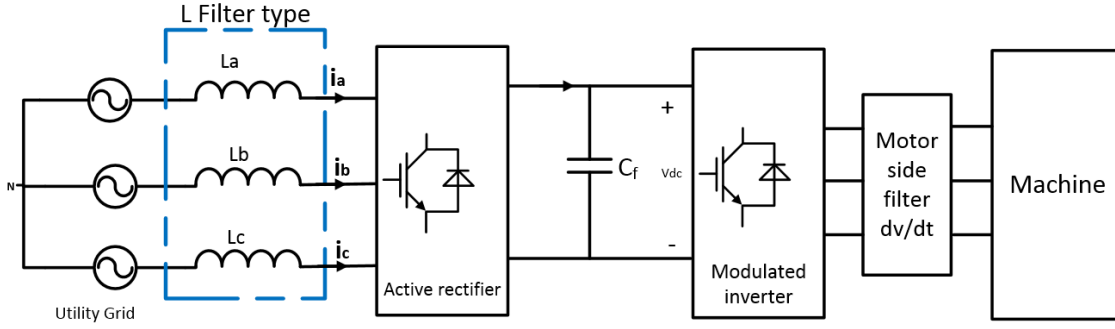
**Table 2-2 Specifications of two prototype motor design**

Drive input power (assuming $\eta=90\%$ ) (kW)	Machine output power (kW)	Phase current of motor (assuming 530 V) (rms)	Input current rms of VSC (assuming 90% efficiency)	Base machine power density (active area) (kW/l)	Machine speed RPM
4.56	4.1	5.7	6.34	7.46	3000
38	34	47.35	53	61.8	25000

In order to integrate passive filter elements (i.e. inductors and capacitors) into an electrical machine, the designer must first determine the specification of these passive components. The following consideration of L and LCL filters in terms of integration is sufficient to provide a comprehensive investigation of the effectiveness of different integration techniques for low- and high-power ratings.

### 2.4.1 L type filter

Three input line inductors have been used as an L type filter to reduce the current harmonics around the switching frequency. The higher the switching frequency of the converters, the higher the degree of attenuation which will be achieved [50]. Figure 2-3 shows three identical input line inductors acting as an interface between the grid and the inverter power circuit.

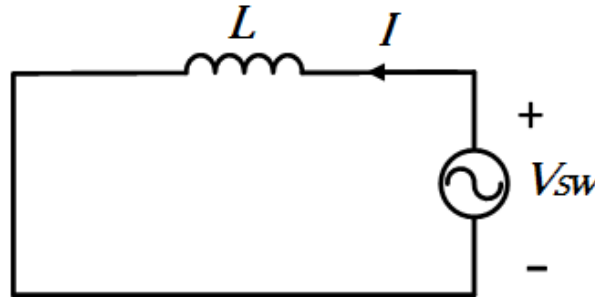


**Figure 2-3 Schematic of permanent magnet machine ASD circuit including three-phase identical input line inductors (L filter type)**

For high-power applications these inductors are large and the system's dynamic response can be poor [46].

#### 2.4.1.1 Frequency response of L filter type

In order to observe the behaviour of the L type filter across a wide range of frequencies, a Bode diagram should be obtained. The per-phase equivalent model of the L filter is shown in figure 2-4, where  $L$  is a series line inductor per phase: an ideal sinusoidal grid voltage profile is assumed and for this analysis the grid voltage is shorted. The transfer function of the L filter assumes an ideal inductor with zero resistance as follows:

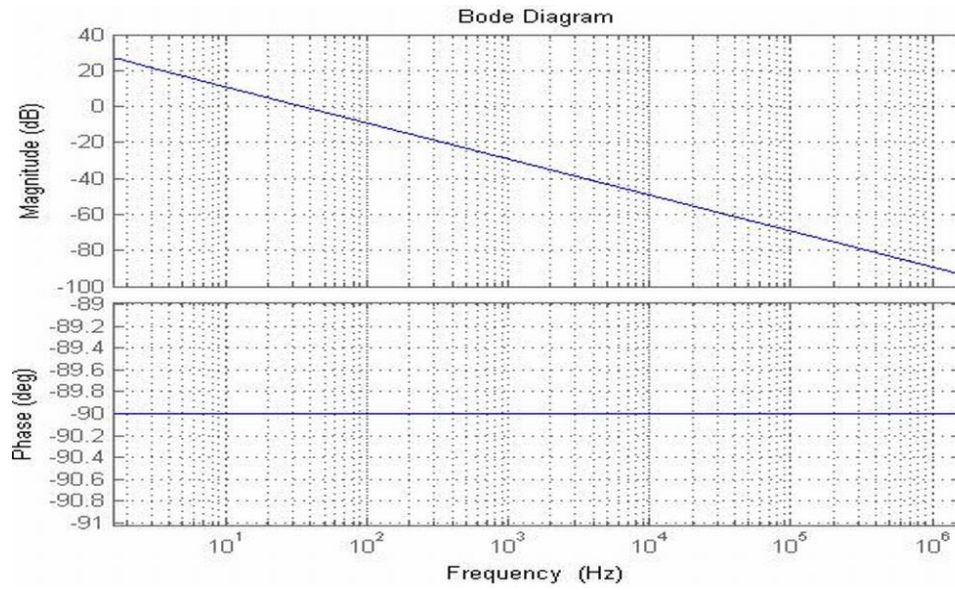


**Figure 2-4 Equivalent circuit of L type filter including only the switching harmonic component**

The transfer function is given in the form:

$$T_L(j\omega) = \frac{I(h)}{V_{sw}} = \frac{1}{j\omega L} \xrightarrow{s\text{-domain}} T_L(s) = \frac{1}{sL} \quad (2.1)$$

The frequency response of the L type filter between 1 Hz and 1MHz is plotted in figure 2-5 with an arbitrary value of filter inductance.



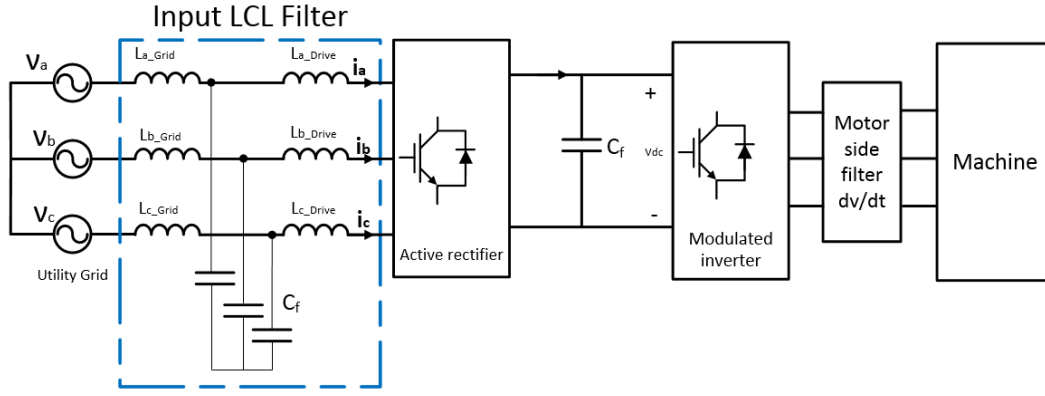
**Figure 2-5 Frequency response of L filter using Bode diagram**

Figure 2.5 shows that the L type filter provides an attenuation of -20 dB per decade for the whole range of frequencies due to its first order nature.

Regarding the design of L filter type, the volt-ampere rating of the inductor has been estimated to be between 2% and 6% of the total volt-ampere of the drive [44]. In order to have an accurate comparison between L type filters and LCL filters, the L filter should achieve the same total harmonic distortion as the LCL filter.

### 2.4.2 LCL Type Filter

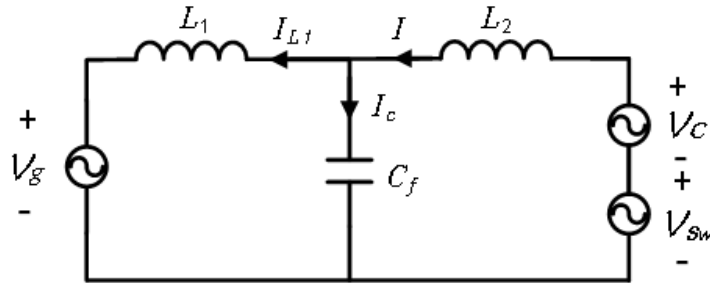
An LCL filter is constructed by adding an LC filter to a boost inductor. This type of filter is attractive and is widely used due to its smaller volume compared to other types of power filter. LCL filters can render better attenuation of switching harmonics and smaller total inductance than L filters [46, 51, 52], this will be further discussed in this study. The design of an optimal LCL filter can be accomplished with two different configurations: star-connected or delta-connected capacitors, further details of which can be found in [52]. Figure 2-6 illustrates a three-phase voltage source rectifier with an LCL star capacitor connection.



**Figure 2-6 Three-phase voltage source rectifier with LCL filter**

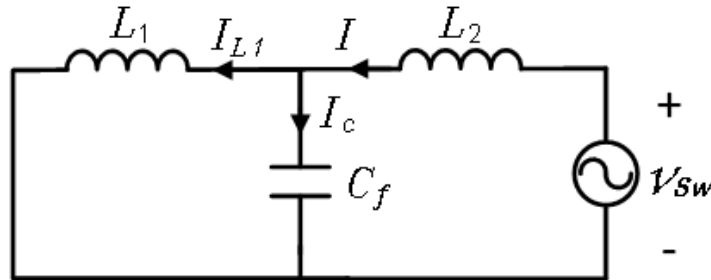
#### 2.4.2.1 Frequency response of the LCL filter

An equivalent single-phase LCL filter including the fundamental input converter voltage ( $v_c$ ) and switching harmonics voltage ( $v_{sw}$ ) components is shown in figure 2-7.



**Figure 2-7 Equivalent circuit of single-phase of LCL input filter showing switch harmonics and voltage fundamental components**

where  $L_1$  and  $L_2$  are the grid side and drive side inductors respectively,  $C_f$  is the filter capacitance and the currents  $I_{L1}$ ,  $I$  and  $I_c$  are grid current, input converter current and capacitor current respectively. Attenuation of the switching harmonics current is considered in figure 2-8.



**Figure 2-8 Equivalent circuit of single-phase LCL input filter considering switch harmonics fundamental component**

The transfer function of the LCL filter is given in the following form:

$$T_{LCL} = \frac{I_{L1}}{V_{s\omega}} \quad (2.2)$$

For this analysis all inductor resistances are once more ignored. For a short circuited grid the transfer function with and without a damping branch can be derived as follows<sup>1</sup>:

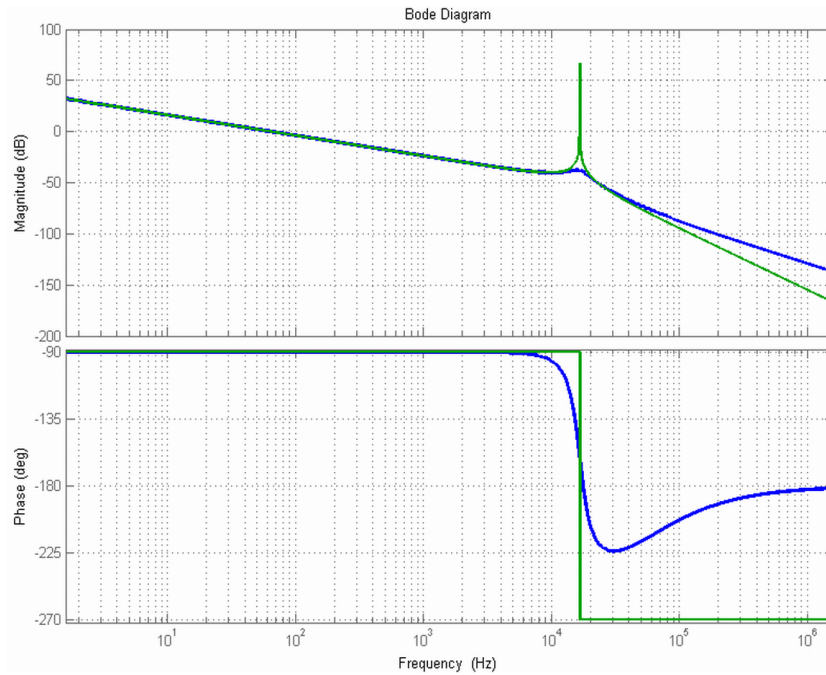
- LCL transfer function derived without damping:

$$T_{LCL}(s) = \frac{1}{L_1 C_f L_2 s^3 + (L_1 + L_2)s} \quad (2.3)$$

- Transfer function taking into consideration the damping resistor  $R_d$ :

$$T_{dLCL}(s) = \frac{C_f R_d s + 1}{L_1 C_f L_2 s^3 + C_f (L_1 + L_2) R_d s^2 + (L_1 + L_2)s} \quad (2.4)$$

The behaviour of these two transfer functions with and without damping has been examined using a Bode diagram. The Bode plots of the LCL filter are illustrated in figure 2-9. It can be seen that the series damping resistor with the capacitor is important to eliminate the spike at the resonance frequency where the impedance of the filter at this resonant frequency is zero [52] and it has rolled off to -180 degrees at higher frequencies.



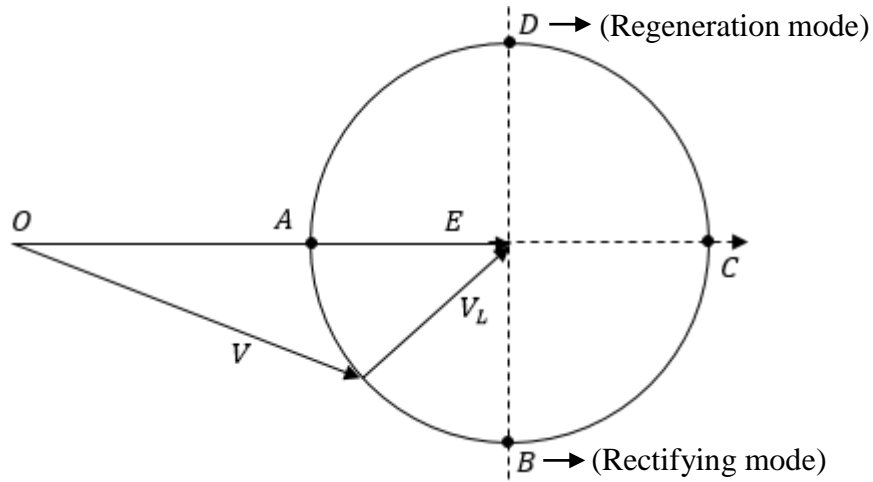
**Figure 2-9 Bode diagram for LCL filter with (blue) and without (green) damping resistor**

<sup>1</sup> The derivation of the transfer function equations of LCL filter is illustrated in Appendix A.



### 2.4.2.2 Constraints on LCL filter parameters

A higher harmonic attenuation factor can be achieved using LCL filters, allowing the use of lower switching frequencies and hence lower switching losses. However, the total inductance of the LCL filter should be appropriate for the required active and reactive power rating of the voltage source rectifier. LCL filters should be carefully designed to meet the standard range of harmonic constraints as given in IEEE-519 [45, 47, 53]. The phasor diagram given for the grid voltage and the input of the voltage source rectifier (VSR) has been derived elsewhere [52] as illustrated in figure 2-10.



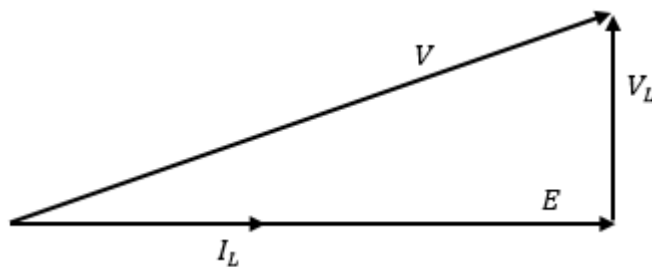
**Figure 2-10 Illustration of the relationship between AC side vectors of VSR [52]**

Here  $E$  is the grid phase voltage,  $V$  is the input voltage of the VSR and  $V_L$  is the voltage across the line inductor and  $I$  is the peak value of phase current.

The trajectory of the input voltage of the VSR around the circle is as given in equation (2.5).

$$|V_L| = \omega L |I| \quad (2.5)$$

It can be seen in figure 2-10 that at points B and D the VSR is operating in rectifying and regeneration modes respectively and the power factor at these points is a unity power factor. As in figure 2-11 the total input filter inductance per phase at a unity power factor can be determined as follows:



**Figure 2-11 Phasor diagram at unity power factor**

$$V^2 = E^2 + V_L^2, \quad \text{where } V(\text{per phase}) = \frac{V_{dc}}{2} \quad (2.6)$$

$$\left(\frac{V_{dc}}{2}\right)^2 = E^2 + (\omega LI)^2 \quad (2.7)$$

$$\omega LI = \sqrt{\left(\frac{V_{dc}}{2}\right)^2 - E^2} \quad (2.8)$$

Thus, the total input filter inductance per phase should be limited to be defined as given in equation (2.9).

$$L_{Total} \leq \frac{\sqrt{\frac{V_{dc}^2}{4} - E^2}}{I \omega} \quad (2.9)$$

where  $V_{dc}$  is the DC bus voltage and  $\omega$  is the angular frequency.

Current harmonics of the switching frequency produced by an active rectifier might cause inductor saturation or filter resonance and hence current harmonic distortion should be within the recommended limit of THD (planning level) which is up to 5% [44]. The input filter inductor should be carefully designed with the optimal inductance value, taking into the account maximum peak-to-peak current ripple. Moreover, the value of  $L$  should be small to give a suitable dynamic response of the system and the capability for current tracking.

#### 2.4.2.3 Design methodology for the LCL filter

The procedure for designing the LCL filter has been carried out step by step to achieve an optimal filter design based on the desired power rating of the converter, line frequency, switching frequency and the applied line-to-line voltage. Indicative, stylised current waveforms for each of the LCL filter components are shown in figure 2-12.

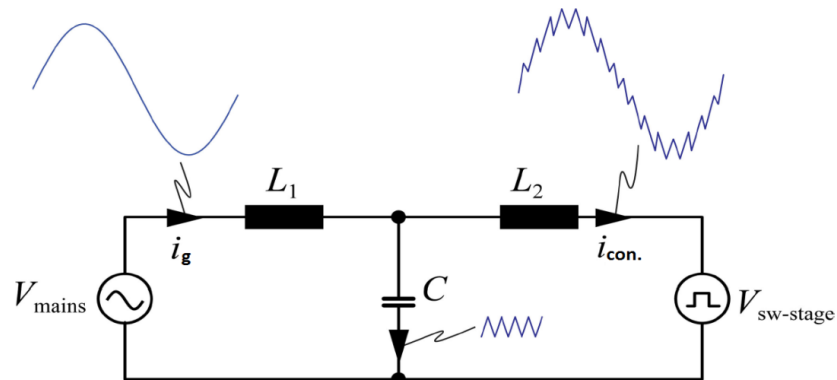


Figure 2-12 Current waveforms for each filter component [51]

In the following calculations, the filter values are a percentage of the base values as follows:

$$Z_b = \frac{E_n^2}{P_n} \quad (2.10)$$

$$C_b = \frac{1}{\omega_g Z_b} \quad (2.11)$$

where  $E_n$  is the line-to-line rms voltage,  $\omega_g$  is the grid angular frequency and  $P_n$  is the rated power absorbed by the converter.

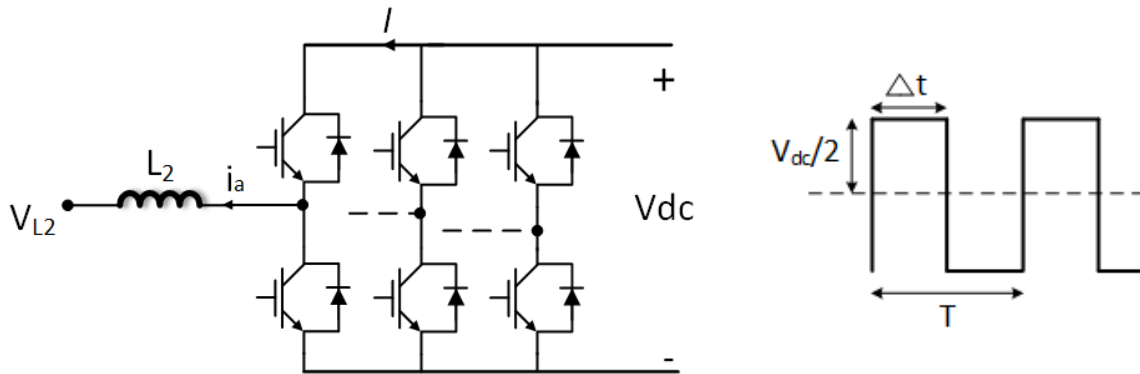
The following equation can be used to find the maximum RMS input current, assuming a unity power factor:

$$I_{max} = \frac{P_n}{3 V_{ph}} \quad (2.12)$$

#### 2.4.2.4 Calculation of drive-side inductance ( $L_2$ )

The maximum current ripple is used to calculate the drive side inductor, which in turn gives a sensible size for the predicted boost inductor design. The minimum value of the drive side inductance  $L_{2min}$  per phase can be calculated as follows:

Figure 2-13 shows a simplified equivalent circuit of the drive-side inductor as a part of the LCL filter.



**Figure 2-13 Illustration of a simplified equivalent circuit of single phase of drive-side filter inductor  $L_2$  in generating mode**

The volt-ampere rating of the drive-side inductor,  $L_2$ , has been estimated to be 1% of the total rating of the drive, and this estimation gives an acceptable value of THD on the grid-side which is consistent with that achieved with the L filter type. The comparison between the L and LCL filters is presented later in section 2.5, in terms of achieving the same value of THD and

different total inductance. A piecewise linear electrical circuit simulation (PLECS) is the tool of choice for high-speed simulations of power electronic systems developed by Plexim. A PLECS circuit was used to confirm that the designed LCL filter achieves the same value of THD as the L filter type with the same specifications of drive used. The minimum value of the drive side inductance  $L_{2\ min}$  per phase can be calculated as given in equations 2.13 – 2.15:

$$V_{L2} = 1\% V_{ph(rms)} \quad (2.13)$$

$$V_{L2} = \omega L_{2\ min} I \quad (2.14)$$

$$L_{2\ min} = \frac{0.01 \times V_{ph(rms)}}{2 \pi f I_{rms}} \quad (2.15)$$

#### 2.4.2.5 Calculation of filter capacitance ( $C_f$ )

In practice, the fundamental reactive power which is absorbed by the filter capacitor should be less than 5% of the rated power of the voltage source rectifier in order to avoid the system suffering from an excessive decrease in power factor [52, 53]. Therefore, the capacitance value is calculated based on equation (2.16), where  $C_b$  is given in equation (2.11):

$$C_f < 5\% C_b \quad (2.16)$$

#### 2.4.2.6 Calculation of grid side inductance ( $L_1$ )

The LCL filter parameters should be designed based on the expected attenuation factor  $K_a$  of the current ripple, which is recommended in literature to be set to 5 on the rectifier side. Further information can be found in [46, 53].

The grid-side inductance can be calculated based on the capacitance value and the angular switching frequency for the expected attenuation factor, as given in equation (2.17):

$$\left( L_1 = \frac{\sqrt{\frac{1}{K_a^2} + 1}}{C_f \omega_{sw}^2} \right) \quad (2.17)$$

#### 2.4.2.7 Calculation of the damping branch $R_d$ and resonant frequency $f_{res}$

As the filter impedance is zero at the resonant frequency, a series resistor is inserted with the shunt capacitor at this frequency so as to prevent resonance through passive damping and hence guarantee a stable system [46]. The Bode diagram in figure 2-9 illustrates the influence of passive damping.

The value of damping resistance should be one-third of the filter capacitor's impedance at the resonant frequency [51]. In order to avoid resonance problems in the lower and upper parts of the harmonic spectrum, the resonant frequency should be in a range between ten times the grid frequency and one-half of the switching frequency [51]. Thereby, the angular resonant frequency and damping resistance are derived as follows:

The total impedance of the input filter is zero at the resonant frequency and from the equation for the transfer function of the LCL filter which is derived in Appendix A, the angular resonant frequency can be calculated at this specific condition by equations 2.18 and 2.19.

$$\omega_{res}^3 L_1 L_2 C_f + \omega_{res} (L_1 + L_2) = 0 \quad (2.18)$$

$$\omega_{res} = \sqrt{\frac{L_1 + L_2}{L_1 L_2 C_f}} \quad (2.19)$$

The values of grid and active converter inductances should then satisfy the following condition [46]:

$$10 f_g < f_{res} < 0.5 f_{sw} \quad (2.20)$$

Thus the desired damping resistance can be calculated based on the resonant frequency as given in equation 2.21.

$$R_d = \frac{1}{3\omega_{res} C_f} \quad (2.21)$$

### 2.5 General comparison between the total inductance of L and LCL filters

Calculation of the L filter inductance as given in equation 2.22 is based on the L filter design constraint in section 2.3.1, with the drop voltage across the filter inductor chosen to be 3%.

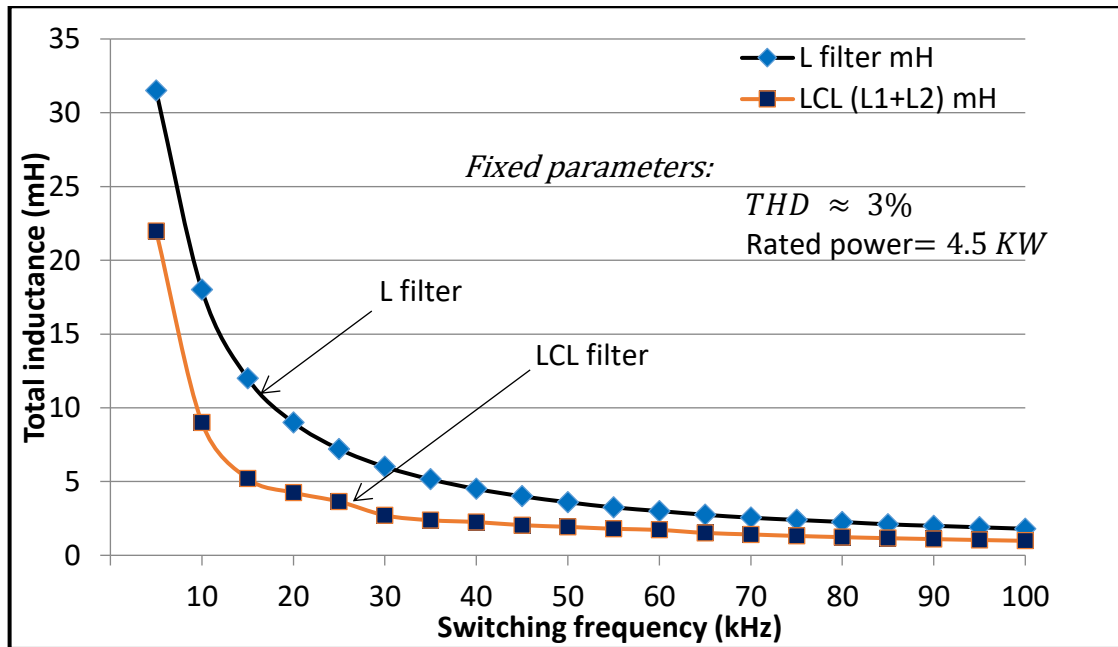
$$V_L = 3\% V_{ph} \quad (2.22)$$

$$V_L = \omega L I \implies L = \frac{V_L}{2 \pi f I} \quad (2.23)$$

Comparison has been made for two different scenarios as follows.

- **Converter power rating and THD are fixed and the switching frequency of the rectifier varies**

In this case study, the values of different L and LCL filter types have been calculated based on a number of constraints. As shown in figure 2-14 the switching frequency of the active rectifier is altered for a wide range of frequencies up to 100 kHz, and the same converter power rating of 4.5 kW is considered for all different filter designs. For integrity of comparison in terms of achieving lower inductance, all filter designs achieved the same attenuation of THD of 3%.



**Figure 2-14 Comparison of L and LCL filters at different switching frequencies**

It can be seen from figure 2-14 that the total inductance of the L filter is almost double that of the LCL filter at different switching frequencies, showing that it is much less attractive for integration due to its larger physical size.

- **Rectifier switching frequency and THD are fixed and the converter power rating varies**

The second case of comparison between L and LCL type filters is conducted when the switching frequency of the active rectifier and the THD are fixed, and the converter power rating is varied up to 40 kW. Figure 2-15 illustrates different total values of inductance in different power rating ranges for L and LCL filters with respect to the shunt capacitor values for the LCL filter.

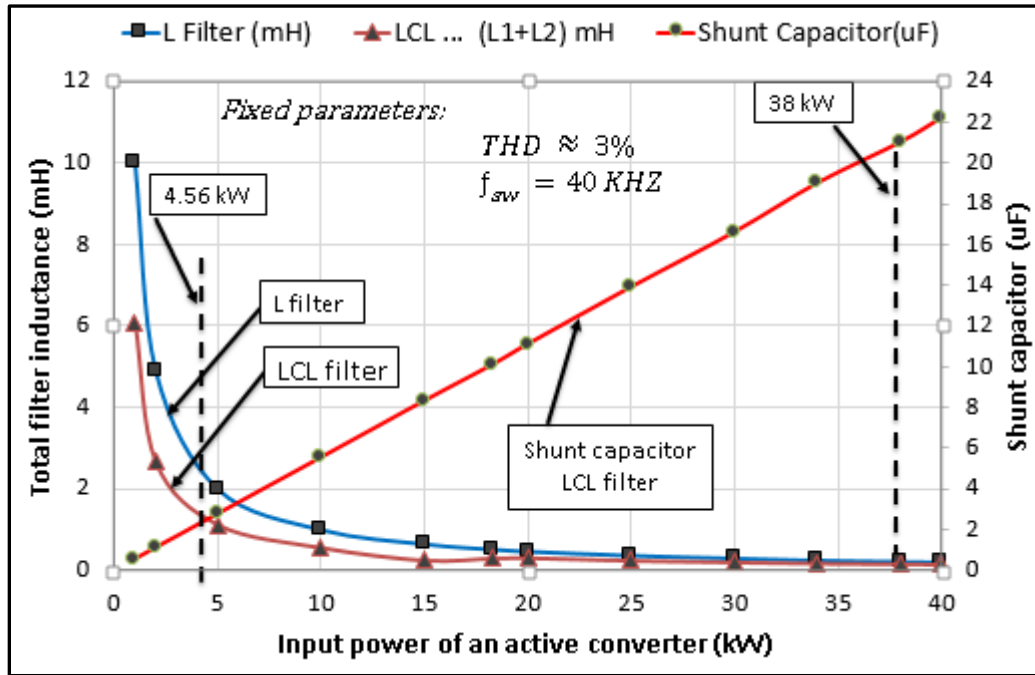


Figure 2-15 Comparison of L and LCL filter types at different power rating values

Figures 2-14 and 2-15 show that the LCL filter has approximately half of the inductance of the L filter type. The size of shunt capacitor of the LCL filter is relatively large but the total envelope is still smaller than the L filter type. The highlighted powers of 4.56kW and 38 kW in figure 2-15 are the desired power ratings for the chosen grid-connected drives throughout this study. A brief summary of L and LCL filters types is given as follows.

### 1. L type filter

- An attenuation of -20 dB decay per decade for all frequency ranges.
- For the effective attenuation of high order harmonics, the switching frequency needs to be high.
- To reduce the current harmonics around the switching frequency a high value of input inductance should be used.

### 2. LCL type filter

The key advantages of using the LCL filter over an L type are as follows:

- Attenuation of -60 dB decay of frequencies in excess of the resonance frequency.
- It is possible to operate with relatively low switching frequency for the given harmonic attenuation.
- Compared to the L filter type, LCL filters can provide better attenuation of switching harmonics using lower inductance.

Due to improved current harmonic attenuation of the LCL filter along with smaller physical size, it is considered the most appropriate choice for integrated drives.

## 2.6 Determination of lumped parameters for low- and high-power LCL filters

The two electric drives have been specified with power ratings as shown in table 2-3. LCL filters for both these drives have been designed and analysed.

**Table 2-3 Specifications of two proposed electric drives**

Drive input power (kW)	Machine output power (KW)	Machine speed (RPM)	Rectifier switching frequency $f_{sw}$ (KHZ)	Input voltage (RMS)	Input current (RMS) (assuming 90% efficiency)	Current density (A/mm <sup>2</sup> )	DC-link voltage (V)
4.56	4.1	3000	40	415	6.34	12	750
38	34	25000	40	415	53	12	750

Although the power of the two drives is very different, both drives have the same torque rating and hence similar motor sizes. The approach of having two different power levels is to examine how the size of AC filter inductors may affect the integration approach.

### 2.6.1 LCL filter parameters for the low-power drive of 4.56 kW at 3000 RPM

Following the design steps for the LCL filter outlined in section 2.4.2.3, the low power filter parameters are calculated as follows:

$$1. \quad \begin{cases} Z_b = \frac{E_n^2}{P_n} = \frac{415^2}{4.56 \times 10^3} = 37.77 \, \Omega \\ C_b = \frac{1}{\omega_g Z_b} = \frac{1}{2\pi f_g \times 37.77} = 84.28 \, \mu F \\ I_{max} = \frac{P_n}{3 V_{ph}} = \frac{4.56 \times 10^3}{3 \times 240} = 6.34 \, A_{rms} \end{cases}$$

2. Drive side inductance  $L_{2 \min}$  calculation:

$$L_{2 \min} = \frac{0.01 \times V_{ph(rms)}}{2 \pi f I_{rms}} = \frac{0.01 \times 240}{2 \times \pi \times 50 \times 6.34} = 1310 \, \mu H$$



3. Shunt capacitor calculation  $C_f$ :

$$C_f = 3\% C_b = 0.03 \times 84.28 \mu F = 2.5284 \mu F$$

4. Grid side inductance  $L_1$  (assuming that the attenuation factor  $K_a$  is 20%):

$$L_1 = \frac{\sqrt{\frac{1}{K_a^2} + 1}}{C_f \omega_{sw}^2} = 37.56 \mu H$$

5. The resonant frequency of the desired LCL filter is determined as follows:

$$\omega_{res} = \sqrt{\frac{L_1 + L_2}{L_1 L_2 C_f}} = 104.07 \times 10^3$$

Then the effectiveness of the values of  $L_1$  and  $L_2$  must verify the condition of operation of the resonant frequency as follow.

$$10 f_g < f_{res} < 0.5 f_{sw}$$

$$10 \times 50 < f_{res} < 0.5 \times 40 \times 10^3$$

6. Damping resistance calculation:

$$R_d = \frac{1}{3\omega_{res} C_f} = 1.27 \Omega$$

The parameters of the low power LCL filter are shown in table 2-4.

**Table 2-4 LCL filter parameters for input power drive 4.56 KW**

Parameter	Variable	Value	Unit
Grid side inductance	$L_1$	37.56	$\mu H$
Drive side inductance	$L_2$	1310	$\mu H$
Capacitor (Star connection)	$C_f$	2.5284	$\mu F$
Damping resistor	$R_d$	1.27	$\Omega$

The total LCL filter inductance should conform to equation (2.9) to guarantee adequate dynamic system response.

$$L_{Total} = L_1 + L_2 = 1347.56 \mu\text{H} \xrightarrow{\text{Should be satisfied}} L_{Total} \leq \frac{\sqrt{\frac{V_{dc}^2}{4} - E_m^2}}{I \omega} \quad (2.24)$$

$$L_{Total} = 1347.56 \mu\text{H} \implies L_{Total} < \frac{\sqrt{\frac{750^2}{4} - (240 \times \sqrt{2})^2}}{6.34 \times \sqrt{2} \times 2 \times \pi \times 50} = 0.056 \text{ H} \quad (2.25)$$

The computation of total filter inductance ( $L_{Total}$ ) pursued in equation (2.25) satisfies the inductance limitation implying that the derived parameters of the LCL filter achieve the design constraints.

### 2.6.2 LCL filter parameters for the high-power drive of 38 kW at 25000 RPM

The parameters of the high power LCL filter have been calculated by following the same design procedures for the low filter design taking onto the account the specifications of the high power drive listed in table 2-3. The determined parameters for high power LCL filter are tabulated as shown in table 2-5.<sup>2</sup>

**Table 2-5 LCL filter parameters for drive input power 38 kW**

Parameter	Variable	Value	Unit
Grid side inductance	$L_1$	5	$\mu\text{H}$
Drive side inductance	$L_2$	160	$\mu\text{H}$
Capacitor (Star connection)	$C_f$	21	$\mu\text{F}$
Damping resistor	$R_d$	0.4	$\Omega$

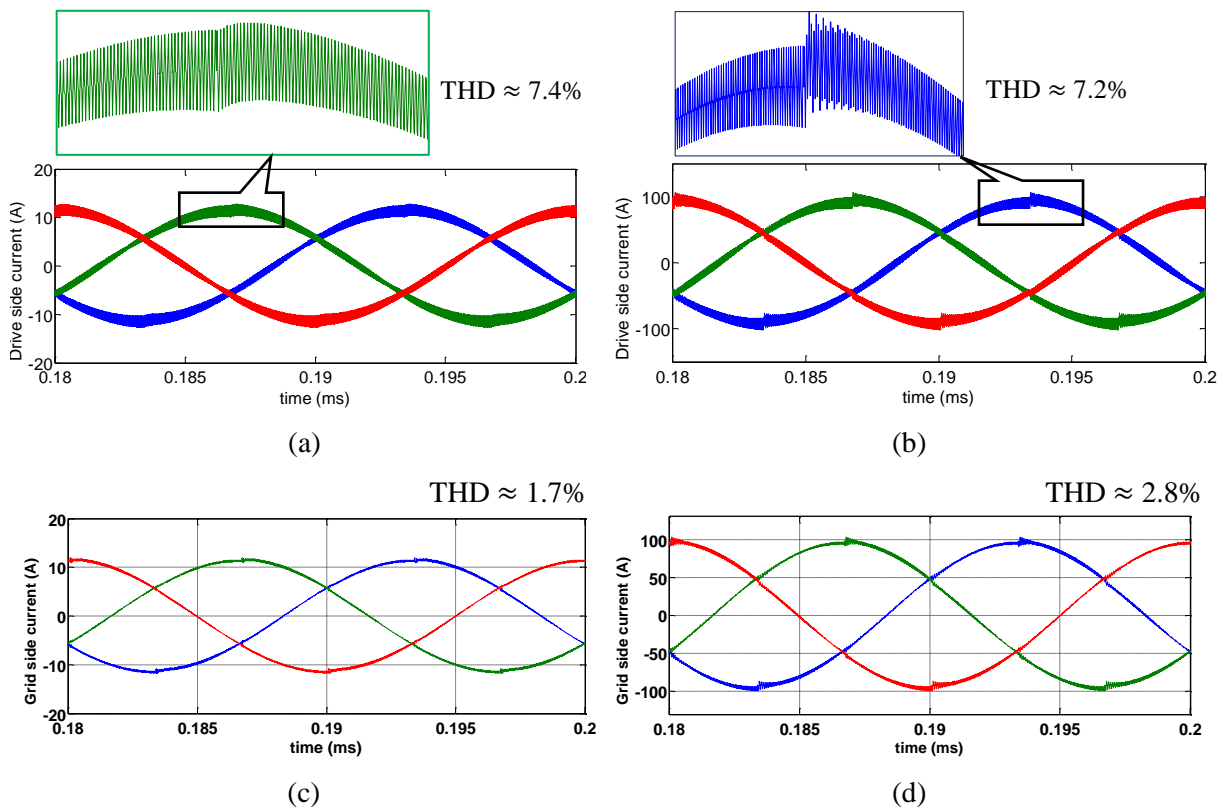
The total inductance of the designed LCL filter is  $165 \mu\text{H}$  in which the limit of filter inductance based on equation (2.9) is  $56 \text{ mH}$ . This means that the filter inductance does not affect the system dynamic response and the voltage drop across the filter is not significant, producing an acceptable filter design.

<sup>2</sup> The LCL filter parameters shown in table 2-5 have been calculated step by step in Appendix (A) based on the specifications of the high-power drive achieving an optimal filter design.

### 2.6.3 PLECS Simulation results for low-and high-power LCL filter

The two designs of LCL filter for the low- and high-power drives have been analysed using a PLECS simulation of an appropriate converter and LCL filter parameters. The switching frequency of the converter is 40 kHz and a Space Vector Modulation (SVM) switching scheme is utilised. The drive side filter inductor is used as a boost choke to obtain higher DC link voltage which is an alternative solution fewer active components than using a DC-DC converter.

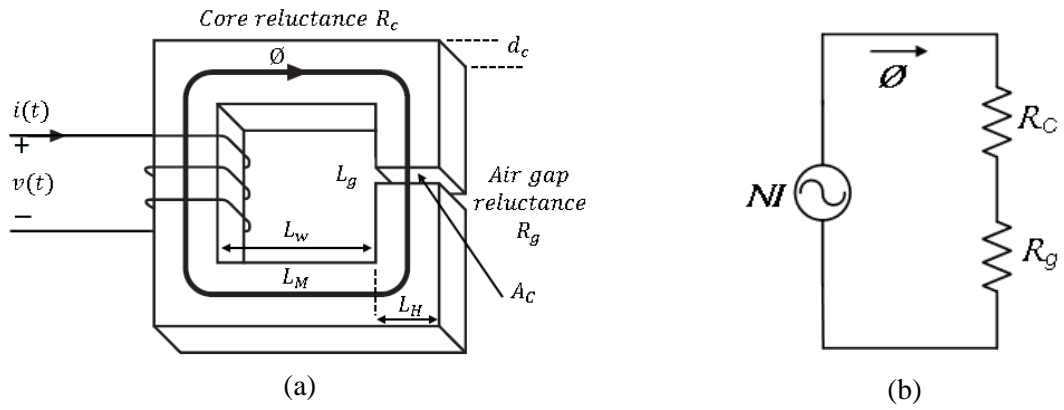
The unfiltered drive input currents for low- and high-power drives are shown in figure 2-16 (a and b) giving a THD of 7.4 and 7.2 respectively while the grid-side three-phase current waveforms achieve an acceptable THD for both low- and high-power filters within the recommended interval of THD (which is limited to be up to 5%) as shown in figure 2-16 (c and d).



**Figure 2-16 Grid-side 3-phase current waveforms: a) and b) unfiltered currents of low- and high power drives of 4.56 kW and 38 kW respectively; c) and d) filtered currents of low- and high power drives of 4.56 kW and 38 kW respectively**

## 2.7 A conventional inductor design at low- and high-power ratings

After determining the magnitude of the lumped parameters of LCL filters for the low- and high-power ratings, some fundamentals of AC inductor design are now described. A single-phase inductor design is considered for simplicity and its magnetic equivalent circuit is presented. The geometry of a single-phase inductor is shown in figure 2-17 and its dimensions are defined as follows:  $d_c$  is the core depth,  $L_H$  is the inductor height,  $L_M$  is the magnetic path length,  $L_W$  is the width of slot,  $A_c$  is the cross-sectional area of the core and  $L_g$  is the air gap length.



**Figure 2-17 Characteristics of AC inductor: a) geometry of single phase inductor; b) magnetic equivalent circuit**

Equations (2.27) to (2.30) help understand the influence of inductor dimensions upon the achievable inductance, the governing equation for inductor design is given in equation 2.26:

$$N I = \Phi R_{eq} \quad (2.26)$$

It can be seen from figure 2-17 (b) that the equivalent reluctance,  $R_{eq}$ , comprises that of the core and the air gap, denoted by  $R_c$  and  $R_g$  respectively. In general, the reluctance is defined by the geometry of the inductor and the medium's permeability as given in equation (2.27):

$$R_{eq} = R_g + R_c = \frac{1}{(\mu_o A_c)} (L_g + \frac{L_M}{\mu_r}) \quad (2.27)$$

To ensure linearity of inductance the design should avoid significant magnetic saturation. The magnetic flux density and inductance are given as follows:

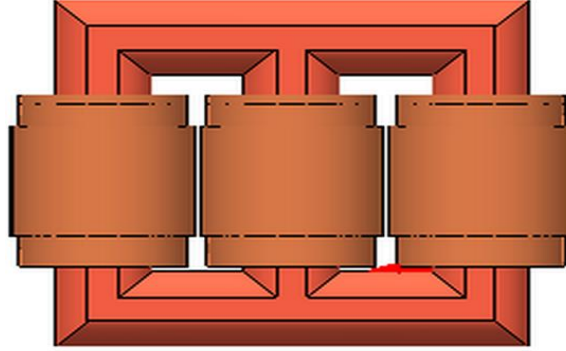
$$B = \frac{\Phi}{A_c} \quad (2.28)$$

$$\hat{\Psi} = N \hat{\Phi} = L \hat{I} \quad (2.29)$$

$$L = \frac{\hat{\Psi}}{\hat{I}} = \frac{N^2}{R_{eq}} \quad (2.30)$$

### 2.7.1 Design of drive-side 3-phase inductors ( $L_2$ ) for the low-power rating at 4.56 kW

Since the LCL drive-side inductor  $L_2$  is much larger than that of the grid-side inductor  $L_1$  (see tables 2-4 and 2-5), the design of the 3-phase  $L_2$  inductor is addressed first. The following schematic shows the general features of conventional 3-phase AC inductors.



**Figure 2-18 Features of conventional 3-phase AC inductors**

For initial design, it can be assumed that all the inductors' energy is stored in the air-gap. The air gap volume can be determined using this energy and the chosen air-gap flux density.

The optimal air gap length is calculated using an iterative approach to give the optimal mass. The following design steps for the 3-phase boost inductor  $L_2$  on the drive side have been taken.

The calculation of the air gap volume of the inductor which is essentially based on the filter parameters. The required storage energy can be directly calculated as given in equation 2.31 and hence the volume of the air gap can be calculated from equation 2.32.

$$\text{Energy stored} = \frac{1}{2} L i_{peak}^2 \quad (2.31)$$

$$(\text{energy stored}) = \frac{1}{2} \frac{B^2}{\mu_0} \times \text{airgap volume} \quad (2.32)$$

To avoid significant magnetic saturation in the iron circuit the magnetic flux density is limited to 1.2 T. This is based on the B-H curve of the chosen core material of 10JNEX-900.

Figure 2.19 shows a simple iterative process in which the air-gap length is varied in an attempt to optimise the design. A relatively high current density of 12 A/mm<sup>2</sup> and a slot fill factor of 50% is assumed. Such a high current density is possible when integrated into the machine, which will be intensely cooled, but it should be noted that industrial drive filter inductors cannot work at such high current densities because they normally have only natural convection to cool them.

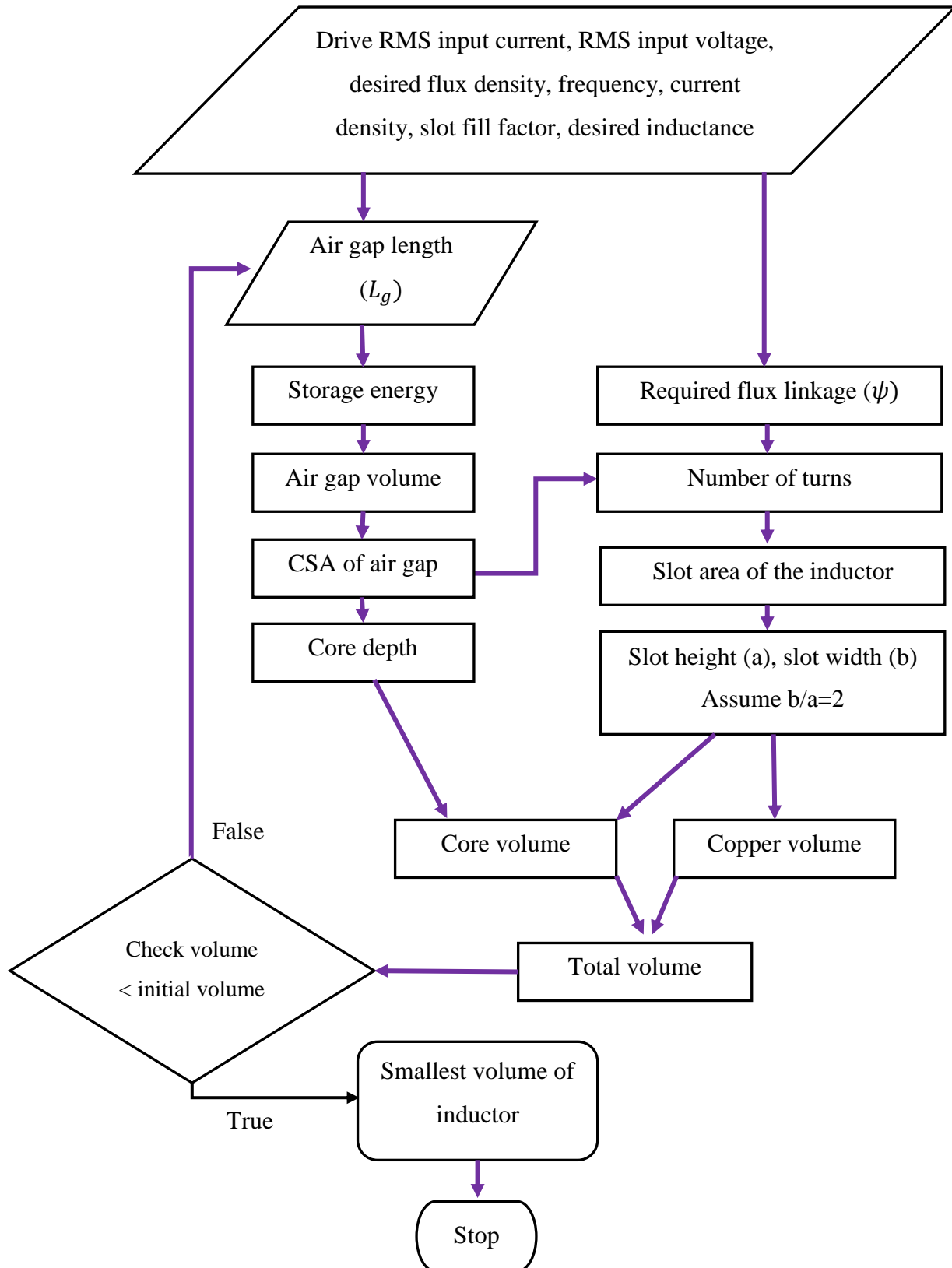
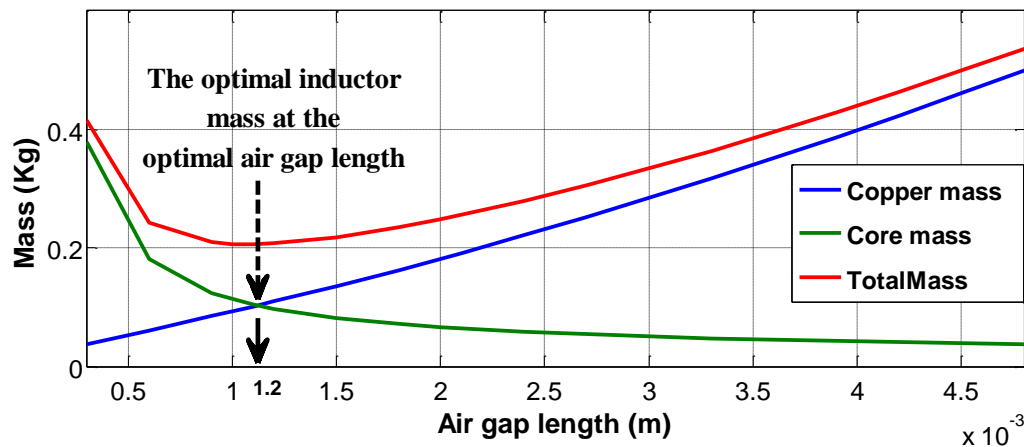


Figure 2-19 Optimisation chart loop of conventional inductors design

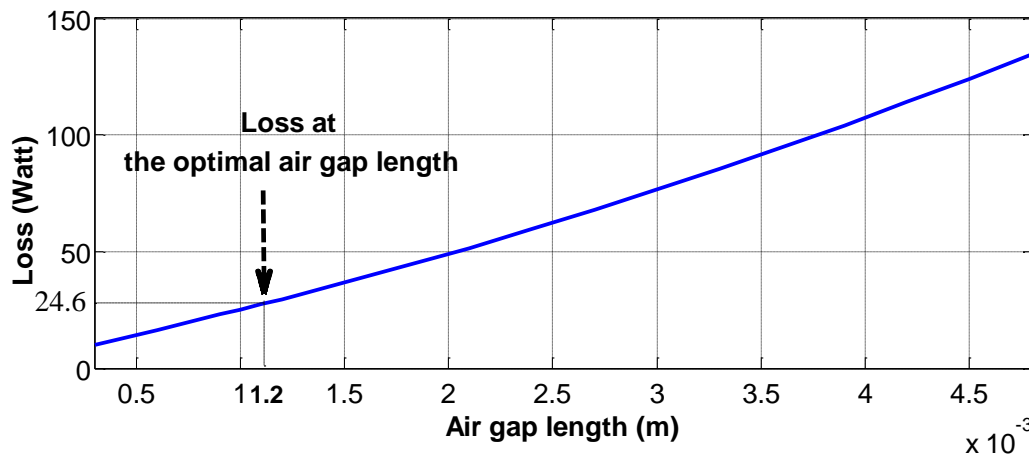
Figures 2-20 and 2-21 illustrate the effect of varying air-gap length upon the 3-phase inductor design for the low-power drive (4.56kW / 3000 RPM).

Figure 2-20 illustrates the lowest achievable mass of the desired inductor at different lengths of the inductor air gap. The optimal total mass for the 3-phase inductors, including copper and core mass is achieved with an inductor air gap length of 1.2 mm.



**Figure 2-20 Optimisation process of the EE 3-phase inductor design for low power drive at 4.56 kW**

As the copper mass is determined, the total conduction losses can be simply calculated and are shown in figure 2-21. There are 24.6 Watts of winding loss with an air gap length of 1.2 mm.



**Figure 2-21 Total conduction loss of the predicted design of the EE3-phase inductor for the low power drive at 4.56 kW**

The predicted parameters of a single inductor design for the low power drive are tabulated in tables 2-6 and 2-7.

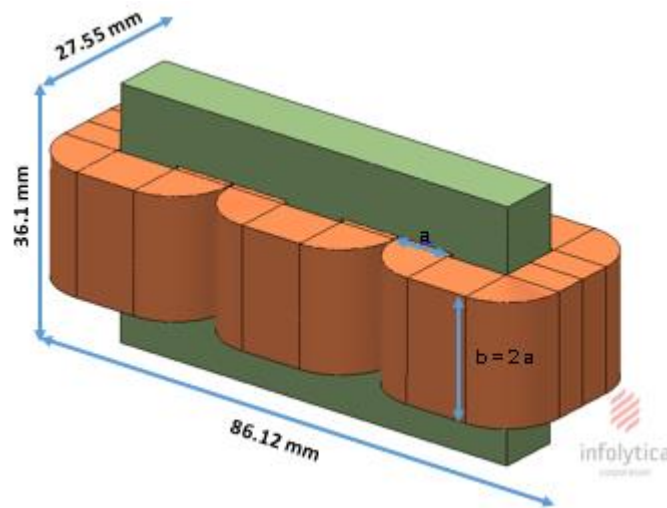
**Table 2-6 Inductor dimensions per phase**

Variable	Value
Core depth	10.75 mm
$L_H$	10.75 mm
$L_W$ (a)	8 mm
Height of window (b)	16 mm
$L_G$	1.2 mm
$L_M$	97.85 mm
$A_C$	115.56 mm <sup>2</sup>

**Table 2-7 Inductor electrical characteristics**

Variable	Value
Inductance L	1310 $\mu H$
N	97 turns
Current	8.966 $A_{pk}$
Current density	12 A/mm <sup>2</sup>
$B_{air\ gap}$	1.2 T
$B_{core}$	1.3 T
$\mu_{eff}$	$\approx 4050\mu_0$ H/m

The conventional 3-phase inductor design has been modelled using FEA MagNet software. A 3D representation of the drive filter inductors  $L_2$  situated in the drive side is shown in figure 2-22. The total volume of 3-phase inductors  $L_2$  for the low power drive is approximately 85.65 cm<sup>3</sup>.



**Figure 2-22 3D presentation of the predicted design of the 3-phase drive-side inductors  $L_2$  for the low power drive of 4.56 kW**

This design is taken as a benchmark for the low power filter inductors when they are integrated into the low-speed machine using different integration techniques.



### 2.7.1.1 FEA simulation results

The 3D model of 3-phase drive side inductors shown in figure 2-22 has been simulated and the resultant inductance and voltage across the three-phase AC inductors  $L_2$  were determined. Figure 2-23 (a and b) illustrates the simulation results of the 3-phase voltage and flux linkage across the designed drive-side boost inductors  $L_2$ .

The predicted inductance and voltage per phase across  $L_2$  are verified, and as such the following fundamental equations (2.33) and (2.34) validate the FEA results.

$$V_L = \omega \hat{\psi} = 100 \pi \times 0.01175 = 3.7 \text{ V} \quad (2.33)$$

$$L = \frac{\hat{\psi}}{\hat{i}} = \frac{0.01175}{8.966} = 1311 \mu\text{H} \quad (2.34)$$

It can be seen that the inductance per phase achieved by the 3D finite element model is  $1311 \mu\text{H}$ , which is very close to the predicted inductance of  $1310 \mu\text{H}$  (see table 2-4). The simple predictions of the lumped parameter model tend to underestimate the inductance because they neglect all leakage and fringing flux.

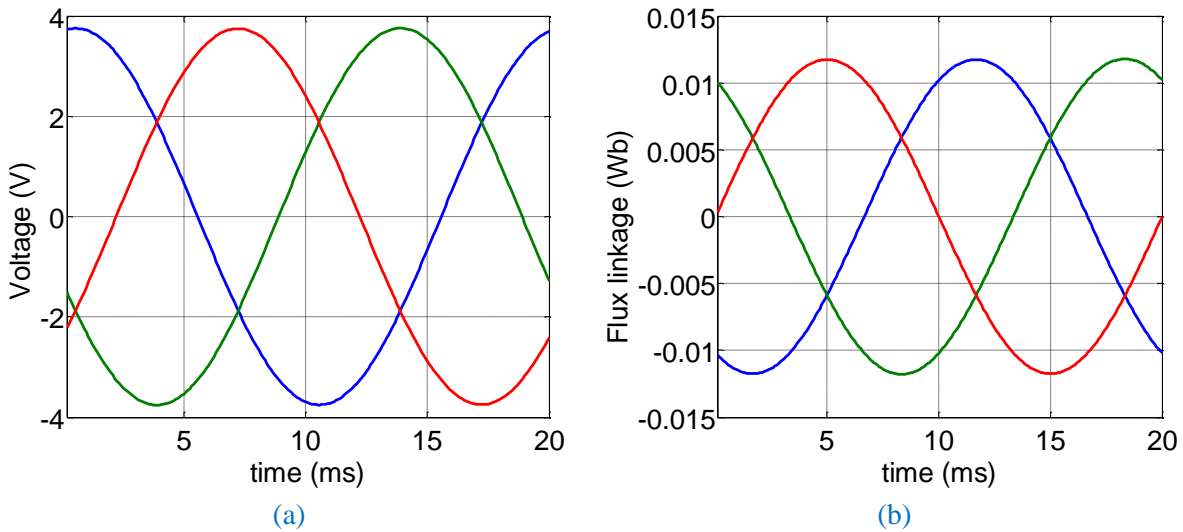


Figure 2-23 3-phase waveforms for  $L_2$  for the power drive of 4.56 kW: a) voltage; b) flux linkage

The grid side inductors,  $L_1$ , are designed using the same optimisation loop and have a volume of  $4.46 \text{ cm}^3$ .

### 2.7.2 Design of drive side 3-phase inductors $L_2$ for the high-power drive at 38 kW

The conventional 3-phase inductors  $L_2$  have been designed, optimised and simulated by following the same design procedures of the low-power drive inductor, taking into

consideration the specifications of the high-power drive. The predicted parameters of the single high-power inductor are tabulated in tables 2-8 and 2-9.

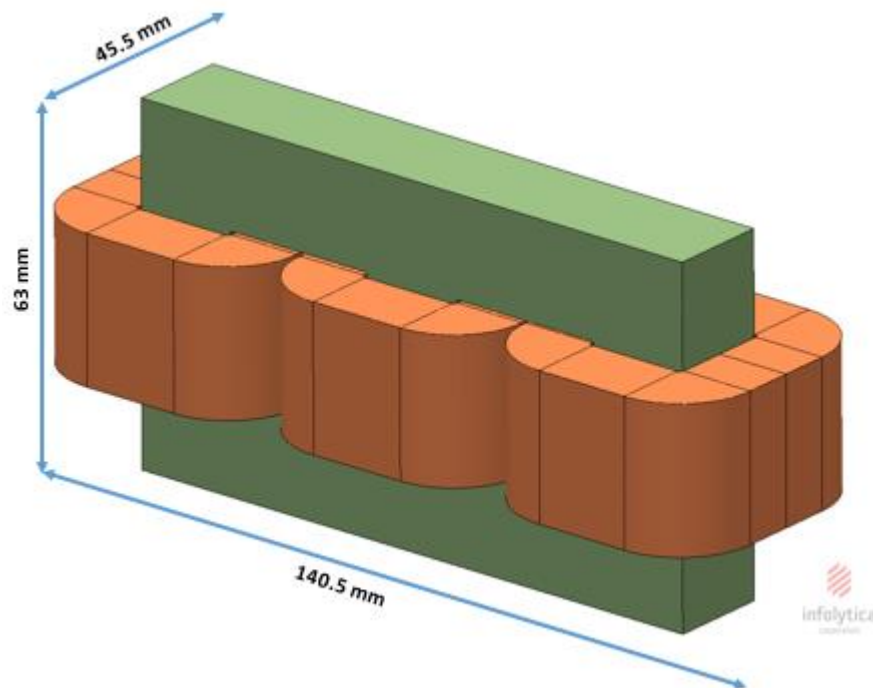
**Table 2-8 Inductor dimensions/ phase**

Variable	Value
Core depth	17.5 mm
$L_H$	17.5 mm
$L_W$ (a)	14 mm
Height of window (b)	28 mm
$L_G$	3.3 mm
$L_M$	156 mm
$A_C$	306.25 mm <sup>2</sup>

**Table 2-9 Inductor electrical characteristics**

Variable	Value
Inductance L	160 $\mu H$
N	33 turns
Current	75 $A_{pk}$
Current density	12 A/mm <sup>2</sup>
$B_{air\ gap}$	1.2 T
$B_{core}$	1.35 T
$\mu_{eff}$	$\approx 4050\mu_0$ H/m

Figure 2-24 illustrates the 3D geometry of the conventional 3-phase inductor  $L_2$  which forms the larger inductor within the LCL input filter. The total volume of the designed 3-phase inductors at the high power rating is 402.75 cm<sup>3</sup>.

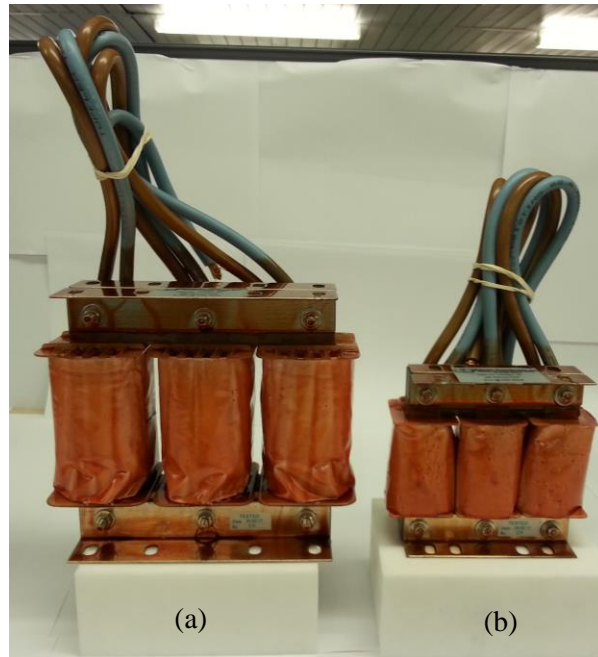
**Figure 2-24 Conventional 3-phase input AC inductor for the high-power drive of 38 kW**

From FEA simulation, the voltage drop across the high-power filter inductor is the same as that of the low-power inductor at 3.77 V and the predicted inductance for the high-power filter inductor is approximately  $160.85 \mu H$  per phase, which is almost the same value predicted by the simple analytical method.

The grid side inductors,  $L_1$ , are designed in the same manner and have a total volume of  $24.75 \text{ cm}^3$ .

### 2.7.3 Manufacturing of LCL filter inductors for the high-power drive at 38kW

For comparison purposes, some commercial input filter inductors were purchased. Figure 2-25 shows these inductors, which correspond to those of the LCL type filter of the 38 kW drive. These are manufactured in the UK by the Majestic Transformer Company.



**Figure 2-25 Manufactured 3-phase LCL filter inductors for the drive of 38kW: a) drive-side inductors  $L_2$ ; b) grid-side inductors  $L_1$**

The volume of the 3-phase drive side inductors ( $L_2$ ) shown in figure 2-25 (a) is  $2430 \text{ cm}^3$  and the other set of grid-side inductors (figure 2-25 (b)) is  $990 \text{ cm}^3$ . They are large because of the low current density necessitated by natural convection.

## 2.8 An overall comparison study of input LCL filters at different power ratings.

Since the low- and high-power LCL filter inductors have been designed and optimised, the net volume of the grid- and drive-side inductors ( $L_1$  and  $L_2$ ) are calculated. Three different conventional designs of input LCL filter are carried out in the previous section. The first two

filter designs are FEA models in which the third design is the industrial demonstrator of the high-power filter inductors. Table 2-10 illustrates these three different designs of the 3-phase LCL filter inductors. As shown in table 2-10, the industrial filter is designed with a low current density of  $3.3 \text{ A}_{\text{rms}}/\text{mm}^2$  while the FE models designed with  $12 \text{ A}_{\text{rms}}/\text{mm}^2$  because those industrial inductors have to operate without any active cooling system. Industrial inductors are approximately five times physically larger than those designed in FE in this chapter. Also, table 2-10 shows that filter inductors,  $L_2$ , occupy a much larger volume than that of the grid-side inductors  $L_1$ .

**Table 2-10 Comparison of low-and high-power conventional 3-phase inductors**

	Variable	Low-power inductors (4.56 kW) FEA model	High-power inductors (38 kW)		Unit
			FEA model	Industrial inductors (Demonstrator)	
Drive rated power	$P$	4.56	38	38	$kW$
Rated peak current	$\hat{I}$	8.966	75	75	$A$
Frequency	$f$	50	50	50	$HZ$
Drive side inductance per phase	$L_2$	1310	160	160	$\mu H$
Grid side inductor	$L_1$	37.56	5	5	$\mu H$
Current density	$J$	12	12	3.3	$A/\text{mm}^2$
Winding fill factor ( $L_1$ & $L_2$ )	$ff$	50	50	$L_1: 40, L_2: 60$	%
Volume of 3-phase inductor ( $L_1$ )	$V_{L1\_3\text{-phase}}$	4.46	24.75	990	$\text{cm}^3$
Volume of 3-phase inductor ( $L_2$ )	$V_{L2\_3\text{-phase}}$	85.65	402.75	2430	$\text{cm}^3$
Power loss	$P_{Loss}$	73.5	367.05	561.8	W
Energy density	$E$	$E_{L_1}: 3.36 \times 10^{-4},$ $E_{L_2}: 5.7 \times 10^{-4}$	$E_{L_1}: 5.65 \times 10^{-4},$ $E_{L_2}: 1.12 \times 10^{-3}$	$E_{L_1}: 1.41 \times 10^{-5},$ $E_{L_2}: 1.85 \times 10^{-4}$	$\text{J}/\text{cm}^3$

## 2.9 Conclusion

Input filters have been designed and simulated for the chosen low- and high-power drives. Due to improved current harmonic attenuation of the LCL filter, along with smaller dimensions, an LCL filter is chosen. The low- and high-power LCL filter inductors have been designed according to the chosen power ratings of drives. For each filter design, the optimal volume of copper and steel has been obtained.

To give a baseline comparison with standard industrial input filters an industrial LCL filter inductor has been purchased, corresponding to that required for the high-power drive. The industrial filter is approximately five times physically larger than those designed in this chapter because it has to operate without any forced cooling.

# CHAPTER 3

## High-Speed High-Power (HSHP) Electrical Machine Design

---

**Summary:** In this chapter, low- and high-speed PM machines are identified and designed to form the foundation of an integrated motor drive. The proposed low- and high-speed machines are identically dimensioned, but operate at different shaft speeds of 3000 RPM and 25000 RPM respectively. The high-speed, high-power (HSHP) machine of 25000 RPM is manufactured in the final stage of this study, with the LCL filter inductors included in a single-packaged unit. Advanced materials have been chosen to reduce the machine's size in terms of achieving high power density.

The HSHP machine is chosen to be the base machine for this research due to the challenges with integration of passive filter elements into electrical machines of high power density. The losses from the high-speed machine and integrated filter inductors are analysed.

### 3.1 Background

In recent years the demand to achieve higher torque density and more compact electrical motors has rapidly grown, particularly for applications which require high efficiency and smaller motor size [54]. Permanent magnet (PM) motors are widely used for various applications due to their merits of high torque-to-volume ratio, and high efficiency when operating in the constant torque region [54, 55]. Therefore, a PM type motor is chosen in this study to form the foundation of an integrated motor drive.

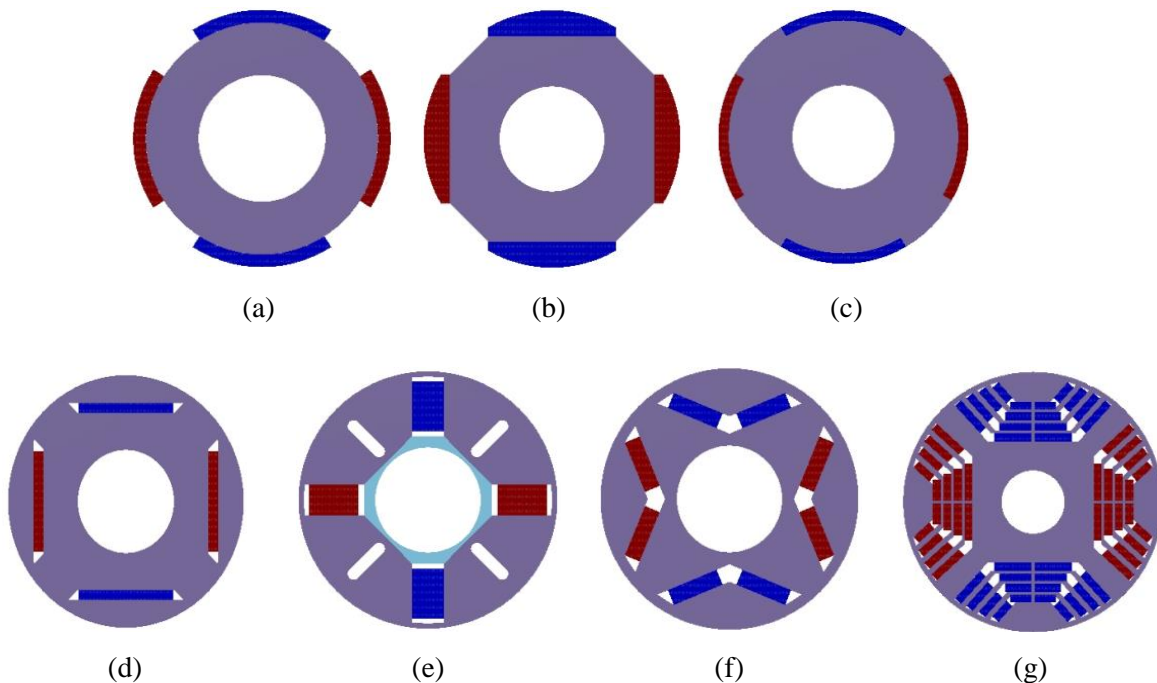
### 3.2 Permanent magnet machine

There are different types of PM machines, including radial, axial and transverse flux machines and flux switching machines [56]. Due to the simplicity of its structure and manufacturing process, the surface-mounted permanent magnet (SMPM) motor, driven from a PWM voltage fed inverter (VSI), is chosen as a base machine type for this study.

Different winding configurations and the choice of slot/pole/phase have significant impact upon the contents of the space harmonics in the machine's air gap and on the efficiency of the machine, including rotor losses, cogging torque and machine torque ripple. Different approaches have been implemented to determine the influence of stator teeth, magnet pole shape, magnet design with skewing and the arrangement of winding coils upon these unwanted effects [57-66].

Fractional-slot concentrated-winding (FSCW) synchronous PM machines have attracted interest due to their high power density, high efficiency and short end windings. However, one of the challenges of using FSCW is the rotor losses, particularly for high-speed machines which introduce large space-harmonic components of MMF that are not synchronised with the rotor. Parasitic effects such as vibration, noise, unbalanced magnetic forces and machine torque ripple are also potentially higher in FSCW PM machines because of the additional harmonic contents [66].

There are different topologies for the rotor design, including the magnet shape and location. The magnets can be placed either on the surface of the rotor body, inset or buried in the rotor. Figure 3-1 shows the general structures of PM machine rotors.



**Figure 3-1 Some rotor possibilities: (a) and (b) surface PM; (c) inset PM; (d), (e), (f) and (g) interior permanent magnet (IPM)**

For applications with significant field weakening requirements the inset PM rotor topology is preferable due to the additional reluctance torque produced by the structure of the rotor.

However, this research focuses on the integration packaging techniques of passive filter components into electrical machines and the consideration of field weakening region is ignored, for the simplicity of machine design, the surface-mounted PM rotor type is chosen. With this choice, easily the magnet can be bounded to the rotor core where the manufacturing processes will be easier than the inset magnet rotor type.

### **3.3 Materials**

The choice of materials for any design depends on the type of application, including operating conditions, mechanical constraints and thermal aspects. In order to choose an electrical steel material for an electrical machine core, sleeve or magnets, the most important key factors are electromagnetic material properties, the strength to weight ratio, thermal capability and the side of cost.

#### **3.3.1 Stator material**

Magnetic steel materials vary in properties in terms of the ability to operate at different magnetic flux densities. This is based on the maximum achievable knee point which is dictated by the BH curve of each material. Laminated cores are widely employed in making the stators of electrical machines and the selection of lamination thickness depends on the machine's electrical frequency, manufacturing processes and cost. Generally, for HSHP machines, the choice of a thin lamination is preferable, because the effect of eddy current losses are significantly reduced. However, the manufacturing cost and assembly of thin laminations in forming a machine stator are greater compared to that of thicker laminations.

Powder metallurgy has evolved to produce consistent magnetic components for soft magnetic applications. This approach allows precise material control, the capability to have three-dimensional magnetic flux distribution and the ability to build relatively complex shapes. Soft magnetic composite (SMC) materials now form a well-established process for producing powdered iron stators which offer performance levels approaching that of steel laminations. Furthermore, they offer design advantages due to the isotropic nature of the material [67, 68].

Super core (JNEX-Core) is the lowest loss non-oriented magnetic steel sheet of SiFe currently on the market: it is manufactured using an innovative process compared to conventional silicon steel sheets. The magnetic characteristics of silicon steel sheets are improved by increasing the silicon content, peaking at 6.5%. Figure 3-2 illustrates the principles of the manufacturing



process for 6.5% silicon steel sheets by chemical vapour deposition (CVD). The JNEX-Core material is widely used for high-frequency applications because of its low core loss and high permeability [69, 70]. Note, however, it does have a lower saturation flux density than lamination materials of lower silicon content. Figure 3-3 illustrates the manufacturing process of the silicon steel sheet, where the maximum permeability is achieved at a silicon content of 6.5%.

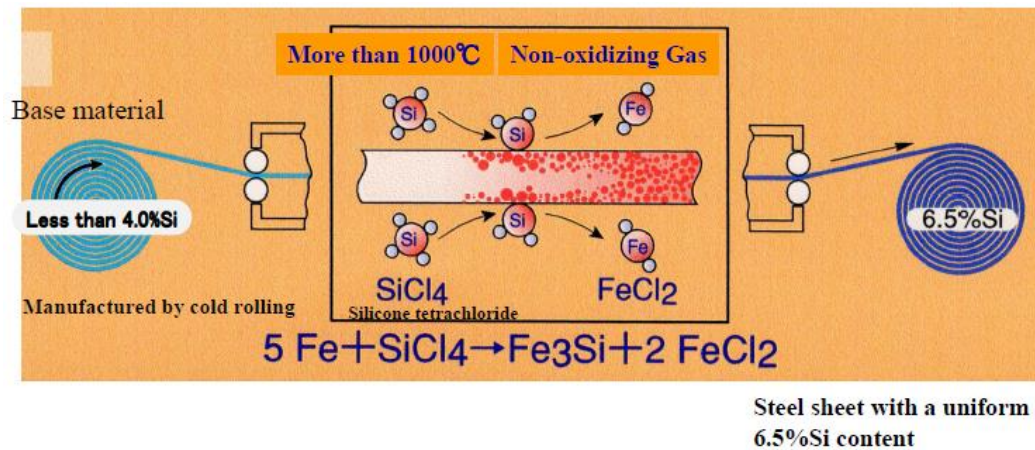


Figure 3-2 Illustration of enhancement of manufacturing process of siliconizing steel sheets [71]

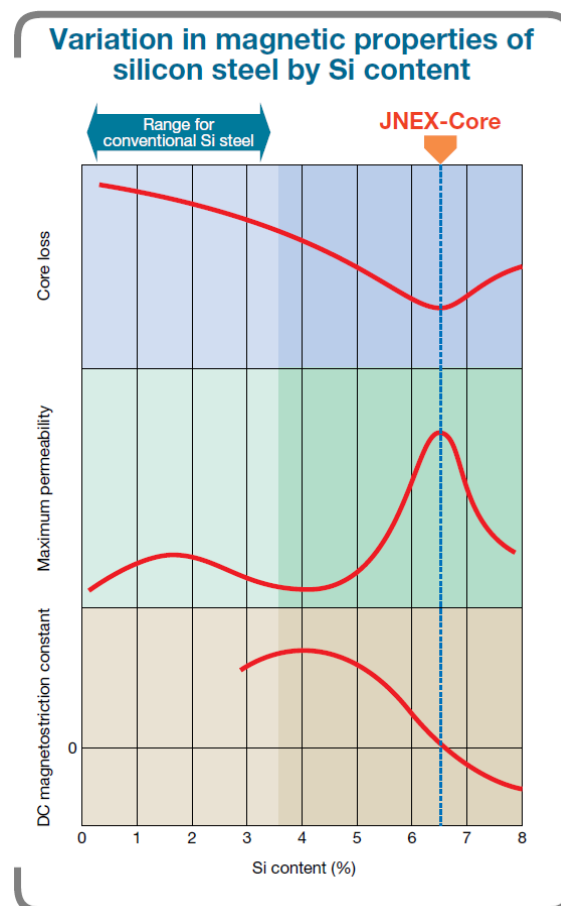


Figure 3-3 Magnetic characteristics of super core 10JNEX-900 [72]

Another electrical steel material is cobalt-iron based (CoFe) laminations which provide high performance at high electrical frequencies since laminations thickness of a CoFe can be thin up to 0.05 mm. However, this type of materials is expensive in terms of manufacture and material handling [73-75].

10JNEX-900 has been chosen in this study based on a comparison with more conventional electrical steel materials carried out later in this chapter.

### **3.3.2 Magnet materials**

In order to achieve the desired magnetic loading of the machine and to sustain large armature currents without the possibility of demagnetisation, the designer should calculate and choose the maximum residual flux density of the magnet material. The residual flux density indicates the maximum magnetic loading which could be achieved with very deep magnets, though for high-speed machines where a rotor sleeve is needed, the effective air-gap is large and the achievable magnetic loading is much lower. The magnet's tensile and compressive strength should also be considered when designing the stress requirements for the sleeve. The magnets are the most expensive component of all the materials in the HSHP machine.

A significant factor in terms of the selection of magnet material is its ability to resist demagnetisation at high operating temperatures and stator current, at which point it has maximum exposure to a demagnetising field produced by the armature stator windings.

In practice an encased high-speed rotor may need a high temperature to cure the chosen rotor sleeve and therefore the magnet strength of the chosen magnet type should be high enough to withstand the temperature used during the manufacturing process.

### **3.3.3 Sleeve materials**

Rotor sleeve materials have evolved to be used at higher operating stress along with reduced mass. Inconel and stainless-steel sleeves were widely used in the past as they are simple to manufacture and assemble on the rotor. Carbon Fibre Reinforced Polymer (CFRP) sleeves have been introduced to push the limits of stress and self-stressing. The carbon fibre sleeve is a composite material which is commonly used for HSHP rotor machines to give better strength-to-weight ratios compared to stainless steel and Inconel sleeves [76]. However, CFRP has low thermal conductivity, which adds challenges to rotor design in terms of high temperature impact on the rotor magnet's performance. Note that, although metallic sleeve materials have better

thermal conductivity, they generally have a high electric conductivity and significant eddy currents may be generated in them which can itself increase the thermal challenge.

The thermal conductivity of the sleeve material type used affects the capability to conduct losses to the rotor surface, where they can be removed by convection in the machine air gap. HSHP rotors which use CF sleeves often a forced convection cooling system to avoid any excessive temperature generated by rotor eddy currents.

### 3.4 Specifications of low- and high-speed PM machines

The initial specifications of the low- and high-speed surface mounted machines are shown in table 3-1. The two machines have similar dimensions, but operate at different rated speeds.

**Table 3-1 Specifications of low- and high-speed machines**

Machine speed (RPM)	Current density ( $A_{rms}/mm^2$ )	DC-Link voltage (V RMS)	Machine stack length (mm)	Outer machine diameter (mm)
3000	12	530	70	109
25000	12	530	70	109

Design of the HSHP machine at 25000 RPM is first presented in detail. Then, the low-speed machine at 3000 RPM is designed and optimised using the same approach.

### 3.5 Design optimisation of the HSHP machine at 25000 RPM

The HSHP machine has been modelled using a Visual Basic Script (VBS) file, enabling to parameterise each vertex path of the machine geometry. The parametric model was used in electromagnetic finite element software

Optimisation of the HSHP machine has been carried out using commercial FEA packages including Infolytica Magnet, OptiNet, Ansys and MotorSolve. In order to be certain that the final motor design is formally optimised, an evolutionary optimisation (i.e. Genetic algorithm) was used, aiming to achieve high torque density at fixed current density, machine stack length and stator outer diameter.

The objective of the optimisation process is to obtain high power density. One of the key factors in achieving high power density is to operate near the capacity limits of each component in the design, including electromagnetic, thermal and mechanical limits.

An objective function aiming to achieve a high-power density under some machine constraints has been defined as given in equation 3.1. The objective function is targeted at maximising machine torque under some constraints: back-EMF, slot fill factor and current density.

$$\text{Maximise } \{F(z)\} = \left\{ \frac{\text{Machine Torque}}{\text{Machine torque}_{\max}} \right\} \quad (3.1)$$

where the machine torque is the highest achievable torque in relation to the machine torque (maximum value which is targeting by the optimisation). In equation (3.1)  $F(z)$  is a vector of optimisation variables including magnet dimensions and stator tooth, slot dimensions and stator core back depth. The details of optimisation including the initial variable and fixed parameters, intervals for the constraints are given in sections 3.5.1.

### 3.5.1 Parameters and constraints for optimisation

The optimisation process fixes the following parameters:

- Axial lamination stack length (70 mm)
- Air-gap length (1.5 mm – to accommodate a rotor sleeve)
- Winding slot fill factor (0.6)
- Current density ( $12 \text{ A}_{\text{rms}}/\text{mm}^2$ )
- Number of poles (8 poles)
- Number of slots (12 slots)

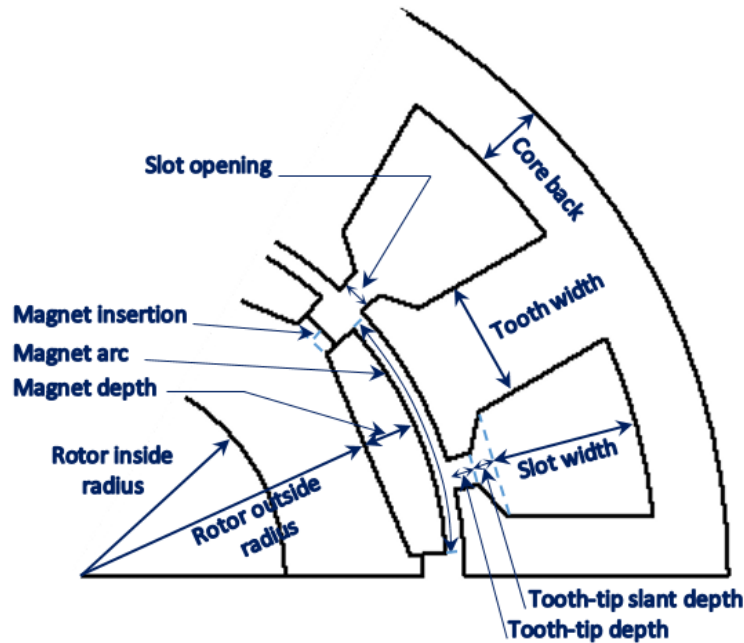
It is to be noted that, because both motor and filter losses have to pass through to the water jacket, the presence of the filter will reduce the thermal performance of the motor. The chosen current density of  $12 \text{ A}_{\text{rms}}/\text{mm}^2$  was still considered achievable, despite this effect.

The variable parameters are as follows:

- Stator inside diameter
- Stator core back depth
- Tooth width
- Tooth-tip depth
- Tooth-tip slant depth
- Magnet arc
- Magnet depth
- Magnet insertion depth
- Stator slot opening

- Slot depth
- Rotor inner/outer diameter

These variables are illustrated in figure 3.4.



**Figure 3-4 Illustration of parameters set for optimisation in 12 slot/8 pole HSHP PM motor**

The optimisation tends to make the magnet arc large, as shown in figure 3-4, in order to produce the maximum back EMF. The saliency effect was found to be insignificant. The tooth width and stator core back were minimised to give flux densities of around 1.4T and 1.3T respectively, which are consistent with the limits of the magnetic characteristics of the 10JNEX-900 material used. The choice of magnetic material of JNEX-core is based on work in section 3.5.5.2.1.

All the varying machine parameters have an influence on the objective function which necessitates some constraints such as back EMF, current density and slot fill factor, targeting to limit key specifications. In the design of HSHP machine, the objective function searches the candidate machines under those constraints in user-defined intervals. The constraints have been implemented in OptiNet to achieve more acceptable design results.

There are other considerations, including the following:

1. The choice of a modular machine stator: as the chosen machine forms the foundation of an integrated motor drive, the choice of a modular stator is important in terms of the incorporation of other magnetic components which share the same machine stator geometry; this is covered in Chapter 4.
2. The simplicity of design of the chosen base machine.

3. A compressed coil approach: a high slot fill factor can be achieved and lower machine slot area is required for the same amount of MMF, which in turn can help in achieving a high power density.
4. The avoidance of magnet demagnetisation at maximum armature current and high operating temperature.
5. Good thermal design to permit a high current density and consequently a higher power density.

Based on the optimised FE model after carrying out optimisation with OptiNet and MagNet, some key materials have been identified for further investigation as given in Table 3-2. At 25000 RPM the fundamental electrical frequency is high (1.66 kHz), so AC losses in laminations and copper windings are likely to be high. The JNEX-Core lamination material has been chosen for the HSHP machine to reduce iron loss. For the windings copper Litz wire is chosen to reduce proximity losses; further details are included later in this chapter.

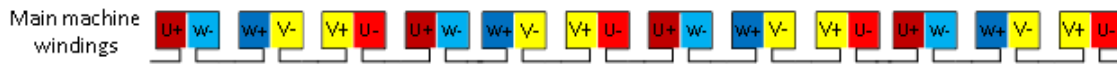
**Table 3-2 Chosen materials for HSHP machine 25000 RPM**

Item	Chosen material	Units
Magnet material	Neodymium iron boron (N42UH)	---
Sleeve material: fibre	AS4C Carbon Fibre	---
Stator lamination material	10 JNEX-900	---
Rotor lamination material	M-270-35A	---
Non-magnet wedge insulation	Hylomar ST574	---
Ground wall insulation	Peek	---
Shaft material	High strength steel	---
Type of copper wire	Copper Litz wire	20 × 30 AWG
Winding thermal class	CA 200	°C
Winding type	Concentrated – double layer (parallel connection)	---
Target slot fill factor (%copper in slot)	60	% (in per cent)

Because the carbon fibre sleeve is a poor thermal conductor, a forced cooling system is used for the rotor. A hollow shaft design utilising forced air cooling has been chosen and designed such as to be the only cooling for the rotor. The design of the hollow shaft is beyond the scope of this research.

By increasing the pole number of the machine the end-winding length and core back depth can be reduced, giving a smaller machine. However, the impact upon electrical frequency must be considered. An 8 pole machine design is chosen to give a compromise: the peak fundamental electrical frequency is 1667Hz. Higher frequencies are difficult to achieve because of limits upon power electronic switching frequency and increased iron loss at very high frequency.

The chosen winding layout for a 12 slot - 8 pole HSHP-PM machine is illustrated in figure 3-5, showing that the proposed machine has a double layer concentrated winding configuration.



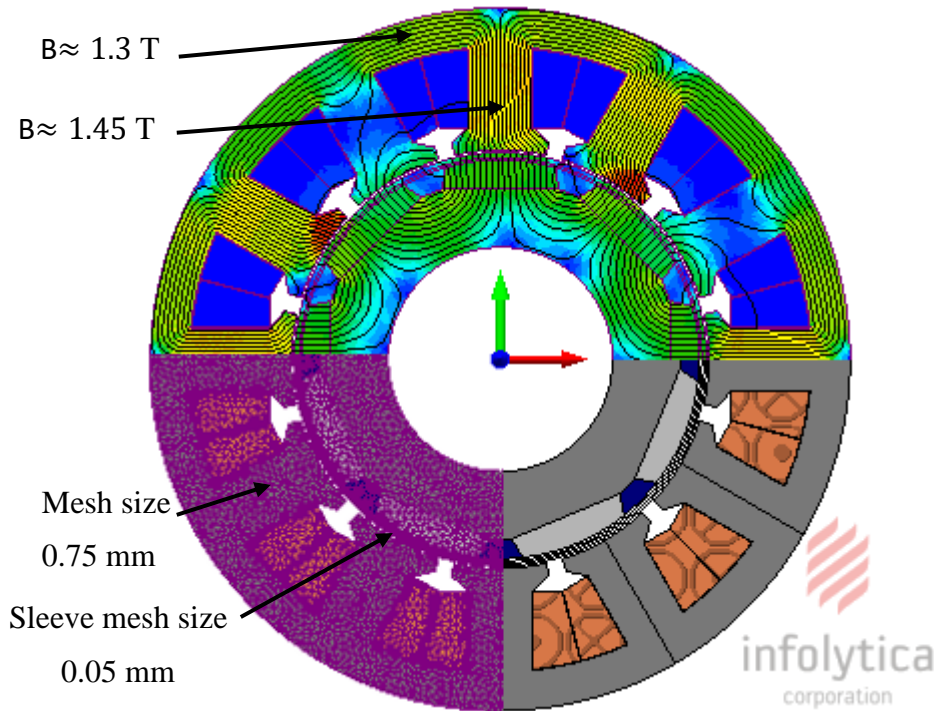
**Figure 3-5 12 slot - 8 pole HSHP machine windings layout**

### 3.5.2 Unbalanced magnetic pull in rotating electrical machines

Unbalanced magnetic pull (UMP) tends to occur due to rotor eccentricity or from having an odd number of slots in the machine stator. Since the chosen machine design has an even number of slots and the effective air-gap including the sleeve, is large, the problem of UMP is not expected to be an issue in the base machine.

### 3.5.3 FEA Results

A 2D model of the proposed PM machine has generated and simulated over one full electrical cycle by using Infolytica-Magnet and it is solved using transient 2D with motion. There is an internal boundary condition of flux tangential is applied for the rotor shaft area, assuming magnetic material. The final machine geometry is given in figure 3-6, which presents the full load flux density with the meshes overlaid to illustrate the model. In order to gain more accurate results from the simulated 2D model, different mesh size regions were used in the model. Mesh size for the complete model was 0.75 mm except for the sleeve mesh size of 0.05 mm; this is considered suitable for a sleeve thickness of 0.35 mm. Further details are presented later in this chapter.

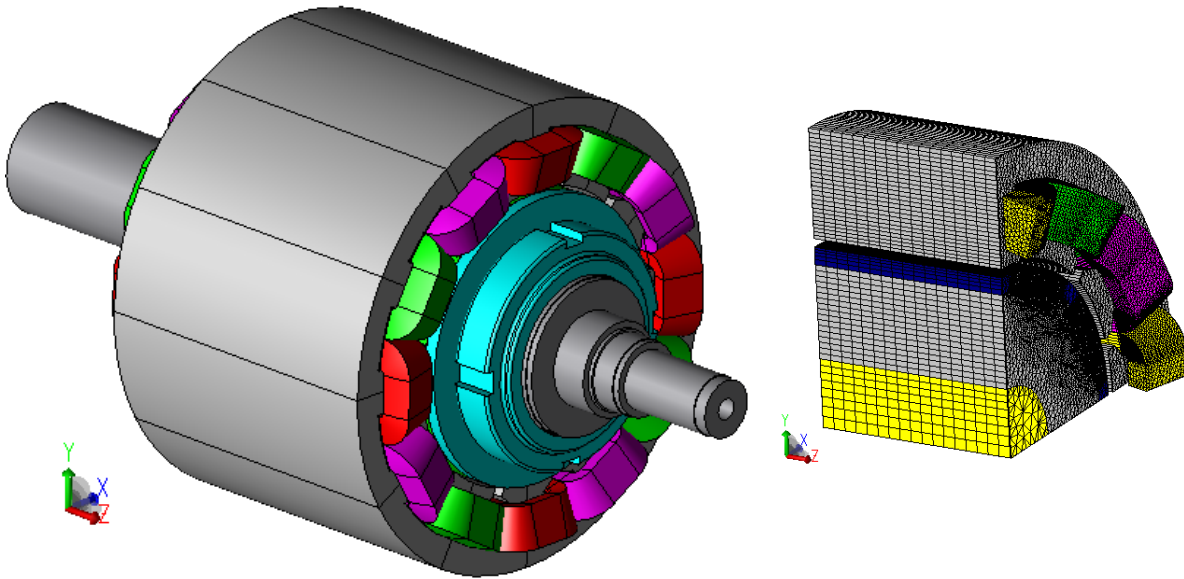


**Figure 3-6 Illustrates FEA model with the mesh size elements and contour plot at 25000 RPM**

### 3.5.3.1 Machine torque prediction and back EMF

A three-dimensional electromagnetic FEA model was built and simulated as shown in figure 3-7, based on the final optimised parameters of the 2D model, in order to assess the torque capability and back EMF. The 3D generated model included all the enhancement techniques in terms of improving machine performance, such as a segmented magnet rotor, embedded nonmagnetic ring within the fixed magnetic collar built within the rotor shaft, and also uses copper Litz wire for a significant reduction in AC losses. Due to an asymmetry of the axial length of the complete design of the HSHP machine in the Z-axis direction, as shown in figure 3-7, including the rotor shaft and front-end collars along with the influence of end windings on the machine performance, the full model design was simulated in a 3D time transient simulation.

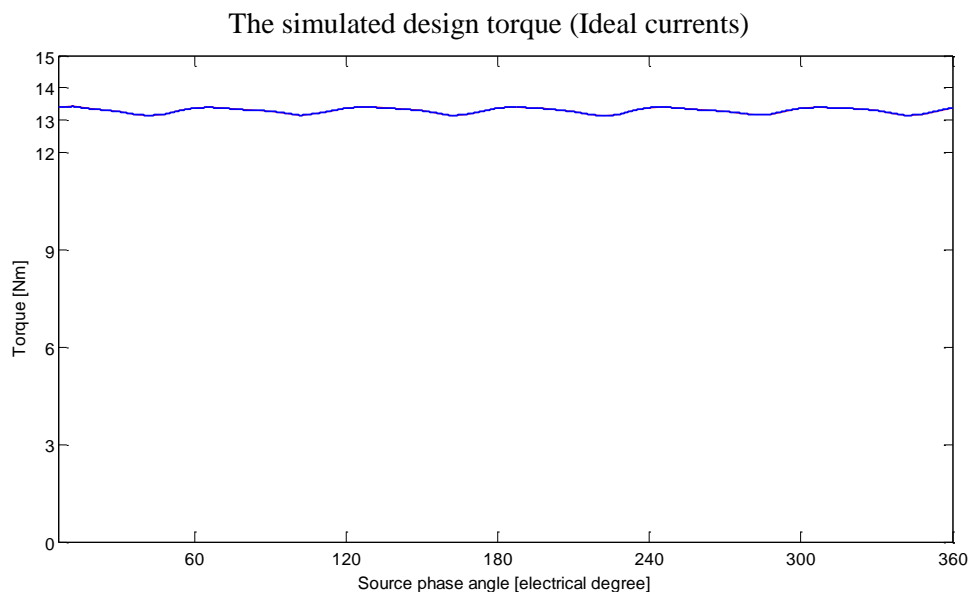




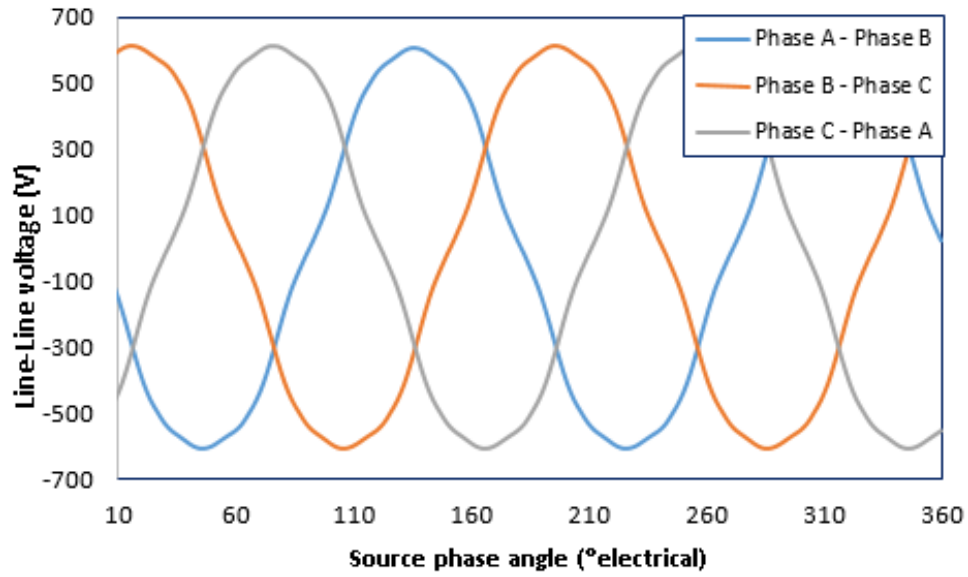
**Figure 3-7 3D Magnetic FEA model of the HSHP machine at 25000 RPM**

The predicted mean torque performance using the model in figure 3-7 is shown in figure 3-8 for one mechanical revolution, with an output of 13.2 Nm at normal operating conditions, the machine rated current and base speed are 47.4 A<sub>rms</sub> and 25000 RPM respectively. Since the machine torque is affected by cogging torque and back EMF harmonics, the mean torque was calculated over an electrical cycle.

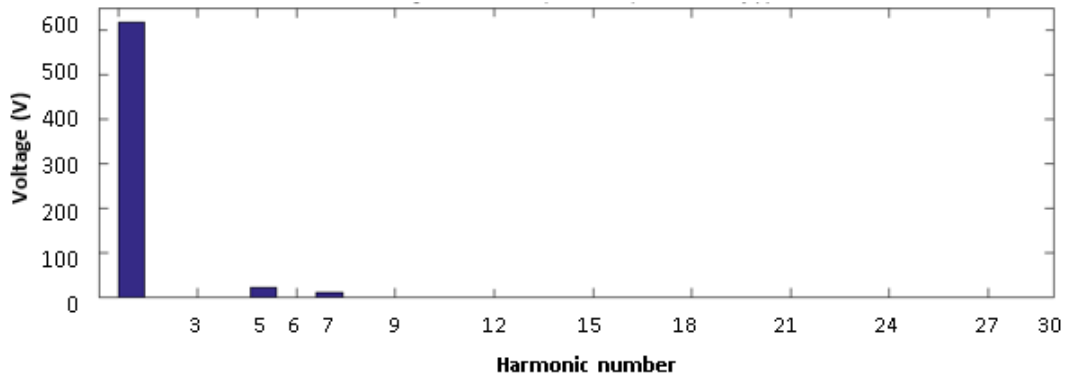
The line-line back EMF at a shaft speed of 25000 RPM is shown in figure 3-9, while the harmonic spectrum for the chosen design derived from FE results is shown in figure 3-10.



**Figure 3-8 3D torque performance prediction at 25000 RPM**



**Figure 3-9 3D Back EMF voltages at 25000 RPM**



**Figure 3-10 Harmonic spectrum of Line-Line back EMF at a fundamental frequency of 1.67 kHz**

In figure 3-9, the line-line back EMF voltage achieved is about 83% of that of the maximum line voltage available from the drive used. The contents of the back-EMF harmonics were investigated and are presented in figure 3-10. The most troublesome low order harmonics are the 5<sup>th</sup> and 7<sup>th</sup> harmonics [56].

### 3.5.3.2 Machine inductance

Using the 2D and 3D models shown in figures 3-6 and 3-7, an estimate of machine inductance for both models, including the effect of end windings was derived. Due to the non-salient rotor, the inductances in the q and d axes are approximately the same. In order to investigate the influence of machine excitation upon the machine inductance, the method of frozen permeability was carried out. Different methods of estimating machine inductance were employed as follows:

- A static simulation was performed by applying DC currents in the windings and setting the magnets residual flux density to zero. The 2D model gave a result of 0.249 mH, while the 3D model including the end windings effect gave a result of 0.2522 mH. It is noticeable that the contribution of the inductance by the end windings is 0.0032 mH.
- A frozen permeability solution was carried out in order to estimate the machine inductance under saturation conditions representative of the loaded condition. The first nonlinear simulation was performed with the machine at normal operating conditions (i.e. the machine at load). A frozen permeability solution was conducted where element permeabilities were taken from the original nonlinear solution. In the second simulation, the contribution of phase currents solely was considered by turning off the magnets, and in this case the coercivity ( $H_c$ ) of the PM materials was set to zero. Thus, in the second simulation, the resulting field effect in the machine stator from the previous nonlinear simulation is included in the calculation of the machine inductance. The machine phase inductance was calculated using a 2D FEA model, giving a result of 0.2411 mH.

Table 3-3 shows the results for predicted machine inductance using the static and frozen permeability solutions.

**Table 3-3 Validation the HSHP machine inductance (25000 RPM)**

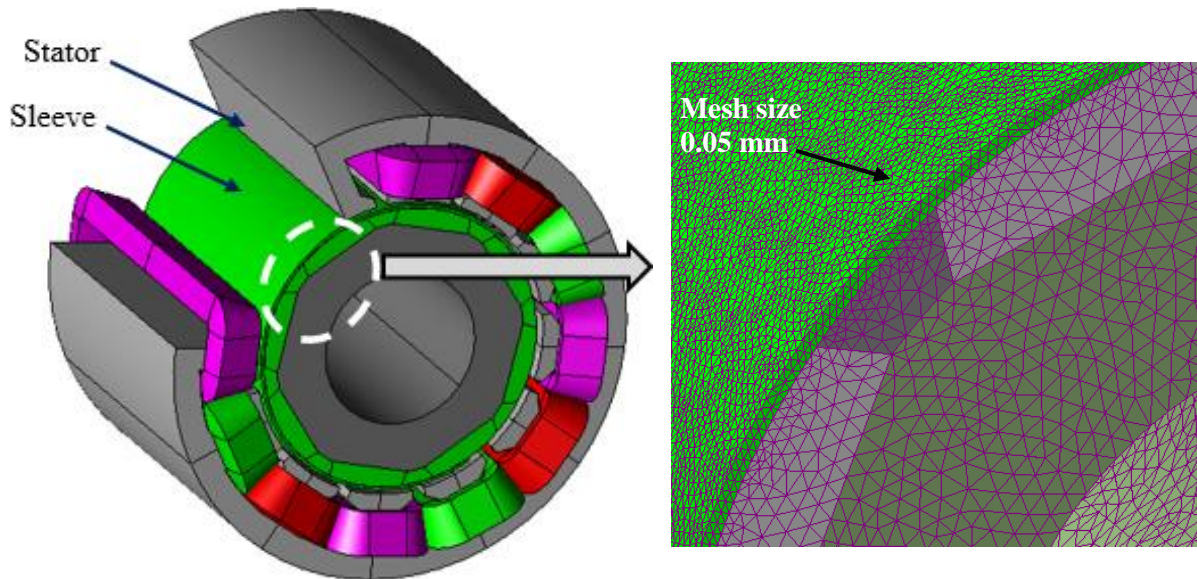
<b>Static solution</b> <b>3D FEA model (mH)</b>	<b>Frozen permeability solution</b> <b>2D FEA model (mH)</b>
0.2522	0.2411

It can be seen that the influence of stator permeability associated with magnetic flux density on machine inductance is small. The frozen permeability solution should be applied when a machine is heavily loaded, and hence the side effect of saturation in this case could be determined.

### 3.5.4 Rotor stress analysis validation

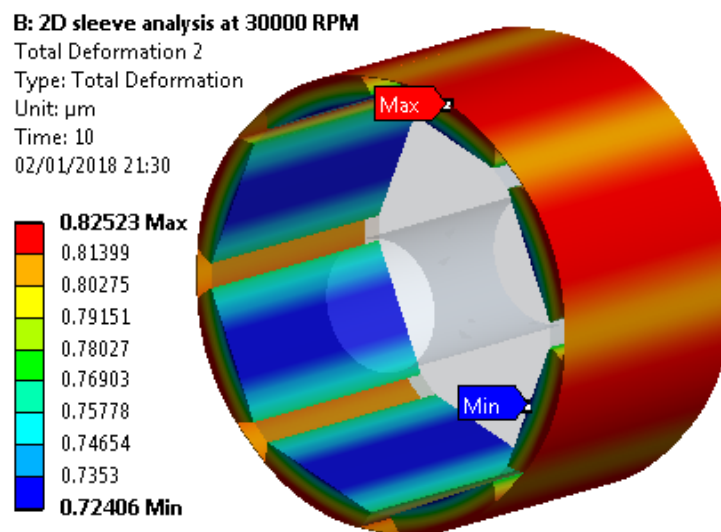
Rotor stress prediction was performed using the Ansys software package. A 2D rotor model including the CFRP sleeve was modelled: the complete rotor model and mesh are shown in figure 3-11. For this mechanical analysis, all magnet segments are assumed to be bonded to the rotor core. Therefore, bonded contact was used in mechanical FE software between the magnets and rotor core. The magnets must be resistant to centrifugal forces (remain attached to the rotor) at all operational speeds: a safety factor was introduced to ensure that the rotor could operate at

20% above the maximum designed speed i.e. at 30,000 RPM. The segmented magnets were constructed by bonding them to the rotor core and all the gaps between the magnets poles to be filled with a resin epoxy material. A CFRP sleeve with a final thickness of 0.35 mm was then wrapped at a tension of 700 MPa (room temperature) over the full assembly. The machine air gap is fixed in the optimisation process based on the electromagnetic machine design and as it is large enough to accommodate the sleeve. However, the sleeve thickness has been chosen based on the construction limitation advised by Arnold Magnet company.

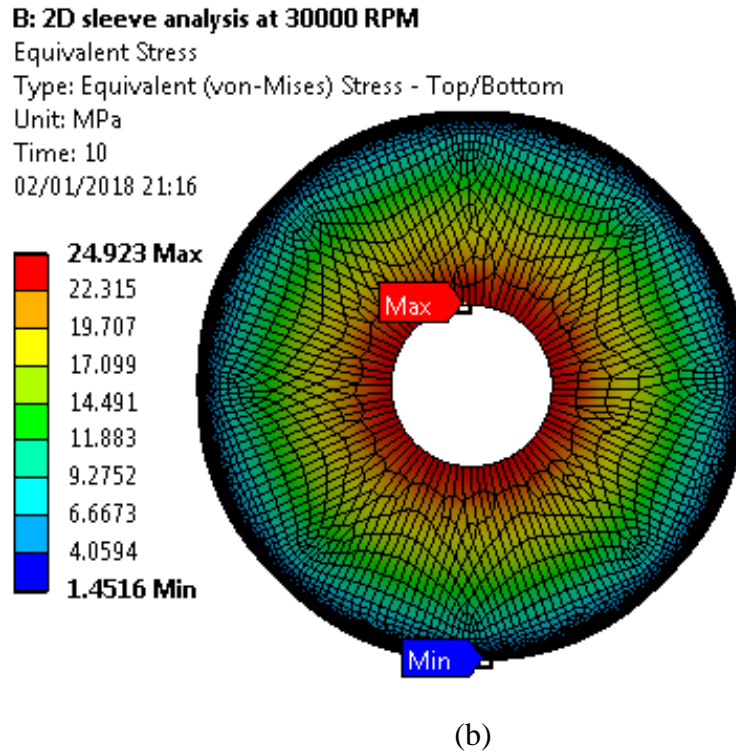


**Figure 3-11 Rotor components including sleeve with mesh overlaid**

The results of the predicted deformation and stress models are shown in figure 3-12, showing that the CFRP sleeve at 30,000 RPM is still capable of keeping the rotor structure safe.



(a)



**Figure 3-12 Rotor structure analysis: a) deformation on sleeve; b) equivalent von-Mises stress on rotor structure**

Figure 3-12 (a) shows that the maximum deformation is  $0.825 \mu m$ , while the maximum stress occurring on the sleeve is approximately 5.03 MPa while the ultimate tensile strength of the CFRP is over 4600 MPa [77]. Due to the chosen sleeve thickness, the stress on the sleeve is very small. In figure 3-12 (b), the equivalent von-Mises stress on the rotor structure is 24.92 MPa, while the tensile strength of the rotor material (M-270–35A) lamination is 450 MPa. As a consequence, the mechanical integrity of the rotor structure, including the magnets and sleeve is considered secure. Clearly the sleeve is operating at only a tiny percentage of its stress capability. However, it is not possible to further reduce sleeve thickness because of construction limitation.

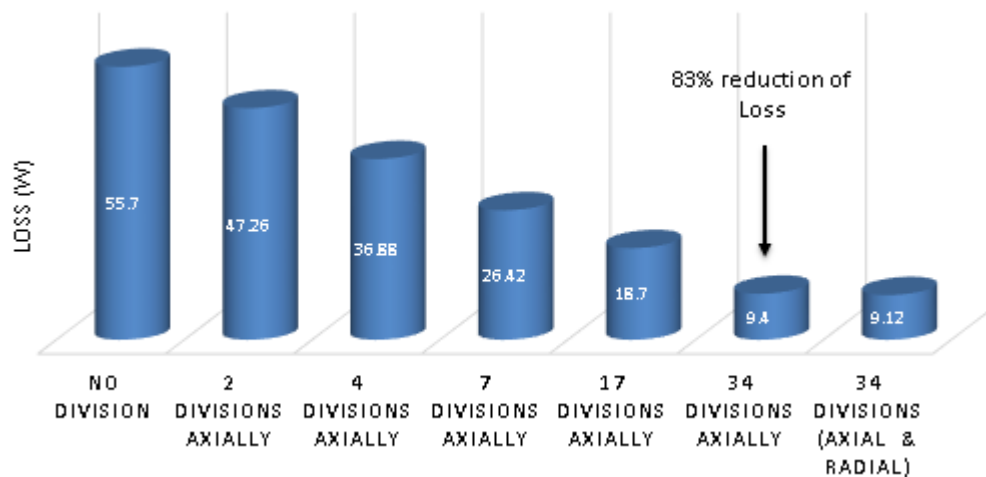
### 3.5.5 Loss estimation

High-speed high-power machines introduce significant sources of loss. High electrical frequencies cause significant additional AC losses in the armature windings, along with introducing large iron losses, so forced cooling systems are required to maintain safe operating temperatures. The low inductance of the machine, in conjunction with low switching frequencies in the associated drive tend to cause significant time harmonics in the machine current waveforms, which can lead to large losses in armature conductors and the rotor. Windage and friction losses lead to additional other sources of losses.

### 3.5.5.1 Rotor losses

Rotor losses are a major problem because they are difficult to remove. Generally, there are two techniques that employed to reduce these losses: stator based methods and rotor based methods. Stator based methods reduce the MMF harmonics by changing the winding configuration, altering the dimensions of the machine slot opening or increasing the air-gap length. Rotor based methods are focused on reducing the impacts of the harmonics by altering the conductivity of rotor elements such as magnet segmentation, using eddy current shields and bonded magnets that have low conductivity [78-81].

For the proposed HSHP machine, the rotor magnets were segmented axially to reduce the flux driving eddy currents around any one path. The predicted magnet loss was reduced by 83%. This achievement was accomplished by segmenting the magnet axially into 34 slices in each pole. Another attempt was then made to achieve lower magnet losses. The rotor magnets were segmented radially and axially at the same time, but the additional reduction in losses was only 1% as shown in figure 3-13. In addition, this is not a cost-effective method because extra manufacturing processes would be needed, so this was not considered further. Generally, magnet segmentation is also very costly, particularly at low segment widths, as material removed by the cutter becomes a large proportion of the final magnet. Figure 3-13 illustrates the different losses in one pole of the rotor magnet which obtained from the 3D model at normal operating conditions, full armature current and the base rotor speed 47.4 A<sub>rms</sub> and 25000RPM respectively.



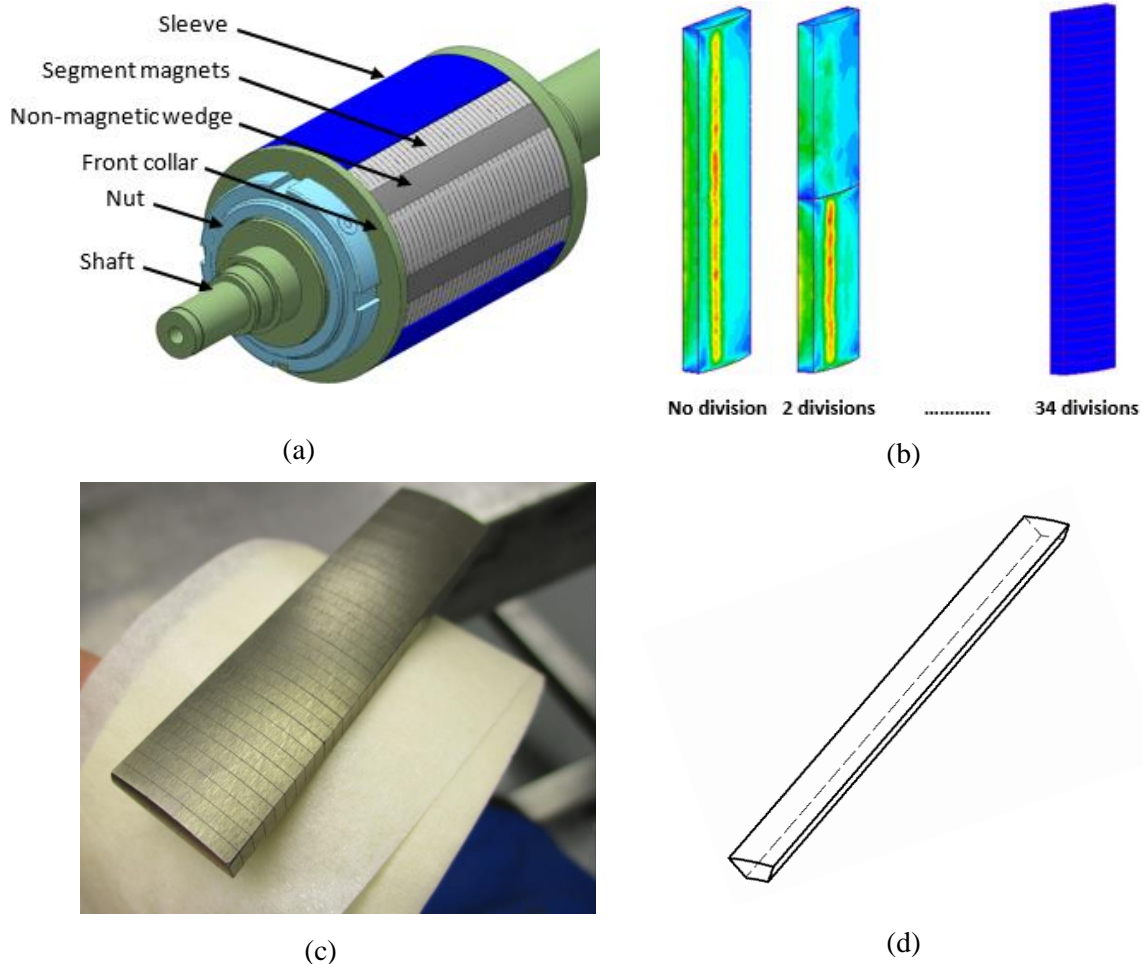
**Figure 3-13 Effect of magnet segmentation on losses at rated current and shaft speed**

Figure 3-14 (a) illustrates an eight-pole rotor assembly modelled using the PM material grade N42UH<sup>3</sup>, laminated axially in 34 slices which were cylindrically ground and contained in a

<sup>3</sup> The B-H curve of the magnet material used is presented in Appendix B.

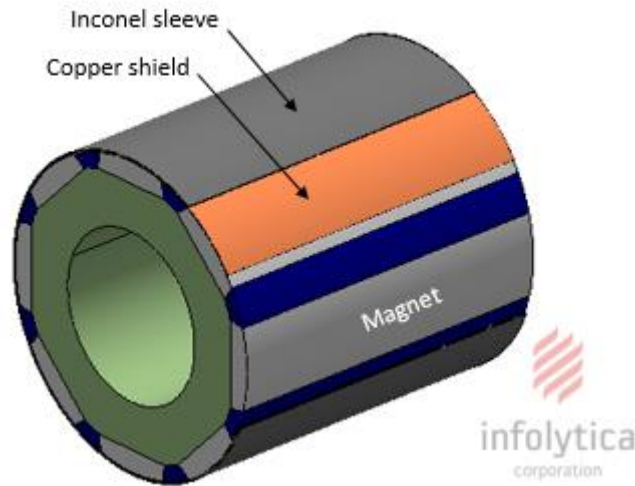


filament-wound carbon fibre sleeve. The eddy currents in each individual magnet are demonstrated in figure 3-14 (b). The manufactured segmented magnet for one pole is shown in figure 3-14 (c).



**Figure 3-14 High rotor speed: a) rotor assembly, showing segmented magnets; b) effect of segmentation on eddy current paths; c) manufactured segmented rotor magnet for one pole; d) representation of the wedge filled by the resin**

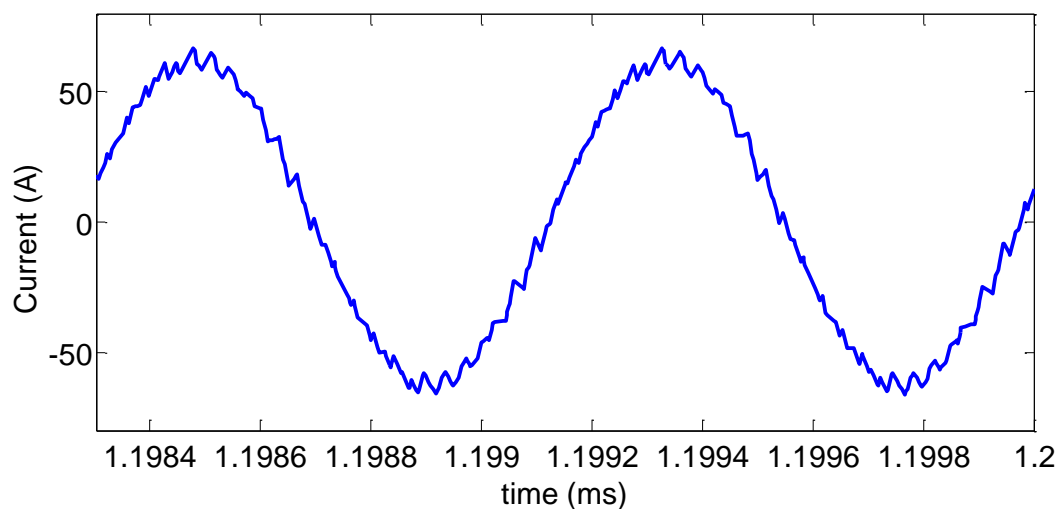
Utilising an eddy current shield [82] to reduce the magnet losses has been investigated. The machine rotor including the magnets was surrounded by a copper sheet and then an Inconel sleeve, as shown in figure 3-15. The main function of the copper shield is to prevent the major harmonics in the machine air gap from reaching the magnets. However, the loss caused by the copper shield is over five times the magnet losses and hence the eddy current shield was not considered further. As a consequence, the method chosen to reduce the magnet losses for the proposed machine rotor was magnet segmentation.



**Figure 3-15 Eddy current shield applied to the high-speed rotor**

### **MMF time-harmonic losses in magnets**

The three-phase drive to power the motor used in this work produces phase current with a THD of 7.18%. The resulting phase current waveform is shown in figure 3-16. These time harmonics increase the magnet loss to 11.58 W per pole.



**Figure 3-16 Drive phase current with 7.18%THD**

### **3.5.5.2 Stator losses**

The various components of stator losses are studied in this section.

#### **3.5.5.2.1 Iron losses**

Different approaches have been introduced by various authors in relation to improving the accuracy of iron loss estimation and the literature in this field is extensive. The prediction of



core losses in rotating electrical machines proposed by Bertotti et al. [83, 84] has been developed as a frequency domain model which separates the losses into three components: hysteresis, eddy current (or classical), and anomalous (or excess, or dynamic) losses, as shown in equation 3.2.

$$P_{Iron\ Loss} = P_{Hysteresis} + P_{Eddy\ current} + P_{Anomalous} \quad (3.2)$$

- **Eddy current loss density**

The magnetic flux variation in a solid stator creates induced voltages which produce eddy currents circulating within the stator steel. These eddy currents will have a negative impact on the reaction magneto-motive force (MMF) towards any useful MMF. A previous study [83] investigated many factors which affect eddy current limitations, as given in equation (3.3). The eddy current loss density is proportional to lamination thickness squared ( $t^2$ ), operating machine frequency squared ( $f^2$ ), and flux density squared ( $B^2$ ), while it is inversely proportional to material resistivity as illustrated in equation (3.2).

$$P_{EC} = \frac{t^2 \omega^2 B^2}{24 \rho} \quad (3.3)$$

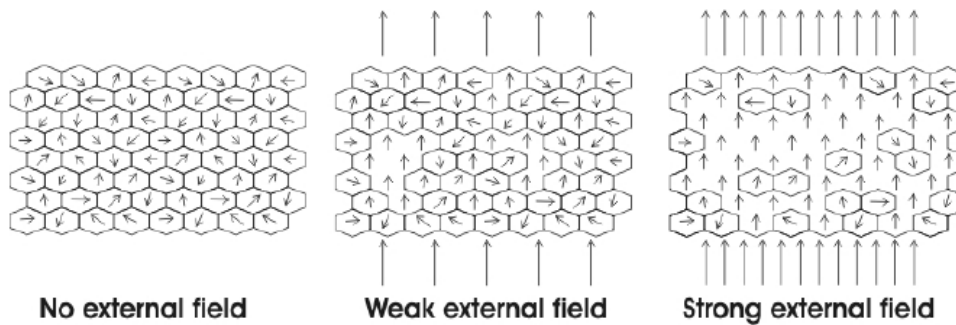
Consequently, Bertotti's equation can be rewritten as adopted elsewhere [9] in the following form:

$$\text{Eddy current loss (in watts per kilogram)} P_{EC} = K_e f^2 B^2 \quad (3.4)$$

where  $K_e$  is a function of lamination thickness squared and material resistivity.

- **Hysteresis and anomalous losses**

The hysteresis loss in a stator core is caused by localised irreversible changes through the process of magnetisation [85]. The domain structure of magnetic material with an external magnetic field where the domains are aligned with the applied field is as shown in figure 3-17.



**Figure 3-17 Behaviour of domain alignment for an external magnetic field [86].**

This type of loss is known as hysteresis power loss ( $P_{Hy}$ ) and it can be calculated as given in equation 3.5:

$$\text{Hysteresis loss (in watts per kilogram)} P_{Hy} = K_h f B^\alpha \quad (3.5)$$

The external magnetic field of an application will accelerate the domains and increase the velocity, resulting in a micro-eddy current loss, and this is known as anomalous or excess loss ( $P_{An}$ ) as given in equation 3.6.

$$\text{Domain loss (in watts per kilogram)} P_{An} = K_a f^{1.5} B^{1.5} \quad (3.6)$$

Losses of the machine core are a function of machine frequency and the magnitude of flux density, where  $K_h$ ,  $K_e$ ,  $K_a$  and  $\alpha$  are material dependent constants [42]. The total iron loss can be calculated as given in equation 3.7.

$$P_{Iron\ Loss}(\text{in watts per kilogram}) = K_h B^\alpha f + K_e B^2 f^2 + K_a B^{1.5} f^{1.5} \quad (3.7)$$

However, it has been stated [83] that measured core losses will be about 20% higher than predicted. In addition, the discrepancy between finite-element analysis predictions and real measurements can ultimately be attributed to the additional losses caused by eddy currents in the stator cage and the degradation of material properties due to manufacturing processes, including cutting, material-handling and machine core assembly. Since the electrical frequency of the proposed high-speed machine is relatively high, it was important to employ an efficient magnet steel material which would give as low iron losses as possible. Different magnet materials have been simulated at the same operating conditions, as shown in figure 3-18.

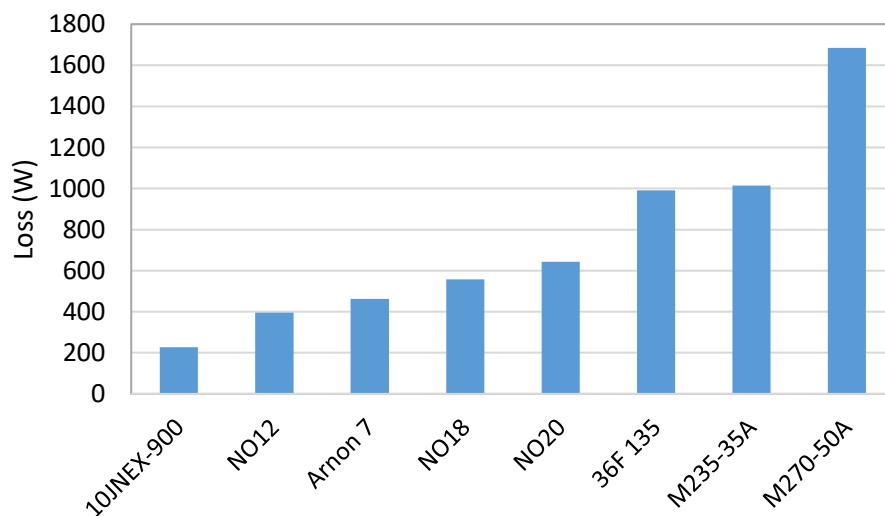


Figure 3-18 A comparison of iron loss for different core materials

The 10JNEX-900 material achieved the lowest iron losses compared to the other candidates and was therefore chosen in this research.

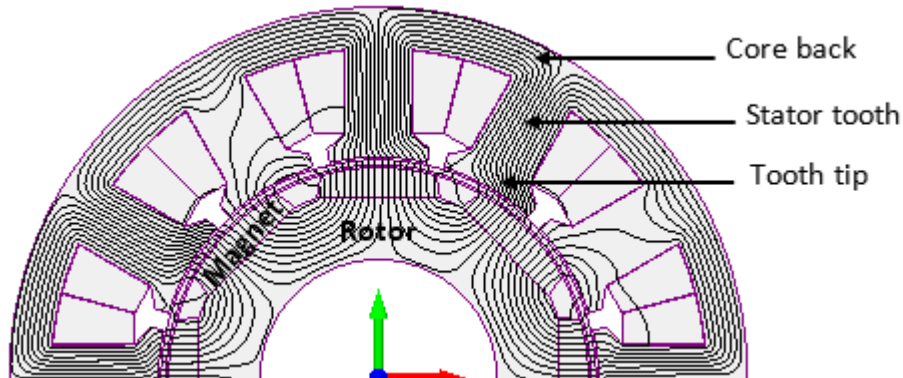
### 3.5.5.2.1.1 Prediction of iron losses based on the Steinmetz equation for the HSHP machine

The operating electrical frequency of the proposed HSHP machine is 1.666 kHz, and the super-core 10JNEX-900 has low core loss around the fundamental machine frequency [69]. The material constants of the JNEX-Core are given in table 3-4 along with a negligible anomalous loss which is very small compared to the eddy and hysteresis losses and is therefore ignored.

**Table 3-4 Material dependent constants for the super-core of 10JNEX-900**

Material constant	Value
$K_h$	0.00475872
$\alpha$	1.14821
$K_e$	5.41279e-006

Figure 3-19 shows different components in the machine stator where the losses in each part have been calculated individually. In order to assess the accuracy of this method, the peak value of flux density in each iron component was obtained from a 2D FE model of the machine as shown in table 3-5. In order to investigate the variation of magnetic flux density within the machine stator, the resulting full load flux densities for each stator part (figure 3-19) are shown in table 3-5. The electric load flux density is obtained at full armature current when the magnets are turned off and then the strength of electric load flux density can be noticeable. The resultant flux density values are used in order to calculate iron losses using Steinmetz equation.

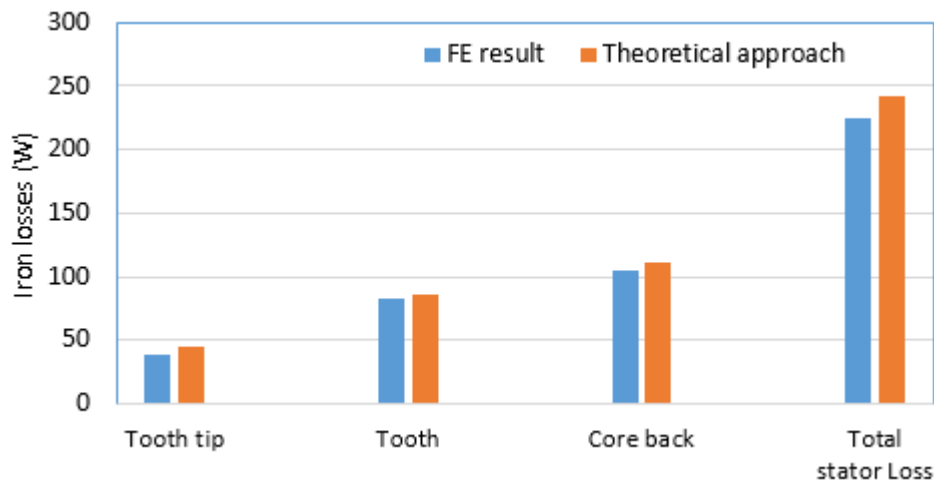


**Figure 3-19 Different stator components**

**Table 3-5 Magnet and electrical load flux densities in the stator regions**

	Stator components		
	Core back	tooth	Tooth tip
Electrical-load flux density (T)	0.77	0.72	0.65
Magnet-load flux density (T)	1.14	1.36	0.92
Resultant flux density (T)	1.35	1.5	1.08

The resulting full load flux densities were applied in equation 3.7. Figure 3-20 illustrates the calculated iron losses compared to those obtained from the 2D FE model. Although the resultant flux density is obtained from the FE model, the results calculated from the Steinmetz equation are still valid for those obtained from the FE model. The rotor losses, which are about 0.6W, are not included in the calculation, because the magnetic flux is synchronised with the rotor speed.

**Figure 3-20 Composition of full load iron losses for the HSHP machine stator**

The percentage error between the theoretical and FE results is about 7%. The total losses calculated theoretically are 242 W while the FE model gives a result of 225 W.

In practice, the measured values of iron losses might be slightly different from the FE results due to bearing friction losses, effects of the stator casing and the manufacturing process of the machine.

Further information about other practical measurements of iron losses can be found in [87].

### 3.5.5.2.2 Copper losses

The composition of copper losses in high-speed high-power machines includes not only purely resistive loss. Elevated frequencies in high-speed, high-power machines lead to proximity and skin phenomena which cause significant additional losses. The windings losses consist of two components as follows:

1. DC losses, which are mainly caused by the RMS current;
2. AC losses, due to the proximity and skin effects at the high operating frequency caused by the currents flowing in the conductors;

The operating frequency of the HSHP machine is 1.666 kHz, and the AC losses will, therefore, add a significant additional loss to the overall machine losses.

- **DC winding loss**

The HSHP PM machine has 36 bundles per coil and each bundle has 20 strand Litz wire, where each phase has 4 parallel coils. The approximate mean length of the end windings  $l_{End\ w.}$  in one side of a tooth is 28 mm with a slot axial side-length  $l_a$  of 70 mm. The copper resistivity  $\rho$  is  $1.68 \times 10^{-8} \Omega m$  at a temperature of 20°C, the cross-sectional area (C.S.A) of each strand is  $0.0509 mm^2$ , and the predicted resistance per phase of the armature windings is 29.11 mΩ, as can be calculated as shown in equation 3.8:

$$R_{DC} = \frac{\rho_c \times 2 (l_{End\_1side} + l_{a\_1side}) N}{C.S.A \times 20_{strand} \times 4_{coils\ per\ phase}} \quad (3.8)$$

The total estimated DC loss of the armature 3-phase windings (PM machine windings) based on Ohm's law equation  $I^2 R$  is 195.8 W.

A feature of the DC losses in conductors that must be considered in the design of high-speed machines is the variation in the resistivity of copper with temperature. The temperature coefficient of the resistivity of a conductor material has a significant impact on DC losses in the winding corresponding to the operating temperature. Since the expected machine winding temperature under normal operating conditions is 80°C and the temperature coefficient is  $0.00399 K^{-1}$ , the DC resistance at the specified operating temperature is 36.08 mΩ, as calculated from equation 3.9 [56]. Although, the expected winding operating temperature is below the thermal class of copper winding used in the construction demonstrator, this would help protect machine coils from an excessive thermal stress when they work closer to the thermal

limit. In the meanwhile, the type of copper Litz wire which was bought for the prototype is met with the required specifications such as the crosssectional area of wire and number of strands and it is enhanced with a high thermal class up to 200 C. Therefore, it was accepted to be used for the constructed prototype.

$$R = R_{ref}[1 + \alpha (T - T_{ref})] \quad (3.9)$$

where  $R$  is the conductor resistance at temperature  $T$ ,  $R_{ref}$  is the conductor resistance at the reference temperature  $T_{ref}$ , and  $\alpha$  is the temperature coefficient of resistance for the conductor material.

As a result, the predicted total DC loss at the specified operating temperature is 242.67 W.

- **AC winding losses**

The AC losses in most low-speed machines are very low as the electrical machine frequency is not very high. The additional AC loss in HSHP machines is caused by proximity due to the type, shape and arrangement of coils within the machine slots associated with skin effect.

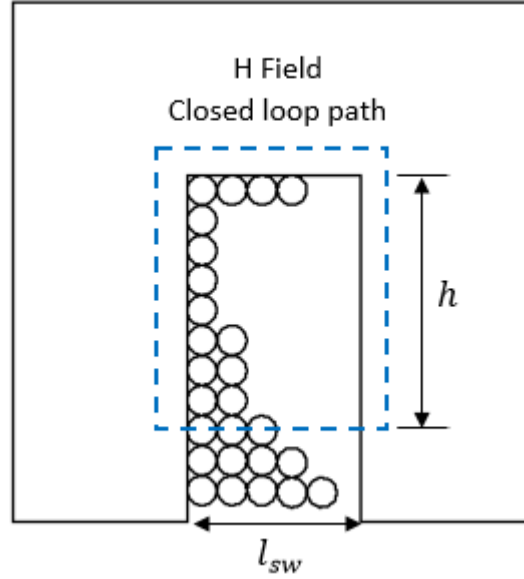
The skin effect describes the depth for high frequency currents to flow close to the surface of a conductor, as illustrated in equation 3.10. If the skin depth is larger than twice the conductor diameter, then the effect can be ignored. The electrical frequency of the HSHP machine is 1.666 kHz and hence the skin depth is  $1.598 \times 10^{-3}$  m, as calculated from equation 3.10 [56, 88].

$$\delta = \sqrt{\frac{2}{\omega \sigma \mu_o}} \quad (3.10)$$

where  $\delta$  is the skin depth,  $\omega$  is the electrical angular velocity,  $\sigma$  is the copper conductivity and  $\mu_o$  is the permeability of free space.

In this analysis, a 0.25 mm diameter of a copper strand is approximately 6 times smaller than the skin depth and hence the skin-effect is not significant.

In order to predict AC losses, a method called the squared field derivative has been introduced by Charles [89] for calculating eddy current losses due to the proximity effect. The current flowing through each conductor will produce a magnetic field which crosses other conductors in the slot and causes an induced eddy current circulating in each conductor, subsequently producing heat loss in the slot. Figure 3-21 illustrates the closed loops of the magnetic strength field (H-field) within a machine slot.



**Figure 3-21 MMF flow chart within a slot with conductors**

In the slot shape shown in figure 3-21, the MMF is assumed to be evenly distributed across the slot cross-sectional area and the MMF drop in the stator iron is assumed negligible. Utilising Litz wire results in uniform current density distribution,  $J$ , and hence the leakage field across the slot at a given depth of  $h$  (shown in figure 3-21), from the stator iron can be related to current distribution within the slot.

$$MMF_{slot}(t) = \oint H(t) dl = \iint J dS \quad (3.11)$$

$$B(h) = \frac{\mu_o \times MMF_{slot}}{\text{slot width at } h} = \frac{\mu_o J l_{sw} h}{l_{sw}} \quad (3.12)$$

$$B(h) = \mu_o J h \quad (3.13)$$

This approach is that of a mainly time-dependent magnetic field varying within each conductor due to the conductors in the slot carrying current, and the instantaneous AC loss can be calculated in each layer,  $m$ , as given in equation 3.14 where  $N_m$  is the number of conductors in each layer at a slot depth of  $h_m$  [89]<sup>4</sup>.

$$P_{AC}(t) = \frac{N_m \pi l_a D_c^4}{64 \rho_c} \left( \frac{dB_m(t)}{dt} \right)^2 \quad (3.14)$$

$$\text{where } B_m(t) = \mu_o J h_m \sin(\omega t) \quad (3.15)$$

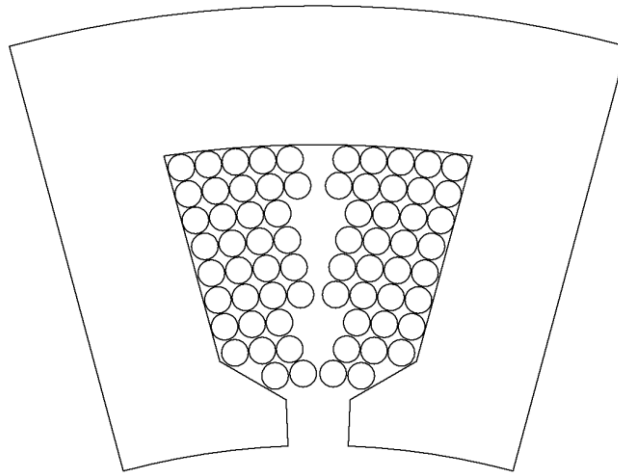
<sup>4</sup> The analytical derivation of the AC losses equation is illustrated in Appendix A.

Here  $\mu_0$  is the permeability of free space,  $B$  is the flux density in the conductor,  $\omega$  is the electrical frequency,  $l_{sw}$  is the slot width,  $D_c$  is the conductor diameter,  $l_a$  is the conductor axial length, and  $\rho_c$  is the resistivity of copper.

The above formula assumes there are no circulating currents between strands. This is an accurate assumption for Litz wire, where transposition of superconductors should virtually eliminate this effect.

Although the accuracy of this analytical approach is sufficient with an open slot, this method will not be adequate when slot closure features are considered. The fringing magnetic fields between tooth tips will affect the concentration of flux density in the bottom of the slot, and therefore the estimated flux density given in equation 3.15 is no longer be correct. The AC losses have been extensively investigated in literature in order to derive power losses in Litz wire [90-95].

In the proposed machine design, the slot is a conventional slot shape as shown in figure 3-22 and the slot closure effect must be taken into the account with regards to estimating AC losses accurately along with avoiding any design concessions.



**Figure 3-22. Geometry of the proposed machine slot**

As a result, a 2D FE model has been simulated with the rated machine input current to determine the contribution of fringing flux between slot tips in the lower windings layers. This simulation initially examined the AC winding loss conversion factor which is defined as:

$$AC \text{ Loss Conversion ratio } (K_{AC}) = \frac{R_{ac}}{R_{dc}} \quad (3.16)$$

It can be seen from the definition of  $K_{AC}$  that the highest AC resistance gives the highest conversion factor. Therefore, reducing the cross-sectional area of the conductors will reduce



the AC losses as the proximity losses and skin effect will be reduced. This argument leads to the use of Litz wires with an appropriate diameter and number of strands in each bundle. The advantages of using compressed Litz coils are that they have the following characteristics:

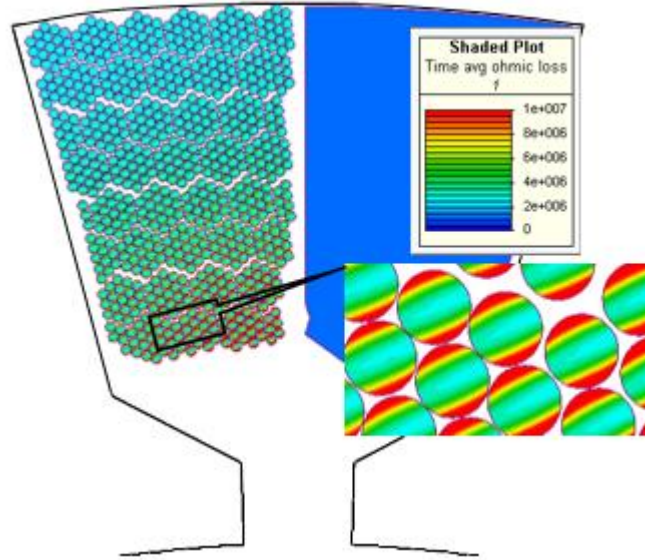
- Higher efficiency
- Limited proximity and skin effects
- Mitigated eddy current loss
- Lower heat windings
- Significant weight reduction
- High slot fill factor

Due to the flexibility of litz wires, the coil shape within the machine slot can be easily formed and positioned using the technique of compressed coils associated with impregnation glue process. The machine coil has been designed and simulated in a 2D FE model (shown in figure 3-23) as it can be practically performed. Firstly, all copper conductors within the machine slot were simulated in a case of stranded type, then DC loss was obtained by solving the model in transient 2D with motion. Secondly, in order to calculate the DC loss and AC losses collectively, all copper conductors simulated again in a case of solid type. Different numbers of strands in each bundle have been simulated to achieve minimised AC winding losses as shown in table 3-6, in which end windings losses are not included.

**Table 3-6 Improvement in AC winding loss conversion power factor  $K_{AC}$  via 2D FEA**

Type of wire	DC loss/phase (W)	AC loss/phase (W)	$R_{dc}$ /phase m $\Omega$	$R_{ac}$ /phase m $\Omega$	$K_{AC}$
36 solid turns	49.67	55.65	20.79	47	2.26
36 bundle/4 strands	49.67	10.78	20.79	27	1.29
36 bundle/20 strands	49.67	5.5	20.79	24	1.18

The results for AC losses conversion ratios reveal that the contribution of the AC winding losses is reduced by a ratio of 1.08 when using the Litz wire of 20 strands  $\times$  30 AWG. Figure 3-23 illustrates the effect of fringing flux on the bottom bundles of the chosen Litz wire, where the effect of magnetic fringing flux is obvious in the lower windings which are near to the closure of the machine slot.



**Figure 3-23 Field and current contributions of adjacent conductors within the slot**

The strength of the electric fields produced by the current flowing through each conductor reduce gradually with the height of coil because of there are fewer turns remaining towards the top of the coil.

As the total winding power loss is known, the AC resistance can be calculated from equation 3.17, which gives a result of 1.18  $\Omega$ :

$$R_{AC} = P_{Total} / I_{RMS}^2 \quad (3.17)$$

It is important to note that the AC effects in the winding active length are dominant as compared with the end winding region. Therefore, the end winding resistance was considered only in the calculation of DC resistance.

### 3.5.5.3 Windage losses of a rotating machine

High-speed machines with relatively large rotor diameters will have significant windage losses. The windage loss is the power absorbed by the air that flows between the stationary stator and the moving rotor (shearing stress). This type of loss depends on various operating conditions and contributes to the overall machine efficiency.

Another undesirable characteristic is where the dissipated power in the air is converted into heat, which may overheat the rotor and increase the stator bore surfaces which are in contact with the air gap. Thus, the prediction of windage loss in the proposed machine is widely accepted to be important in order to determine its workability. The presence of windage loss is dictated by several different conditions, such as the speed of the rotor and the properties of the

air such as temperature and pressure and the roughness of the rotor and interior stator surfaces. An analytical approach for predicting the windage power loss has been presented [96], where basic equations have been developed to calculate power loss in the air gap of an alternator. To determine the windage loss of a rotating machine with a concentric cylinder, various assumptions should be satisfied as follows:

1. The windage loss is generated in the air gap between the rotor and stator with laminar flow.
2. The air filling the gap is homogeneous.
3. The gap between the rotor and stationary part is small compared to the length and radius of the cylinder.

The windage loss of the HSHP machine which is generated between the stationary cylinder and rotating cylinder with no axial flow was estimated from the following equations [96, 97]:

- Shaft rotational speed:

$$\omega = \frac{2\pi N}{60} \quad (3.18)$$

- Reynold number:

$$\text{Re} = \omega r \frac{\rho}{\mu} l_{rg} \quad (3.19)$$

- Skin friction coefficient ( $C_d$ ) for turbulent flow:

$$\frac{1}{\sqrt{C_d}} = 2.04 + 1.768 \ln(\text{Re} \sqrt{C_d}) \quad (3.20)$$

- Windage power loss:

$$W = C_d \pi \rho \omega^3 r^4 l_a \quad (3.21)$$

where  $\rho$  is the density of air surrounding the machine rotor (in  $\text{kg}/\text{m}^3$ ),  $\omega$  is the angular velocity (in  $\text{rad}/\text{s}$ ),  $r$  is the radius of the rotor (in m),  $l_a$  is the rotor axial length (in m),  $N$  is the rotor speed (in rpm),  $l_{rg}$  is the radial air gap length between rotor and stator and  $\mu$  is the viscosity of the air (in  $\text{m}^2/\text{s}$ ).

An air gap temperature of 100 °C has been assumed as a worst case giving by a research staff who working on the thermal side of the integrated motor drive, the air density and viscosity are 0.9413  $\text{kg}/\text{m}^3$  and  $2.317 \times 10^{-5}$   $\text{m}^2/\text{s}$  respectively. The predicted windage loss is therefore calculated as follows:

$$Re = \omega r \frac{\rho}{\mu} l_g = 2617.994 \times 0.031 \times \frac{0.9413}{2.317 \times 10^{-5}} \times 0.0015 = 4945.65 \text{ rad/s}$$

$$Cd = 2.384 \times 10^{-3}$$

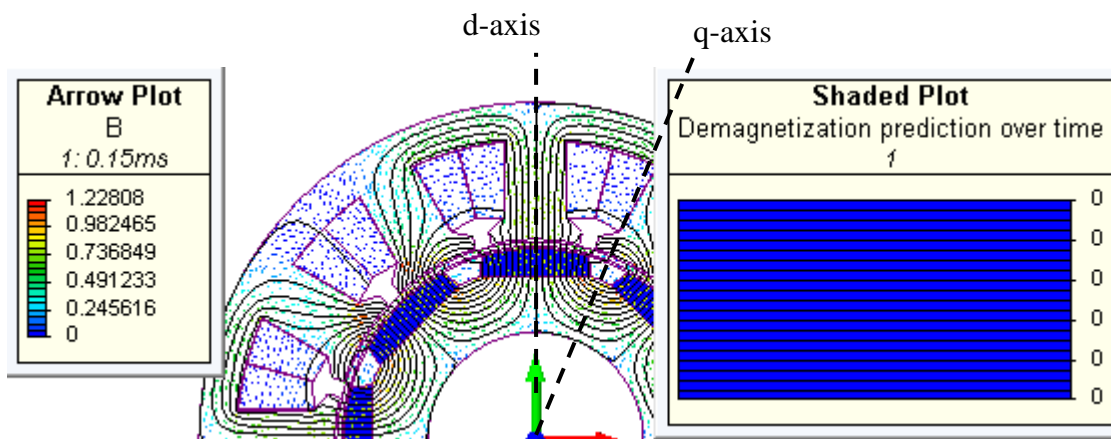
$$W = C_d \pi \rho \omega^3 r^4 l_a = 8.18 \text{ W}$$

The key results for the 12 slot / 8 pole PM machine at rated operating conditions are summarised in table 3-7.

**Table 3-7 Results for 12 slot/8 pole PM machine at 25000 RPM**

Main Machine Specifications:		
Diameter of stator	109	mm
Diameter of rotor	62	mm
Tooth width	10	mm
Core back depth	6	mm
Magnet depth	3	mm
Magnet span angle	38	degree
Sleeve thickness	0.35	mm
Number of turns	36	turns
Winding type	Concentrated - double layer / parallel connection	
Torque:		
Mean torque	13.2	N.m
Torque ripple	≈ 1	% (in per cent)
Cogging torque (peak)	0.021	N.m
Losses:		
Copper loss (DC + AC)	165.5	Watt
Magnet ohmic loss	92.6	Watt
Iron loss (Hysteresis + Eddy current)	225	Watt
Windage loss	8.18	Watt
Efficiency	98	%
Machine inductance and power factor		
$L_d$ , d-axis inductance	0.158	mH
$L_q$ , q-axis inductance	0.163	mH
Power factor	0.886	---
Fundamental winding factor (Kw)	0.866	---
Least common multiple	24	---

It was important to check that the design would not cause demagnetisation of the magnets. The worst scenario for the magnet to be demagnetised, along with its high operating temperature, is when the full armature current is in the negative d-axis, where the armature magnetic flux is opposed to the flux produced by the rotor magnets. Using the 2D FEA model, a prediction of demagnetisation over time was determined at 25000 RPM with a magnet temperature of 80 °C, as shown in figure 3-24. Demagnetisation could be an issue when the magnet experiences a hot spot due to elevated operating temperature inside the magnet, this might cause partial demagnetisation but it is greater when the armature current fully lie on the negative d-axis.



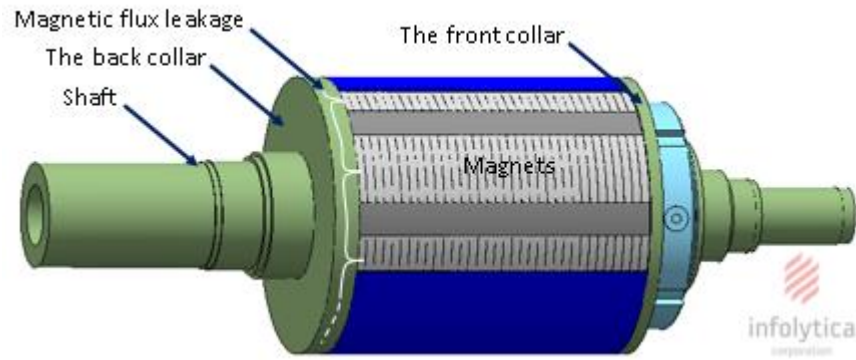
**Figure 3-24 Demagnetisation obtained at full rated current and speed**

As shown in figure 3-24 under the worst case scenario for demagnetisation the magnet retains a flux density of around 1 T meaning demagnetisation is not expected to occur anywhere within the magnet.

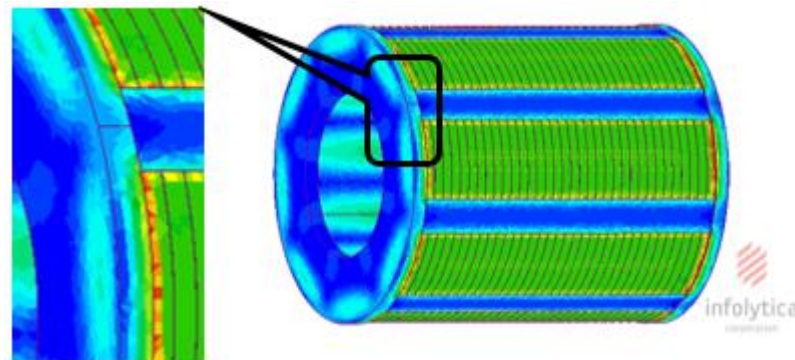
### 3.5.6 Axial location of rotor magnets

The original rotor design had retaining collars, giving axial location of the magnets, as shown in figure 3-25. The back collar was proposed to be integral with the shaft, which was specified to be constructed from a magnetic steel, with the front collar a removable disk. It was postulated that the collars could act as a magnetic short-circuit to the magnets and consequently reduce the mean air-gap flux density. For this reason an alternative design was considered in which the back collar was cut back and replaced with an additional nonmagnetic ring of 6mm radial depth and 3mm axial length. Non-magnetic steel was also considered for the removable front collar.

Figure 3-25 (b) is a pictorial view of the rotor magnetic flux with magnetic collars.



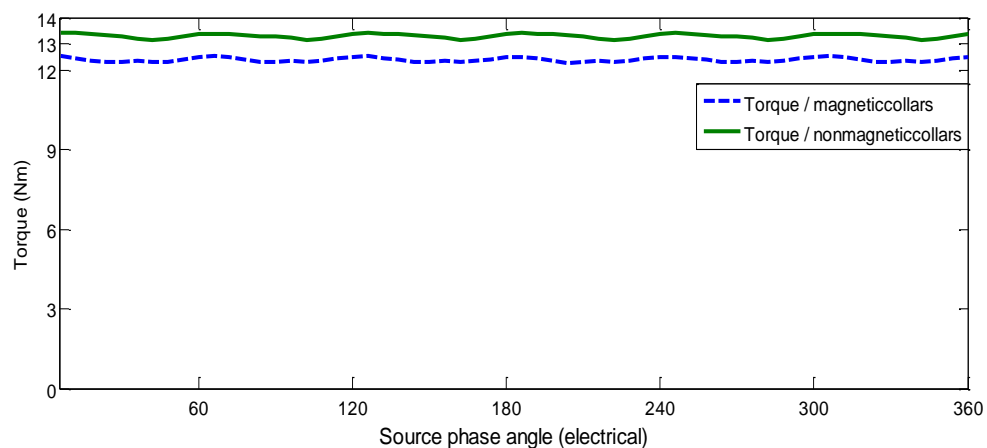
(a)



(b)

**Figure 3-25 The effect of front-end rotor collars: a) assembly of rotor; b) contour plot demonstrating the shorting of the end magnets**

The effect of collar material on the machine torque capability was modelled in 3D and is shown graphically in figure 3-26. Non-magnetic collars gave 6% greater performance than their magnetic counterparts, with a mean torque of 13.2 Nm and so the choice to modify the design was justified.

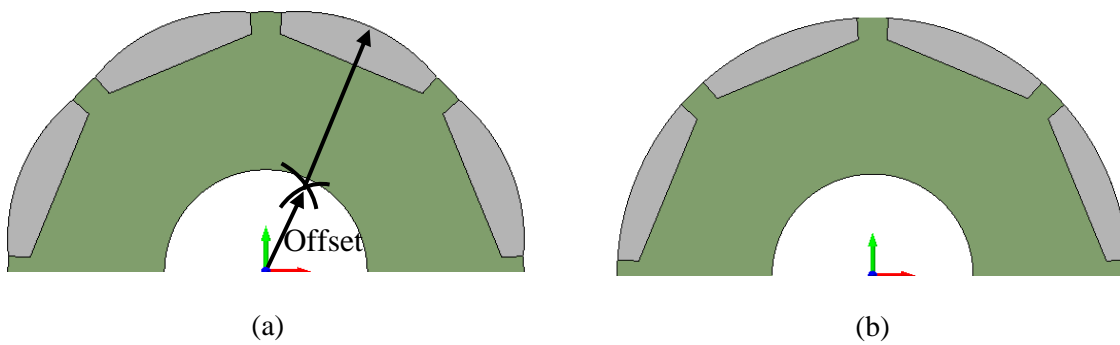


**Figure 3-26 Effect of collars on torque performance at 25000 RPM**

### 3.6 Design of the low speed machine

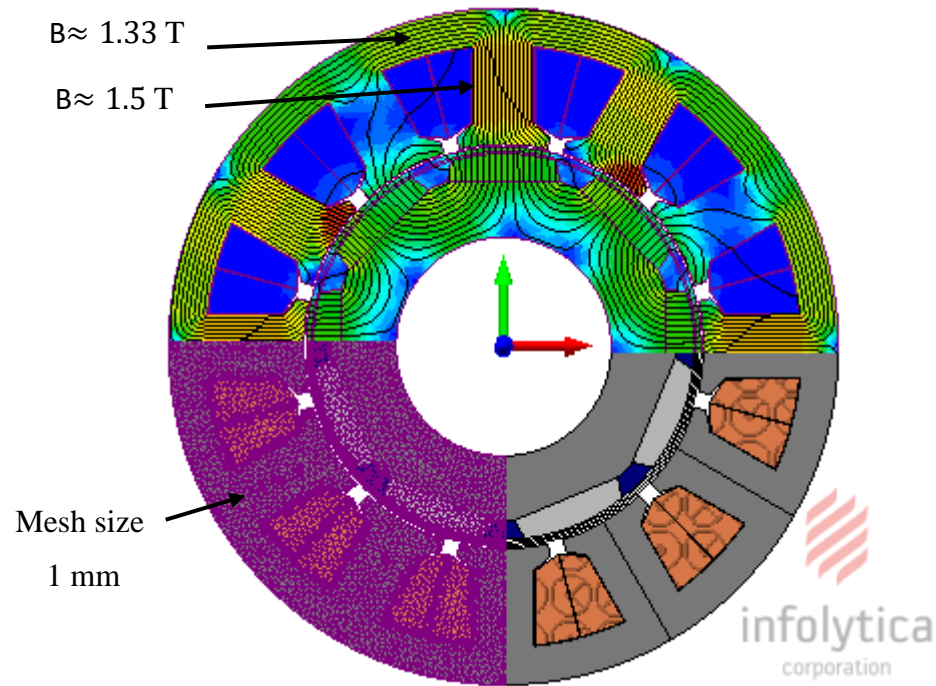
The design procedures of the HSHP machine have been explained in the previous section, the low-speed machine design has followed with the same process. The main difference between low- and high-speed machines is that, as the shaft speed is decreased by a ratio of 25000 rpm/3000 rpm the number of turns is increased by the same ratio in order to maintain the armature back EMF. Although the low-speed machine design has been conducted in parallel with the HSHP machine in order to validate the effectiveness of different integration techniques, the low-speed machine design was not built because of its simplicity in terms of integrating passive filter components into electrical machines.

The rotor design differs from that of the high-speed machine as at low speeds there is minimal rotor stress and so a rotor sleeve is not required. Two simple magnets shapes were considered, as shown in figure 3-27. As the simplicity of the design leads to an applicable machine design at low cost, the chosen option for the magnet shape is as shown in figure 3-27 (b).



**Figure 3-27 Suitable rotor topologies for low-speed machines: a) SPM rotor with offset; b) inset SPM rotor**

However, the “bread loaf” magnet shape of figure 3-27 (a), can be dimensioned to produce a more sinusoidal air-gap field, reducing both EMF harmonics and cogging torque. Although many efforts to design a simple low speed machine and for the purpose of this research, the low-speed machine design is as same as that of the high-speed design by modifying number of turs. The final machine geometry is given in figure 3-28, showing the full load flux density with mesh overlaid.



**Figure 3-28 FEA model with mesh size elements and contour plot at 3000 RPM**

Although the shaft design for the low-speed machine design is simple compared to that of the encased high rotor speed, as here is no need for a rotor cooling system, the shaft design process is not included in this research. The heat generated by magnets for the low-speed rotor is easily removed at the air-gap.

The performance results at rated operating conditions for the 12 slot / 8 pole low-speed PM machine are summarised in table 3-8<sup>5</sup>.

<sup>5</sup> FE simulation results of the low-speed machine design are including in Appendix D.



**Table 3-8 Performed results for 12 slot/8 pole PM machine at 3000 RPM**

<b>Main Machine Specifications:</b>		
Diameter of stator	109	<i>mm</i>
Diameter of rotor	62	<i>mm</i>
Tooth width	10	<i>mm</i>
Core back depth	6	<i>mm</i>
Magnet depth	3	<i>mm</i>
Magnet span angle	38	degree
Sleeve thickness	0.35	<i>mm</i>
Number of turns	75	turns
Winding type	Concentrated / series connection	---
<b>Torque:</b>		
Mean torque	13.3	<i>N.m</i>
Torque ripple	2	% (in per cent)
Cogging torque (peak)	0.0225	<i>N.m</i>
<b>Losses:</b>		
Copper loss	171.24	<i>Watt</i>
Magnet ohmic loss	$\approx 8$	<i>Watt</i>
Iron loss (Hysteresis + Eddy current)	12.15	<i>Watt</i>
<b>Efficiency</b>	95.7	%
<b>Machine inductance and power factor</b>		
$L_d$ , d-axis inductance	17.6	<i>mH</i>
$L_q$ , q-axis inductance	17.9	<i>mH</i>
Power factor	0.898	—

### 3.7 Conclusion

In this chapter, two machines have been proposed: one for high speed operation and one for low speed. Since the two machines have similar dimensions, and the low speed machine is much less challenging in terms of loss and filter integration, more attention is directed to the high speed machine design. The two machines are supplied with low- and high-power drives at power ratings of 4.5 kW and 38 kW respectively.

The prototype high-speed, high-power permanent magnet synchronous motor (PMSM) has been designed to form the foundation of an integrated motor drive. The machine is fed by an active, three-phase two-level inverter, and it has a surface-mounted neodymium-iron-boron permanent magnet rotor. The following conclusions can be made:

- (a) A 0.35 mm carbon fibre sleeve is required to give mechanical integrity to the rotor.
- (b) Single tooth windings minimise overall volume, but introduce spatial harmonics of flux: axial segmentation of the magnets is needed to reduce the resulting rotor eddy current losses to a manageable level.
- (c) A ( $20 \times 30$  AWG) Litz copper wire is needed to give AC losses winding conversion factor,  $K_{AC}$ , up to 90%.
- (d) A 6.5% silicon, 0.1mm lamination material (JNEX-900) will result in relatively low iron loss.
- (e) Axial location of the rotor magnets should be undertaken using non-magnetic steel rings.

The following research in this thesis mainly concerns how the AC filter inductors can be integrated into the proposed low- and high-speed machines without significant increases in size and losses.

## CHAPTER 4

# The Integration of LCL Filter Inductors in Electrical Machines

---

**Summary:** The aim of this chapter is to investigate the effectiveness of integrating input filter inductors into electrical machines, to mimic conventional filter inductors in the same manner as in separate drive systems but with lower volume and losses to give a smaller envelope compared to that of conventional systems. In particular, the approach reported in this chapter relates to two drives where the underlying machine in each is identically dimensioned, but they operate at two different rated speeds. A drive with 38 kW input power at 25,000 RPM is identified as the baseline, with a 4.6 kW drive operating at 3,000 RPM for comparison.

### 4.1 Introduction

The first generations of ASDs produced during the latter part of the 20th century traditionally treated the various subsystems of the drive (electric machine, power electronics, passive converters etc.) as mechanically isolated entities. As ASD technology has matured, the trend has been towards greater mechanical and operational integration of the various subsystems. Integrated motor drives promise higher power density, and lower production and commissioning costs through single package installations [2]. With specific reference to the topic of this work, there are previous examples in literature where considerable effort has been developed to integrating and reducing the size of passive components in integrated drives [20, 29, 98, 99].

In particular, the results from the preliminary calculation of LCL filter parameters described in Chapter 2 are used in different integration techniques in this chapter. Figure 4-1 illustrates the first of the LCL filter elements to be considered for integration into the two proposed low- and high-speed machines which are the larger inductors ( $L_2$ ) located on the drive side. The larger inductors are considered first as they have the greatest impact on the volume of the integrated system.

Since the filter inductors will share the machine's magnetic circuit, a brief summary of the specifications of the designed low- and high-speed machines at 3000 RPM and 25000 RPM respectively (for more details, see Chapter 3) is provided in table 4-1 along with the parameters of the LCL filter inductors.

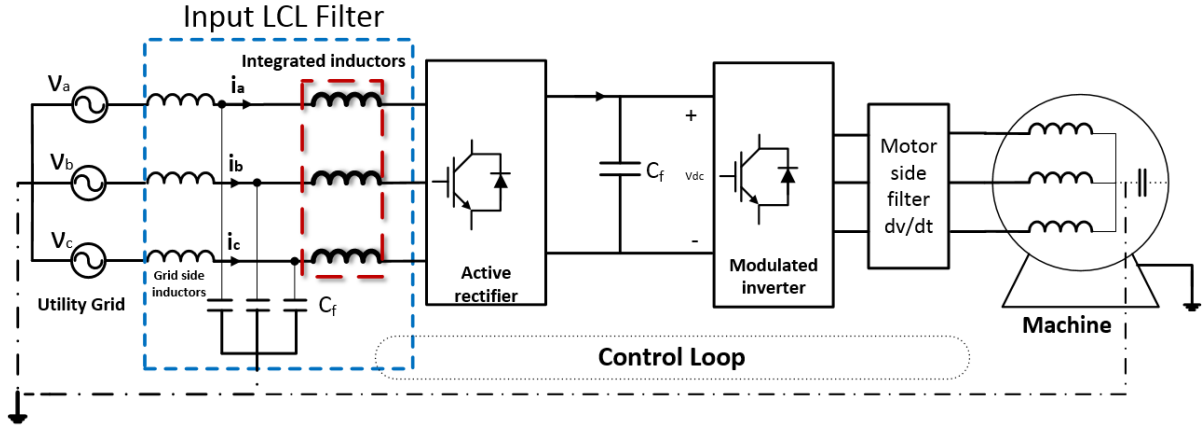


Figure 4-1 Electrical drive configuration with the highlighted 3-phase inductor in the drive side

Table 4-1 A summary of proposed machine specifications

Parameter	Variable	Value (4.56kW drive)	Value (38kW drive)	Unit
Shaft speed	$N_{shaft}$	3000	25000	RPM
Pole number	$n_p$	8	8	poles
Machine torque	T	13	13	Nm
Tooth number	$n_t$	12	12	teeth
Rotor diameter	$d_r$	62	62	mm
Machine lamination diameter	$OD_m$	109	109	mm
Winding type	---	Concentrated	Concentrated	---
<b>Parameters of LCL filter inductors</b>				
Drive side inductance	$L_2$	1310	160	$\mu H$
Grid side inductance	$L_1$	37.56	5	$\mu H$
Grid-input current	$i_g$	6.34	53	A <sub>rms</sub>
Active rectifier switching frequency	$f_{sw}$	40	40	kHz

The energy stored in the filter inductor to be integrated scales with the power rating of the drive. Therefore, a higher power rating will result in a drive with a larger input filter inductor. The demand for storage energy for the high power inductor is scaled by a factor of 8.33 compared to that of a low power inductor based on the variance in the input power of drives:

$$\text{Energy stored} = \frac{1}{2} L \hat{I}^2 \quad (4-1)$$

where  $L$  is a phase filter inductance and  $\hat{I}$  is the peak fundamental current in  $L$ .

Although the underlying machine size remains the same in the two drive specifications, the integration of filter inductors for the high power drive is more challenging as the physical size of the filter inductors might even be larger than the original machine size.

## 4.2 Study of balanced and unbalanced magnetic pull for integrated machines

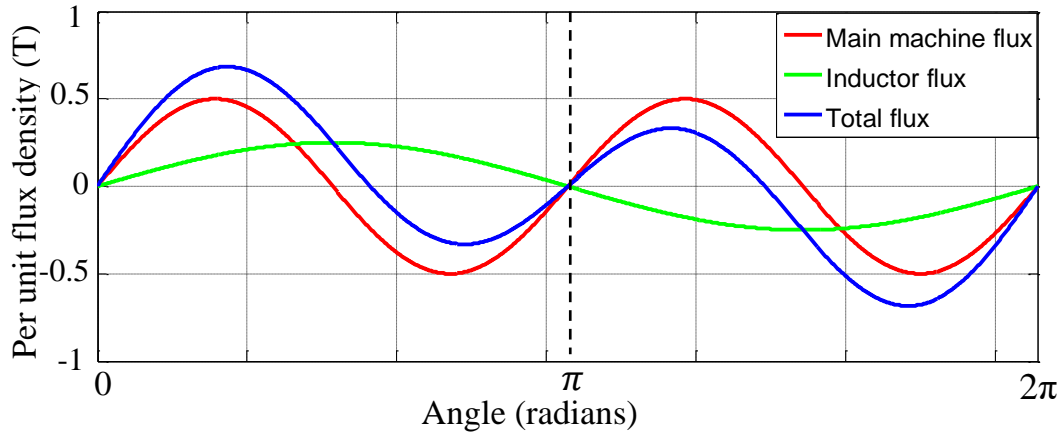
The first two integration methods presented in this chapter (see figures 4-6 and 4-8) make use of the machine air gap in the magnetic circuit for the inductors. In these cases, the pole number combinations must be considered as they can produce unbalanced rotor forces (identical pole numbers cannot be used as the machine and filter fields would couple directly). The governing equation 4-2 for balanced magnetic flux density in the machine's air gap is defined as follow:

$$\int_0^{2\pi} B^2 d\theta = 0 \quad (4-2)$$

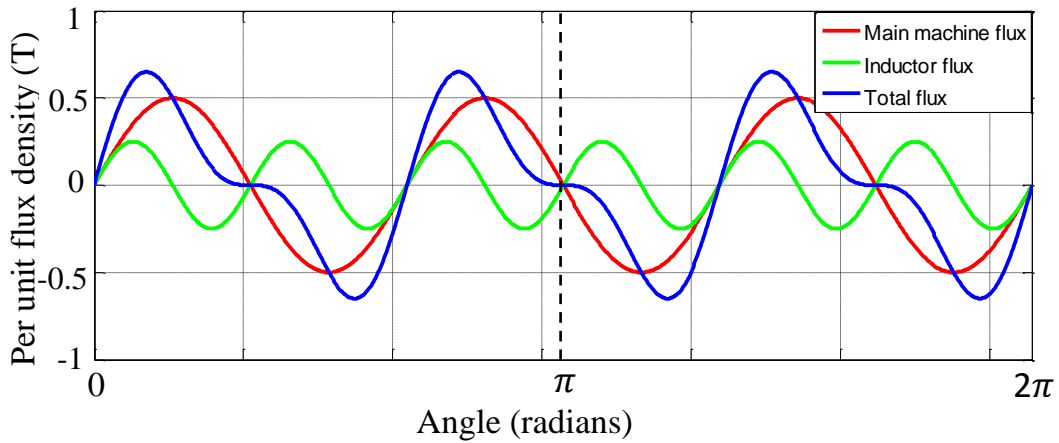
The following sections present an investigation into balanced and unbalanced rotor force cases resulting in a general case statement for achieving balanced magnetic forces where multiple three-phase airgap fields exist. The arbitrary flux value was used as a reference to normalised results for the following balanced and unbalanced cases is 2T.

### 4.2.1 Unbalanced magnetic pull (UMP)

As shown in figure 4-2, different combinations of possible pole numbers for the main machine and inductor windings give unbalanced total air gap flux density (blue wave) for both cases.



(a) 2-pole inductor windings / 4-pole main machine windings



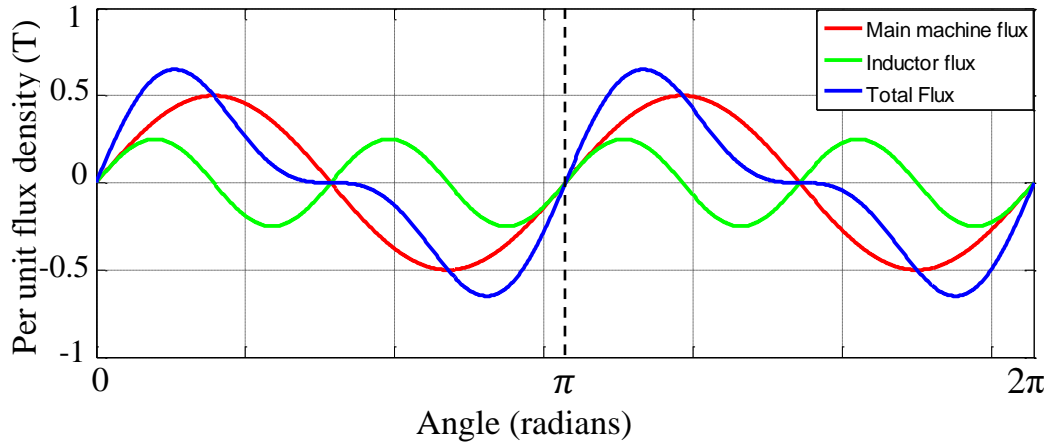
(b) 12-pole inductor windings / 6-pole main machine windings

**Figure 4-2 Unbalanced total flux density for different machine and filter inductor pole numbers**

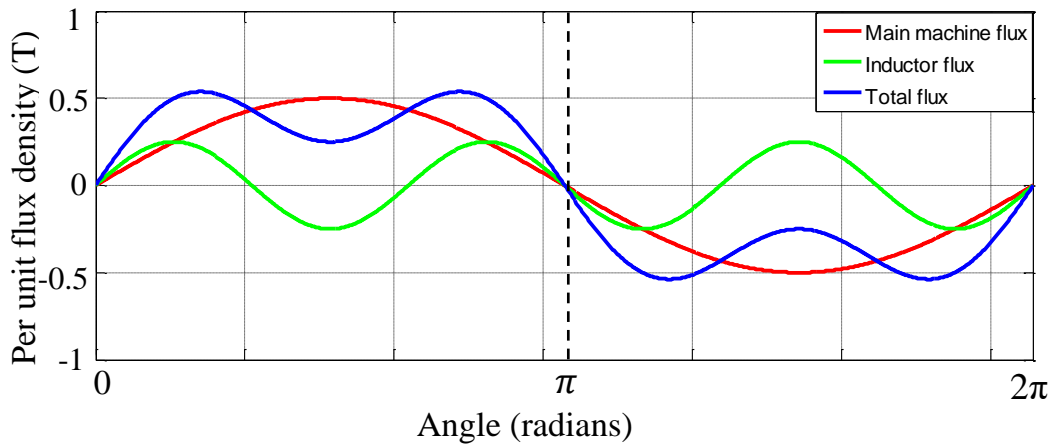
Figure 4-2 shows that, for these examples of pole combinations, the total flux density is unbalanced, where the value of the total flux density is different after 180 radians. The governing equation for balanced magnetic flux density is not satisfied in these two different examples.

#### 4.2.2 Balanced magnetic pull (BMP)

In figure 4-3, two further examples of different pole combinations for the main machine and inductor windings give balanced air gap flux density in each case.



(a) 8-pole inductor windings / 4-pole main machine windings



(b) 6-pole inductor windings / 2-pole main machine windings

**Figure 4-3 Balanced total flux density for different machine and filter inductor pole numbers**

In order to achieve a balance total flux density in the air gap, the machine and inductor pole numbers must be separated by a multiple of two pole pairs, and hence the pole number for the inductor windings  $n_{ind.}$  and the original machine windings  $n_{mach.}$  are governed by the general equation 4-3 where  $x$  is an integer:

$$n_{ind.} - n_{mach.} = 4x \quad (4-3)$$

Table 4-2 shows different cases of pole combinations for the inductor and armature winding configurations and hence some cases of balanced and unbalanced magnetic pull (BMP and UMP) act on a machine rotor are determined.

**Table 4-2 Different BMP and UMP cases for different pole numbers of the filter inductor and main machine windings**

Pole number of inductor windings	Pole number of armature windings					
	2	4	6	8	10	---
2	X	X	✓	X	✓	---
4	X	X	X	✓	X	---
6	✓	X	X	X	✓	---
8	X	X	X	X	X	---
10	✓	X	✓	X	X	---
---	---	---	---	---	---	X

### 4.3 Constraints of preliminary integrated design and fundamental equations

Since, for the first two proposed integration methods, the filter inductor windings are integrated into the machine stator and share the machine stator core back or stator teeth, the original dimensions of the base machine stator must be amended to avoid saturation in the stator and to maintain the main machine performance while the inductor air gap is fixed by the machine design.

#### 1. Calculation of stator core back depth

Due to the extra flux produced by incorporating inductor windings  $\Phi_{\text{inductor}}$  in the machine stator core along with the main magnetic flux of the armature windings  $\Phi_{\text{armature}}$ , the total magnetic flux per phase in the stator core can be calculated as follows.

- a) The magnetic flux of the filter inductor per phase can be calculated as stated in equation 4-5 [56, 88]:

$$\hat{\Phi}_{\text{inductor}} = \frac{L \hat{I}}{N_{\text{inductor}}} \quad (4-5)$$

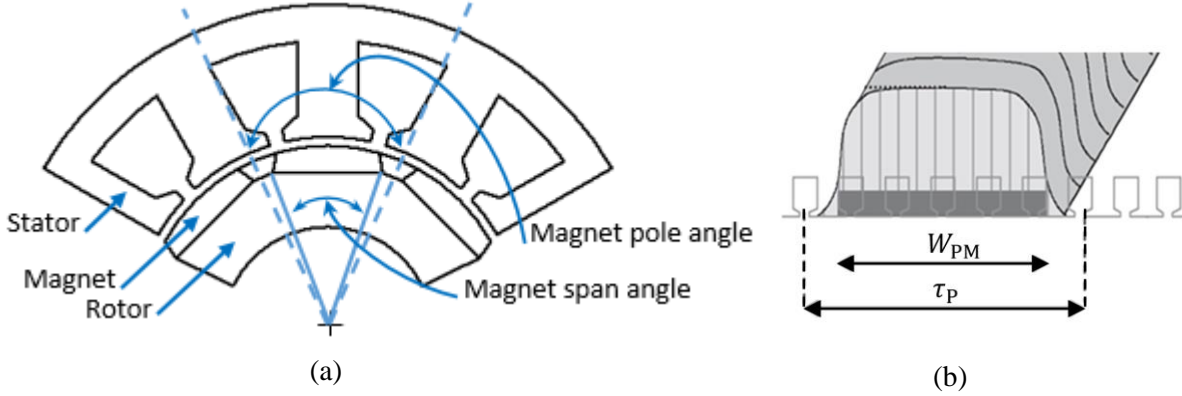
where  $\hat{I}$  is the peak value of the filter inductor current and  $N_{\text{inductor}}$  is the number of turns per phase inductor.

- b) The main machine flux can be calculated based on the following parameters:

- **Stator pole pitch ( $\tau_p$ ):** the circumferential length of the stator bore is divided equally among the number of machine poles, where the actual length along the stator bore



between two borders for one pole represents the stator pole pitch as shown in figure 4-4 (b).



**Figure 4-4 Stator pole pitch and the effective magnet width**

The stator pole pitch can be calculated as given in equation 4-6:

$$\tau_P = \frac{\pi D_s}{2 \text{ Pole pairs}} \quad (4-6)$$

where  $D_s$  is the diameter of the stator bore.

- **The relative magnet width ( $\alpha_{PM}$ ):** As shown in figure 4-4 (a), this is the percentage of effective magnet span angle compared to the magnet pole angle as given in equation 4-7:

$$\alpha_{PM} = \frac{\text{Magnet span angle}}{\text{Magnet pole angle}} \quad (4-7)$$

Therefore, the magnetic flux produced by the main machine windings can be calculated as given in equation 4-8:

$$\Phi_{armature} = \alpha_{PM} \tau_P B_{gmax} SL \quad (4-8)$$

where  $B_{gmax}$  is the maximum air gap flux density of the base machine,  $SL$  is the machine stack length and the effective magnet width ( $W_C$ ) is equal to ( $\alpha_{PM} \tau_P$ ).

As a result, the total magnetic flux which travels in the machine stator core is given by 4-9:

$$\hat{\Phi}_{Total/phase} = \hat{\Phi}_{armature} + \hat{\Phi}_{inductor} \quad (4-9)$$

The new depth of the core back is therefore given by equation 4-12, where the total flux passing the machine tooth divides into two in the core back as shown in equations 4-10 and 4-11 (more details can be found elsewhere [88]):

$$\frac{1}{2} \times \Phi_{Total/phase} = B_{Tooth} A_{core\ back} \quad (4-10)$$

$$\frac{1}{2} \times \Phi_{Total/phase} = B_{Tooth} d_{cb} SL \quad (4-11)$$

$$Stator\ core\ back\ depth = \frac{\Phi_{Total/phase}}{2 \times K_{fe} \times SL \times B_{Tooth}} \quad (4-12)$$

where:  $d_{cb}$  is the stator core back depth,  $K_{fe}$  is the space factor of the stator core,  $B_{Tooth}$  is the flux density in the stator tooth, and  $A_{core\ back}$  is the stator core back area.

## 2. Calculation of stator tooth width

- **New air gap flux density:** since the total magnetic flux has been calculated, the new peak value of the flux density in the machine air gap can be determined by rewriting equation 4-8;

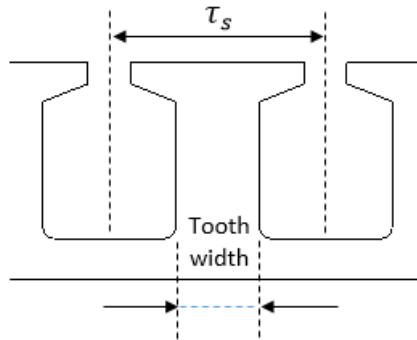
$$B_{gmax} = \frac{\Phi_{Total/phase}}{\alpha_{PM} \tau_p SL} \quad (4-13)$$

- **The stator slot pitch ( $\tau_s$ ):** Figure 4-5 illustrates the length of the stator slot pitch and the stator tooth width. The stator slot pitch can be defined as given in equation 4-14 [88]:

$$\tau_s = \frac{\pi D_s}{Q} \quad (4-15)$$

$$Q = 2 \times Pole\ pairs \times m_{(no.\ of\ phases)} \times q_{(no.\ of\ slots\ per\ pole\ per\ phase)} \quad (4-16)$$

where  $Q$  is the number of stator slots.



**Figure 4-5 Stator slot pitch definition and tooth width**

Due to the contribution of inductor flux within the main machine stator, the stator tooth width must be increased to avoid saturation in the tooth. The new width of the stator tooth can then be calculated from equation 4-17 [56, 88]:

$$Tooth\ width = \frac{B_{gmax} \tau_s}{B_{Tooth}} \quad (4-17)$$

The copper slot area should accommodate both the windings of the main machine and the filter inductors. Assuming identical fill factors for the different coils this results in a greater required slot area. The outer diameter of the machine stator must be increased to accommodate the larger slots.

In conclusion, where the machine air gap forms part of the inductor winding magnetic circuit two design considerations are paramount:

- The possible pole number combinations are limited to remove cross-coupling and unbalanced rotor forces
- The original machine stator must be resized to accommodate additional magnetic flux due to the addition of the integrated inductors.

#### 4.4 Integration of 3-phase filter inductors $L_2$ into the HSHP machine at 25000 RPM

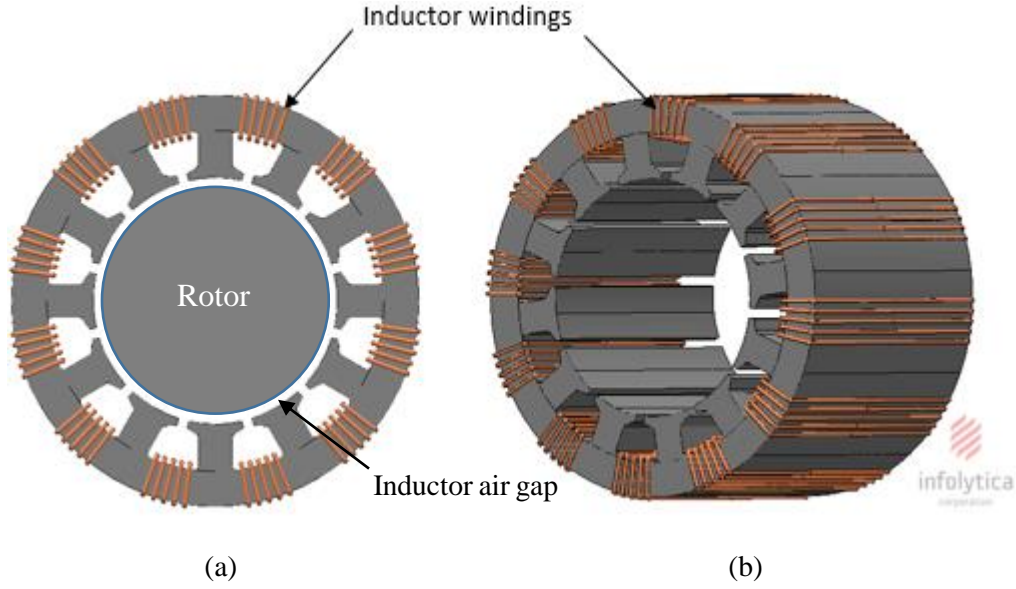
In order to combine filter inductors and an electrical machine in a single packaged unit, the structural integration design should be simple to comply all other constraints such as simplicity of manufacturing and assembly processes, evenly distributed thermal paths, sufficient for offering high power density. For example, symmetrical integrated design is suitable for the simple design of housing and cooling system.

Five methods of integrating the larger 3-phase LCL filter inductors ( $L_2$ ) into the proposed HSHP machine have been investigated in a drive specified at 38 kW/25000 RPM. The specification for this machine is described in table 4-1. As the drive side inductor is dominant this has been considered first. In all cases, the electrical performance of the integrated filter inductors has been designed to match conventional separate filter inductors with traditional E-core structures.

##### 4.4.1 Method 1: filter inductor windings $L_2$ around the stator core back

This concept is illustrated in figure 4-6 and is driven by a desire to maintain the basic structure of the machine's magnetic circuit by utilising the same slots as the machine windings. The inductor windings are wound around the stator core-back of the machine where the magnetic flux path includes the machine air gap and rotor. The ring flux produced by the inductor windings travels around the machine stator core back and in the same physical volume as the

machine flux and as described above creates the necessity for not-insubstantial additional sizing of the teeth and core-back. In this method, only dimensions can be amended are tooth width and core back depth while the inductor air gap is fixed by the machine's air gap design, more details are in section 4.3.



**Figure 4-6 General schematic of the AC inductors integrated into a motor: a) 2D FEA model; b) 3D representation**

Equations 4-18 to 4-21 have been used to calculate the number of turns required in the inductor in order to achieve the desired value of filter inductance per phase. Thereby, the 2D FE model shown in figure 4-6 (a) was simulated with one turn in each phase inductor ( $N = 1 \text{ turn}$ ) carrying the full MMF. In equation 4-21 the flux linkage and input current per phase obtained represent the magnetic flux ( $\phi$ ) and the magneto-motive force (MMF) respectively.

$$\hat{\psi} = L \hat{I} = N \phi \quad (4-18)$$

$$MMF = N \hat{I} \quad (4-19)$$

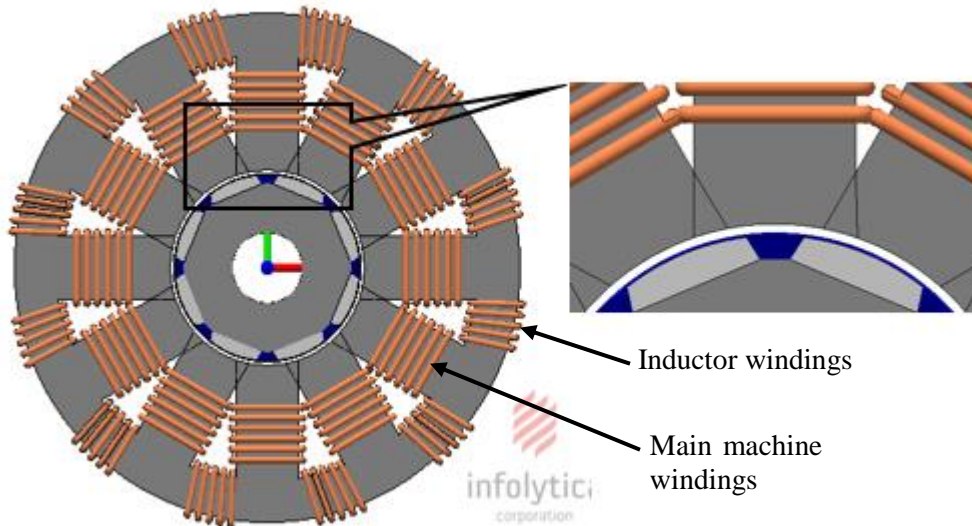
$$L = \frac{N^2 \phi}{MMF}, \quad \text{where } (MMF = \hat{I} \text{ \& } \phi = \psi) \text{ at } N = 1 \text{ turn} \quad (4-20)$$

$$N = \sqrt{\frac{L I}{\phi}} \quad (4-21)$$

Due to the inductor and main machine windings sharing the same stator slot, the final slot area can be calculated as given in equation 4-21 [56]:

$$\text{Slot area} = \frac{(N_{\text{armature/slot}} + N_{\text{aux./slot}}) I_{\text{rms}}}{J \times \text{fill factor}} \quad (4-22)$$

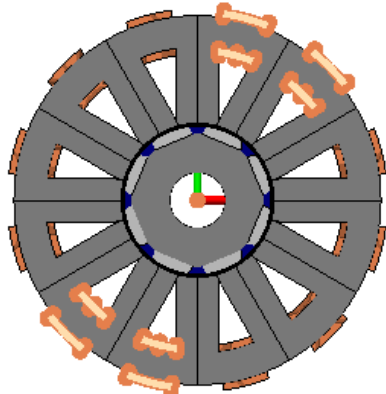
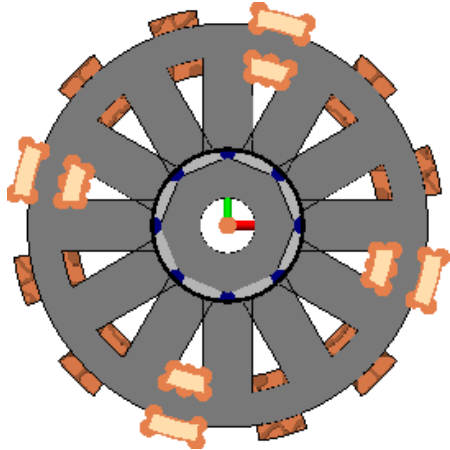
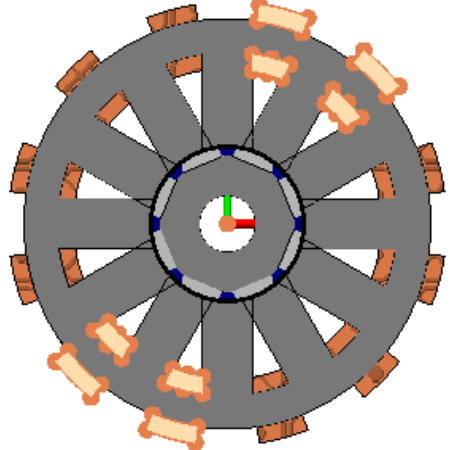
Figure 4-7 illustrates the final geometry for a ten-pole inductor winding field (the machine has an 8-pole field) after the core back and tooth resizing exercise is complete. The geometry clearly shows that the additional tooth-width and core back required renders this method unusable.



**Figure 4-7 Illustration of the effect of integrating AC inductor into the HSHP machine**

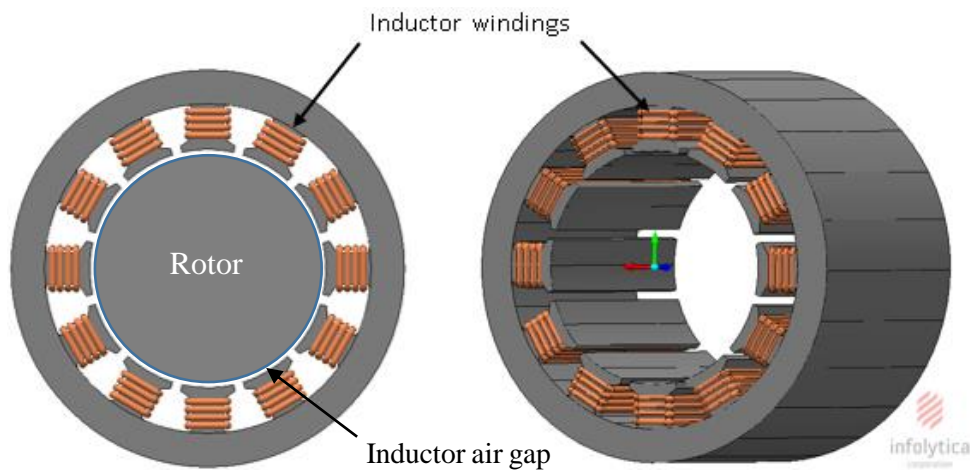
Additionally, Table 4-3 indicates that inductor windings with 2 and 8-pole fields (which have been investigated to examine the effectiveness of this approach regardless of rotor force considerations) are equally impractical for this drive specification however, this method may be worth exploring for larger machines at lower shaft speeds as this would result in a lower ratio between the required filter and machine magnetics sizes.

**Table 4-3 Illustration of the integration of 3-phase filter inductors around the stator core back in a 38 kW drive**

Pole number ( $L_2$ )	Amended stator geometry due to integration		Parameters	Increase OD (original motor OD = 109 mm)
2 poles		N/A	OD: 156 mm	+ 43.12 %
			N: 4turn	
			$L$ : 0.16 mH	
			$V_L$ : 4.7 V	
8 poles		N/A	OD: 177 mm	+ 62.38 %
			N: 9 turn	
			$L$ : 0.16 mH	
			$V_L$ : 4.7 V	
10 poles		N/A	OD: 179 mm	+ 64.22 %
			N: 8 turns	
			$L$ : 0.16 mH	
			$V_L$ : 4.7 V	
Symbol: OD: outer diameter of the PM motor; N: number of turns per phase; $V_L$ : voltage per phase across the filter inductor ( $L_2$ ); N/A: not applicable				
Note: The highlighted slots form a single phase in each case.				

#### 4.4.2 Method 2: inductor windings around stator teeth

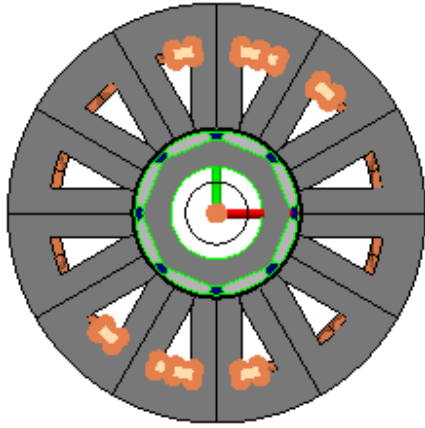
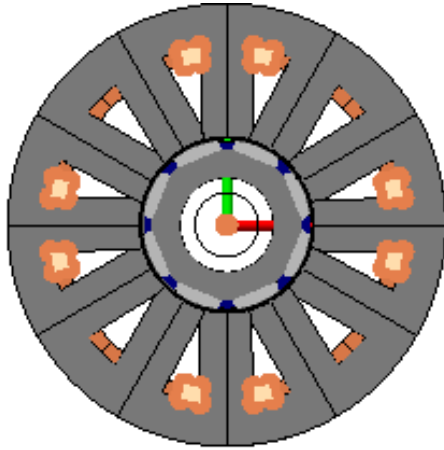
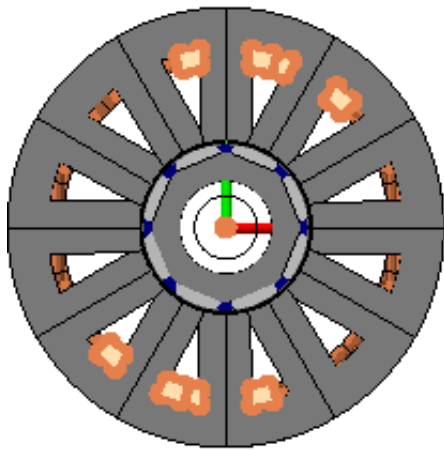
In this case, the inductor windings are wound around the teeth of the machine stator in the same way as the main torque producing windings, the concept is shown in figure 4-8. The same pole combinations have been considered as in the previous approach. The method used to calculate the increased dimensions of the integrated machine stator is the same as that applied for the first integration method as in this approach, the additional magnetic flux which is produced by the incorporated 3-phase filter inductor windings  $L_2$  also shares the machine air gap.



**Figure 4-8 Layout of auxiliary windings into the PM motor**

Table 4-4 illustrates three 2D FE models representing three different pole combinations of inductor windings which share the machine stator teeth. As for the previous integration method this approach proves unsuitable for a drive of this specification (although again, it may be worth considering for a lower speed larger machine).

**Table 4-4 Illustration of the integration of 3-phase filter inductors around the stator teeth in a 38 kW drive.**

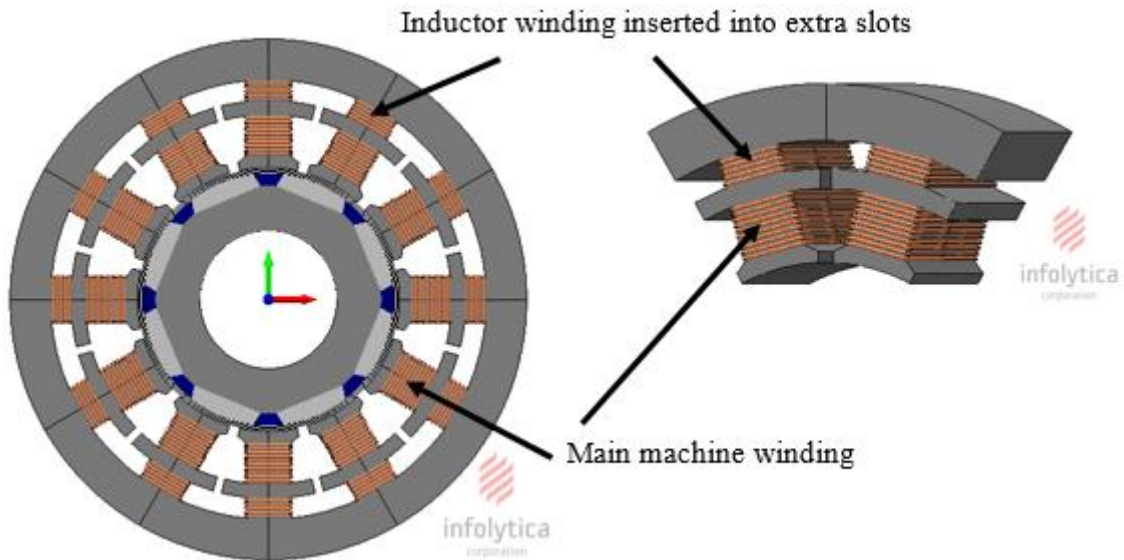
Pole number ( $L_2$ )	Amended stator geometry due to integration		Parameters	Increase OD (original motor OD = 109 mm)
2 poles		N/A	OD:153.44 mm	+ 40.77 %
			N: 3 turn	
			L: 0.16 mH	
			$V_L$ : 3.72V	
8 poles		N/A	OD: 163.28 mm	+ 49.8 %
			N: 6 turn	
			L: 0.16 mH	
			$V_L$ : 3.72V	
10 poles		N/A	OD: 165 mm	+ 51.37 %
			$N$ : 5 turn	
			L: 0.16 mH	
			$V_L$ = 3.72 V	
<b>Symbol:</b> OD: Outer Diameter of the PM motor; N: number of turns per phase; $V_L$ : voltage per phase across the filter inductors $L_2$ ; N/A: not applicable				
<b>Note:</b> The highlighted slots form a single phase in each case.				



#### 4.4.3 Method 3: additional interior slots forming 3-phase inductors $L_2$

In the first two methods, the air gap between rotor and stator formed part of the magnetic circuit for the integrated inductors. As the effective magnetic air gap is relatively large and is restricted by the machine design, this severely limits the design choices available for the optimisation of integration methods and results in a far higher number of turns than is the case for the separate inductor. This leads to a significant volume increase compared to the separate inductor case.

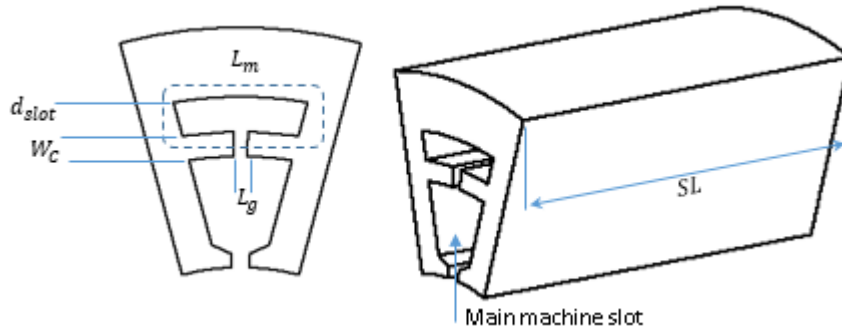
In this proposed integration method, additional interior slots within the machine stator geometry form the 3-phase filter inductors as shown in figure 4-9. These extra slots are located radially outwards from the main machine slots. The primary goal of forming these extra slots is to remove the machine air gap from the main inductor magnetic circuit path and to utilise separate slots with geometries not dictated by the requirements of the machine. This method gives greater control over the inductor magnetic circuit reluctance, as the inductor air gaps can be modified without affecting the performance of the base machine and therefore the amount of inductor copper and hence ultimately the increase in volume is more controllable. In this approach, the chosen pole numbers for the filter inductors  $L_2$  and the main machine windings are 10 and 8 poles respectively.



**Figure 4-9 Geometry of the extra slot forming the 3-phase filter inductors**

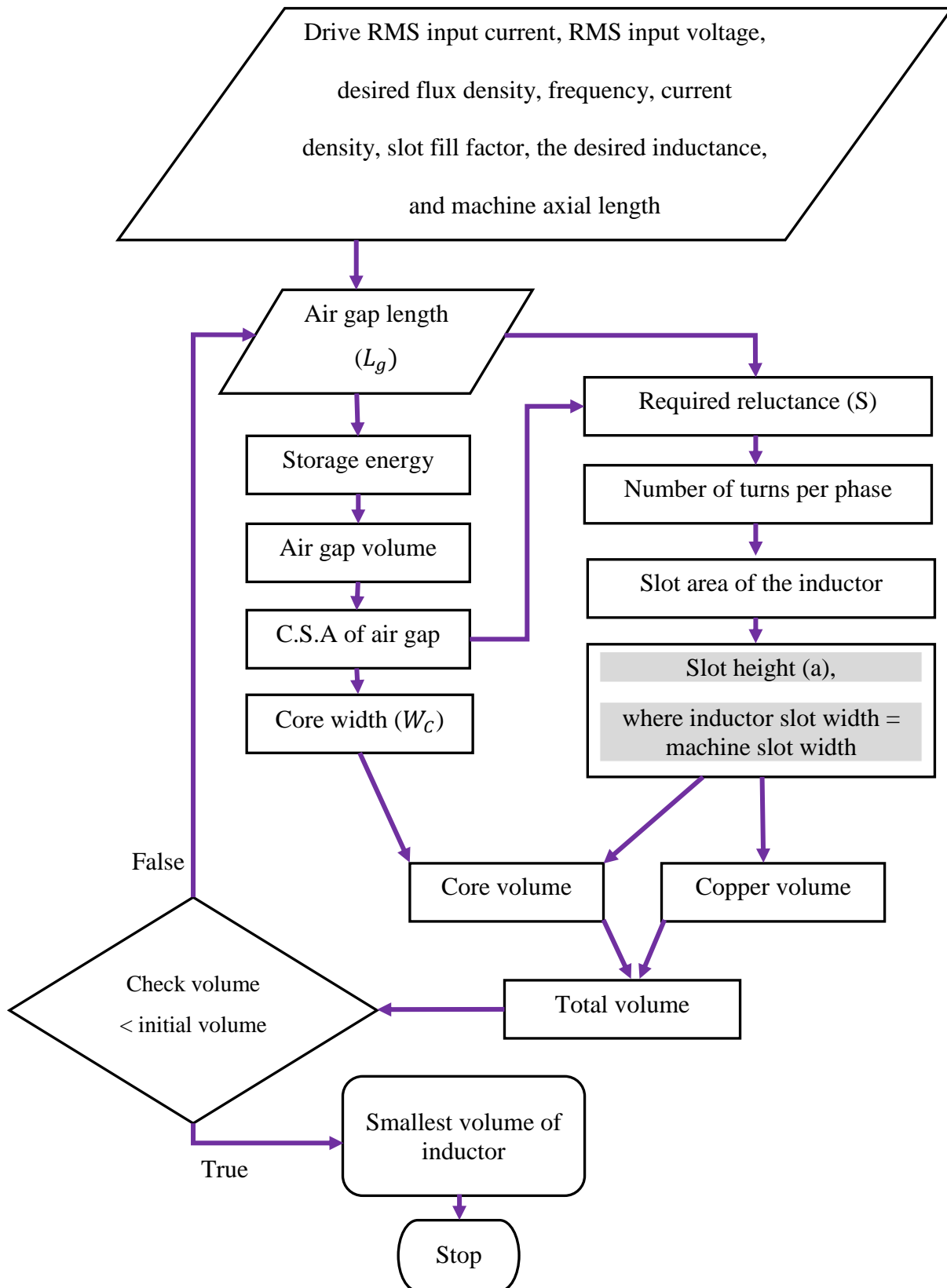
Some geometries of this method remain restricted by the machine design; the stack length of the original machine is fixed and is part of the inductor's dimensions. However, the air gap volume is fully adjustable as the radial length and circumferential gap remain free from restriction.

The machine stator has twelve main slots and the extra inductor slots have been designed similarly to lie radially outward of the main machine slots to aid manufacturability. Similarly, as the main machine is wound with concentrated windings the same principle is used for the inductor windings. The design can be broken down into single slot analysis as shown in figure 4-10. The design dimensions are  $SL$ , the machine stack length;  $W_c$  the inductor core width;  $L_m$  the magnetic path length;  $d_{slot}$  the inductor slot depth; and  $L_g$  the air gap length.



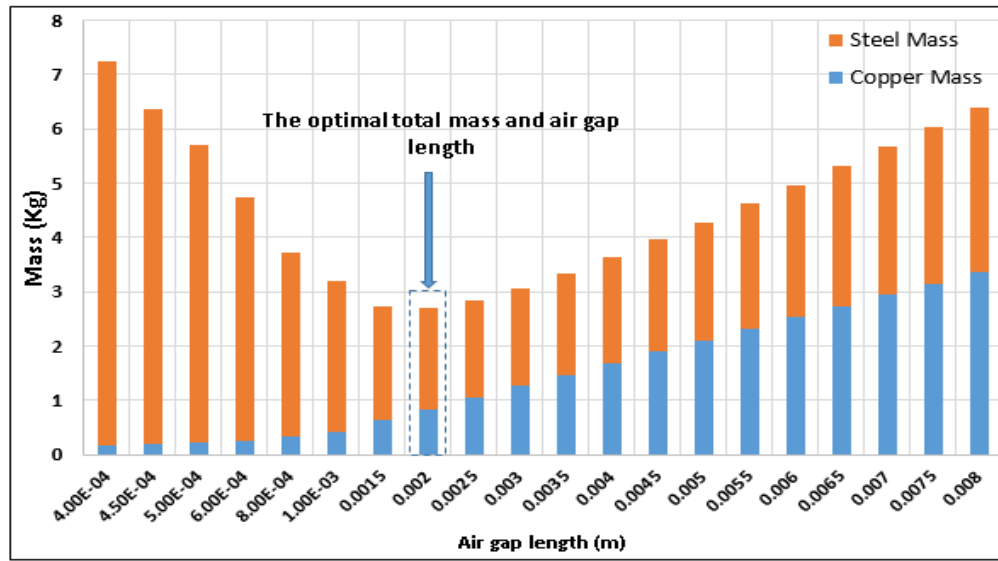
**Figure 4-10 A single tooth of interior extra slots demonstrating a part of the phase inductor geometry**

In this approach, the upper portion of the tooth and core-back are shared by the main machine and inductor magnetic circuits. Figure 4-11 shows a simple iterative process varying the air-gap length in an attempt to arrive at an optimal design. It should be noted that the width of the extra slot is assumed to be equal to that of the main machine slot, as shown in the text box highlighted in figure 4-11. The values of current density and the slot fill factor are 12 A/mm<sup>2</sup> and 50% respectively, which are similar to those of the conventional discrete 3-phase inductor design described in Chapter 2. Since the filter inductors are integrated into the machine, working at such high current densities is accepted since the base machine and filter inductors can be cooled down by a common unique cooling system.



**Figure 4-11** Flow chart of optimisation process for the integration of 3-phase filter inductors into the machine stator as extra slots

As a result, the optimal air gap length of the integrated filter inductors is 2 mm, as shown in figure 4-12, which gives the lowest mass of copper and steel.



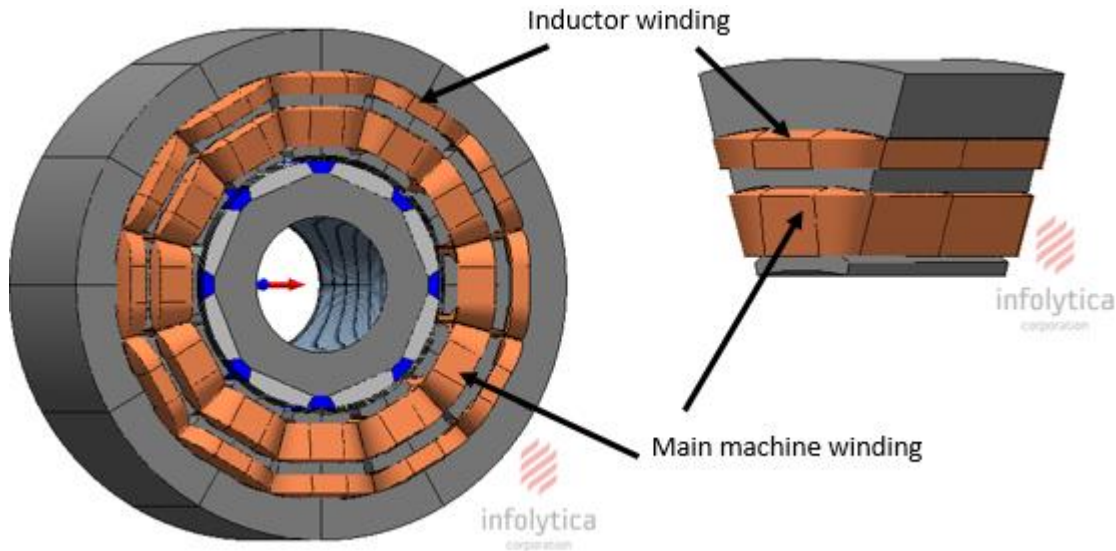
**Figure 4-12** The required masses of copper and steel at different air gap lengths in a power drive of 38 kW

The dimensions obtained for inductor slot geometry are specified in table 4-5.

**Table 4-5** Specifications of a single inductor slot within IDS stator

Parameters	Value	Unit
Air gap length ( $L_g$ )	2	mm
Core width ( $W_C$ )	3.6	mm
Slot depth ( $d_{slot}$ )	5	mm
Slot fill factor ( $ff$ )	50	%
Number of turns ( $N$ )	5	turns
Current density ( $J$ )	12	A/mm <sup>2</sup>

Figure 4-13 presents the structure of an integrated interior slot machine and shows where the machine and inductor coils are positioned in the machine stator.



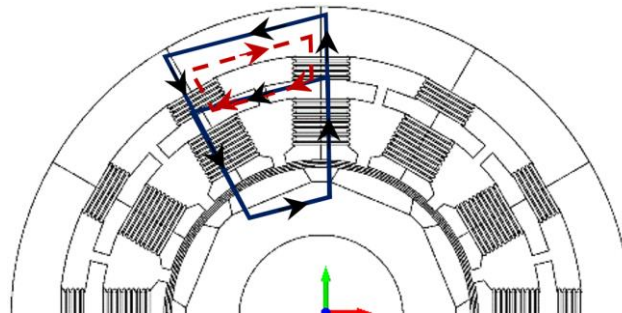
**Figure 4-13 3-phase filter inductors sharing the HSHP machine stator**

The outer diameter of the base machine is increased by approximately 23%, (increasing the volume by 51%) while the volume of the integrated 3-phase inductors,  $L_2$ , is reduced by approximately 35% compared to that of the discrete 3-phase filter inductor described in Chapter 2, section 2.7.2 resulting in a net decrease in volume of 24.3% along with working at the same current densities of  $12 \text{ A/mm}^2$ .

#### 4.4.3.1 FE Simulation results for interior extra slot technique

Figure 4-14 illustrates the shared parts of the stator which could be heavily saturated and hence adversely affect machine performance.

Figure 4-15 shows the flux density plot for the FE model of the integrated machine, including the filter inductors windings, carrying a rated current of  $53 \text{ A}_{rms}$  and the original HSHP machine is at full load ( $47.35 \text{ A}_{rms} / 25000 \text{ RPM}$ ). The saturated regions in the integrated stator (see figure 4-15) show the shared magnetic paths of the main machine and filter inductors.



**Figure 4-14 Magnetic coupling behaviour between the filter inductors and the HSHP machine**

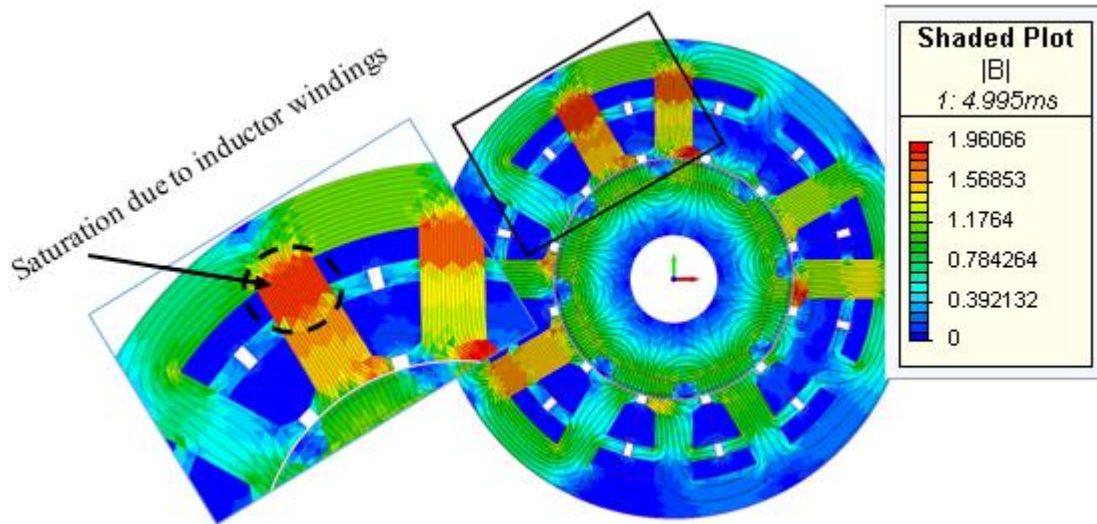


Figure 4-15 Contour plot of integration technique using interior extra slots

It is clear that this method poses significant potential saturation problems in the areas of the teeth and core back which are shared by both magnetic circuits.

#### 4.4.3.2 Magnetic cross-coupling between the fields of the filter inductors and the HSHP machine

Further investigation of cross-coupling has been carried out for the integrated high-speed machine considering different operating conditions as shown in figures 4-16 to 4-19 by simulating passing a rated current in one of the windings and inspecting the voltage induced on the other;

**Case 1:** the base machine's magnetic circuit, including magnets and armature windings are active while a zero current in the filter inductor windings.

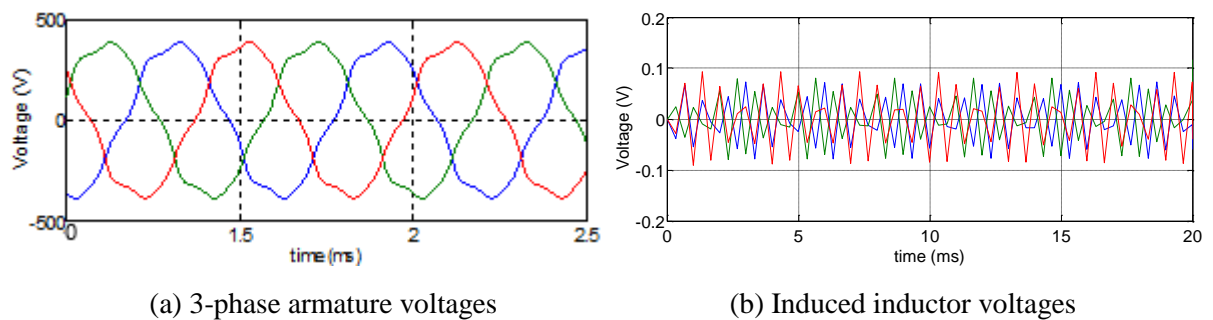
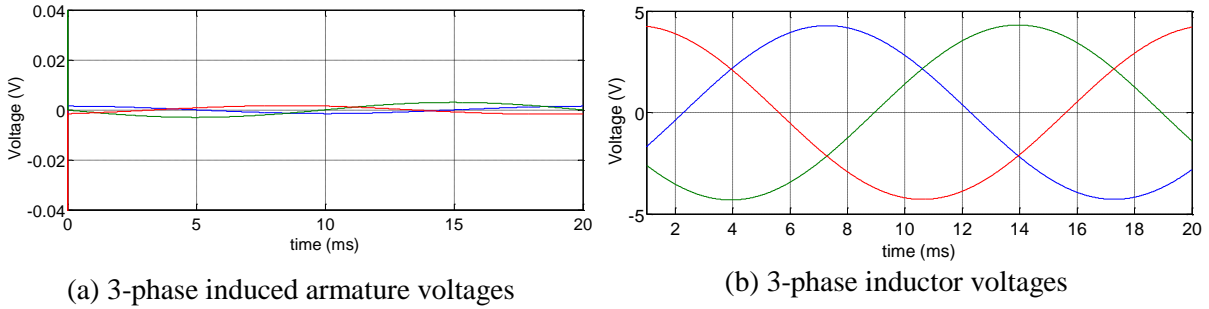


Figure 4-16 Voltage induced in inductor windings due to rotor magnets and armature fields

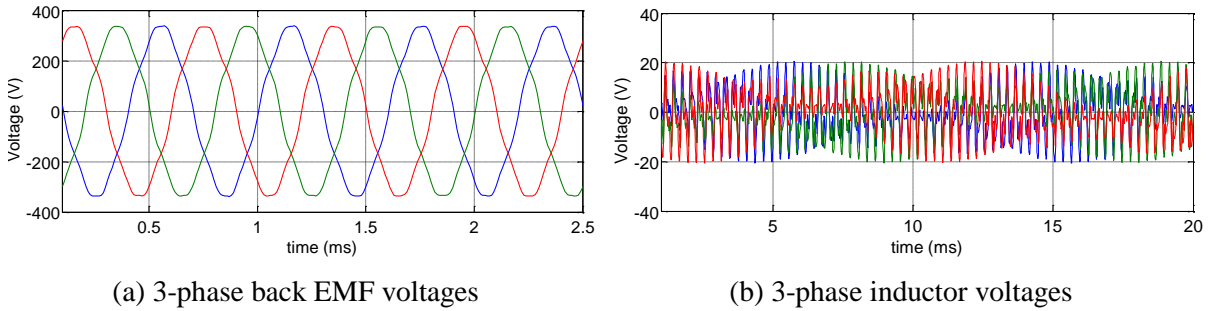


**Case 2:** the rotor magnets of the base machine is turned off with a zero current in the armature winding while the filter inductor windings are energised.



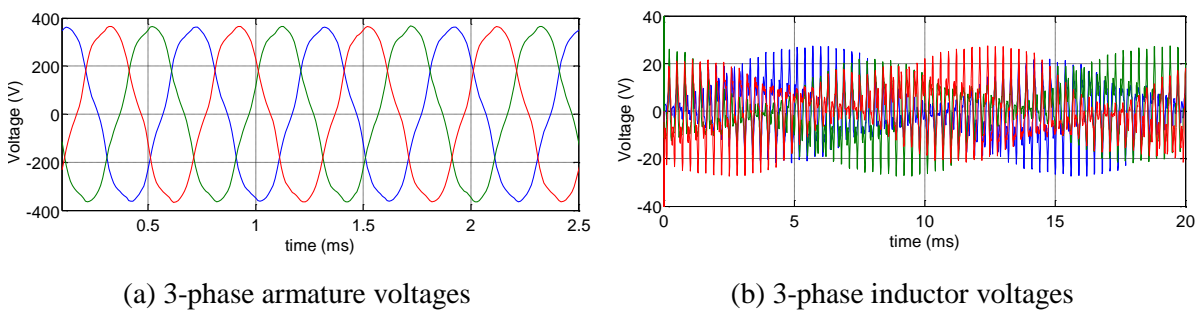
**Figure 4-17 Voltage induced in armature windings solely due to the inductor magnetic field**

**Case 3:** the rotor magnets of the base machine is active with a zero current in the armature windings while the filter inductor windings are energised.



**Figure 4-18 Magnetic flux cross-coupling between rotor magnets and filter inductor windings**

**Case 4:** the magnetic circuits of the base machine and filter inductors are active.

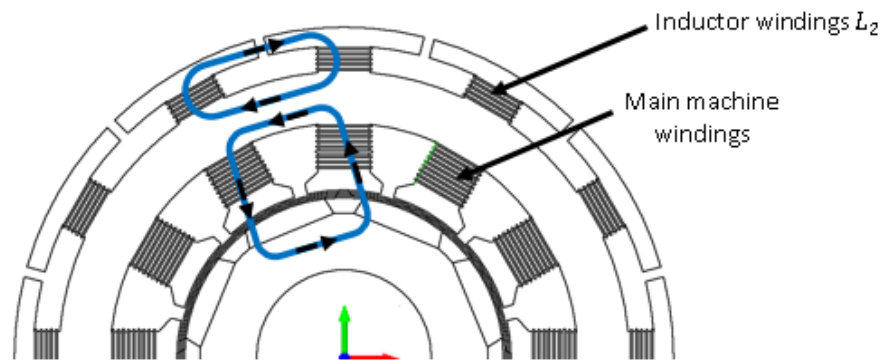


**Figure 4-19 Magnetic flux cross-coupling at full operation condition**

Figure 4-16 indicates that the induced voltage in the filter coils due to the presence of the rotor magnets is approximately 0.1 V, showing there is minimal coupling with the PM field when there is no inductor excitation. Equally, Figure 4-17 demonstrates that current in the inductor winding does not induce a voltage in the main machine winding, however, as shown in Figures 4-18 and 4-19 there is a significant interaction between the PM and inductor fields when both are energised.

#### 4.4.4 Method 4: additional outer slots (double slot machine)

The investigation of the first three proposed methods results in the conclusion for these drive specification methods which share the machine air gap and have significant potential coupling should be avoided. Whilst method three removed the machine airgap it retained the potential for inter-field interference. This integration method introduces a superior solution which attempts to decouple the machine and filter inductor windings. In this case, the extra slots have been redistributed to the outer surface of the stator effectively removing the shared tooth segment and utilising a shared inner core back as shown in figure 4-20.



**Figure 4-20 Geometry of a half model of a double slot machine with the incorporation of 3-phase AC inductors into the HSHP machine at 25000 RPM**

As this method can be thought of as moving the main core back inboard it is clear that the dimensions of this proposed method will be largely similar to the previous method (it actually gives a wider inductor slot which slightly reduces the outer diameter). The reduced shared steel also reduces coupling capability.

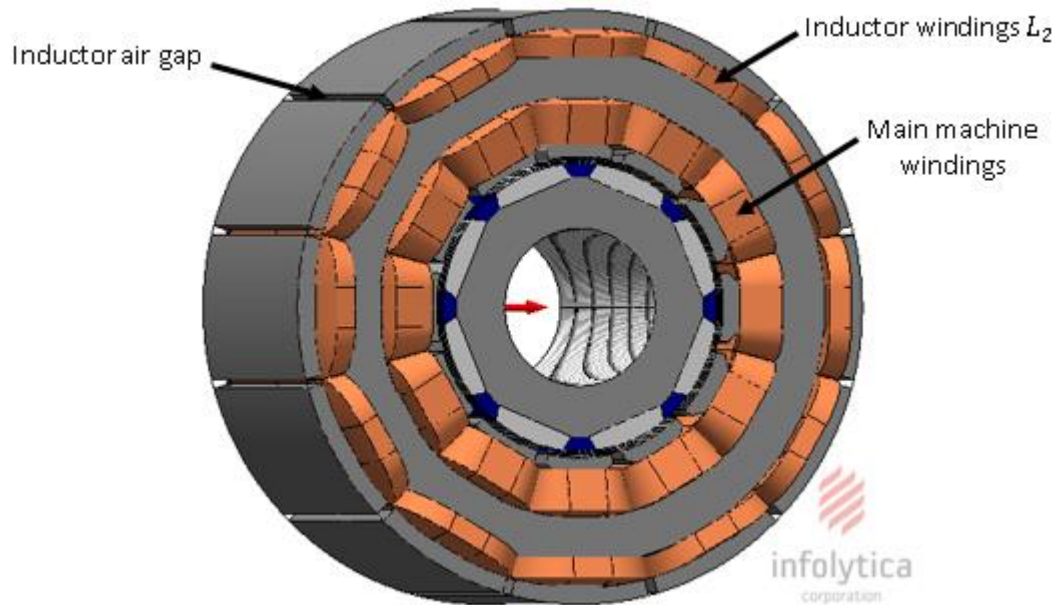
The winding layout for the two different pole combinations of the main machine and filter inductor windings with 8 and 10 poles respectively is illustrated in figure 4-21.



**Figure 4-21 Winding layout of the IDS machine**

A 3D representation of the outer slot design is shown in figure 4-22.

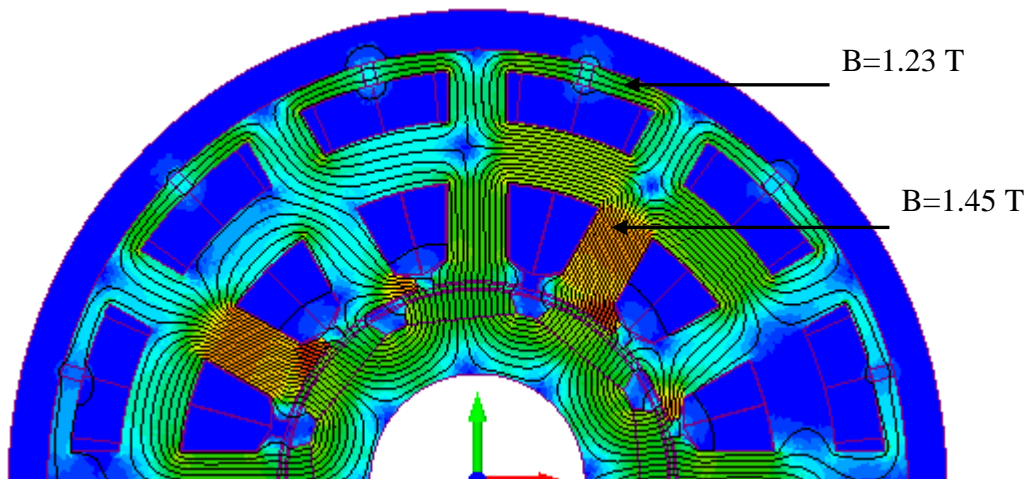




**Figure 4-22 3D representation of integrated double slot (IDS) machine**

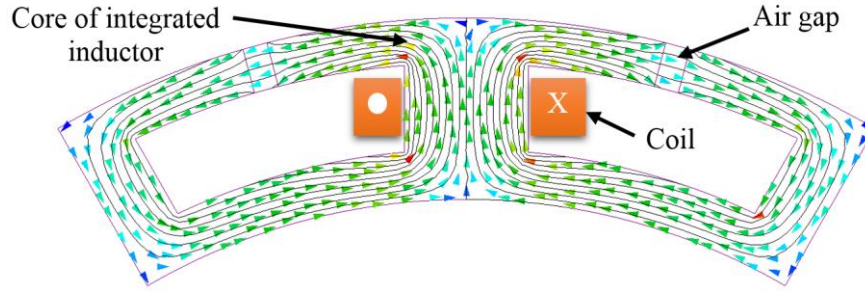
#### 4.4.4.1 FEA results

This integration method has been simulated using Infolytica MagNet software with both the machine's torque-producing windings and the auxiliary windings energised. The whole stator arrangement is considered to be uniform material -10JNEX-900. Figure 4-23 shows a magnetic flux density plot.



**Figure 4-23 Contour of dual magnetic flux of 8 pole machine and 10 pole inductors windings**

For this geometry, the outer slot arrangement can initially be considered independently of the main machine geometry simplifying analysis. Figure 4-24 represents a single coil of the phase inductor where the flux behaviour within the proposed geometry can be observed.



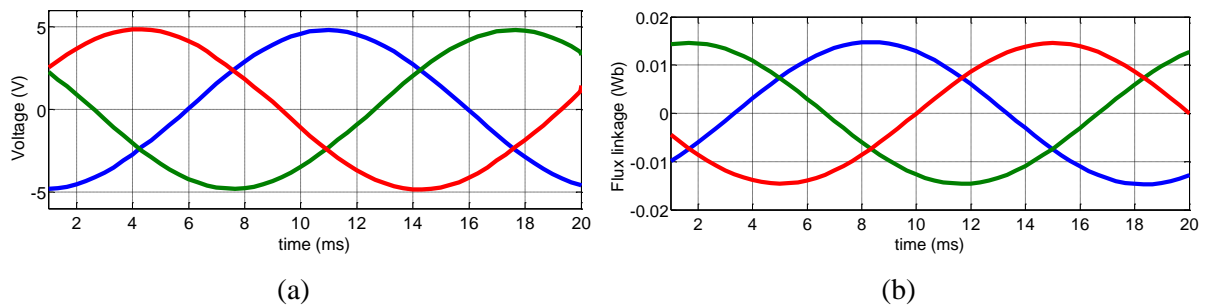
**Figure 4-24 Magnetic flux behaviour within a single inductor slot**

The inductance and reluctance values for one coil as shown in figure 4-24 can be calculated as given in equations 4-23 and 4-24 respectively:

$$L i = \psi = \frac{1}{2} N \Phi = \frac{1}{2} N B C S A \quad (4-23)$$

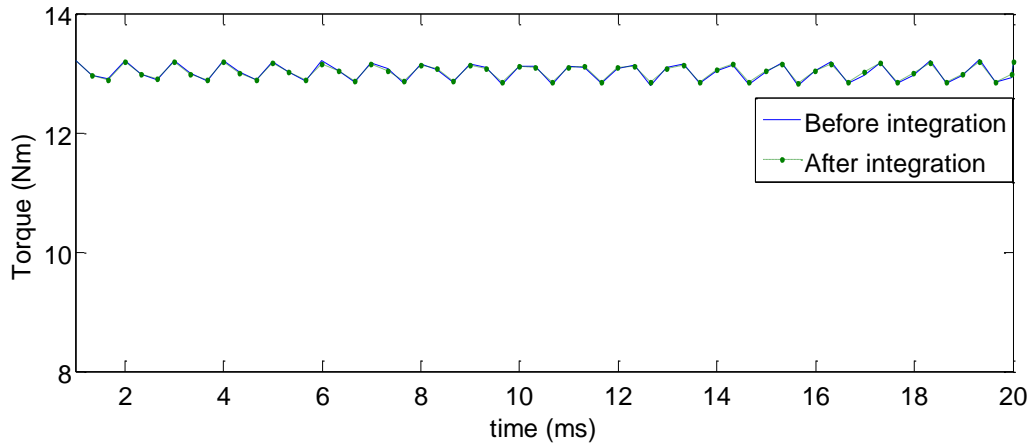
$$R_{eq} = \frac{1}{2 \mu_0 C S A} [L_g + \frac{L_M}{\mu_r}] \quad (4-24)$$

This geometry has been simulated with a drive current of  $53 A_{rms}$ . The resulting inductor voltage and flux linkage are 4.77 V and 0.0147 Wb respectively as shown in figure 4-25. The phase inductance  $L_2$  can then be calculated from equation 4-23, resulting in a value of 0.196 mH which is 22.5% greater than that predicted by the simple analytical method. This difference relates to the difficulty in achieving the exact predicted inductance with an integer number of turns within the FE model, and therefore it was preferable to achieve a higher inductance with 7 turns rather than achieving lower inductance with 6 turns in each coil of the phase inductor.



**Figure 4-25 FE results for integrated 3-phase filter inductors  $L_2$ : a) voltage; b) flux linkage**

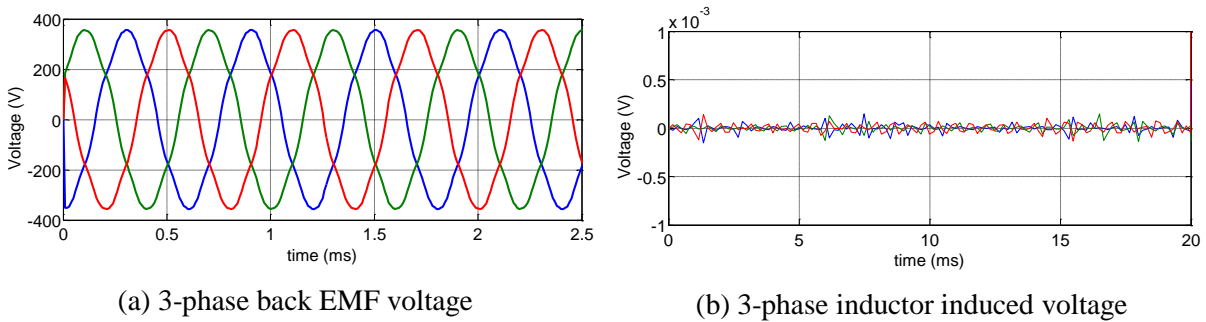
Figure 4-26 shows the rated machine torque before and after incorporating the filter inductors  $L_2$  into the HSHP machine, where the mean torque is 13.2 Nm for the two cases. This indicates that, the performance of the original HSHP motor is not affected by the integration.



**Figure 4-26 Machine rated torque before and after integrating 3-phase AC inductors**

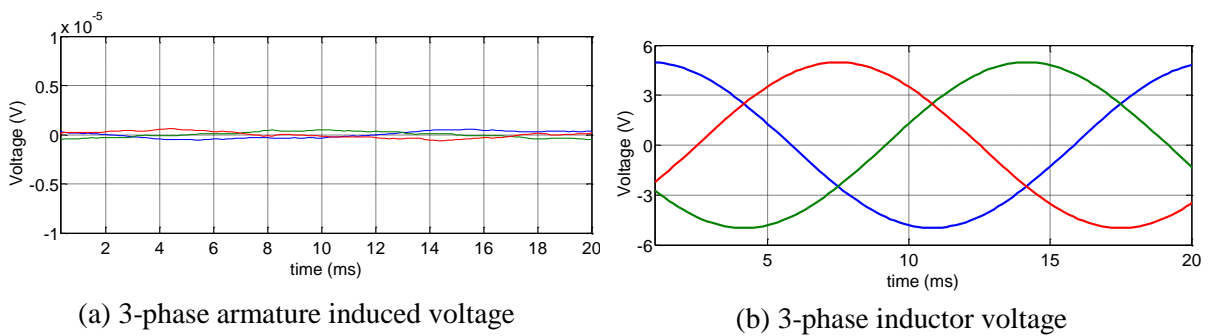
Further investigation has been carried out in order to observe the influence of integrating drive-side inductors  $L_2$  into the HSHP machine. Different cases of operating conditions have been considered for the IDS machine to investigate the possibility of induced voltage in the inductor windings as explained below.

**Case 1:** magnets rotor of the base machine is active and zero current in both armature and filter inductor windings.



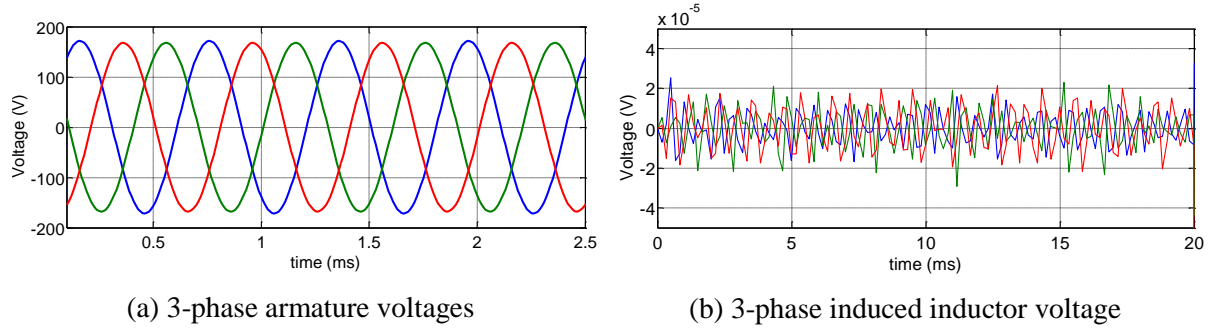
**Figure 4-27 Induced voltage in inductor windings due to the magnetic field of rotor magnets**

**Case 2:** the rotor magnets of the base machine is turned-off with a zero current in the armature winding while the filter inductor windings are energised.



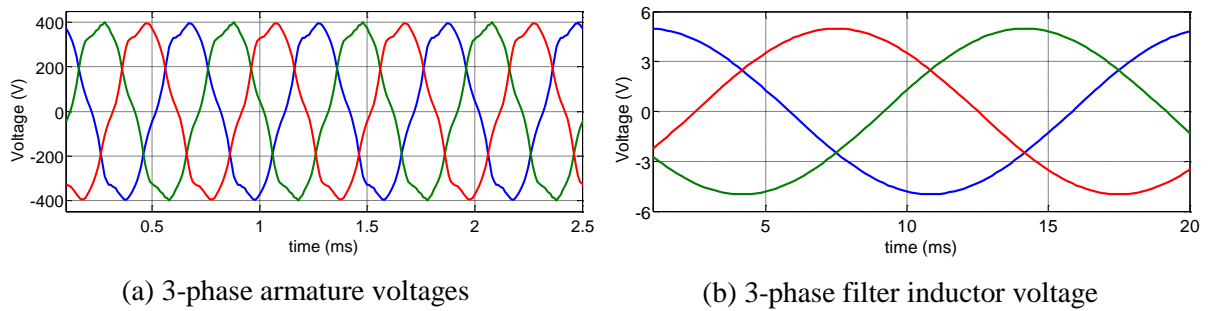
**Figure 4-28 Voltage induced in armature windings due to energising filter windings only**

**Case 3:** the rotor magnets of the base machine are turned-off and the armature windings are energised while the filter inductor windings are open.



**Figure 4-29 Voltage induced in inductor windings due to the magnetic field of armature fields only**

**Case 4:** the magnetic circuits of the base machine and filter inductors are active.

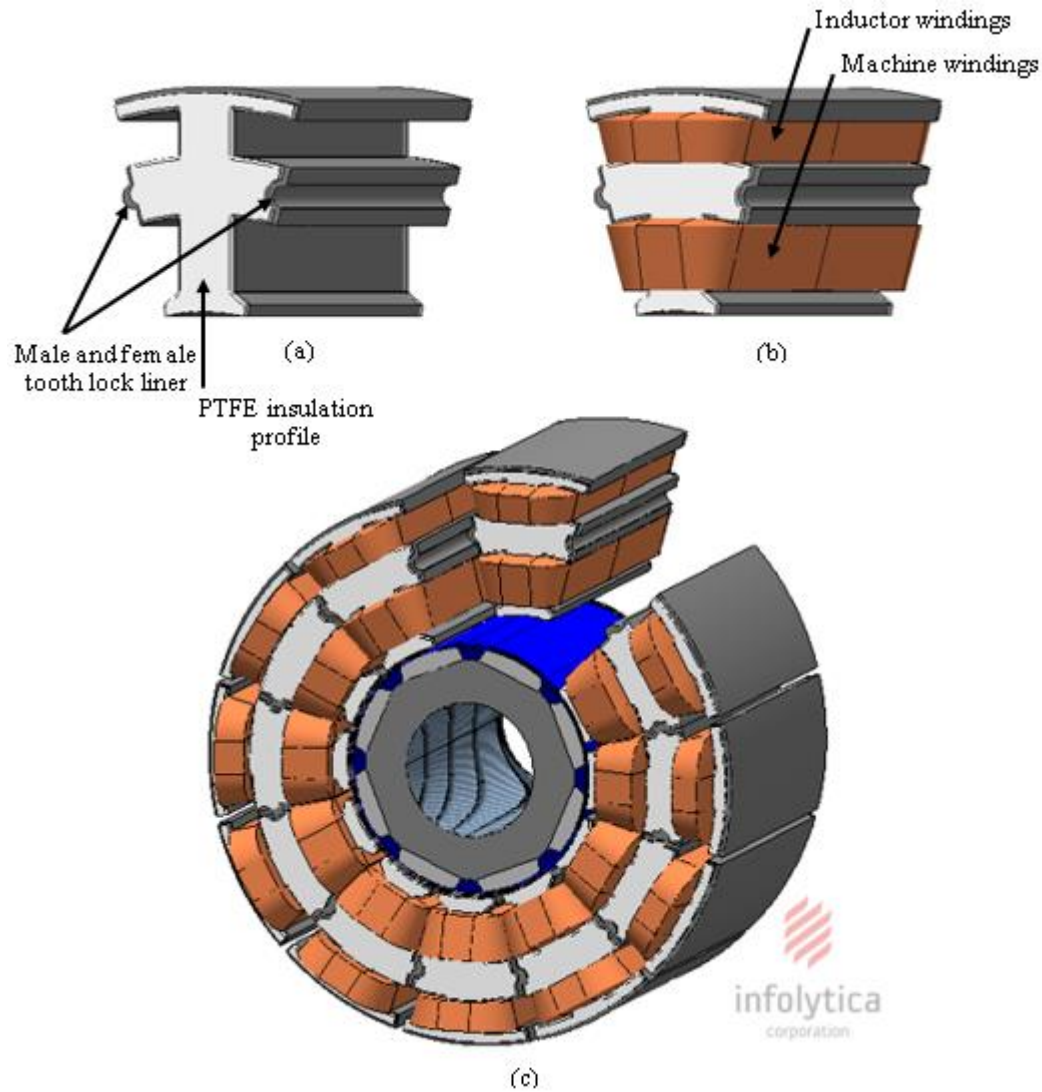


**Figure 4-30 Magnetic cross-coupling between integrated filter inductors and the HSHP machine**

The outer slot approach achieves the goal of reducing the overall volume whilst maintaining drive performance.

#### 4.4.4.2 Modularity option for the IDS machine.

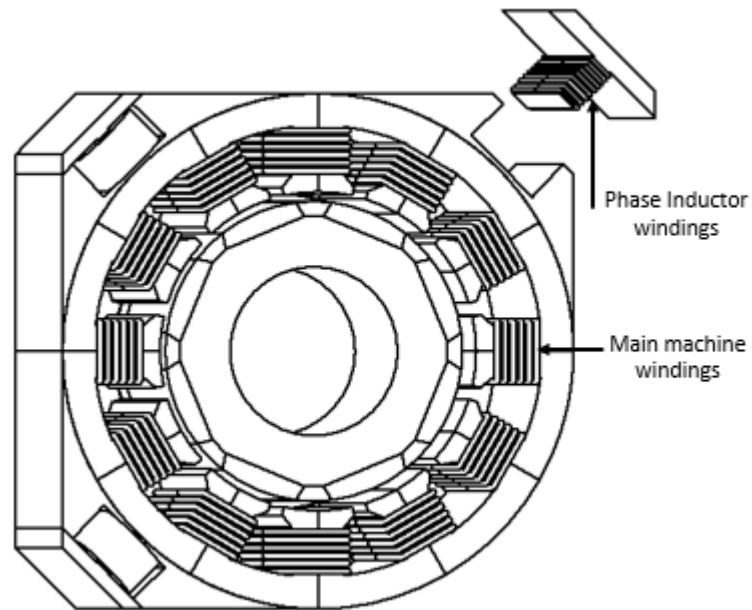
Segmented stator construction significantly increases manufacturability of the windings and helps to improve the fill factor [67]. The additional outer slots have not affected the rotational symmetry of the stator hence the stator can be constructed from twelve identical segments with interlocking mating geometries. A single tooth 3D representation of the proposed geometry is shown in figure 4-31.



**Figure 4-31 Integration of 3-phase drive-side inductors with stator modularity option: a) double slot tooth; b) double slot tooth with pressed coils; and c) assembly of stator of integrated double slot (IDS) machine**

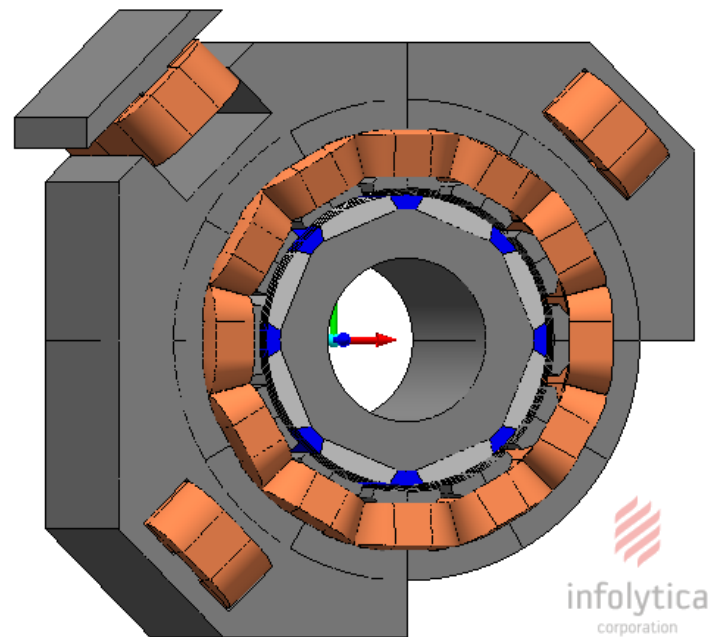
#### 4.4.5 Method 5: corner inductors

In this approach, the circular form of the stator laminations is converted into a square and each phase inductor is formed of discrete coils each situated in a corner of this square as shown in figure 4-32. In this technique, the filter inductors  $L_2$ , have an independent air gap for each phase and hence they have magnetic flux paths which are totally independent of each other and from the machine magnetic circuit. The design has been optimised using the same iterative method that was used for the previous two methods. The proposed method is promising in terms of ease of manufacture, where the inductor coil can be wound to the independent tooth and then easily fitted to the motor's corner.



**Figure 4-32 Utilization of motor corners for integrating AC inductors**

The fourth corner can feasibly be utilised to integrate the grid-side inductors,  $L_1$ , as these inductors are much smaller than the drive side inductors. A 3D representation of this proposed method is shown in figure 4-33.



**Figure 4-33 A 3D representation of integrated 3-phase filter inductors  $L_2$  within motor corners**

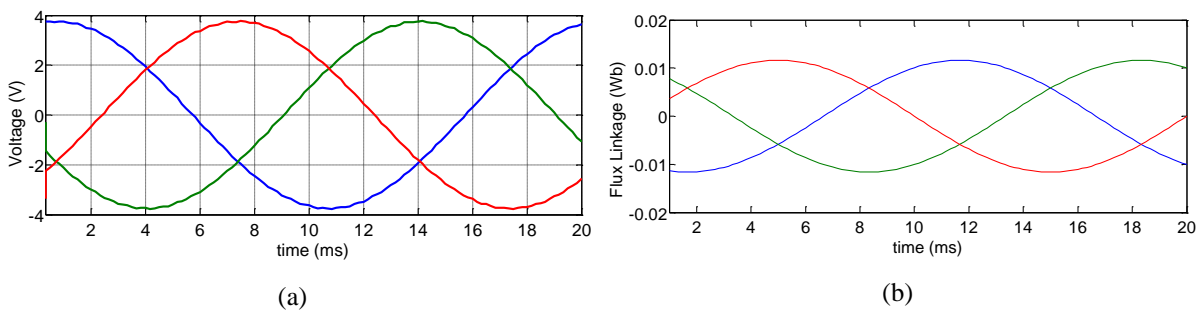
The required diagonal profile for the required drive specification in this work is 153.11 mm, while the outer diameter of the base motor is 109 mm. This gives a rise in the total volume of 1052.52 cm<sup>3</sup>, which is large compared to those achieved in the double slot proposed method.



However, this technique is likely to be an improvement on the overall volume for slower, larger machines.

#### 4.4.5.1 FE Results

The 3-phase filter inductors within the square motor profile were simulated with a current of  $53 A_{rms}$  and the main machine operating at full load. Figure 4-34 shows the resulting inductor voltage and flux linkage, where the achievable peak value of the latter per phase is 0.0115 Wb giving a phase inductance  $L_2$  of 0.153 mH, while the value of the analytical predicted inductance is 0.16 mH.



**Figure 4-34 FE Results for 3-phase filter inductors  $L_2$ : a) 3-phase voltages; b) 3-phase flux linkage**

The desired filter inductance is achieved along with maintaining the base machine performance. It can be seen in figure 4-34 (a) that the 3-phase voltages of the filter inductors are magnetically independent from the base machine's magnetic circuit.

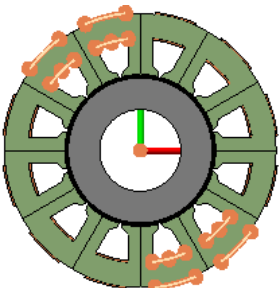
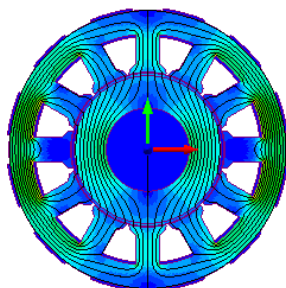
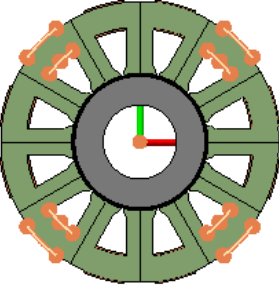
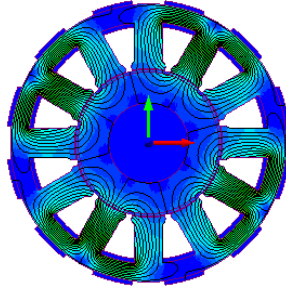
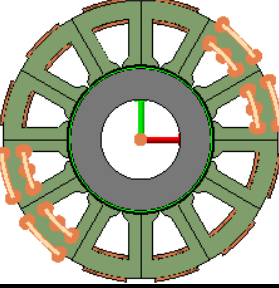
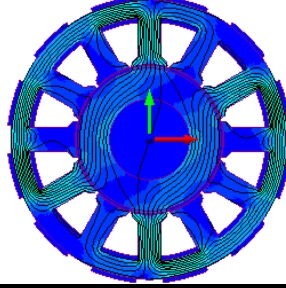
#### 4.5 Integration of drive-side filter inductors $L_2$ in a power drive of 4.56 kW at 3000 RPM

The same proposed integration techniques have been studied in a low-power drive of 4.56 kW where the base machine is identical but with a rated speed of 3000RPM.

- The results of the first two methods of integration (inductor windings around stator core back and around stator teeth) are presented in brief in tables 4-6 and 4-7. Since the size of the inductors at this power level is significantly smaller, as noted in the FEA design presented in chapter 2, the integration of these inductors at the specified drive power is mechanically feasible. For these integration methods, the main machine stator accommodates the windings of the main machine and the filter inductors, but the original stator slot has been amended resulting in increased machine outer diameter.

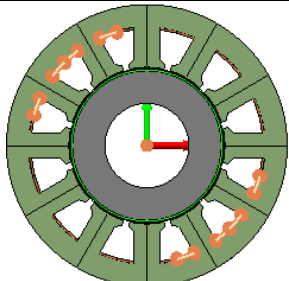
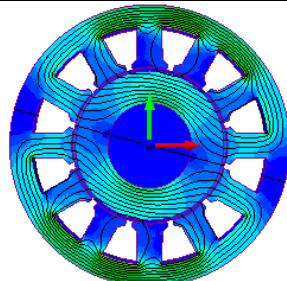
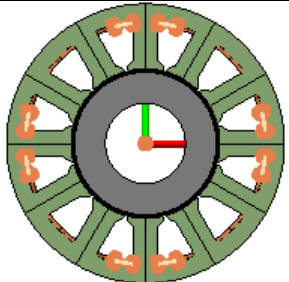
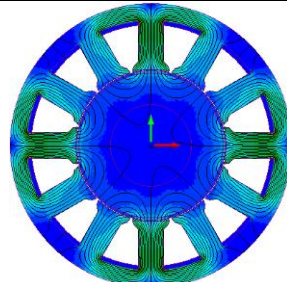
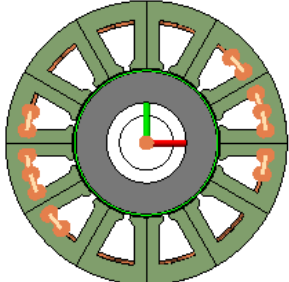
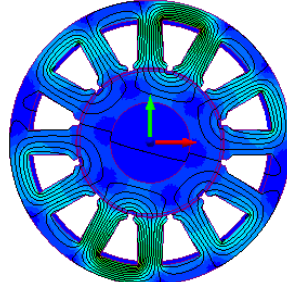
- The fourth integration method (additional outer slots) is still promising, giving good windings management which prevents magnetic cross-coupling between the filter inductor and machine windings compared to that of the interior double-slot stator.
- The fifth integration technique with corner motor inductors is judged the best method for this power level as the filter inductors fit into the motor's corners profile without increasing the original machine diameter. This method's main advantages (e.g. no end-winding interconnections) can be fully realised at this power level.

**Table 4-6 Illustration of the integration of 3-phase filter inductors around the stator core back at 4.56 kW drive: Method 1**

Number of inductor poles ( $L_2$ )	Integrated AC inductor geometry wound around the core back		Parameters	Increase OD (original motor OD = 109 mm)
2 poles			OD: 120.4 mm	+ 10.46 %
			N:10 turn	
			$L$ :1.37 mH	
			$V_L$ : 3.86 V	
8 poles			OD: 124.86 mm	+ 14.55 %
			N:24 turn	
			$L$ : 1.34 mH	
			$V_L$ : 3.77V	
10 poles			OD: 126 mm	+ 15.59 %
			N: 22 turn	
			$L$ : 1.36 mH	
			$V_L$ : 3.8 V	
<b>Symbol:</b> OD: outer diameter of the PM motor; N: number of turns per phase; $V_L$ : voltage per phase across the filter inductors $L_2$ .				
<b>Note:</b> The highlighted slots form a single phase in each case.				



**Table 4-7 Illustration of the integration of 3-phase filter inductors around the stator teeth at 4.56 kW drive: Method 2**

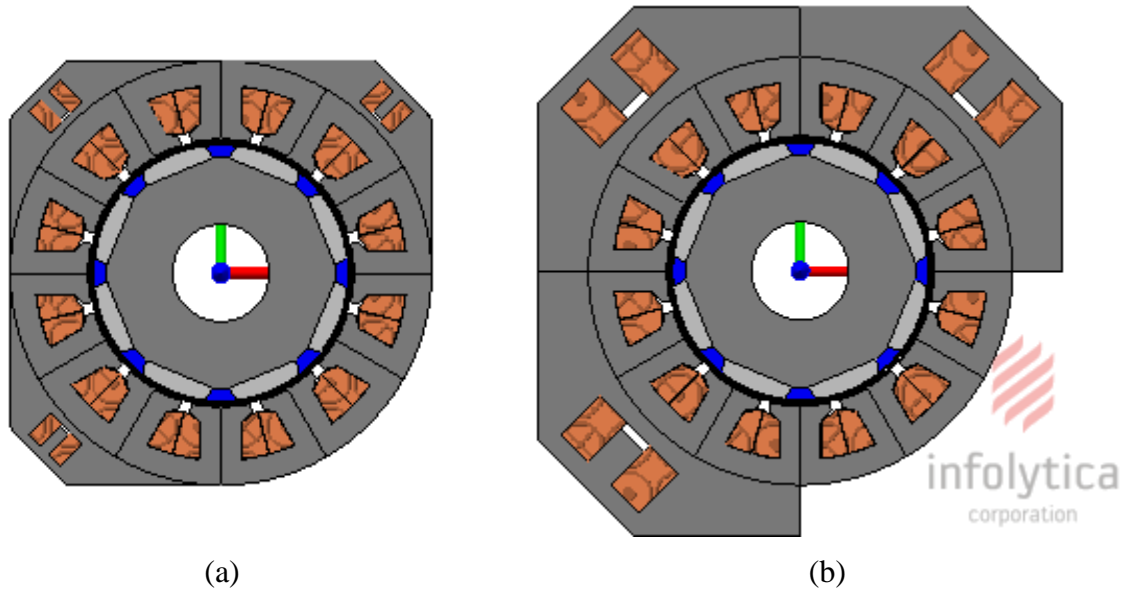
Number of inductor poles ( $L_2$ )	Integrated AC inductor geometry wound around the core back		Parameters	Increase OD (original motor OD = 109 mm)
2 poles			OD: 119.46 mm	+ 9.59 %
			N: 6 turn	
			$L$ : 1.3 mH	
			$V_L$ : 3.7V	
8 poles			OD: 121.6 mm	+ 11.56 %
			N: 14 turn	
			$L$ : 1.38 mH	
			$V_L$ : 3.88V	
10 poles			OD: 123.6 mm	+ 13.39 %
			N: 13 turn	
			$L$ : 1.3 mH	
			$V_L$ : 3.7V	
<b>Symbol:</b> OD: outer diameter of the PM motor; N: number of turns per phase; $V_L$ : voltage per phase across the filter inductors $L_2$ .				
<b>Note:</b> The highlighted slots form a single phase in each case.				

#### 4.6 Discussion

The first two integration methods have been examined for different inductor pole numbers which mainly govern the number of turns. Here the size of inductor air gap is dictated by the machine design. The magnetic flux of the integrated filter inductors which shares the machine's air gap affects the net forces acting upon the rotor. Table 4-8 shows that these two methods are not applicable for the integration of the specified high-power inductors into the proposed HSHP machine, while they are feasible for low-power inductors but would give poor power density compared to the benchmark volume (discrete 3-phase filter inductors).

In method 4, the approach using the double slot machine offers significantly less coupling between the two magnetic paths and achieves higher power density for either the high- or low-power inductors compared to the specified benchmark and other integration methods, as shown in table 4-8. This technique is applicable for the proposed low- and high-speed machines in order to integrate the input filter inductors without affecting the base machine performance, however, the level of shared magnetic path produces unwanted coupling between the different fields.

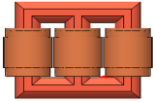
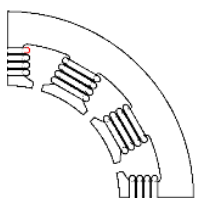
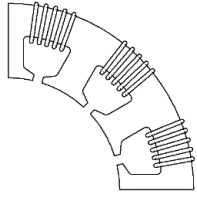
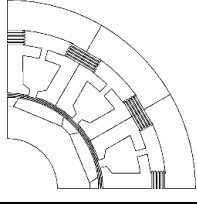
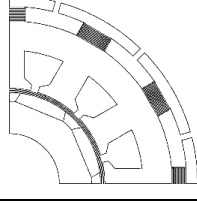
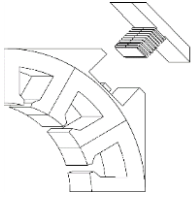
Method 5 for the integration of filter inductors at low-power ratings gives a better envelope associated with the square profile of the original machine, while the high-power inductors exceed the main machine dimensions due to their large size as shown in figure 4-35.



**Figure 4-35 Illustration of the final motor profile associated with the 3-phase filter inductor  $L_2$  in: a) low-power drive of 4.56 kW; b) high-power drive of 38 kW**

Table 4-8 gives an indication of the size and copper loss for each option for both power ratings.

**Table 4-8 Different topologies for integrating low and high power electric drives**

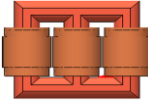

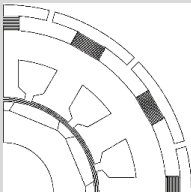
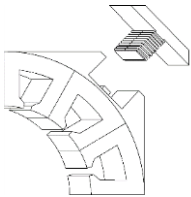
Method	Methods of integration		Outer diameter (mm)		Volume (cm <sup>3</sup> )		Copper loss (W)	
			L. P. 4.1kW	H. P. 34 kW	L. P. 4.1kW	H. P. 34kW	L. P. 4.1kW	H. P. 34kW
<b>Discrete inductors</b>			---	---	85.65	402.75	32.73	367.05
<b>1</b>		2 poles	119.46	N/A	131.38	N/A	15.36	---
		8 poles	121.6	N/A	159.74	N/A	30.6	---
		10 poles	123.6	N/A	186.7	N/A	30.73	---
<b>2</b>		2 poles	120.4	N/A	143.77	N/A	21.88	---
		8 poles	124.86	N/A	203.91	N/A	52.68	---
		10 poles	126	N/A	219.63	N/A	48	---
<b>3</b>		10 poles	115	134.2	73.89	336.94	21.6	110.4
<b>4</b>		10 poles	115	134.2	73.89	336.94	21.6	110.4
<b>5</b>			109	127.3	86.05	399.33	30.45	114.48
			125.8	147.31 (Diagonal)				

As a result, although the first two methods do not appear to be promising, it can be seen that the corner and double slot techniques achieve the lowest volumes with the smallest outer diameters for these scaled drives.

In addition to the previous comparison, which considers theoretical maximum power densities of the discrete E-core filter, a commercially, bespoke manufactured E-core inductor, is

compared with the most promising proposals in table 4-9. The commercial inductor is significantly larger than the theoretical high power case in table 4-9. It should be noted that the net volume of both conventional and integrated inductors are solely considered in which packing factors are ignored such as housing, the necessary foundation for inductors and surrounded space for ventilation.

**Table 4-9 Comparison of integrated and discrete commercial filter inductors**

Method	Methods of integration	Outer Diameter (mm)	Volume (cm <sup>3</sup> )	Copper loss (W)
		H. P. 34 kW	H. P. 34kW	H. P. 34kW
Discrete high power inductors		---	402.75	367.05
Discrete commercial inductors		---	2430	561.8
4		134.2	336.94	110.4
5		127.3	399.33	114.48
		147.31 (Diagonal)		

It can be seen from table 4-9 that the volume achieved by the method of the double-slot machine (method 4) is approximately 86.13% and 16.34% smaller than that achieved by industrial filter inductors and high power inductors respectively, while integration method 5 gives a reduction in the volume of 86.04% and 8.49%. This significant reduction in volume is possible because these industrial filter inductors cannot work at such high current densities since they usually do not utilise an active cooling system.

#### 4.7 Summary of design options

The integration of additional outer slots in method 4, the integrated double slot (IDS) machine, is the best candidate to integrate the specified filter inductors into the proposed machines. The higher speed drive of 38 kW presents a greater design challenge and hence the greater potential for performance gain. Therefore, the remaining work in this thesis concentrates on the integration of input LCL filter inductors in the higher-power specification (38 kW / 25000 RPM).

The following section demonstrates the addition of the smaller grid-side inductor into the same generic geometry without significantly altering it dimensionally.

#### 4.8 Design of integrated magnetic filter (grid-side inductors $L_1$ )

In the previous chapter it was shown that using an integrated “double-slot” (IDS) geometry [100], the integration of the (larger) drive side inductors ( $L_2$ ) achieved lower volume and losses compared to traditional discrete 3-phase drive side inductors. This integration method requires the modification of the base machine stator laminations to include a further slot radially outward from the main machine windings. In the chosen method of the IDS machine, the second slot held the drive side inductor and it was shown that such an arrangement, with prescribed pole-pair combinations, decouples the main machine and filter winding coils.

The small grid-side filter inductors ( $L_1$ ) are subsequently incorporated into the same slots as the drive-side inductors requiring a slightly larger depth of the inductor slot by 1 mm and the copper slot fill factor was increased which is achieved through coil pressing as described in Chapter 5. The proposed geometry for IDS machine, including both filter inductors  $L_1$  and  $L_2$  is illustrated diagrammatically in figure 4-36.

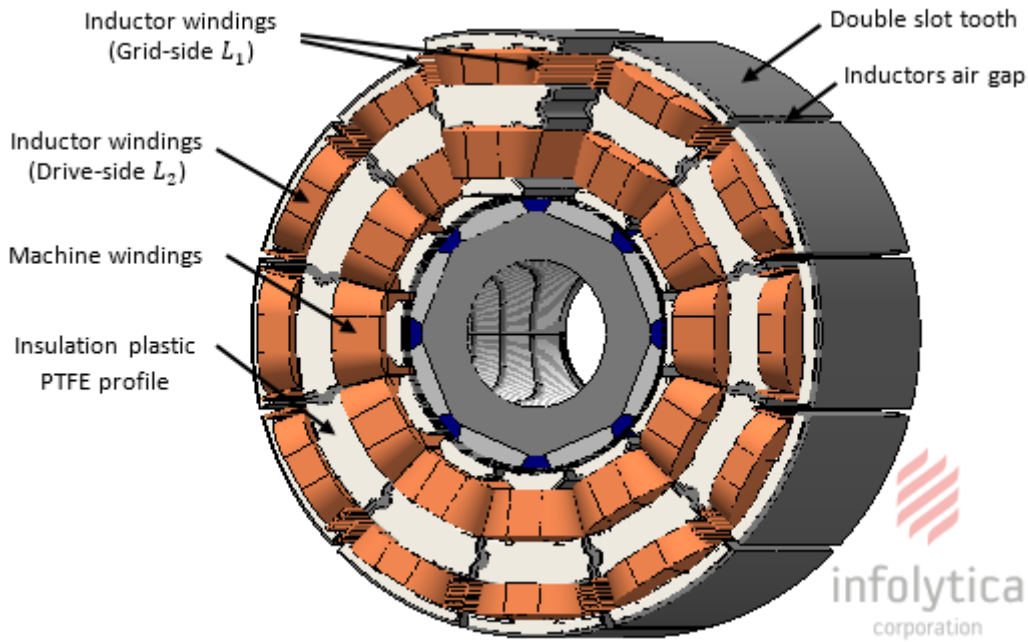
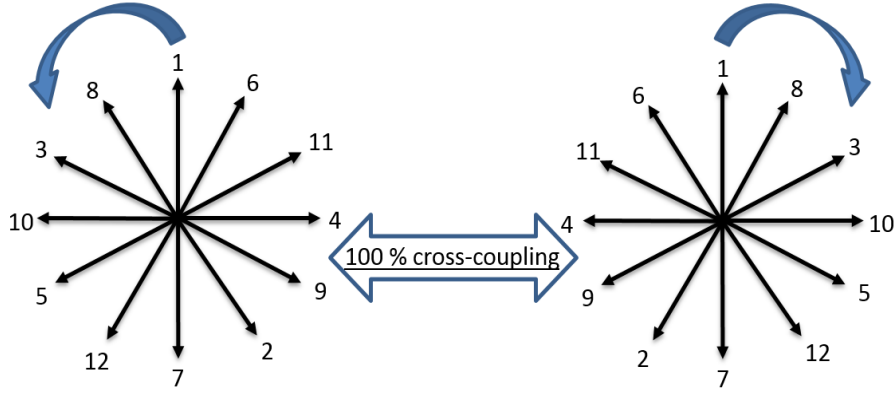


Figure 4-36 3D presentation of the general schematic of the IDS machine

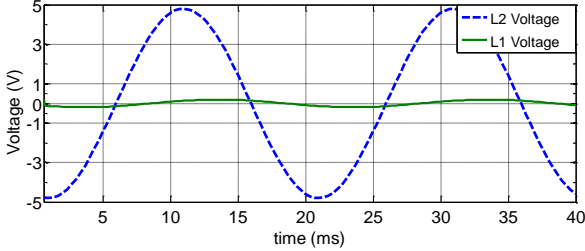
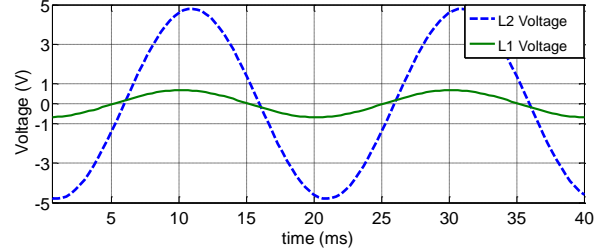
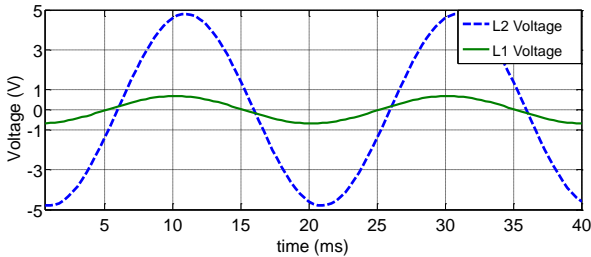
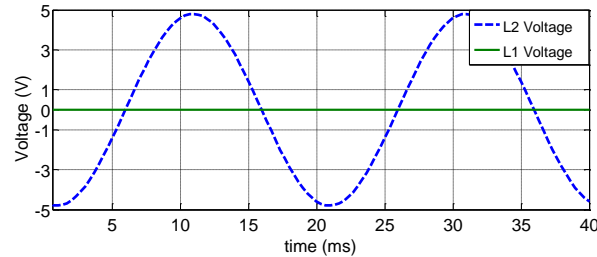
#### 4.8.1 Winding configuration of integrated filter inductors

As in the previous chapter the winding arrangements are further carefully selected so that the main machine windings, grid-side and drive-side inductors all have different numbers of poles so as to avoid cross-coupling and they are selected in such a way as to avoid unbalanced magnetic forces.

The integrated geometry of the filter inductors is intended to minimise the volume of the filter and to combine it with the machine structure in a single envelope. As the coils of both inductors  $L_1$  and  $L_2$  of the LCL filter share the same outer slots, and hence magnetic paths, magnetic cross-coupling between the filter inductors is still possible. A case study of different pole combinations for  $L_1$  and  $L_2$  summarised in figure 4-37 illustrates that the phenomenon of mutual coupling between filter inductors is due to the rotational magnetic field caused by the coil arrangements of the 3-phase filter inductors  $L_1$  and  $L_2$  which are distributed among 12 stator upper slots. In this case, the directions of magnetic fields for the arbitrary pole combinations chosen ( $L_1$  is 14 poles and  $L_2$  is 10 poles) are opposite to each other and hence give 100% coupling between the integrated filter inductors.

(a) Windings configuration of  $L_1$  (10 poles)(b) Windings configuration of  $L_2$  (14 poles)**Figure 4-37 Example of mutual coupling between  $L_1$  and  $L_2$  located in the same slots**

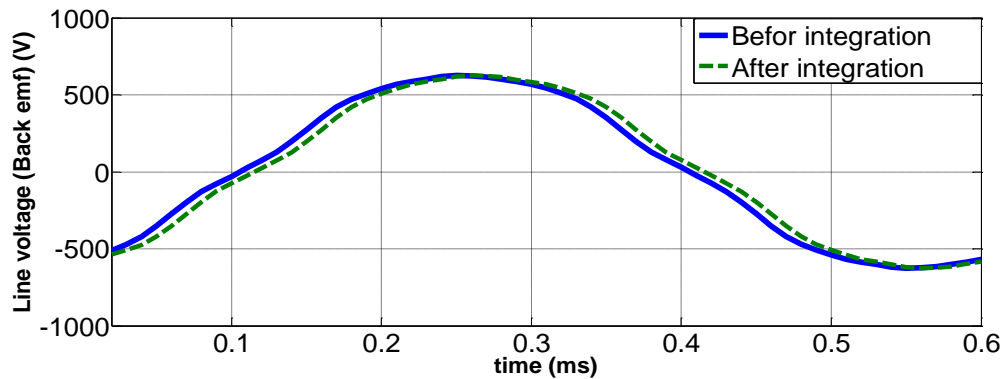
Different pole combinations for  $L_1$  and  $L_2$  have been simulated using FE analysis to investigate the degree of undesired mutual coupling between  $L_1$  and  $L_2$ . Figure 4-38 shows the simulation results of the study of coupling between  $L_1$  and  $L_2$ . Here the number of poles of the larger inductor,  $L_2$ , was fixed at 10 poles while the number of poles of  $L_1$  was varied. The rated current was applied to  $L_2$  and the induced voltage on  $L_1$  is observed (with an  $L_1$  open circuit). The induced voltages on  $L_1$  for single phase LCL filter inductors are presented in figure 4-38.

(a)  $L_1$  is 2 pole &  $L_2$  is 10 pole(b)  $L_1$  is 10 pole &  $L_2$  is 10 pole(c)  $L_1$  is 14 pole &  $L_2$  is 10 pole(d)  $L_1$  is 16 pole &  $L_2$  is 10 pole**Figure 4-38 Results of cross-coupling investigation between integrated filter inductors with different numbers of poles in the stator**

Normalizing for the turns ratio, the four pole combinations studied were 2:10, 10:10, 14:10 and 16:10, which have coupling factors of 22%, 100%, 100% and 0% respectively (10:10 and 14:10 are essentially the same pole combinations). These conclusions can be verified analytically by observing the space harmonics created by the 16 pole and 10 pole windings. Unlike most other

winding combinations, the 10 pole winding wound onto the 12 tooth stator does not have a 16 pole space harmonic and so there should be no mutual coupling between them.

As well as demonstrating the lack of coupling between the two filter windings, it must also be shown that the inclusion of the filter windings in the second slot does not lead to coupling with the main machine windings. A finite element simulation was used to observe the base machine open circuit voltage at the rated speed (i.e. back-EMF) as shown in figure 4-39 both before and after integrating the AC filter inductors into the machine (where the filter windings are conducting the rated current).



**Figure 4-39 The original machine back-EMF line voltage before and after integration**

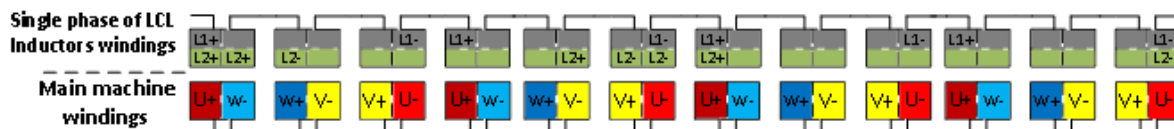
As shown in figure 4-39, the machine circuit is proven to be magnetically isolated from the filter windings, with the machine back-EMF profile almost unaffected by the filter currents. Note, however, that the common part of the stator core back is not heavily loaded, and a reduction in the size of this core back may yield a greater power density for the overall drive. However, the higher magnetic saturation may result in a greater share of the core back material between the various flux paths and therefore greater coupling. Based on the pole combinations given in figure 4-38 (d) for the filter inductors, the IDS machine windings configuration is selected to have 16, 10 and 8 poles respectively for the  $L_1$ ,  $L_2$  and the main machine windings. The various coils carry currents of differing fundamental frequencies (50 Hz and 1.666 kHz for LCL filter inductors and the base machine respectively), and hence comprise of different conductor types. Table 4-10 gives the winding configuration for the IDS machine coils.



**Table 4-10 Winding configurations for direct on-tooth compressed IDS machine coils**

Integrated motor parameters	Base machine windings	LCL filter inductor windings	
		$L_1$ (Grid side)	$L_2$ (Drive side)
Type of copper wire	Litz wire	Stranded solid wire	Stranded solid wire
Winding type	Concentrated	Concentrated	Concentrated
Coil connection	Parallel	Series	Series
Number of turns/phase	36 per coil, 4 coils in parallel per phase (144)	1 per coil, 4 coils in series per phase (4)	7 per coil, 4 coils in series per phase (28)
Conductor diameter	20 strands $\times$ 30 AWG	6 strands $\times$ 18 AWG	6 strands $\times$ 18 AWG
Fill factor	60%	50% (same slot-concentrated windings)	
Phase resistance	0.029 Ohms	0.0025 Ohms	0.022 Ohms
Phase inductance	0.24 mH	5 $\mu$ H	160 $\mu$ H
Number of poles in the stator	8	16	10

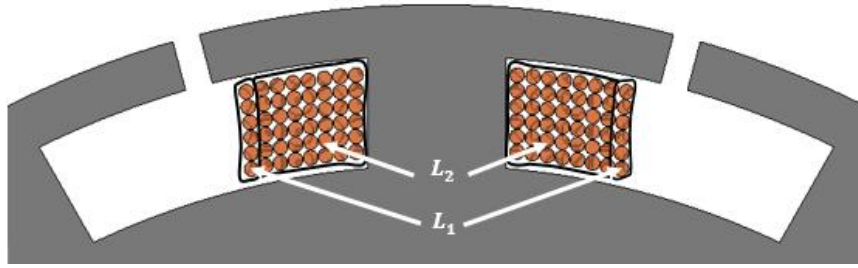
The windings layout per phase of the IDS machine, including the filter and base machine windings, is shown in figure 4-40.



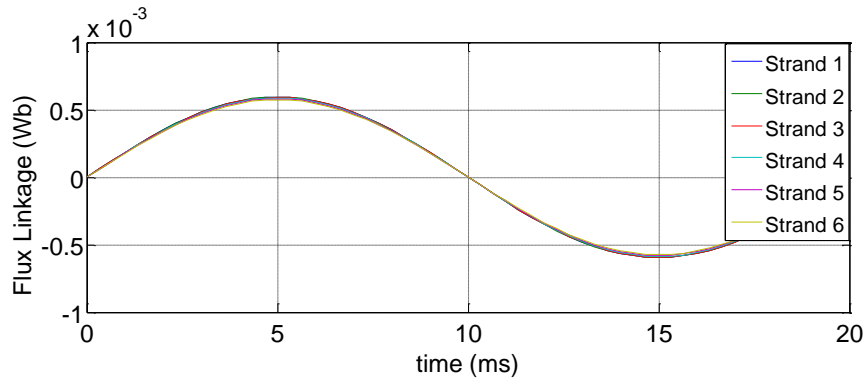
**Figure 4-40 24 slots - 8 pole base machine windings and 16 and 10 poles for filter inductors  $L_1$  and  $L_2$  respectively**

Figure 4-40 shows that the IDS stator has 36 coils and hence 72 end terminals in a very small area. Chapter 5 details the method employed to correctly connect these terminals using space-efficient bus-bar arrangement.

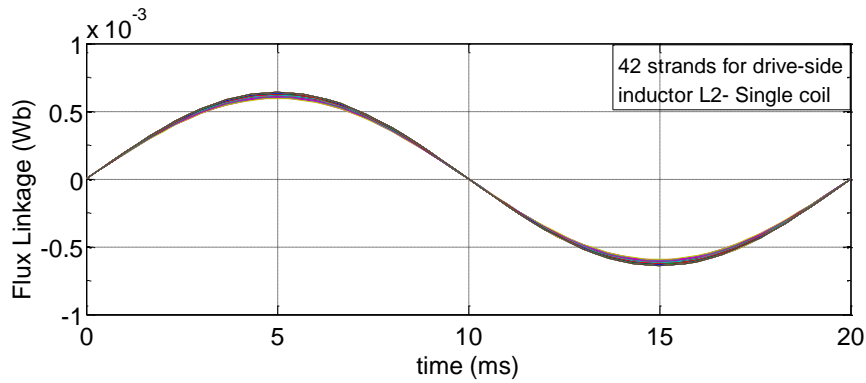
As described in table 4-10, the inductor winding type is solid stranded wire and each turn consists of 6 strands of solid copper wire connected in parallel to increase the fill factor, as shown in figure 4-41. Each solid strand wire was wound around the inductor tooth to form 7 turns individually in the radial direction. A fill factor of approximately 50% was achieved through the careful winding of the individual conductors. However, due to the variation in magnetic flux throughout the inductor slots, the flux linkage in each strand is slightly different for  $L_1$  and  $L_2$ , as shown in figure 4-42.



**Figure 4-41 Filter winding arrangements in a single inductor slot**



(a)



(b)

**Figure 4-42 Flux linkage in single coil strands: a) grid-side inductor; b) drive-side inductor**

Figure 4-42 (a) shows that the variation in flux linkage by single coil strands of  $L_1$  is approximately 3.6%, while this magnetic variation between the strands of  $L_2$  is almost 7%. As there are seven series turns, it is assumed that most strands occupy a range of locations, and that there remains good current sharing between strands.

#### 4.8.2 Verification of mutual coupling for the IDS machine

A 2D FE model of the IDS machine has been simulated with different conditions in order to verify the mutual inductance between the base machine winding and filter inductors in the double slot stator design. In each case, one of the three coils in each tooth is energised and the

other 2 coils are open and hence the resulting mutual inductance was obtained. Table 4-11 shows the mutual inductances between the three coils in the design of IDS machine.

**Table 4-11 Verification of mutual inductance in the design of IDS machine**

The base Machine at full load		$L_1$ is energised		$L_2$ is energised	
Mutual inductance on $L_2$ (open)	Mutual inductance on $L_1$ (open)	Mutual inductance on the base machine (open)	Mutual inductance on $L_2$ (open)	Mutual inductance on the base machine (open)	Mutual inductance on $L_1$ (open)
0.23 nH	4.47 nH	8.1 nH	106 nH	57.3 nH	92.8 nH

It can be seen that the mutual inductances of the filter inductors  $L_1$  and  $L_2$  which caused by the machine's magnetic circuit are very small compared to the self-inductances for both filter inductors while the machine inductance is unsusceptible to the influence of filter's magnetic circuit.

#### 4.9 DC loss of integrated 3-phase filter inductors

The inductor windings work with a grid frequency of 50 Hz and hence the AC losses are very small and it is ignored in the analysis. In order to calculate the DC loss, the same method used for calculating DC loss of armature windings (Chapter 3) was applied. The mean length of one side of end windings is 34 mm, with the machine axial length 70 mm, the number of turns for  $L_1$  and  $L_2$  per tooth are 8 turns  $\times$  6 solid strands carrying 53  $A_{rms}$ , the diameter of each strand is 1 mm and the C.S.A of the strand is 0.785  $mm^2$ . The copper resistivity  $\rho$  is  $1.68 \times 10^{-8} \Omega m$  at a temperature of 20°C and the total strand length of the 3-phase filter inductors is 19.968 m.

The total resistance of the 3-phase filter windings is 0.0712  $\Omega$  which gives a result of the total DC loss for the 3-phase filter inductors of 200W. The effect of temperature on the copper resistivity as the expected filter winding temperature under normal operating conditions is 80°C (clarification of expecting temperature value is stated in Chapter 3, section 3.5.5.2.2) is calculated which gives a result of 0.0882  $\Omega$  and the resulting DC loss of winding filter at this specific temperature is 248W.

#### 4.10 Iron Losses of the IDS machine including the 3-phase filter inductors

The proposed IDS machine has two different frequencies which are sharing the same magnetic circuit, the first frequency is the machine operating frequency and the second is the integrated filter frequency (grid frequency). The core losses have been calculated for each stator region as shown in figure 4-43. The following schematic illustrates different stator regions for the base motor and the integrated filter inductors collectively.

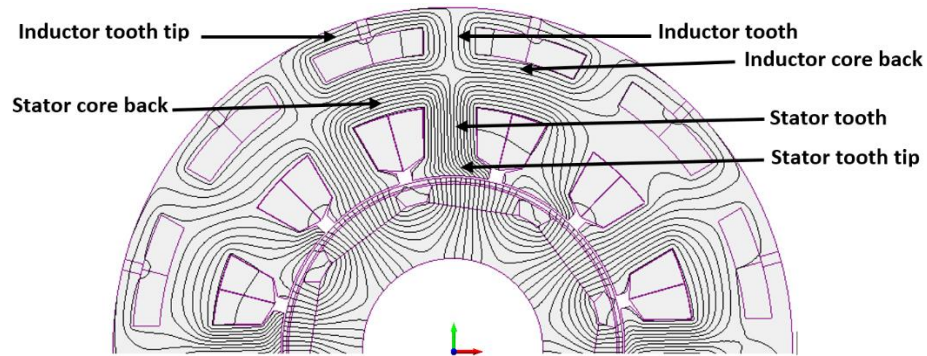


Figure 4-43 Full load flux plot of the double slot machine

The Steinmetz equation has been used to calculate the iron losses in the specified regions shown in figure 4-43 considering the operating frequency for the regions within the IDS stator. The 2D model of the full IDS machine at full load has been simulated which gives results of losses combinations as described in figure 4-44.

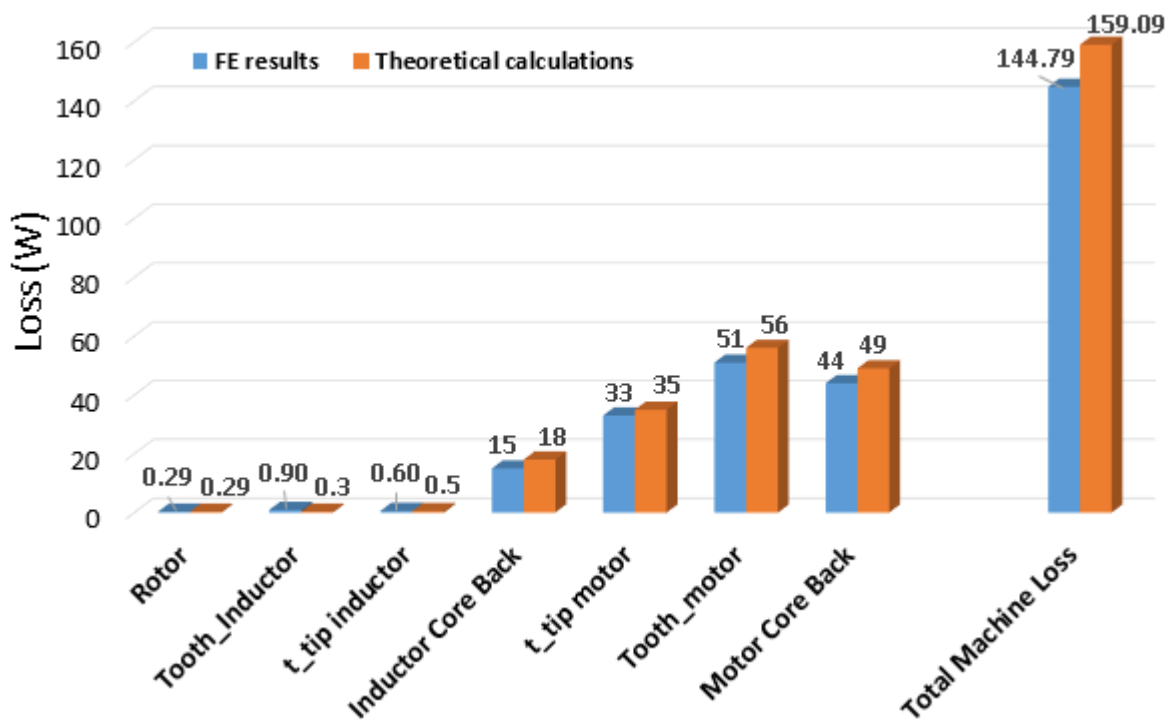


Figure 4-44 The composition of non-load iron Losses for double slot machine

The FE results shown in figure 4-44 illustrate that the total iron losses caused by the filter's magnetic circuit are about 16.5W which is a small value compared to the base machine losses. The low iron losses occurred in the filter's magnetic circuit refers to the low operating frequency (Grid frequency) and relatively low flux densities in these regions. It can be noticed that the losses of the machine tooth tip and stator tooth are more or less the same losses achieved in the original base machine (before the integration) while the core back losses of the IDS machine (FE result: 44W) are decreased by approximately 58% (FE result: 105W, Chapter 3). This significant losses reduction occurred in the core back of the IDS machine increased volume in the core-back reduces the magnetic flux density and hence the loss.

#### 4.11 Conclusion

The 3-phase drive-side inductors of an LCL filter  $L_2$  have been integrated into the two proposed machines using various different integration techniques. Two electric drive specifications with identical base machines have been considered for five integration methods. Volumes and copper loss associated with the integrated inductors have been compared to with those of the convectional discrete component cases (FEA models and industrial filter inductors) and shown to be comparable for the case of outer additional slots (the integrated double-slot (IDS) machine) to house the inductor windings. The inductor winding design has been analytically generated and validated via FEA.

The 3-phase grid-side LCL filter inductors have been successfully integrated into the high-speed machine by sharing the same slots with the drive-side inductors without affecting the performance of the original base machine nor coupling with each other. The resulting envelope is a single package which achieves a significant reduction in volume by 87.6% compared to a design with discrete filter components. Further details are presented in section 5.2.2. The final dimensions of the double slot stator are illustrated in figure 4-45. The challenges related to magnetic interactions between the three different fields resulting from the main machine winding and the two filter windings have been discussed in a careful study of the field interactions of various pole-pair combinations as well as from a finite element analysis of flux paths in the stator core.

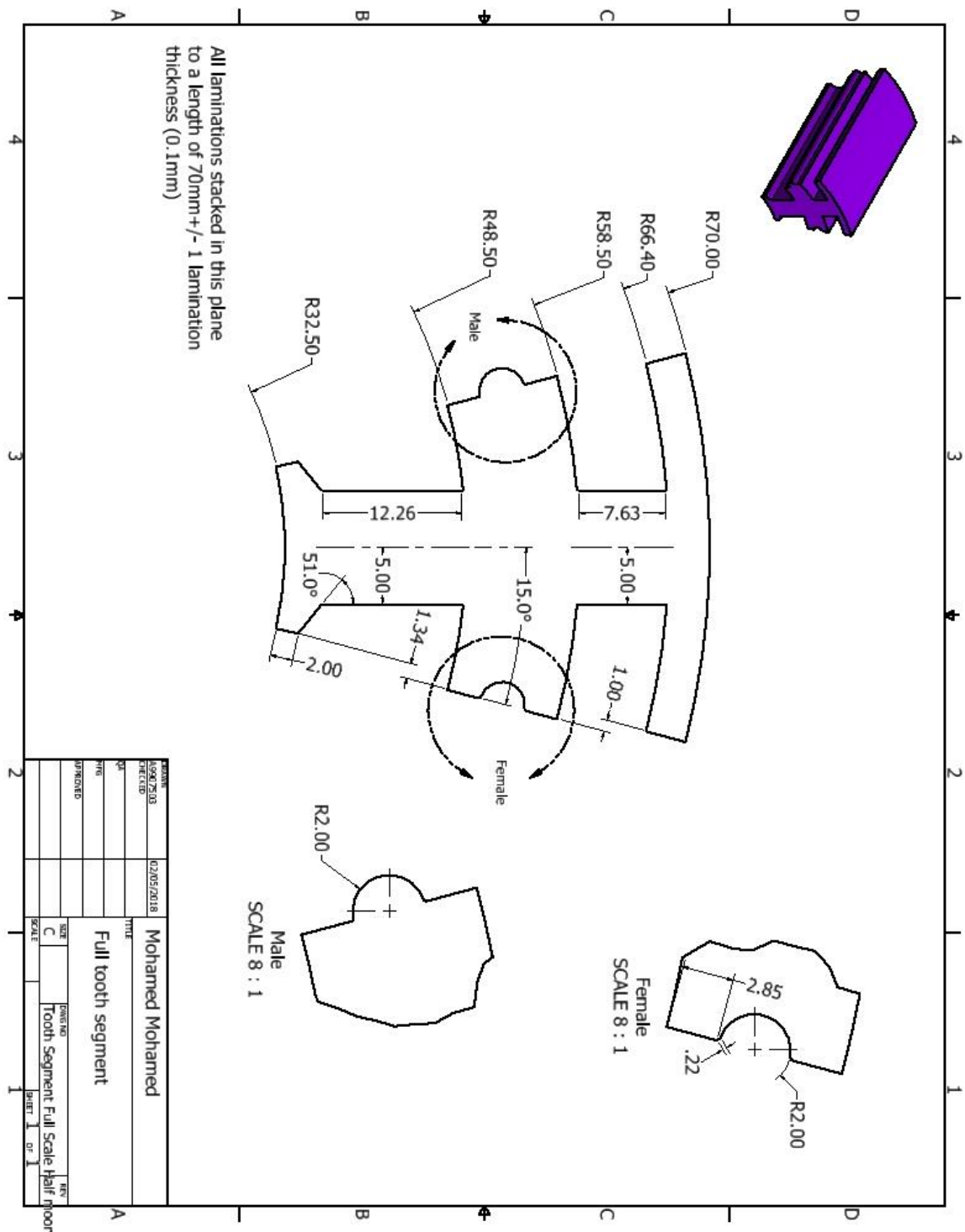


Figure 4-45 Drawing of full segment tooth

## CHAPTER 5

# Machine and Filter Construction

---

The manufacturing of the prototype IDS machine was accomplished with the assistance of four different companies, chosen according to their expertise in specific technical fields. Each of the companies manufactured components to the author's specification.

- The rotor magnetic assembly and composite wrap were made by Arnold Magnetic Technologies Ltd (UK).
- The rotor shaft was manufactured by Newcastle Tool and Gauge Ltd.
- The stator core was manufactured and assembled by the JFE steel company in Japan, which specialises magnetic materials manufacturing.

The stator windings were wound, impregnated and compressed by the author at Newcastle University and there is also a technical staff who conducted the assembling process of the bearing packages, cooling systems, shaft and couplings. The mounted drive electronics were assembled by research staff at the university. Final assembly of the IDS machine as part of the integrated motor drive was also undertaken within the university.

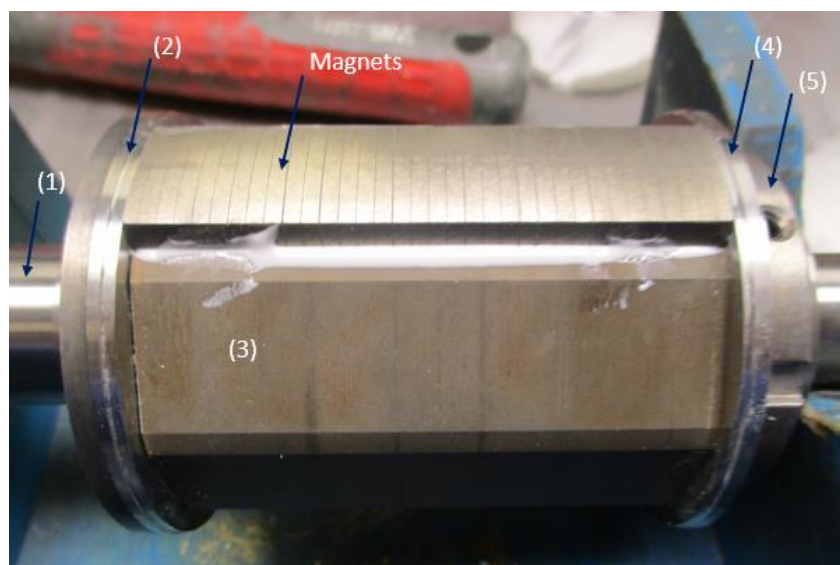
### 5.1 Rotor construction

The detailed design of the rotor magnets and sleeve was undertaken in conjunction with a specialist magnetic materials supplier and handler, who provided useful feedback on some practical processes in the rotor assembly and their effect on machine performance. The magnetic assembly was constructed independently from the rotor shaft to give access in the machining of the shaft.

Figures 5-1 and 5-2 show the construction of the rotor, including collars. The figures show the shaft (1), non-magnetic back collar (2), rotor core (3), non-magnetic front collar (4) and threaded retaining ring for the front collar (5).



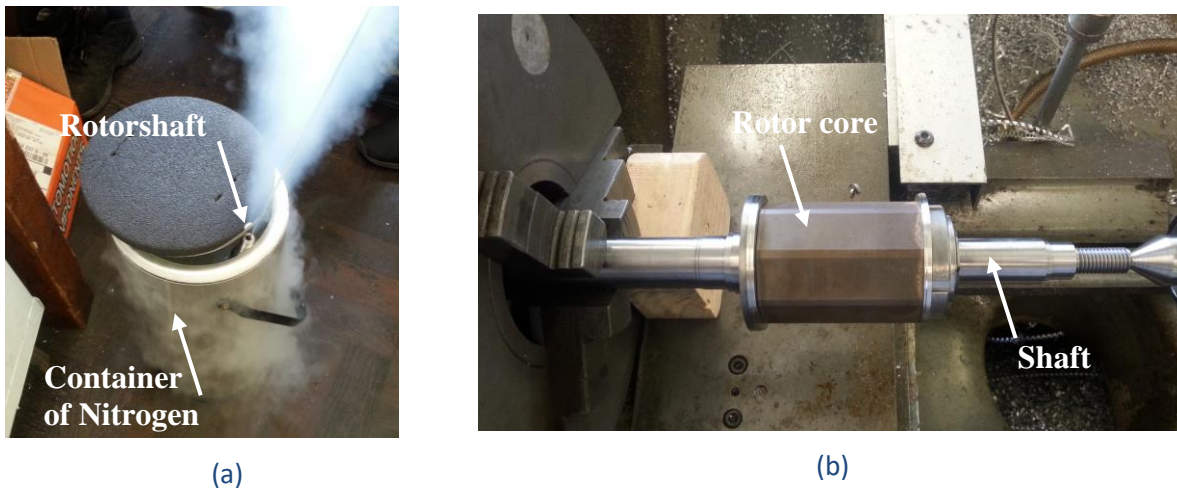
**Figure 5-1 Different components for the high-speed rotor**



**Figure 5-2 Assembly of rotor magnets showing the effect of front-end collars**

As shown in figure 5-3 (a), the shaft was shrunk using liquid Nitrogen at a temperature of  $-196^{\circ}\text{C}$  for approximately 3 minutes to allow the rotor core to fit the shaft. The shaft was pre-assembled with lamination stack and collars fitted in place, as shown in figure 5-3 (b).

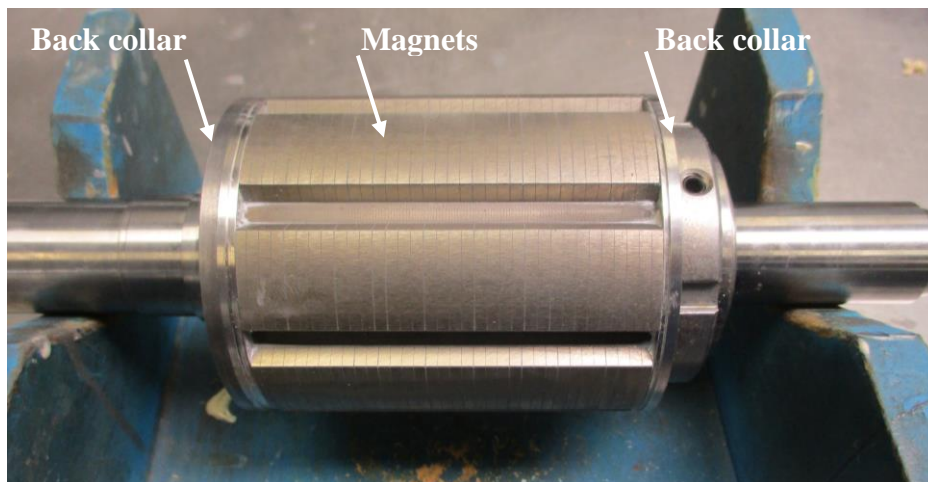




**Figure 5-3 Assembly of the rotor core and collars to the machine shaft**

As the rotor axial length is 70 mm, the overall magnet length is 70 mm +0.00 mm/-0.10 mm, made up from 34 pieces of equal length electrically isolated with a bond line thickness of 0.050 mm. Each segment of magnet was wire-eroded from a pre-magnetised block of Neodymium iron boron N42UH, and the bread loaf magnet shape of each segment, including flat sides, was cut to the required design dimensions and tolerance while the curved outer surface was larger than these dimensions to allow the magnet to be ground back to the correct tolerance.

The first stage of the assembly process of the rotor magnets is shown in figure 5-4, where an appropriate adhesive material was applied to the magnet's flat surfaces on the rotor core.



**Figure 5-4 Assembly process of the rotor magnets**

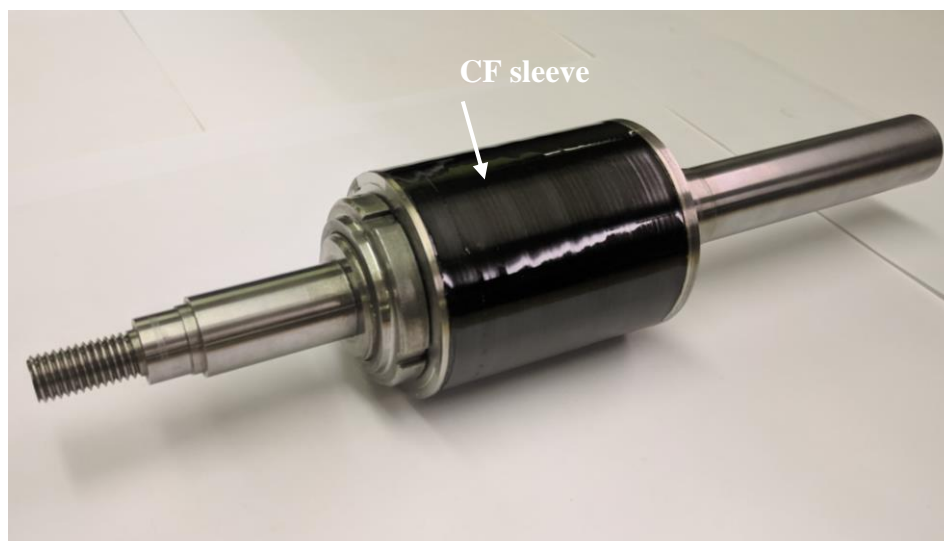
After the magnet was placed on the rotor core, Hylomar epoxy putty ST574 was applied to fill the gaps between the 8 rotor magnetic poles, as shown in figure 5-5. The Hylomar material was originally developed for use in high speed military aircraft and it has been utilised successfully

across industry [101]. This material has to be cured and then it can be ground and generally treated as a metal.

After the magnets and the Hylomar epoxy putty were positioned and ground, the processes of cylindrical grinding and CFRP tension filament winding (sleeve thickness is 0.35 mm) were undertaken to give the final assembly of the high speed rotor, which is shown in figure 5-6. The CFRP sleeve was cured at a temperature of 150 °C.

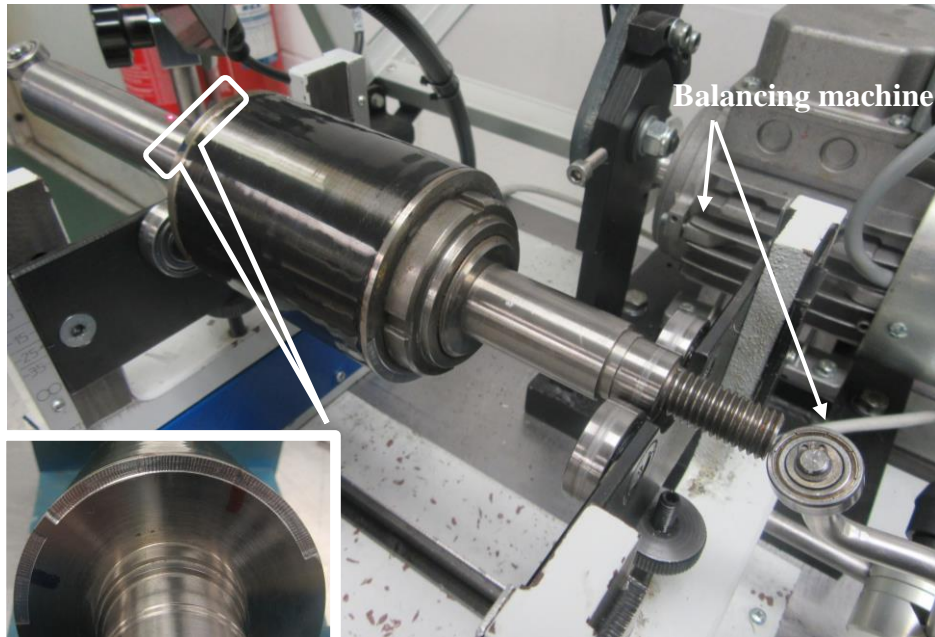


**Figure 5-5 Process of filling gaps between the rotor poles**



**Figure 5-6 HSHP final rotor assembly**

Figure 5-7 shows the high speed rotor on a balancing machine. The balancing of the rotor was achieved to enable a safe operation at 30,000 RPM, where the retained flanges have sufficient material to be removed when correcting for balance.

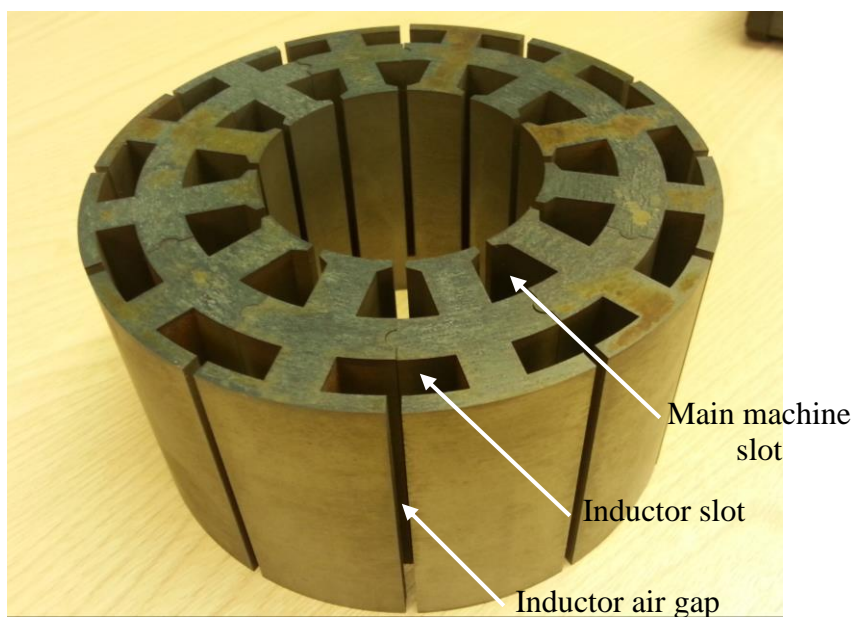


**Figure 5-7 Rotor on balancing machine**

## **5.2 Stator construction of the IDS machine**

### **5.2.1 Construction of the stator laminations**

The manufacturing of the stator lamination stack was contracted to the manufacturer of the specialist laminations. The 10JNEX-900 laminations were cut in a short 70 mm stack with a lamination thickness of 0.1 mm. Figure 5-8 shows the double slot stator core of the IDS machine without the copper windings.

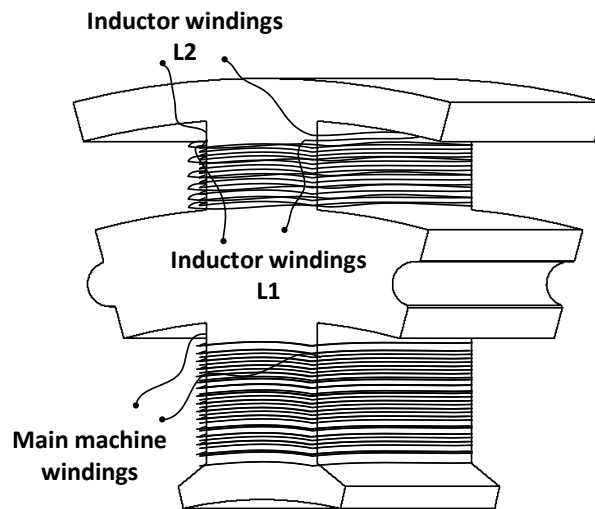


**Figure 5-8 pre-assembly of the double slot stator**

The initial assembly of the stator segments shown in figure 5-8 illustrates an early step of the assembly of the stator to ensure that all its segments fit each other with an acceptable tolerance between them before starting to wind the stator. As the copper slot areas for both of the main machine and filter inductor windings have been designed with a relatively high slot fill factor, the coils in each tooth have been compressed.

### 5.2.2 Direct On-Tooth compressed coils

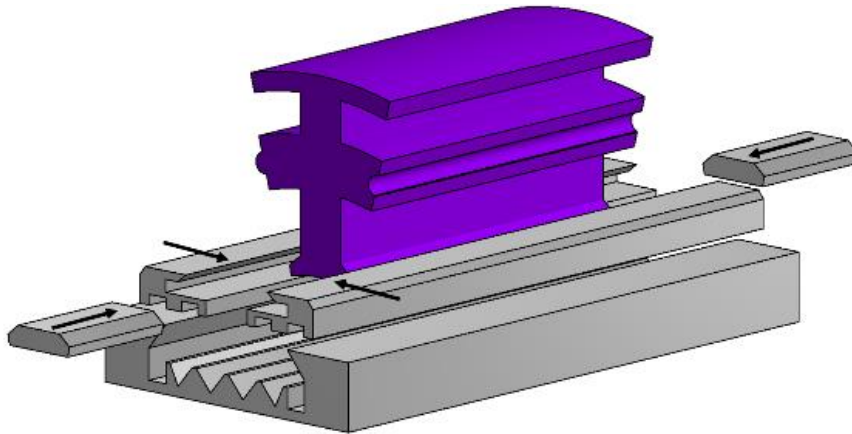
All the stator coils of the IDS machine have concentrated windings, which allows a segmental stator design. The main machine windings are located in the inner slot, with the two filter coils located in the second outer slot, as shown in figure 5-9.



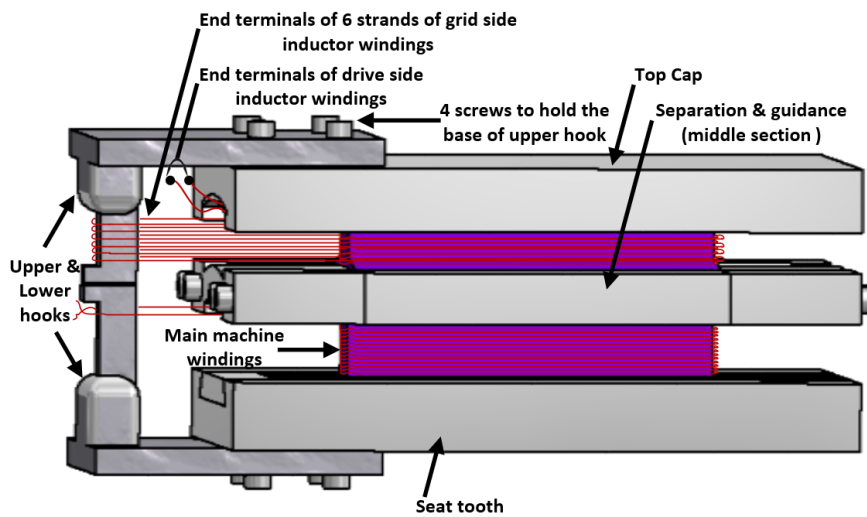
**Figure 5-9 Single tooth stator segment**

As discussed in the previous section, high fill factors are required to attain the power density required for this design example. In the literature, high fill factors have been achieved by pre-pressing coils into a solid form and then inserting them over the tooth structure [67, 102]. The double slot geometry of the IDS machine does not allow for a simple stator design which can utilise this manufacturing process. Moreover, thermal resistance between the coil and the stator, which is the main thermal path for copper losses, significantly increases as the gap between the coil and the stator material grows larger. Thus, a direct on-tooth coil compression has been utilised whereby the coils are directly wound onto a tooth segment, and then compressed onto the stator tooth to create a precise coil formation for each of the three coils. The pressing operation achieves a fill factor of up to 60%; this gives enhanced thermal conductivity between the copper windings and machine stator. The on-tooth pressing method is outlined in figure 5-10.





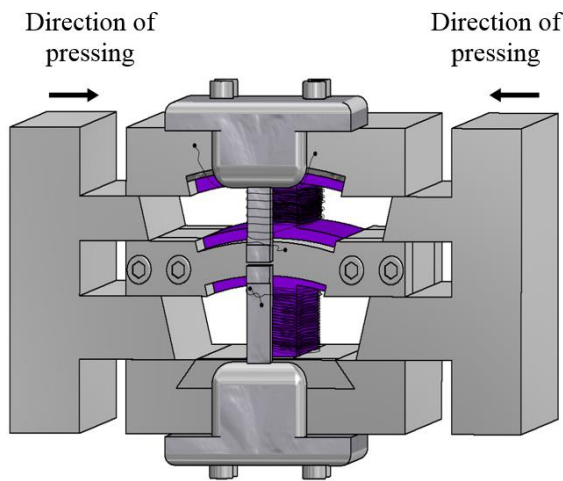
(a) The stator tooth segment is loaded into the winding jig seat



(b) The winding jig is fitted to the tooth segment and the coils wound. Locating hooks hold the wire in place once wound



(c) Coils are impregnated with a thermally activated bonding agent, Ultimag 2002L

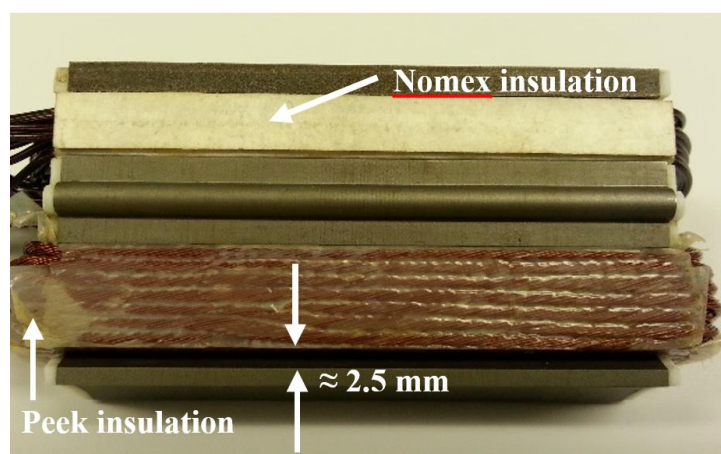


(d) The pressing punch is applied and coils are forced into a regular shape and annealed at 165°C. On-tooth pressing method and tooling

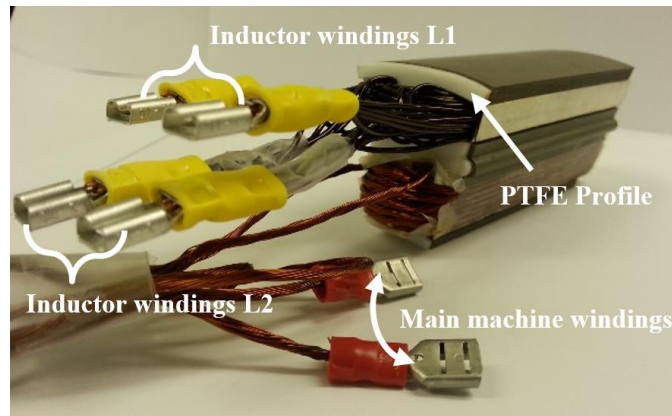
**Figure 5-10 The on-tooth pressing method**

The main machine and filter coils have been impregnated using epoxy resin (Ultimag2002L) [103]. This type of electrical insulation glue should be cured at temperature of 160°C for 4 hours. An added advantage of being able to precisely form the coils in a repeatable and controlled manner is that the coil shaping can be designed to minimize leakage and losses resulting from effects such as fringing at the slot opening. Figure 5-11 shows how precisely shaping the base of the coil helps to alleviate this.

The pressing tool has been designed to force the coil away from the slot opening, thus reducing the losses created from the slot opening fringing effect (figure 5-11). The assembled compressed coils for one double slot tooth segment are shown in figures 5-11 and 5-12.



**Figure 5-11 On-tooth pressed coils with a gap to reduce fringing**



**Figure 5-12 The full assembly of compressed coils of double slot tooth**

Finally, the full double slot stator has been assembled and is shown in figure 5-13 [104]. A temporary plastic motor housing was used to verify the ease of assembly as well as the total filter inductances achievable for both sides of the grid and drive filter inductors ( $L_1$  and  $L_2$ ), and all test results are presented in chapter 6. The temporary plastic housing is replaced with metal housing made from Aluminium in the final design.



**Figure 5-13 Fully assembled integrated double slot stator**

Figure 5-14 shows the achievement of volume reduction by integrating the 3-phase filter inductors ( $L_1 + L_2$ ), which is 87.6% compared to the total volume of the conventional discrete LCL filter inductors. The physical volumes of industrial inductors of LCL input filter were measured along with calculating the volume of the integrated inductors which shared the structure of the HSHP machine. Table 5-1 shows the volumes of discrete and integrated filter inductors and the achievable total volume reduction by the design of IDS machine.

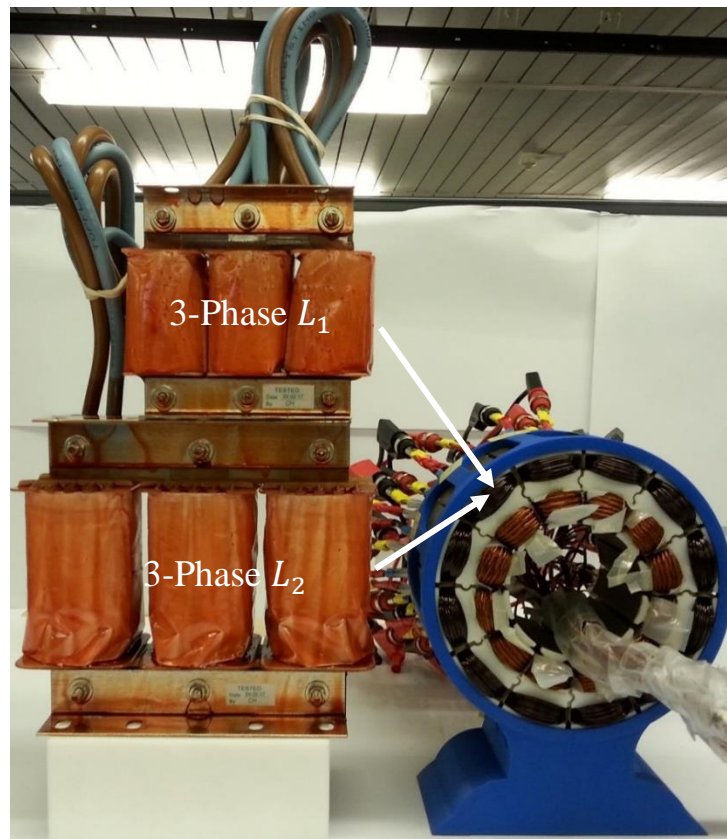
**Table 5-1 Volume comparison between the integrated and discrete 3-phase LCL filter inductors**

Integrated filter inductors ( $L_1$ and $L_2$ ) $\times 10^3 \text{ mm}^3$	Discrete 3-phase LCL filter $\times 10^3 \text{ mm}^3$		Total volume reduction (%)
	$3 \times L_1$	$3 \times L_2$	
424.374	990	2430	87.6

The primary reasons for the mass reduction are twofold:

- The filter inductances are now much better cooled and hence operate with a much greater current density.
- The motor and filter are now in a single package and share a common mechanical structure and cooling source.

Although the filter and motor now share parts of their magnetic circuit, there is little reduction in the magnetic volume as a direct result of this. The magnetic circuit has to be enlarged to accommodate both sources of flux at the same time. The industrial inductors of the input LCL filter ( $L_1$  and  $L_2$ ) shown in figure 5-14 were built based on the same voltage and current rating which has been considered for the integrated LCL filter inductors.



**Figure 5-14 A comparison in volume between the discrete and the integrated AC inductors of the LCL input filter**

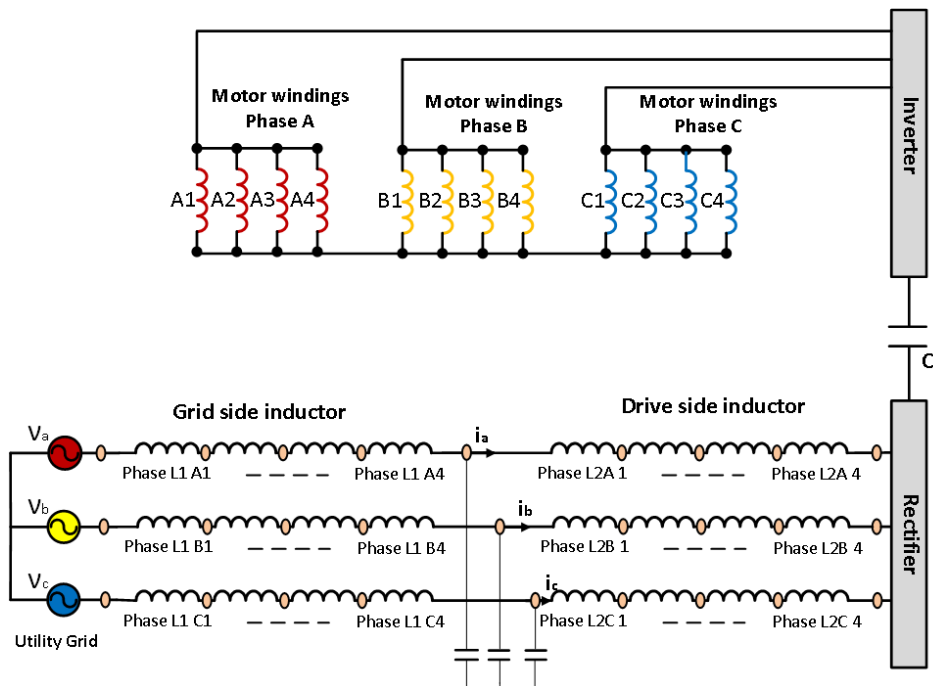


The machine stator presented in figure 5-14 is a part of fully packaged integrated motor drive, which is beyond the scope of this research including all of the other components of the drive such as the power electronics, DC-link capacitors, the shunt capacitors of the input filter, and control electronics. These aspects are described by other authors in different publications.

### 5.3 Interconnection power board for the IDS machine

According to the integrated inductors of the input LCL filter into the machine, each phase of the grid and drive side inductors ( $L_1$  and  $L_2$ ) is comprised of four coils, and therefore 24 coils are located in the 12 inductor slots, with a further 12 coils in the inner slots for the main machine windings. Therefore, 72 end terminals of windings need to be connected to the integrated active converter and the 3-phase power supply. In order to achieve high-power density with these crowded end terminal connections, it was necessary to find an acceptable method of connection for the IDS stator terminals.

Figure 5-15 illustrates the layout of the winding connection required for the LCL filter and the base machine windings for the IDS stator.



**Figure 5-15 Layout of windings in the IDS machine**

The diameter of the stator of the IDS machine is 140 mm, and all connections of the coils should be performed within the stators' periphery. The proposed method of interconnection of windings is accomplished using a four-layer busbar design. All connections of the LCL filter,

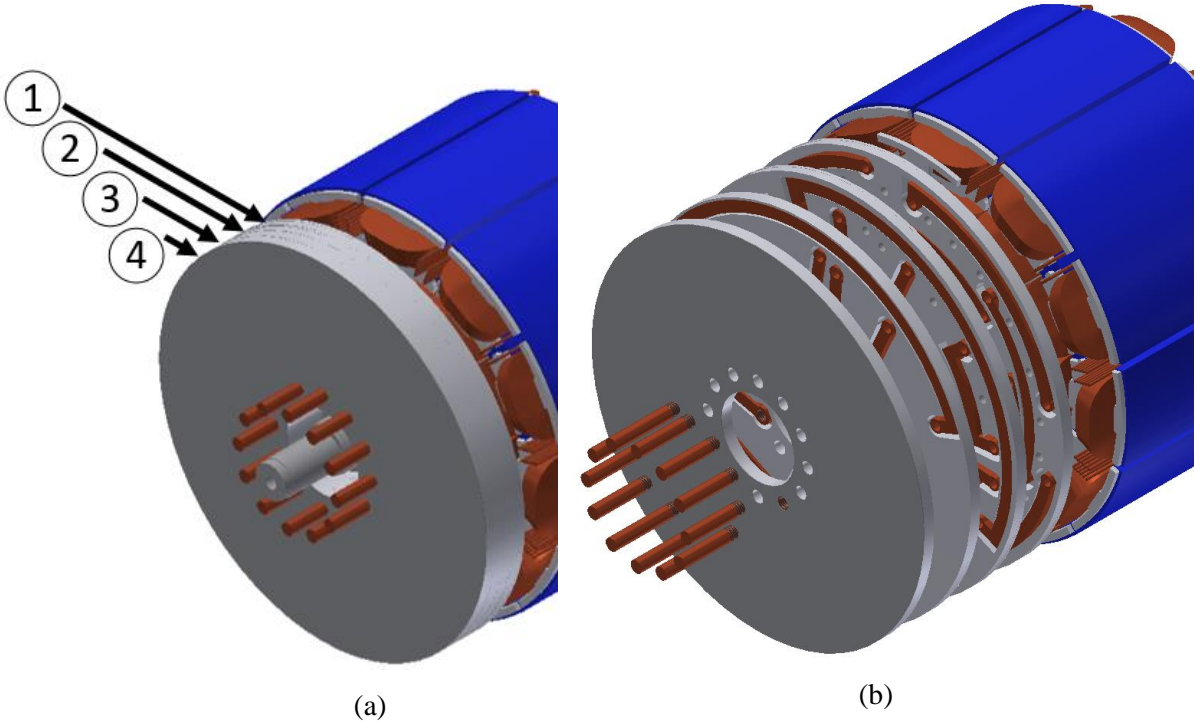
the 3-main input power supply and the main machine windings are included within the four-layer design.

Table 5-2 shows the parameters of the integrated power board design.

**Table 5-2 Parameters of four-layer design**

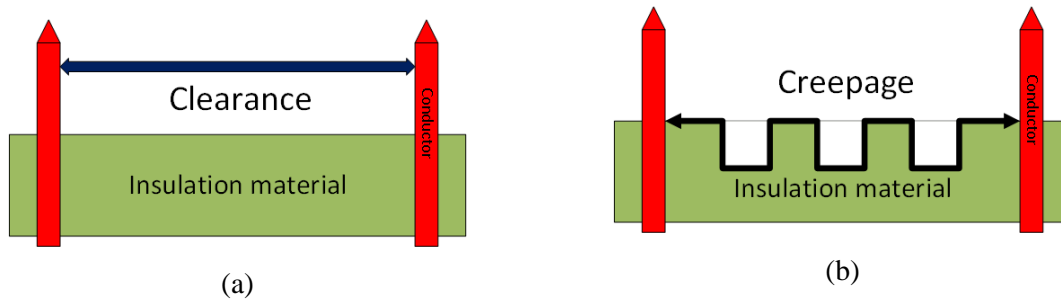
Double slot stator diameter (mm)	140
Rotor shaft diameter (mm)	20
PCBs outer diameter(mm)	136
PCB inner diameter(mm)	30
Current rating of inductors( $A_{rms}$ )	53
Current rating of main windings( $A_{rms}$ )	47.35
Current rating of the neutral point( $A_{rms}$ )	83

Figure 5-16 illustrates the four-layer busbar method which was designed using Autodesk Inventor software. Due to its ease of assembly, the outer diameter of the four-layer design is limited to 136 mm, which in turn allows the motor housing to be assembled easily.



**Figure 5-16 3D presentation of the four-layer busbar design: a) a complete assembly; b) the assembly of the four layers in order**

In order to design a power board, including high voltage copper busbars, the clearance and creepage distances between busbars was taken into consideration. The clearance is defined as the shortest line or path measured through the air between two conductive parts, as shown in figure 5-17 (a), or between a conductive part and the housing of the equipment. In figure 5-17 (b), the creepage is the shortest path measured along the surface of the insulation between two conductive parts or between a conductive part and bounding surface (housing) of the equipment.



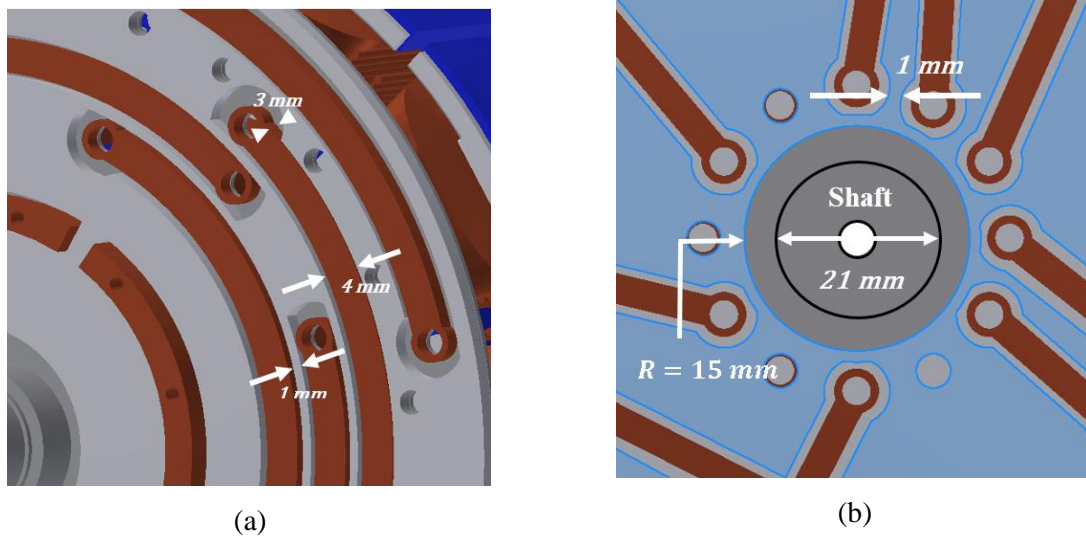
**Figure 5-17 Illustration of clearance and creepage: a) clearance (in air); b) creepage (along a surface)**

Spreading parts out to meet the required clearance and creepage distances is not a sensible solution in view of the packaging needs. A significant reduction in the distance required between high voltage nodes can be achieved by selecting an appropriate sheet barrier of insulating material between them.

The board material used is PTFE (Poly Tetra Fluoro Ethylene) which has very high dielectric strength up to 800 MV/m [105]. For the four-layer busbar design, the thickness of the chosen insulation barrier between the copper busbars is 1 mm. The PTFE dielectric strength for the chosen barrier thickness is 80 KV/mm, while the rated operating voltage is 750 V. The required creepage distance between copper busbars under the rated voltage is about 5 mm [106].

The power board design has different operating frequencies. The grid-side frequency is 50 Hz which gives a skin depth of 9.23 mm, as calculated from equation 3-9, while the operating frequency of the main machine is 1.666 kHz which gives a skin depth of 1.598 mm.

In order to alleviate the burden of high temperature within the four-layer busbar design, all copper busbars were designed radially with a width of 4 mm and a depth of 3 mm. The effect of clearance and creepage was avoided by fully embedding the copper busbars into the board to 3 mm, as shown in figure 5-18. This method enhances the functionality of the design in order to meet the needs of packaging.



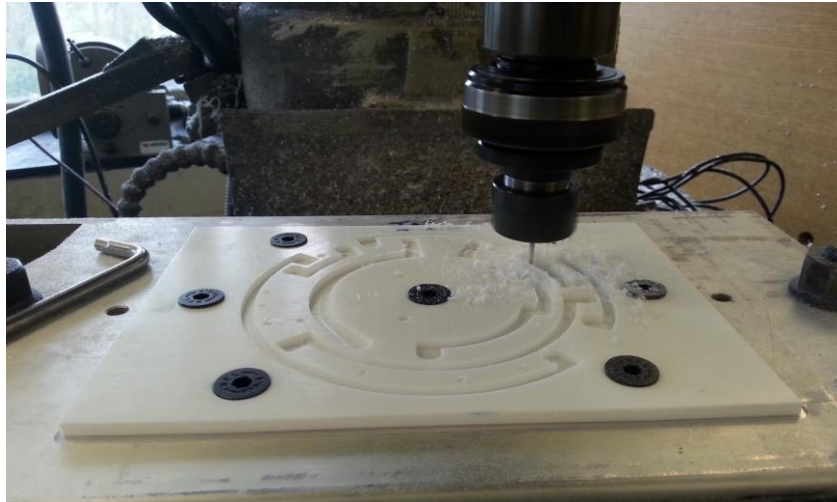
**Figure 5-18 Specifications of power board design: a) thickness of barrier and copper busbars; b) external connections from different layers**

The dimensions of the copper busbars selected for the design of the four-layer busbars are shown in table 5-3.

**Table 5-3 Parameters of four-layer busbar design**

	Radial thickness (mm)	Axial thickness (mm)	Diameter (mm)	Current Density $J(\text{A/mm}^2)$
Busbar of the inductors	4	3	---	4.42
Busbar of the main machine	4	3	---	3.95
Neutral busbar	4	6	---	3.42
Copper wire	---	---	4.5	2.98 – 3.3
Holes (inductor busbars)	---	---	3.3	---
Holes (Neutral busbar)	---	---	1.8	---
Holes (Main windings busbars)	---	---	1.8 - 4.6	---

The four-layer design was manufactured at Newcastle University. A plastic PTFE sheet has been used with a thickness of 4 mm. Figure 5-19 shows the milling CNC machine which was used to engrave the tracks for the copper busbars at a depth of 3 mm. A thickness of 1 mm was left at the back of each board to form an insulation sheet between the power boards.

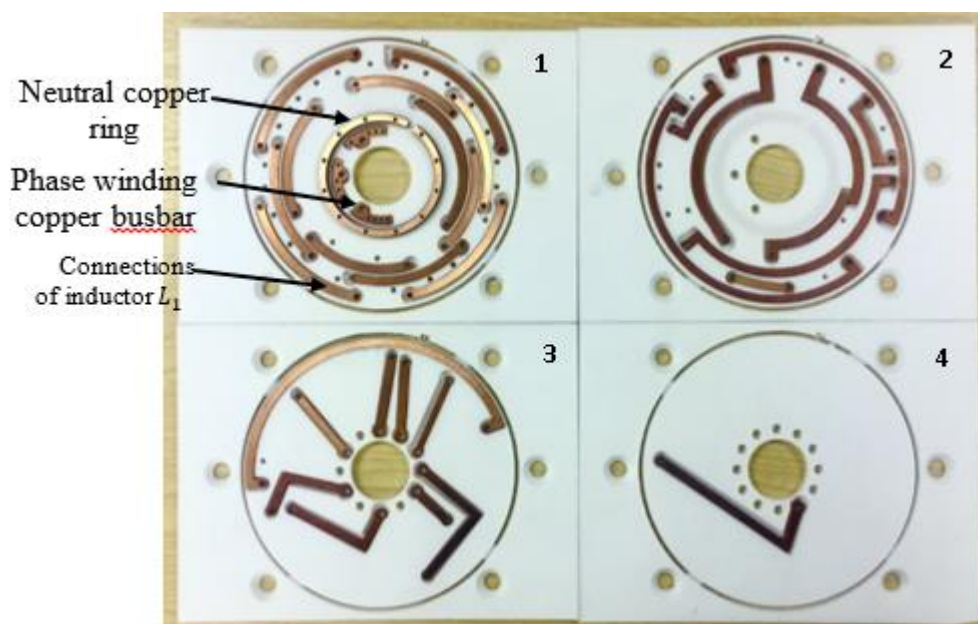


**Figure 5-19 Manufacturing process of power board design**

Figure 5-20 shows the four manufactured power boards, including the copper busbars of the main machine and filter inductors. The arrangement of end winding connections for the IDS machine within the four-layer design was chosen as follows:

- The first board consists of all connections of the main machine windings, the 3-phase filter inductors  $L_1$  and the external connections of the shunt filter capacitors.
- The second board is for the connections of the 3-phase filter inductors  $L_2$ .
- The third and fourth boards are for the external connections of  $L_1$  and  $L_2$ .

In order to start assembling the first power board, the end terminals of the main machine and filter inductors were bared to the right length along with the use of heat shrink insulation tubes to protect the wires in between the machine stator and the first power board, as shown in figure 5-21

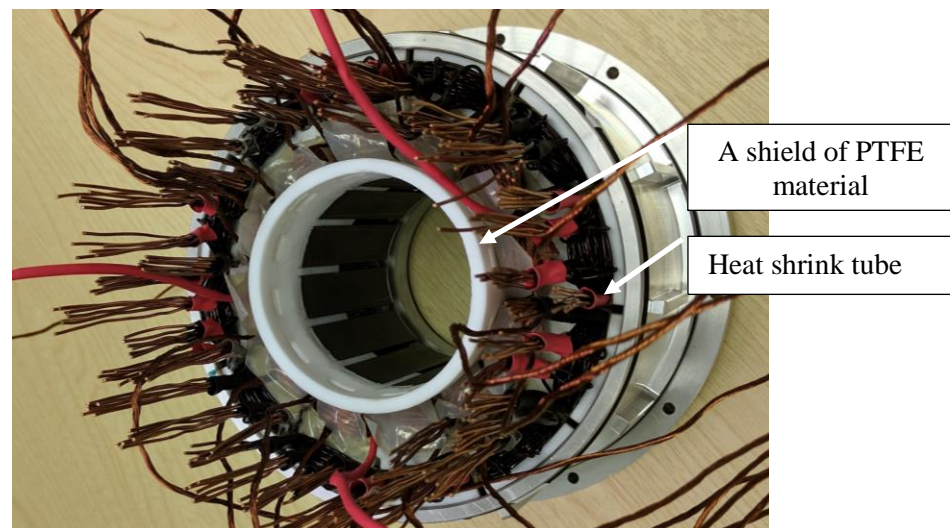


**Figure 5-20 Manufactured copper busbars and the PTFE boards**

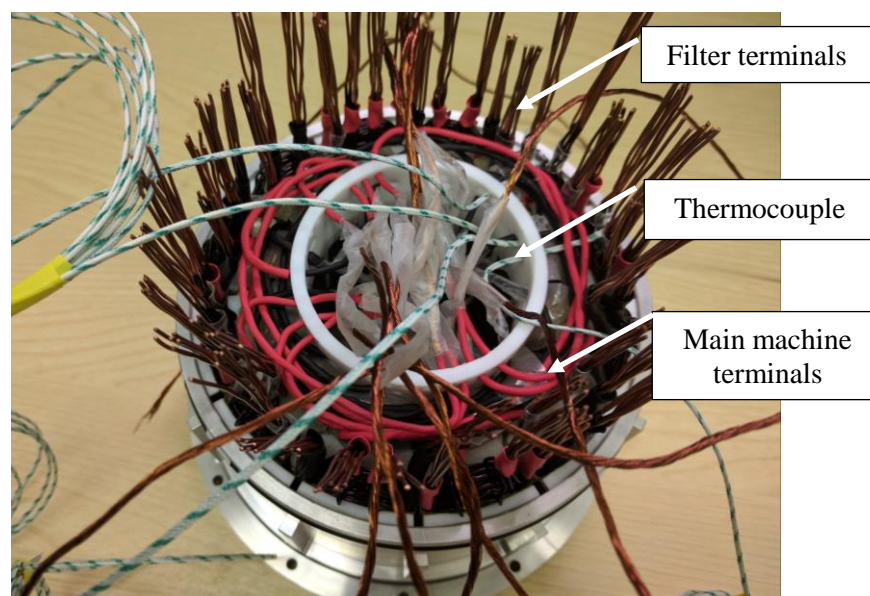


The temporary plastic housing which made earlier for the initial assembly of the machine stator is made from Aluminum for the final design shown in figure 5-21. Due to the flexibility of movement of the machine end terminals (Litz wire) and the likelihood of the risk of contact with the machine shaft, a perforated PTFE ring was fitted to the bottom of the stator to form a shield surrounding the rotor shaft and hence to stop any of the copper wires from having access to touch the shaft.

Figure 5-22 illustrates the management of the end terminals of the main machine windings. An adhesive material (Araldite-instant type) has been used to attach the four thermocouples to the end windings of the IDS stator in order to measure the temperature of the main machine and filter inductor windings.



**Figure 5-21 Arrangement of end terminal**

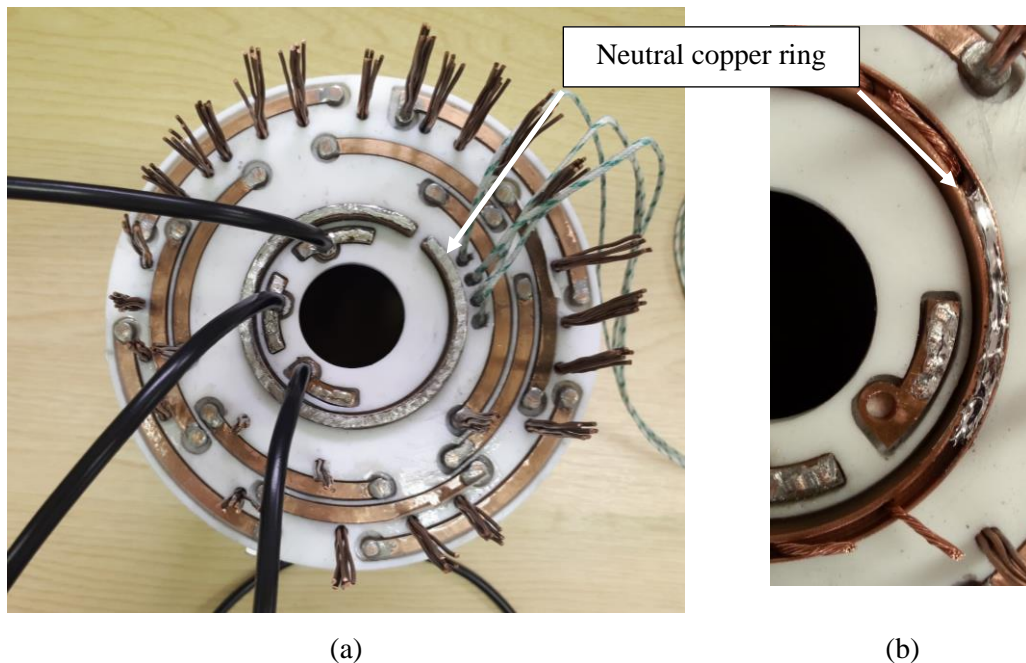


**Figure 5-22 Management of the end terminals of the main machine windings**

The assembly processes of the four-layer design have been carried out as follows:

1. As shown in figure 5-23, the end terminals of the 3-phase machine windings have been soldered to the three small busbars and extended using three flexible copper wires to be connected to the main power supply (the utility grid). The joint points of the copper busbars were first abraded. There are 12 end terminals of Litz wire connected to the ring copper busbar (the star point connections). In order to work at low current density so as to avoid excessive temperature within the board, the thickness of the neutral copper ring was extended to be part of the design of board 2, with dimensions of 4 mm (radially)  $\times$  6 mm (axially).

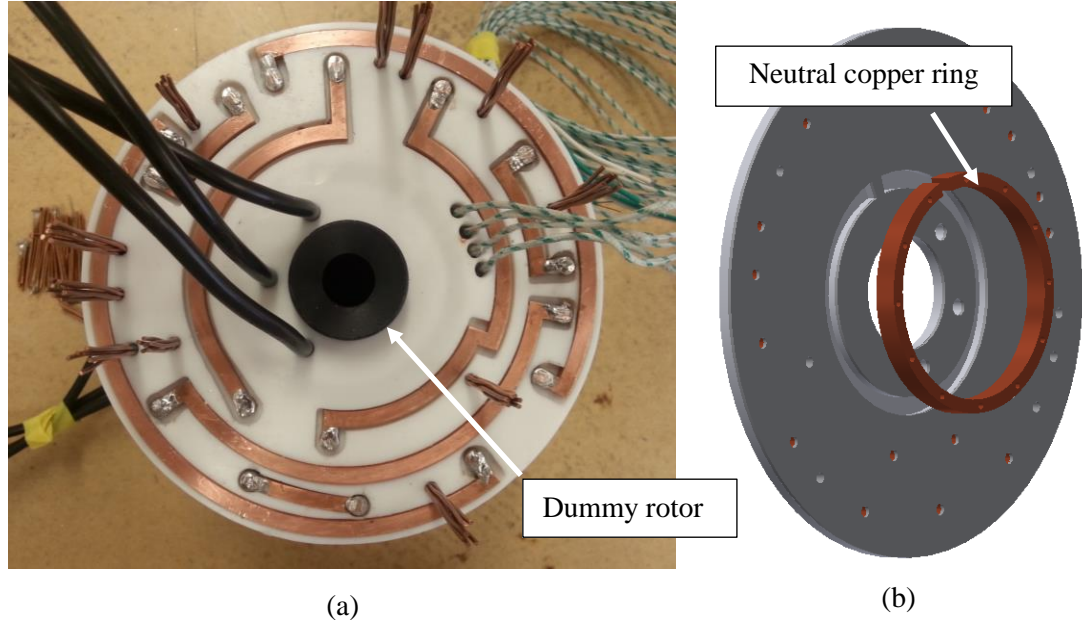
The copper ring was designed with a groove depth of 2.8 mm, as shown in figure 5-23 (b), where the end terminals were soldered inside the copper ring instead of having bulky soldered points on the top of the ring. The second board can, therefore, be placed very close to the first board, enhancing integration of the power board.



**Figure 5-23 Board 1: a) front view; b) the neutral ring copper with groove and the process of filling with solder**

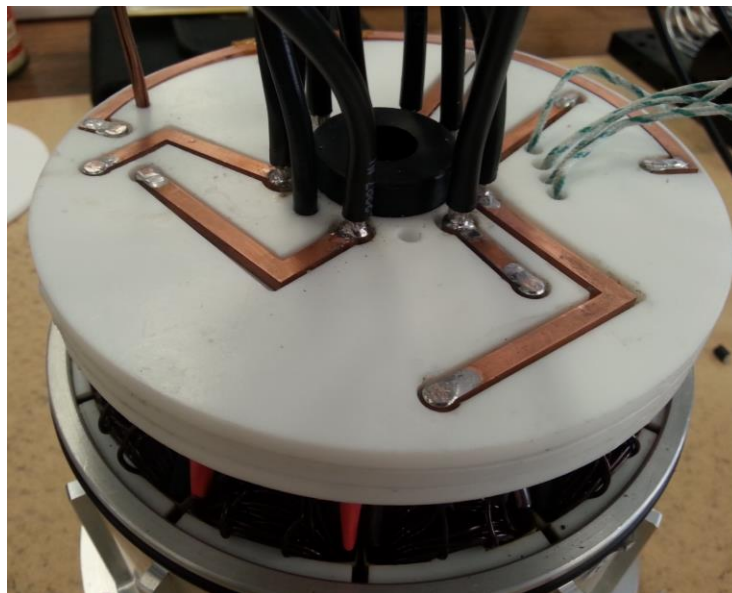
It can be noted in figure 5-23 (a) that the copper busbars were polished and then painted with insulation varnish to enhance the dielectric strength between these busbars. A dummy rotor was made from a plastic material and fitted into the machine, as shown in figure 5-24 (a), to ensure that the four boards were concentric with the machine shaft centre.

2. Figure 5-24 (a) shows the assembly of the second power board, where all copper busbars of the 3-phase drive-side inductors,  $L_2$ , have been soldered. The axial second half of the neutral copper ring was embedded in the back of the second board, as shown in figure 5-24 (b).



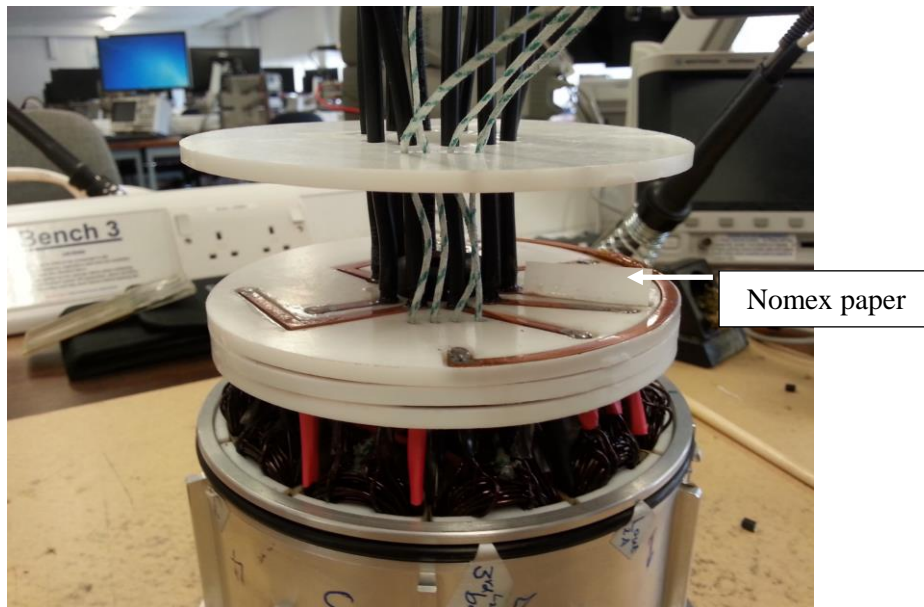
**Figure 5-24 Board 2: a) soldered busbars of  $L_2$ ; b) 3D inventor model (the back side of the second board showing the assembly of the neutral copper ring)**

3. The third and fourth boards are shown in figures 5-25 and 6-26 respectively, consisting of the external busbar connections, including the 3-phase grid power supply, the grid-side filter inductors ( $L_1$ ), the drive-side filter inductors ( $L_2$ ), and the 3 knee connections of the shunt capacitors. Due to the restrictions of space available in the third board, one of the external wire connections had to be placed in board 4.



**Figure 5-25 Board 3: assembly of busbars and external connections of the LCL filter inductors**

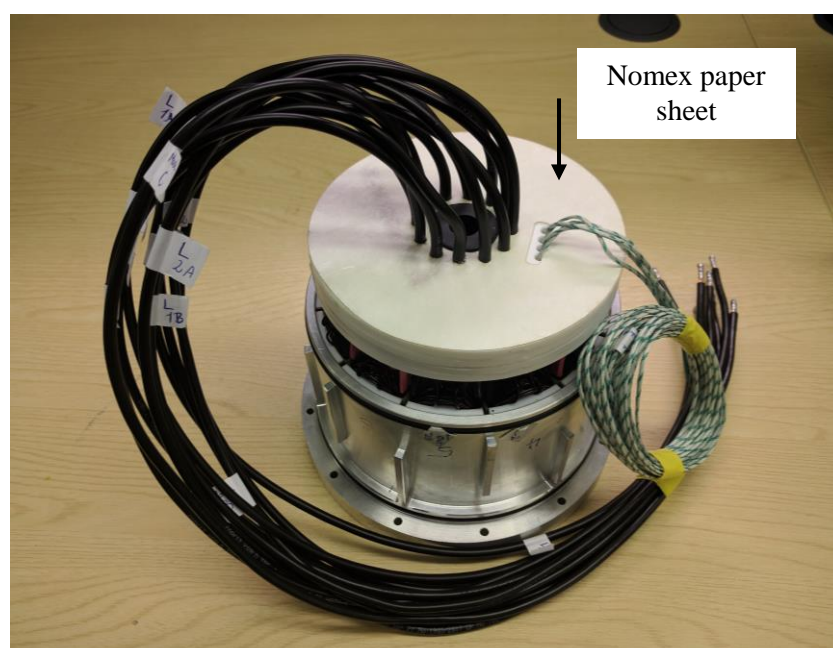




**Figure 5-26 Board 4: process of assembly with a single busbar in the last board**

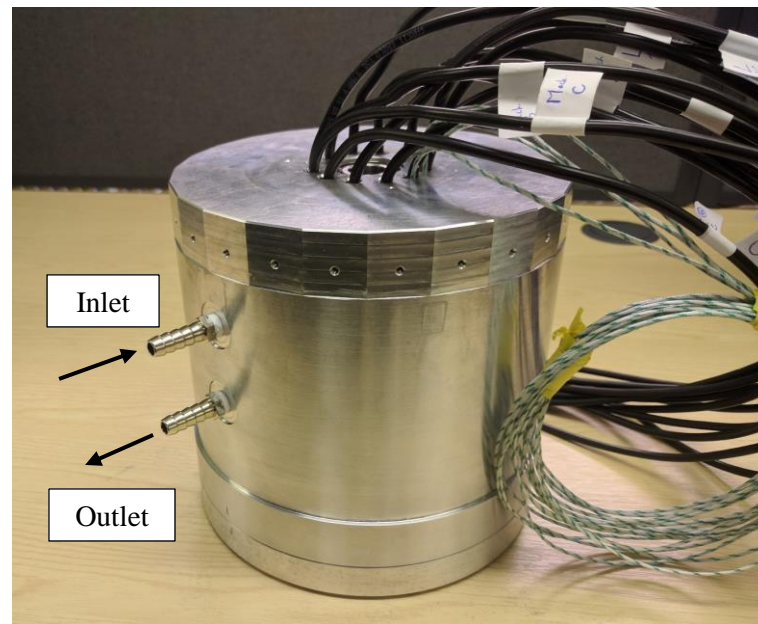
An extra precaution was taken in order to ensure that all busbars are insulated from each other, and therefore small pieces of Nomex paper were inserted as extra insulating support between some of the copper busbars, as shown in figure 5-26.

Figure 5-27 shows the complete assembly of the four-layer design associated with the external copper wires. The fourth board was fully insulated from the machine housing using a Nomex insulation sheet with a thickness of 0.25 mm. The total achievable axial thickness of the four-layer design is 16.25 mm, which meets the needs of the compact system.



**Figure 5-27 The final assembly of the four-layer design associated with external connections**

The complete assembly of the machine housing is shown in figure 5-28, including the inlet and outlet of the cooling water system.

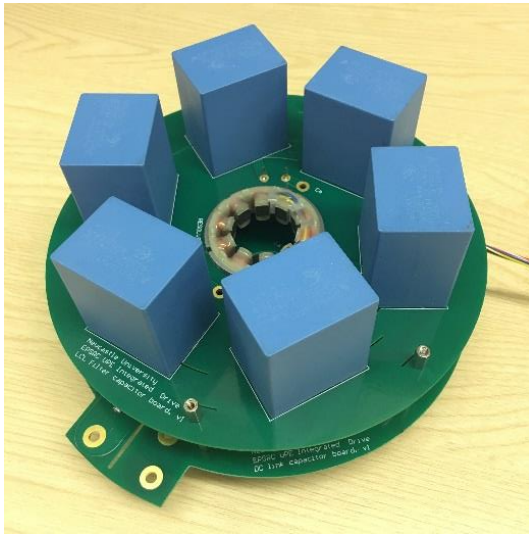


**Figure 5-28 The final assembly of the machine housing**

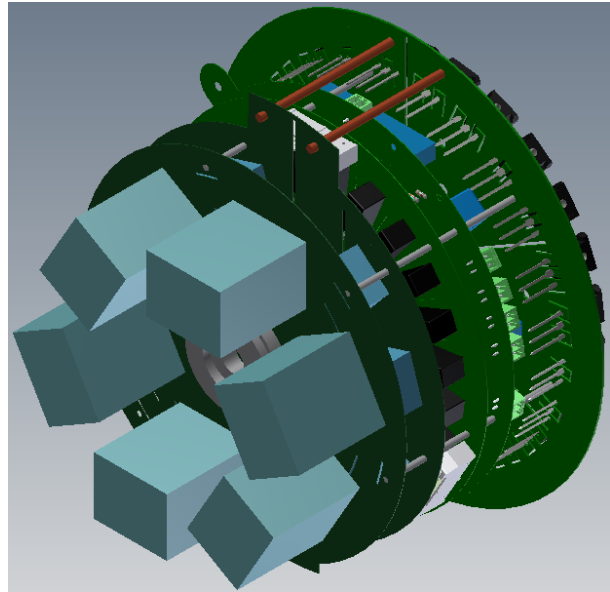
#### **5.4 Manufacturing of shunt capacitors of the LCL filter**

Figure 5-29 (a) shows the arrangement of the 3-phase shunt capacitors of the LCL filter. A film capacitor type was chosen for the design. Due to the lack of standardisation of such capacitors, each phase capacitor was split onto two capacitors which are connected in parallel to give  $22 \mu F$  per phase.

The complete design of the integrated motor drive is shown in figure 5-29 (b). The integrated drive part has been designed and assembled by research staff at Newcastle University. The shunt capacitors of the LCL filter are mounted axially with the machine and the drive.



(a)



(b)

**Figure 5-29 Capacitors and full design: a) 3-phase shunt capacitors of the LCL filter; b) the complete design of the integrated high power drive**

### 5.5 Test stand assembly

The 100kW Dynamometer test rig has an AC load machine coupled to the integrated motor drive via a metal bellow coupling and an extension shaft. The main test rig machine is capable of spinning at up to 30,000 RPM.

The integrated high-speed high-power machine was mounted on to an endplate and it was back-driven by the AC load machine, as shown in figure 5-30. The base speed of the integrated motor drive is 25,000 RPM and the rated shaft power is 34 kW.

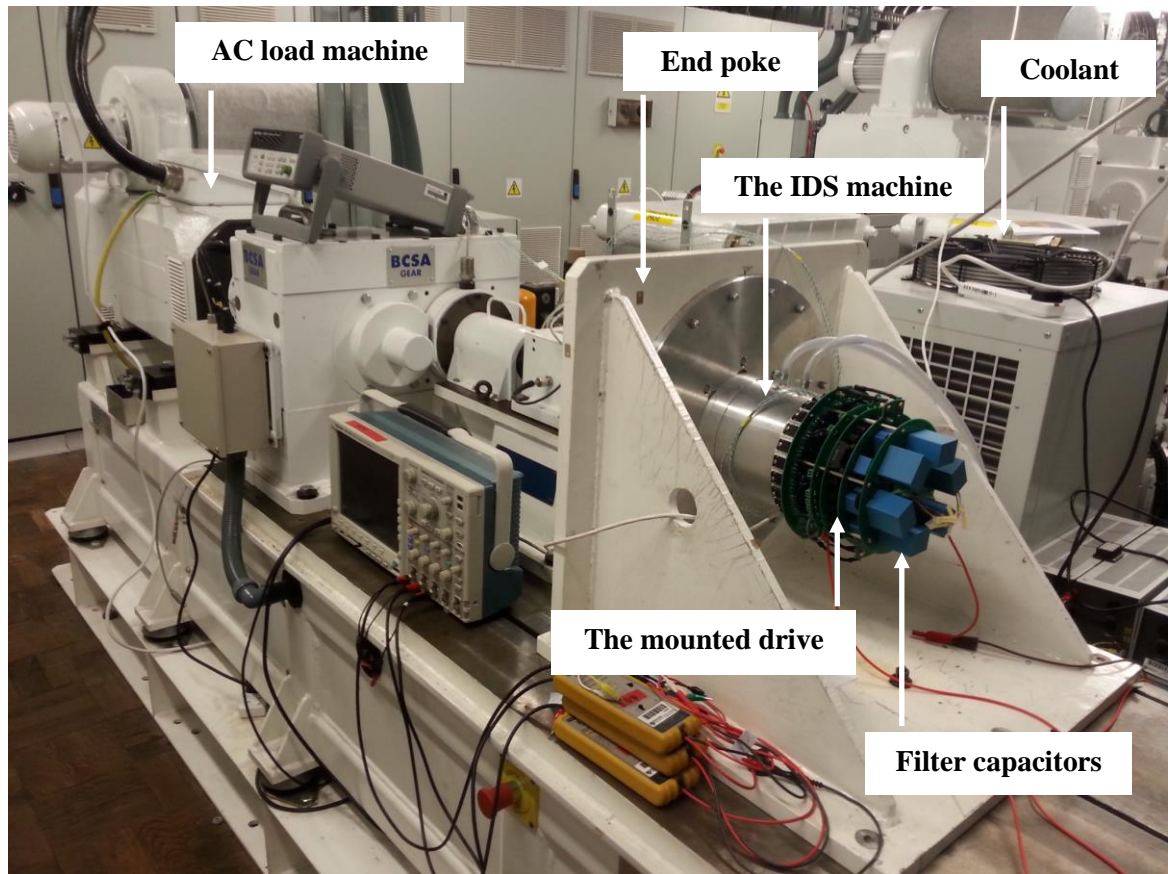


Figure 5-30 High speed no-load test rig

# CHAPTER 6

## Test Results and Evaluation

---

This chapter discusses the results of the testing of the IDS machine, including the LCL filter inductors and the basic HSHP machine. As the IDS machine has been fully assembled, the testing was carried out as follows:

### 1. LCL filter measurements

- The inductance of the grid and drive-side inductors ( $L_1$  and  $L_2$ ).
- The 3-phase current waveforms of the grid and drive-side inductors and the THD achieved.
- Mutual coupling between the integrated filter inductors in the machine.

### 2. HSHP base machine

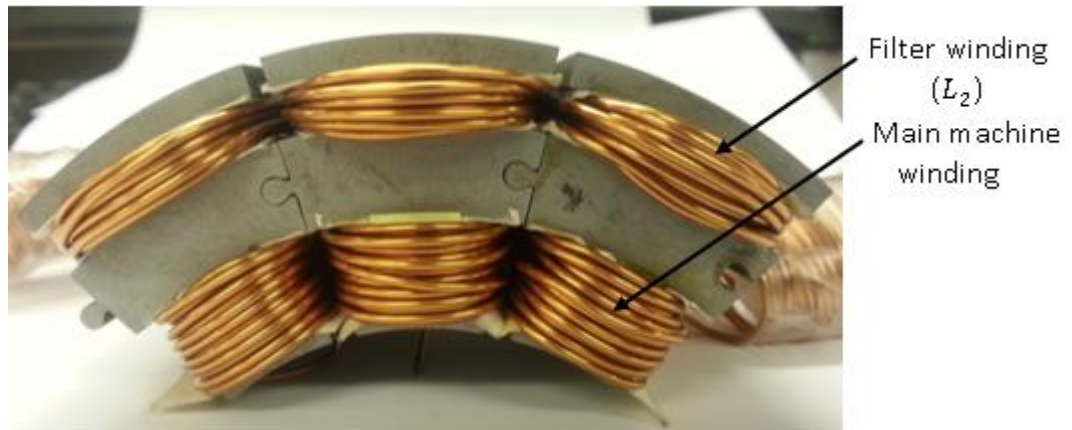
- Back-EMF measurement
- Coil testing (including groundwall insulation and inter-turn)
- Influence of impregnation on the lifetime of the machine coils

## 6.1 Measurements of the integrated LCL filter

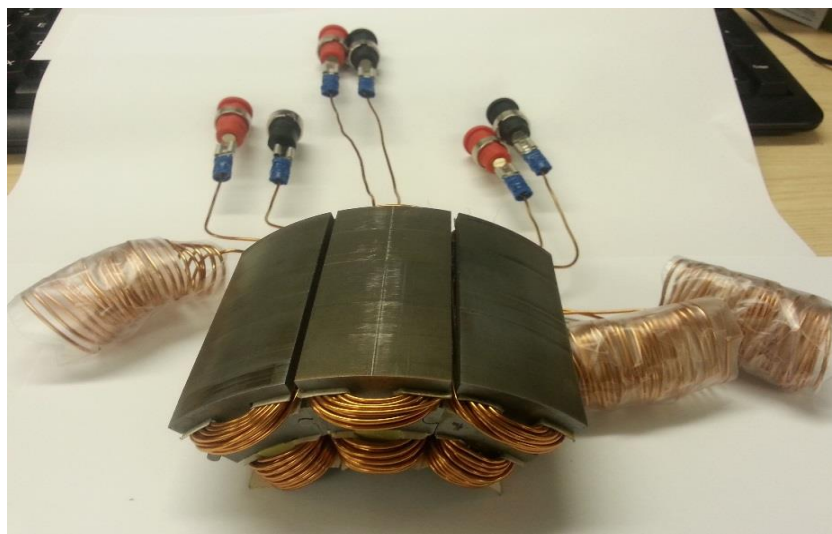
### 6.1.1 Initial experimental results

A three-tooth motorette, as shown in figures 6-1 and 6-2 has been constructed to assess the performance of the outer slot concept for integrated filter inductors.





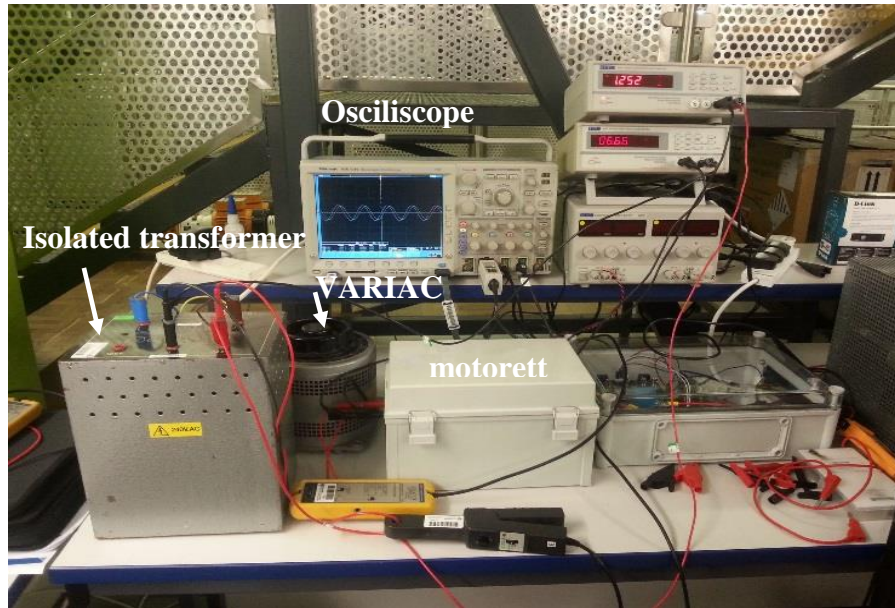
**Figure 6-1 Three-tooth motorette used to test single-tooth inductor coil inductance**



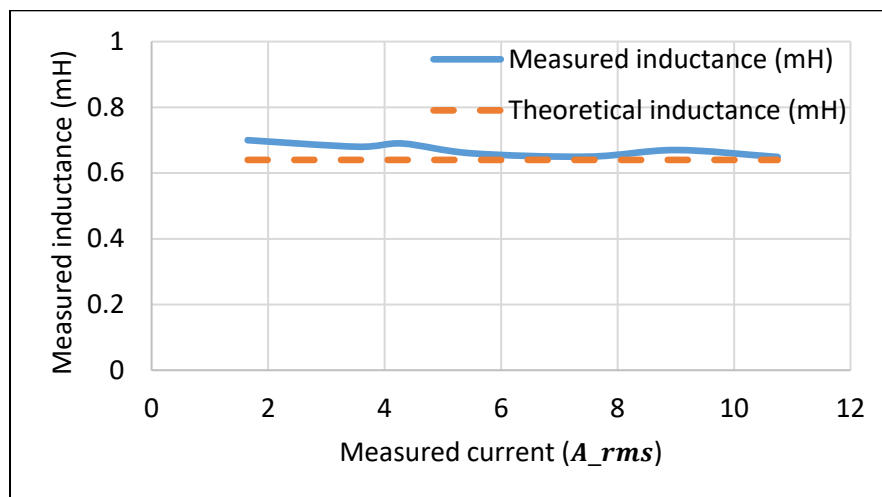
**Figure 6-2 Three tooth motorette with test leads**

Figure 6-3 shows the test rig set up where the motorette is connected to the utility grid via VARIAC and an isolating transformer. In order to test the constructed motorette shown in figure 6-2, the inductance of a single tooth was calculated by passing a 50Hz current through the inductor windings and observing the coil voltage. The design requires a per-phase inductance of 0.16 mH. Each phase is formed from four parallel connected coils, and thus the total inductance for a single tooth should be 0.64 mH.

Figure 6-4 shows the theoretical and experimental results for the constructed motorette (figure 6-2). The measured results show that the inductance of the single tooth motorette at the maximum applied current is 0.65 mH while the predicted inductance value is 0.64 mH. Experimental procedures are explained in the Appendix.

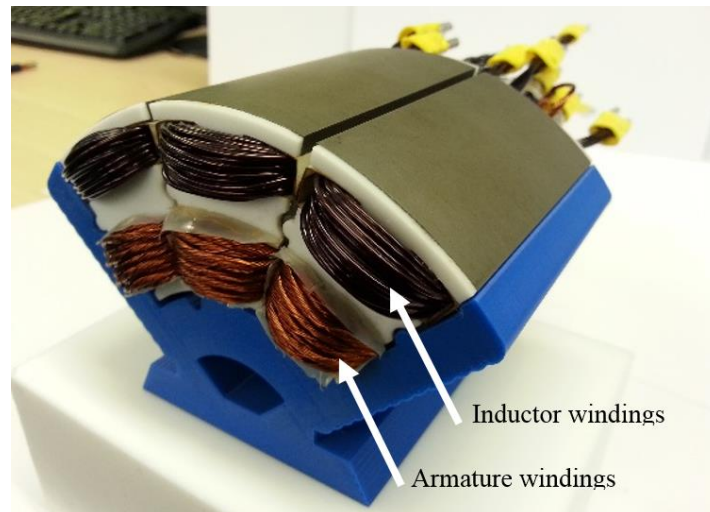


**Figure 6-3 Set up of the test rig**

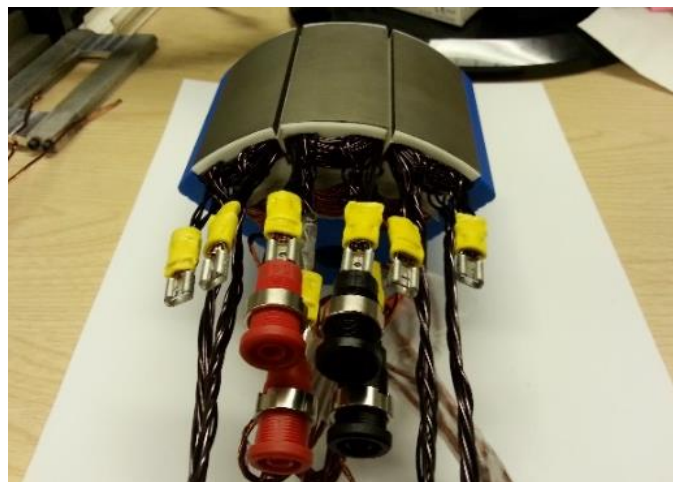


**Figure 6-4 Single tooth inductance measurements of motorett**

Another one-quarter machine motorett as shown in figures (6-5 and 6-6) was constructed including both the LCL filter inductors ( $L_1$  and  $L_2$ ) sharing the same slots to assess the effectiveness of the integrated inductors of the LCL filter ( $L_1$  and  $L_2$ ). Various magnitudes of 50 Hz current were applied to the filter inductors to compare the measured inductances with the FEA simulation results.



**Figure 6-5 Three-tooth fully assembled IDS machine motorette**



**Figure 6-6 Three-tooth motorette with test leads**

The values of inductances for both filter inductors  $L_1$  and  $L_2$  were measured for the middle tooth (experimental procedures are as same as those conducted for prthe evious motorette, figure 6-3) and compared with results obtained from FEA simulation as shown in table 6-1.

**Table 6-1 Simulated and measured inductances for the IDS machine filter windings in the stator motorette**

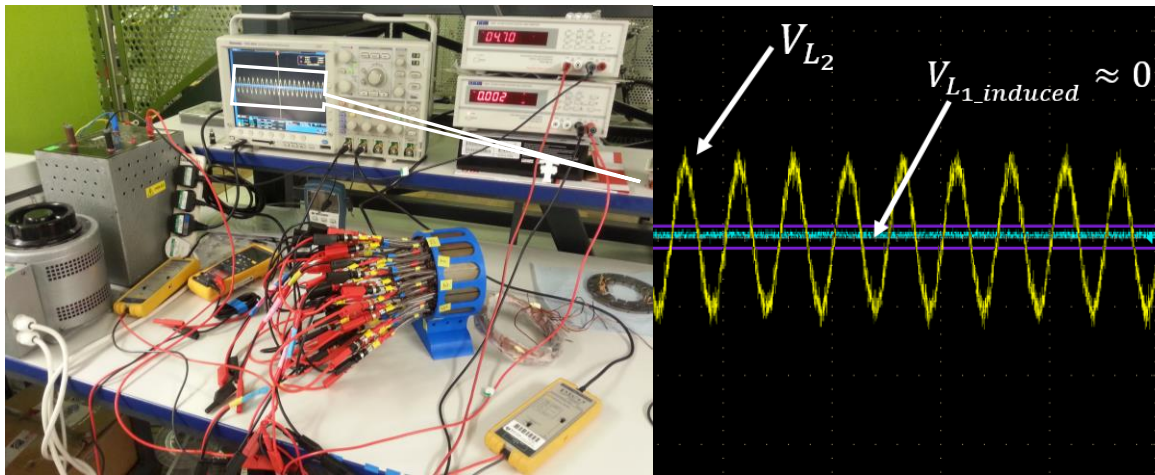
Grid input current ( $A_{rms}$ )	FEA results Inductances of LCL filter ( $\mu H$ )		Measured results Inductances of LCL filter ( $\mu H$ )	
	$L_1$	$L_2$	$L_1$	$L_2$
1.5	1.03	42	0.99	34
2.5	1.03	42	0.99	35
3.5	1.03	42	0.99	36
4.5	1.03	42	0.99	36



It can be seen that the measured inductances for the drive side inductors  $L_2$  are smaller than the FE results by approximately 14% while the measured grid-side inductance  $L_1$  is very close to that achieved by FE simulation. It is noticeable that the deviation of measurement of drive side inductances is large, this might be caused by a non-perfect connection for all end terminals of copper wires of  $L_2$  with clips used. However, these measurements for filter inductors have been obtained at a very low current compared to the full rated current which is  $53 A_{rms}$ . Equally, the motorette is mounted in a 3D-printed housing so the poorer tolerances may account for the difference.

### 6.1.2 Mutual coupling between filter inductors ( $L_1$ and $L_2$ )

The initial assembly of the IDS stator shown in figure 6-7 has been examined to discover the cross-coupling between the integrated filter inductors  $L_1$  and  $L_2$  in the machine stator. As shown in figure 6-7, the phase inductor winding  $L_2$  was energised with a 50Hz current of  $4.7 A_{rms}$  in which the grid-side inductor winding  $L_1$  is an open circuit.



**Figure 6-7 Initial examinations of mutual coupling between the integrated filter inductors**

It can be seen in figure 6-7 that any coupling which exists cannot be discerned above the system noise. This gives confidence that any coupling between the assembled integrated filter inductors  $L_1$  and  $L_2$  is extremely low. The addition of the rotor to the assembly would not be expected to influence this in any way.

Further testing has been conducted with the constructed integrated drive package in order to confirm again that the likelihood that grid- and drive-side inductors are magnetically independent of each other. Figure 6-8 shows that the drive-side inductor,  $L_2$ , for one phase is energised with a peak current up to approximately 21A, and the induced voltage in a phase of

the grid-side inductor,  $L_1$ , has a non-measurable value. This gives confidence that any coupling between the assembled integrated filter inductors  $L_1$  and  $L_2$  is extremely low along with the presence of rotor magnetic flux and verifies that 16 pole ( $L_1$ ) and 10 pole ( $L_2$ ) combination are decoupled.

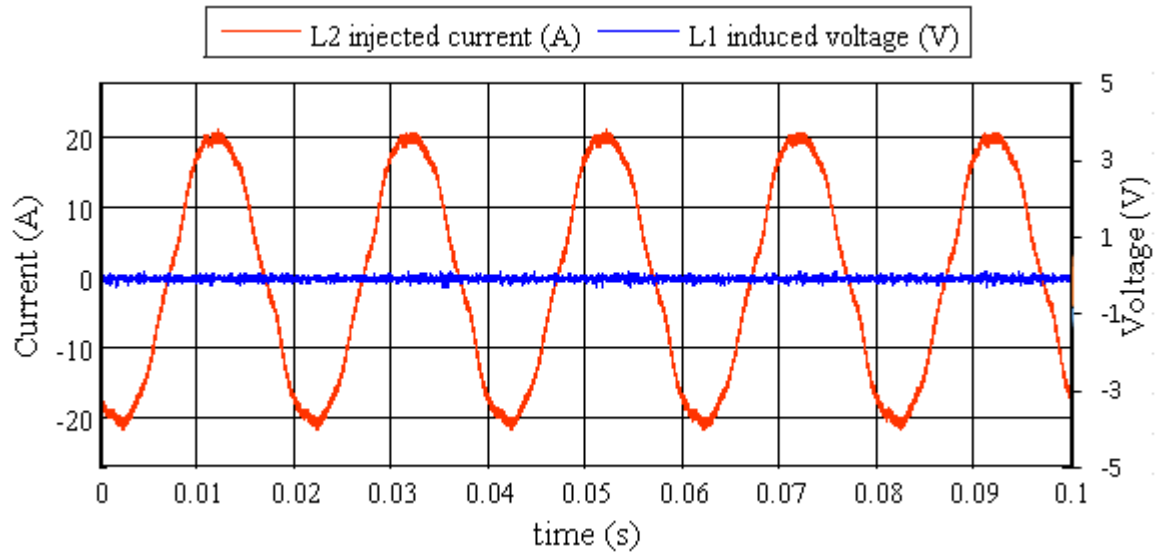


Figure 6-8 Final examination of cross-coupling between the integrated filter inductors

### 6.1.3 Measurements of filter inductance ( $L_1$ and $L_2$ )

The assembly of the double slot stator with the four-layer busbar boards has been carried out (see Chapter 5, section 5.3), the phase inductances of the grid and drive-side were measured using an LCR bridge instrument, as shown in figure 6-9. The measurement setup for phase A of the LCL filter inductors is shown in figure 6-9.



Figure 6-9 Measurement of filter inductance per phase: a) drive-side; b) grid-side

Table 6-2 shows the measured inductance and resistance values of the six integrated inductors of the LCL filter.

**Table 6-2 Measurements of inductance and resistance for the six LCL filter inductors**

Grid-side coils	Measured resistance ( $m\Omega$ )	Measured inductance ( $\mu H$ )	Drive-side coils	Measured resistance ( $m\Omega$ )	Measured inductance ( $\mu H$ )
Phase A	8.3	5.06	Phase A	29.76	182.6
Phase B	8.66	5.3	Phase B	29.1	180
Phase C	8.4	5.2	Phase C	29.7	184

The average measured inductance of the grid-side inductor,  $L_1$ , is approximately  $5.18 \mu H$  while the predicted value is  $5 \mu H$ . The average measured resistance per phase is  $8.45 m\Omega$  which is about 60% greater than the analytical predicted value. This discrepancy might be attributed to the length of the external connection, since the exact lengths of the wires had not yet been determined at the time of the measurement. In addition, the resistance of the copper busbars and solder connections included in the four-layer power boards will contribute to the measured resistance in which the number of turns per phase is just 4 turns and the length of external wire connections is about 1 meter. This extra length of the external wire connections will be cut and it is unlikely to affect the performance of the filter inductors.

The average drive-side inductance is measured as  $182.2 \mu H$  while the predicted value from FE simulation is  $196.4 \mu H$ . The measured phase resistance of the drive-side inductor,  $L_2$ , is  $29.52 m\Omega$  which is 48.82% greater than the predicted analytical resistance value. As there is only one turn on the  $L_1$  coil the proportion of the resistance attributed to the flying leads will be higher hence the greater percentage underestimation in the resistance of the grid-side coil.

#### **6.1.4 The measurement of the 3-phase current waveforms of the grid- and drive-side inductors**

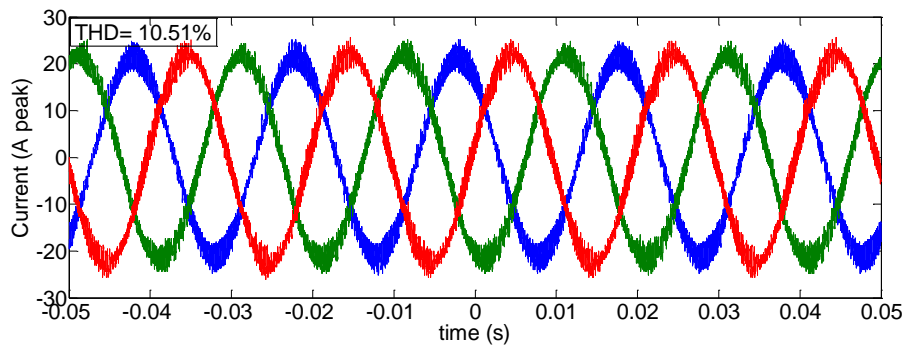
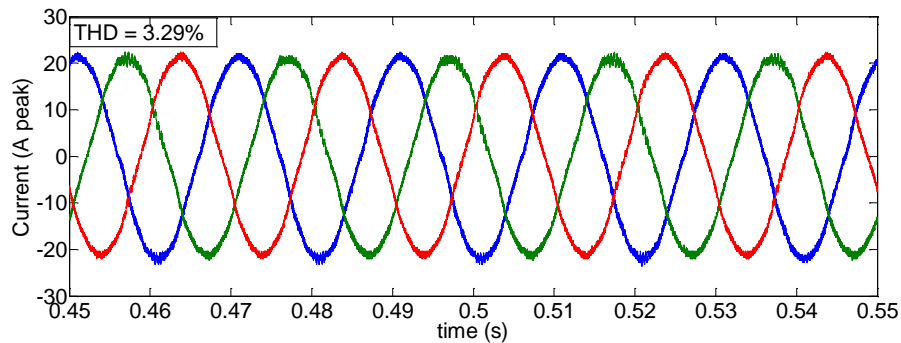
The integrated motor drive was assembled, including its power electronics, controller and cooling circuit. The drive was mounted on to a dyno test rig as shown in Chapter 5, figure 5-28. The specifications of the dyno rig are given in table 6-3.

**Table 6-3 Specifications of the dyno test rig**

<b>Name</b>	Electric motor / Drive test rig
<b>Machine type</b>	3-phase induction motor
<b>Supplier</b>	Torquimeters / Germany
<b>Rated speed</b>	30,000 RPM
<b>Rated power</b>	100 kW
<b><math>\cos \varphi</math></b>	0.86
<b>Approximate weight</b>	2500 kg

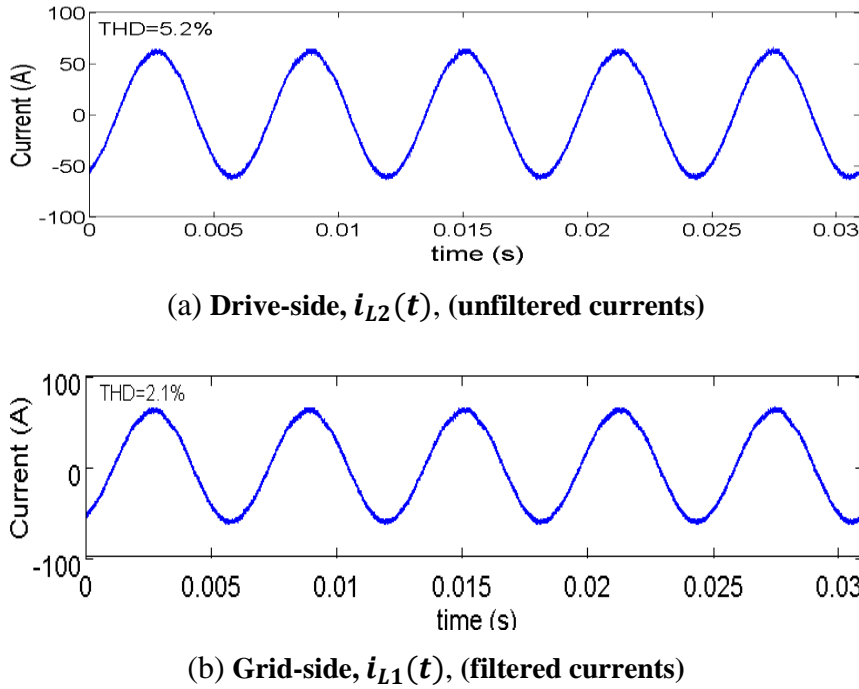
The dyno machine was driven to rotate the integrated drive at a shaft speed of 3000RPM. The drive was operated in the fourth quadrant providing a braking torque of 4Nm to the dyno. The simulation results shown in section 2.6.3 predict a resulting THD of less than 5% of the grid current.

Figure 6-10 illustrates the 3-phase unfiltered,  $i_{L2}(t)$ , and filtered current,  $i_{L1}(t)$ , waveforms of the integrated input filter inductors at a shaft speed of 3000 and a machine torque of 4 Nm.

(a) Unfiltered drive-side currents  $i_{L2}(t)$ (b) Filtered grid-side currents  $i_{L1}(t)$ **Figure 6-10 3-phase currents of the integrated LCL input filter at 3000 RPM**

As shown in figure 6-10, the THD achieved on the grid-side is 3.29% which is still lower than the recommended limit of harmonics [9, 44], while it is 17.5% greater than the predicted simulated value. This additional THD may result from control factors in the power electronic drive which were not included in the simulation such as dead time.

As shown in figure 6-11, further test measurements have been carried out in order to measure the LCL filter currents  $i_{L2}(t)$  and  $i_{L1}(t)$  at a shaft speed 15000 RPM producing the rated torque.

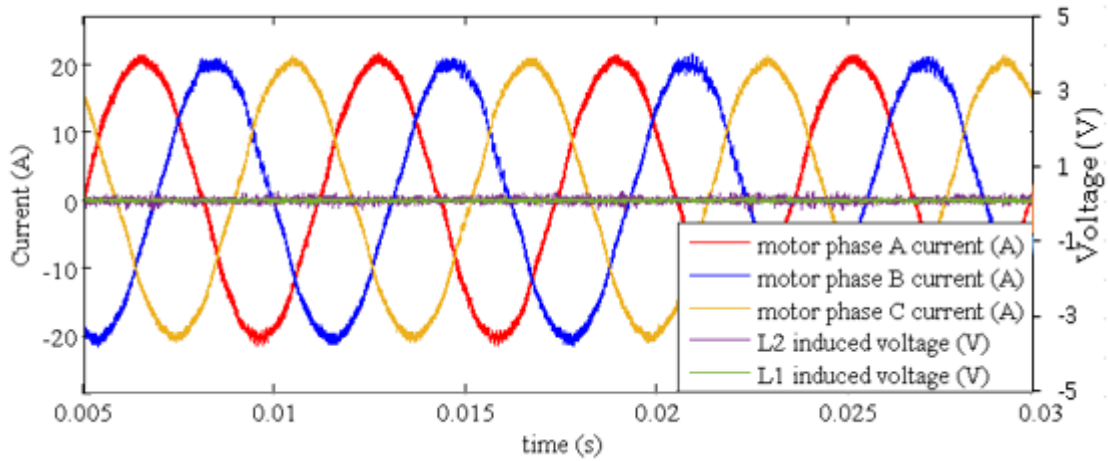


**Figure 6-11 3-phase currents of the integrated LCL input filter at 15000 RPM**

The LCL filter works effectively: it reduces the THD from 5.2% to 2.1% at the rated input current of 66 A<sub>pk</sub> without affecting the normal operation of the PM machine. Due to greater measured L2 inductance, the experimental THD is better than the normal expected grid THD of 3.0%. Although the machine is not at rated speed in this test, it is unlikely to have magnetic coupling between filter inductors and the PM machine unless the machine is heavily loaded.

### 6.1.5 Magnetic cross-coupling between the base machine and filter windings

In order to investigate the decoupling between the machine winding and the integrated filter inductors, the PM machine is firstly driven by an 80.0 V DC power supply at 2500 rev/min with the inverter in which the rectifier was disconnected. Producing an average torque of 3.2Nm at 2500 RPM and a peak motor phase current of 20A. The induced voltages of the filter inductor windings  $L_1$  and  $L_2$  are very small as shown in figure 6-12, which indicates no coupling between the base machine and the integrated filters.



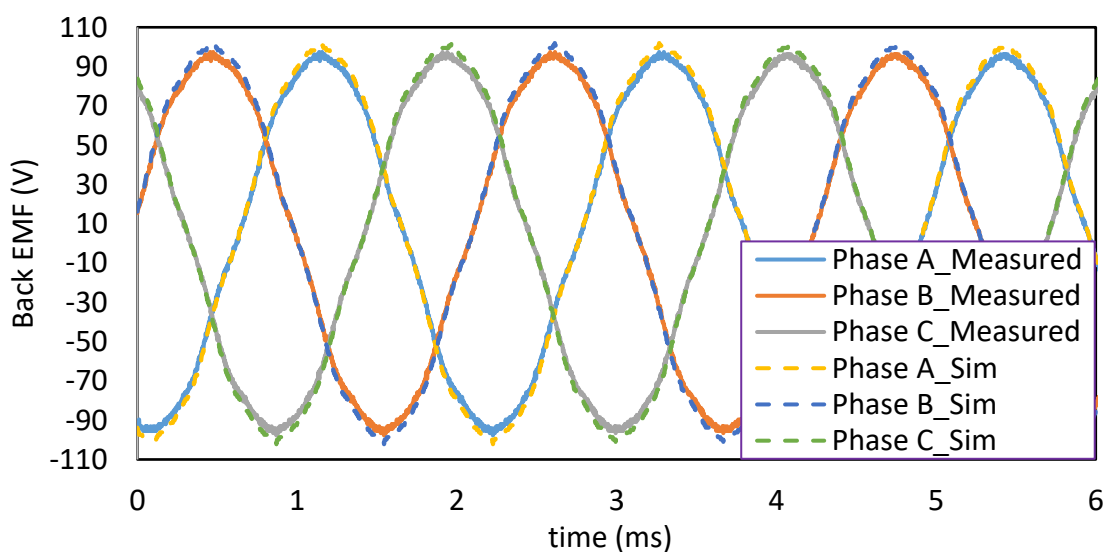
**Figure 6-12 Examination of magnetic cross-coupling between the base machine and filter windings**

Therefore, it is concluded that the base machine's magnetic circuit is magnetically independent of the circuit of the integrated filter inductors.

## 6.2 HSHP machine measurements

### 6.2.1 Open circuit voltages (back-EMF)

The back-EMF represents the voltage induced in the stator windings caused by the rotor magnets at a certain rotational speed. As testing, the whole system is achieved in incremental steps an initial test has been conducted to measure the back-EMF at low speed to confirm the validity of the FE simulation results. Figure 6-13 shows the line back-EMF voltages for both the FE simulation projected and measured values achieved at a speed of 7000 RPM.



**Figure 6-13 Line back-EMF measured and predicted at 7000 RPM**

The peak value of the measured line EMF is approximately 4.62% smaller than that of the predicted line voltage. The difference in voltage between the measured and predicted values may be attributed to the temperature rise of the magnets during measurement, which in turn reduces the magnets' flux.

Table 6-4 shows the values of the projected and measured back-EMF voltages. The deviation from the average of the measured voltages is less than 1%, which gives an indication that the machine is well balanced electromagnetically.

**Table 6-4 Measured and projected back-EMF at 7000 RPM**

Measured line back EMF			3D FEA prediction
Phase A-B	Phase B-C	Phase C-A	
97.41	96.71	96.5	101.91

The machine inductance was validated for the final constructed machine by measuring the phase inductance using RLC bridge at zero armature current. The measured value is 0.241 mH which is almost the same as those predicted values in table 3-3.

### 6.2.2 Coil testing (resistance, groundwall insulation and inter-turn)

The coil testing process for the IDS machine has been performed using two different instruments, which are the Megger-Ohm tester and the Baker instrument (manufactured by an SKF group company). The Meg-Ohm test is used to check for any DC leakage current at  $\leq 1\text{kV}$ , and in this test the dielectric strength of the slot liner is checked to ensure that the ground wall insulation can withstand the maximum line voltage and can prevent any coil-to-ground wall fault. The Baker company has produced a new coil testing equipment which offers several tests that include the HiPot test (to inspect the motor's slot liner) and a surge test (to detect insulation damage between turns within the machine's windings). In particular, it is important to conduct the surge test where there is a compressed coil because the wire enamel might be affected by the compression process.

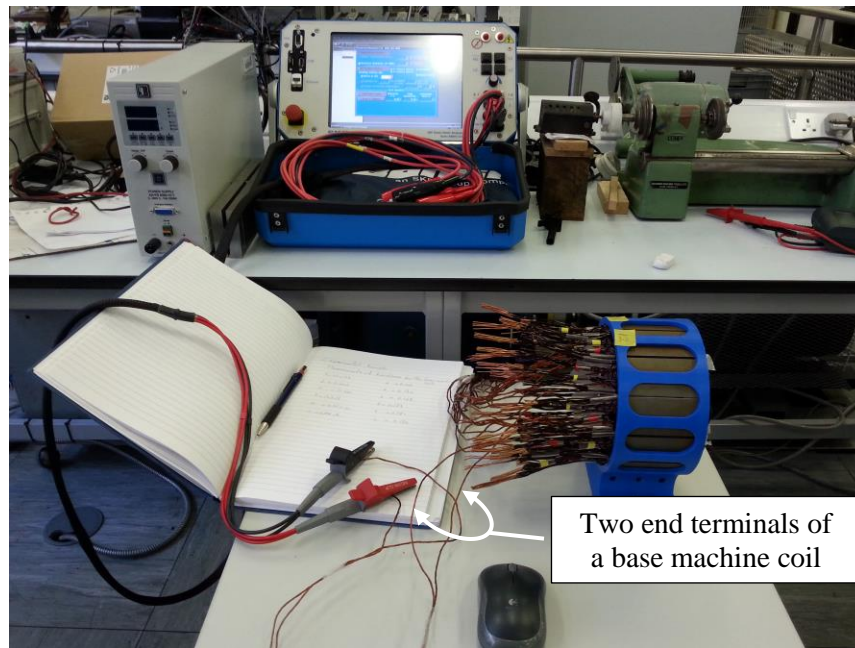
To adequately test the machine, the following test sequence has been performed.

#### 6.2.2.1 Balance resistance test

For the resistance measurement, the two leads (red and black) of the Baker test instrument were connected to the coil terminals as shown in figure 6-14. The resistance of each coil



was measured individually. If a large imbalance in resistance between the coils is found, further Meg-Ohm or surge testing is not necessary.



**Figure 6-14 Measurement of resistance for the high-speed machine coils**

The predicted analytical resistance calculation for each HSHP machine coil is  $0.117 \, \Omega$ , and table 6-5 shows the measured resistance values for the constructed 12 coils belonging to the HSHP base machine.

**Table 6-5 Measured resistance values for the HSHP machine coils**

Number of coils	Measured resistance ( $\Omega$ )	Number of coils	Measured resistance ( $\Omega$ )	Number of coils	Measured resistance ( $\Omega$ )
1	0.177	5	0.171	9	0.181
2	0.195	6	0.17	10	0.174
3	0.191	7	0.19	11	0.196
4	0.172	8	0.183	12	0.182

The differences between the analytically predicted resistance of a coil and the measured values shown in table 6-5 are due to a safety margin length taken for the machine end terminals during measurement, as shown in figure 6-14. There is another reason for this slight deviation of measured values which is the end terminals of copper wires are not tinned, thereby it is expected a number of strands will not be measured. It is noticeable that all measured resistance values shown in table 6-5 are more or less the same and there is no



large imbalance in values of resistance between the machine coils. Therefore, the testing processes can proceed to the next step.

#### **6.2.2.2 Mega and surge test**

These two tests have been carried out successfully where all machine coils have been passed the tests. For further details, all the procedures are explained in Appendix A.

### **6.3 Conclusion**

The results for the constructed IDS machine, including the base machine and the 3-phase LCL filter inductors, have been presented. A good correlation was found between the projected FE simulation and measured results.

The filter inductance per phase ( $L_1$  and  $L_2$ ) was measured, indicating a small difference compared to the FE results. The reduction in the value of the harmonics on the grid-side filter inductor is by 2.1% at a shaft speed of 15000RPM, which proves that the integrated filter inductors mimic the discrete filter inductors but with significant lower volume and a better final envelope associated with the base machine's structure. The examinations of mutual coupling between the filter inductors  $L_1$  and  $L_2$  and also between the base machine and filter inductors have been performed.

The initial no-load test showed that the deviation between the measured line back-EMF and the predicted value is approximately 4.6%. The balance resistance test has been performed using Baker equipment. The groundwall insulation test and surge test have also been carried out. Although the experiment was limited in scope the results suggest that impregnation greatly increases the lifetime of even a compressed coil.

# CHAPTER 7

## Conclusion and Future Work

---

The question highlighted at the start of this work was whether or not it is possible to integrate passive filter components into electrical machines without significant increases in size and losses. This chapter summarises the work described in this thesis and offers recommendations for future work.

### 8.1 Background

Reduced size and system integration are required in electric drives for applications with limited installation space, such as in automotive, aerospace and robotics fields. An integrated drive may be defined as the functional and structural integration of the power electronics converter with the machine, including the passive components, as a single unit taking into consideration the electrical, thermal and structural impacts the components have on each other and the system as a whole. For further cost and size reductions in an integrated system, standardised power electronics and passive components such as inductors and capacitors can be merged with their mechanical environment. The main challenges in the integration of systems are packaging, system integration issues, and the lack of standardised power electronics devices. Passive filter components represent a significant proportion of material costs and volume in grid-connected drives. The envelope of the filter components is rarely congruent with that of the machine, leading to poor utilization of the volume available in which to install the drive. Thus a more fully integrated system and better design tools are required.

Given the considerable size of line inductors used for high power applications and the demand for packaged electrical systems, the integration of magnetic filter components into electrical machines could achieve size reductions compared with conventional inductors with a separate motor and drive plus associated hardware. This study illustrates the limitation of previous integration methods in integrating passive input filter components into electrical machines. Various integration methods have been introduced in this thesis in order to enhance the functionality of passive integration into electrical machines.

## 8.2 Summary of work

The six objectives set out at the beginning of this research have been successfully met. The intent of this work is to reduce the overall volume of the combination of the machine and electromagnetic filter components through the better utilization of the available volume and envelope. The resulting envelope is a single package which achieves a significant volume reduction compared to the use of discrete filter components.

The prototype high-speed, high-power permanent magnet synchronous motor (PMSM) has been designed to form the foundation of an integrated motor drive. The machine is fed by an active, three-phase two-level inverter, and it has a surface-mounted neodymium-iron-boron permanent magnet rotor. A 0.35 mm carbon fibre sleeve will give mechanical integrity to the rotor. Single tooth windings minimise overall volume, but introduce special harmonics of flux and axial segmentation of the magnets is required to reduce the resulting rotor eddy current losses to an acceptable level. The employment of  $20 \times 30$  AWG Litz copper wire is needed to give losses winding conversion factor,  $K_{AC}$ , up to 90%. The use of 6.5% silicon, 0.1mm lamination material (JNEX-900) will provide relatively low iron losses. The rotor magnets should be axially located using non-magnetic steel rings where it helps to prevent shorting magnets' ends and consequently increase the machine efficiency.

This work presents five integration methods in order to integrate line filter inductors into electrical machines. The high speed electric machine with integrated magnetics in an LCL filter has been presented where the resulting design is the IDS machine. The integrated drive has been designed to take full advantage of sharing the machine stator structure in order to achieve a reduction in volume. This work shows the ability to integrate all six LCL filter inductors into the proposed machine sharing the original machine's magnetic circuit without magnetic cross-coupling between the integrated filter inductor windings or with the main machine's magnetic circuit.

On-tooth pressed windings have been introduced and demonstrated in the IDS machine, showing that the main machine and filter inductor coils are compressed directly onto the double slot stator teeth to form a solid component with fill factors for the main machine and filter windings of 60% and 50% respectively. A unique manufacturing method for multi-slot direct on-tooth pressing has been shown to give reliable and repeatable coils formed in such a way as to mitigate poor thermal contact as well as leakage losses due to poor conductor placement. This thesis presents a number of novel electromagnetic design and manufacturing processes

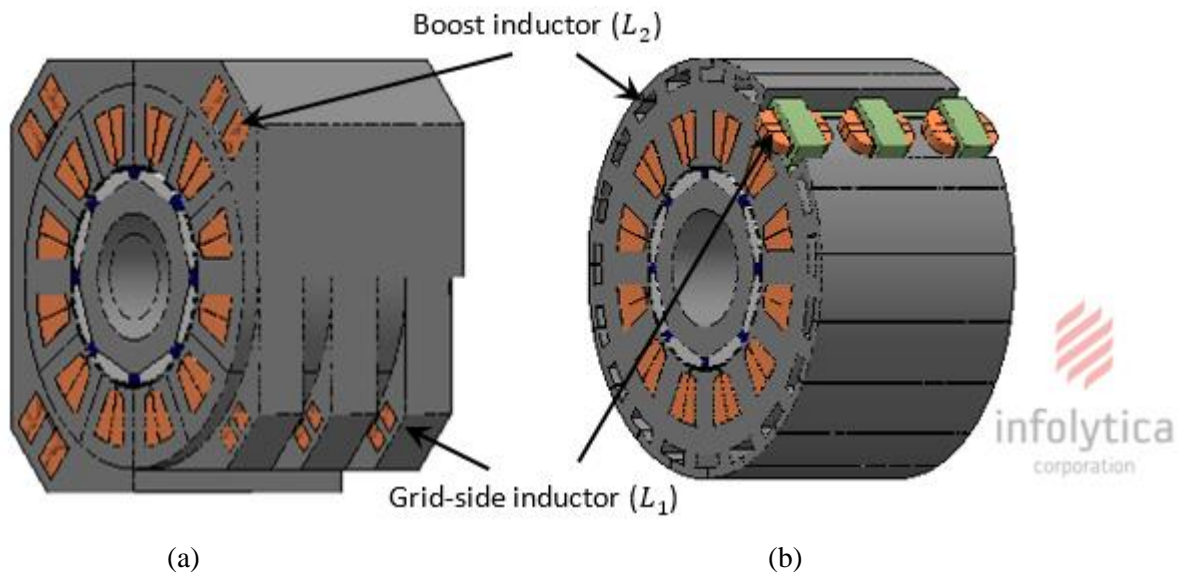
which enhance the performance and functionality of the integrated drive. The manufacturing method described allows the simple assembly of the stator and has been shown to yield measured inductances which correlate with the expected values from FEA simulation.

A prototype demonstration has been constructed using the best available materials and production processes and partially tested. An acceptable THD value of 3.29% was obtained on the grid-side LCL filter which confirms that the integrated LCL filter inductors mimic those of discrete industrial, achieving 87.6% lower volume. The back EMF waveforms and the 3-phase current waveforms of the integrated filter inductors collected from the preliminary tests give confidence in the design process.

### 8.3 Future research possibilities and recommendations

- There are many unknown factors concerning passive integration methods in HSHP machines that would be worth looking at in further research. Chief among these techniques is to integrate capacitors in electrical motor drives where more advanced standardised techniques are needed. The commercial capacitor shape shown in this work is not sufficient to achieve better utilisation of the available volume and motor envelope. A potential solutions can be further investigated in the future in order to reduce the size of filter capacitors when they are integrated in electrical machine drives; for example, a new capacitor design as a circular disk consistent with the outer diameter of the integrated base machine can be designed in which the thickness of the disk will be dictated by the required capacitance value. The circular capacitor disk could then be divided into three pieces to form the 3-phase shunt capacitors of the LCL filter. Thereby, most of the circumferential area within the suggested disk shape will be used and hence this will reduce the total size of the filter capacitors.
- Further experimental work should be carried out regarding the thermal behaviour of the integrated motor drive at rated speed and input current.
- Additional work should be conducted in order to validate the predicted value of THD achieved by the integrated input filter at rated speed and full input current of 25000 RPM and 75 A<sub>pk</sub> respectively. This will validate the integrity of the design of double slot stator at full operating conditions. In this case, the magnetic circuit of both filter inductors and PM machine should be magnetically independent.
- Further integration can be achieved with the two options of corner inductors and a double slot stator in order to integrate the grid-side inductors  $L_1$  into the machine. Figure

7-1 illustrates the arrangement of the 3-phase inductors  $L_1$  for both of these integration methods.



**Figure 7-1 Illustration of the integration of grid-side inductors using two different methods**

The main drawbacks introduced in these suggested methods, as demonstrated in figure 7-1, are that, firstly, there is poor thermal contact due to free space within the stator structure caused by the incorporation of the grid-side inductors  $L_1$ . Secondly, the degree of complexity of the geometry shown in figure 7-1 (b) is relatively high compared to that of the chosen method for the IDS machine where both filter windings  $L_1$  and  $L_2$  are incorporated into the same slots to achieve a better thermal path to the machine's cooling system.

- Additional work can be further conducted to examine the effectiveness of impregnated coils with different types of epoxy resin and ground-wall insulation. It is preferable to examine a number of identical compressed coils in each case by ageing them in an oven at a relatively high temperature, which can be increased to see when the coil insulation in the slot liner and enamel copper wire starts to be degraded.

# References

- [1] M. März, A. Schletz, B. Eckardt, S. Egelkraut, and H. Rauh, "Power electronics system integration for electric and hybrid vehicles," in *Integrated Power Electronics Systems (CIPS)*, 2010 6th International Conference on, 2010, pp. 1-10.
- [2] C. Klumper, F. Blaabjerg, and P. Thøgersen, "Alternate ASDs: evaluation of the converter topologies suited for integrated motor drives," *IEEE Industry applications magazine*, vol. 12, pp. 71-83, 2006.
- [3] F. C. Lee, J. D. Van Wyk, D. Boroyevich, and P. Barbosa, "An integrated approach to power electronics systems," in *Power Conversion Conference, 2002. PCC-Osaka 2002. Proceedings of the, 2002*, pp. 7-12.
- [4] Y. Shakweh, G. H. Owen, D. J. Hall, and H. Miller, "Plug and play integrated motor drives," 2002.
- [5] P. Vas PhD and C. Dsc, "Electrical machines and drives: present and future," in *Electrotechnical Conference on Industrial Applications in Power Systems, Computer Science and Telecommunications (MELECON 96)*, Bari Italy, 1996, pp. 67-74.
- [6] R. Abebe, G. Vakil, G. L. Calzo, T. Cox, S. Lambert, M. Johnson, et al., "Integrated motor drives: state of the art and future trends," *IET Electric Power Applications*, vol. 10, pp. 757-771, 2016.
- [7] S. M. Lambert, B. C. Mecrow, R. Abebe, G. Vakil, and C. M. Johnson, "Integrated Drives for Transport-A Review of the Enabling Electronics Technology," in *Vehicle Power and Propulsion Conference (VPPC)*, 2015 IEEE, 2015, pp. 1-6.
- [8] D. K. Perovic, "Making the impossible, possible—overcoming the design challenges of in wheel motors," in *EVS26 International Battery, Hybrid and Fuel Cell Electric Vehicle Symposium*, 2012, pp. 514-519.
- [9] I. W. Group, "519-2014-IEEE Recommended Practice and Requirements for Harmonic Control in Electric Power Systems," *IEEE Std 519–2014 (Revision of IEEE Std 519–1992)*, pp. 1-29, 2014.
- [10] J. R. Rodríguez, J. W. Dixon, J. R. Espinoza, J. Pontt, and P. Lezana, "PWM regenerative rectifiers: State of the art," *IEEE Transactions on Industrial Electronics*, vol. 52, pp. 5-22, 2005.
- [11] K. Lee, T. Jahns, D. W. Novotny, T. A. Lipo, W. E. Berkopec, and V. Blasko, "Impact of inductor placement on the performance of adjustable-speed drives under input voltage unbalance and sag conditions," *IEEE transactions on industry applications*, vol. 42, pp. 1230-1240, 2006.
- [12] K. Lee, T. M. Jahns, W. E. Berkopec, and T. A. Lipo, "Closed-form analysis of adjustable-speed drive performance under input-voltage unbalance and sag conditions," *IEEE transactions on industry applications*, vol. 42, pp. 733-741, 2006.

- [13] K. Lee, G. Venkataramanan, and T. M. Jahns, "Design-oriented analysis of dc bus dynamics in adjustable speed drives under input voltage unbalance and sag conditions," in *Power Electronics Specialists Conference*, 2004. PESC 04. 2004 IEEE 35th Annual, 2004, pp. 1675-1681.
- [14] C. W. T. McLyman, *Transformer and inductor design handbook vol. 121*: Marcel Dekker New York, NY, USA:, 2004.
- [15] (2016, 22th November). AC Reactor Power Inductor [Online]. Available: <http://dutch.alibaba.com/product-gs/2015-sikes-manufacturer-mvp-input-ac-reactor-power-inductor-for-battery-inverter-current-limiting-reactor-60219993842.html>
- [16] F. J. Bartos, "Combination motors and drives move to make their mark," *Control Engineering*, December, 2000.
- [17] F. J. Bartos, "Integrated motor-drives seek wider market, user acceptance," *Control Engineering*, pp. 19-23, 2000.
- [18] F. Blaabjerg and P. Thøgersen, "Adjustable speed drives-future challenges and applications," in *Power Electronics and Motion Control Conference*, 2004. IPEMC 2004. The 4th International, 2004, pp. 36-45.
- [19] L. Gu, J. Sun, M. Xu, Q. Zuo, and J. Fan, "Size reduction of the inductor in critical conduction mode PFC converter," in *Applied Power Electronics Conference and Exposition (APEC)*, 2011 Twenty-Sixth Annual IEEE, 2011, pp. 550-557.
- [20] N. Zhu, J. Kang, D. Xu, B. Wu, and Y. Xiao, "A novel integrated AC choke for common-mode voltage suppression in power converter systems," in *Electric Machines & Drives Conference (IEMDC)*, 2011 IEEE International, 2011, pp. 1030-1035.
- [21] M. L. Heldwein, L. Dalessandro, and J. W. Kolar, "The three-phase common-mode inductor: Modeling and design issues," *IEEE Transactions on Industrial Electronics*, vol. 58, pp. 3264-3274, 2011.
- [22] A. Muetze and C. R. Sullivan, "Simplified design of common-mode chokes for reduction of motor ground currents in inverter drives," *IEEE Transactions on Industry Applications*, vol. 47, pp. 2570-2577, 2011.
- [23] J. D. Van Wyk and J. A. Ferreira, "Some present and future trends in power electronic converters," in *Industrial Electronics, Control, Instrumentation, and Automation*, 1992. *Power Electronics and Motion Control.*, Proceedings of the 1992 International Conference on, 1992, pp. 9-18.
- [24] I. W. Hofsaier, J. A. Ferreira, J. D. Van Wyk, and M. C. Smit, "Integrated technology and performance for multi-kilowatt power electronic converters-an evaluation," in *Industrial Electronics, Control, and Instrumentation*, 1993. Proceedings of the IECON'93., International Conference on, 1993, pp. 779-784.
- [25] J. D. Van Wyk, J. T. Strydom, L. Zhao, and R. Chen, "Review of the development of high density integrated technology for electromagnetic power passives," in *Proceedings of the 2nd International Conference on Integrated Power Systems (CIPS)*, 2002, pp. 25-34.
- [26] W. Liu, J. Dirker, and J. D. van Wyk, "Power density improvement in integrated electromagnetic passive modules with embedded heat extractors," *IEEE Transactions on Power Electronics*, vol. 23, pp. 3142-3150, 2008.

- [27] J. T. Strydom and J. D. Van Wyk, "Improved loss determination for planar integrated power passive modules," in Applied Power Electronics Conference and Exposition, 2002. APEC 2002. Seventeenth Annual IEEE, 2002, pp. 332-338.
- [28] J. D. van Wyk, F. C. Lee, Z. Liang, R. Chen, S. Wang, and B. Lu, "Integrating active, passive and EMI-filter functions in power electronics systems: a case study of some technologies," IEEE Transactions on Power Electronics, vol. 20, pp. 523-536, 2005.
- [29] S. D. Garvey, W. T. Norris, and M. T. Wright, "The role of integrated passive components in protecting motor windings," IEE Proceedings-Electric Power Applications, vol. 147, pp. 367-370, 2000.
- [30] M. R. Khowja, C. Gerada, G. Vakil, P. Wheeler, and C. Patel, "Integrated output filter inductor for permanent magnet motor drives," in Industrial Electronics Society, IECON 2016-42nd Annual Conference of the IEEE, 2016, pp. 2827-2832.
- [31] M. R. Khowja, C. Gerada, G. Vakil, P. Wheeler, and C. Patel, "Novel integrative options for passive filter inductor in high speed AC drives," in Industrial Electronics Society, IECON 2016-42nd Annual Conference of the IEEE, 2016, pp. 1137-1142.
- [32] P. Thelin, "New integral motor stator design with integrated filter coils."
- [33] P. Thelin and H. P. Nee, "Development and efficiency measurements of a compact 15 kW 1500 r/min integral permanent magnet synchronous motor," in Industry Applications Conference, 2000. Conference Record of the 2000 IEEE, 2000, pp. 155-162.
- [34] J. K. Cornell, "Shading band compensation for continuous transformer and motor," ed: Google Patents, 1989.
- [35] J. J. Wolmarans, M. B. Gerber, H. Polinder, S. W. H. De Haan, J. A. Ferreira, and D. Clarenbach, "A 50kW integrated fault tolerant permanent magnet machine and motor drive," in Power Electronics Specialists Conference, 2008. PESC 2008. IEEE, 2008, pp. 345-351.
- [36] G. K. Andersen, L. Helle, and P. O. Rasmussen, "An Integrated single phase power factor controlled switched reluctance motor drive with minimum of passive components," in Epe'99: European Conference on Power Electronics and Applications Session L2d, September 1999, Lausanne, Switzerland, 1999.
- [37] N. R. Brown, T. M. Jahns, and R. D. Lorenz, "Power Converter Design for an Integrated Modular Motor Drive," in 2007 IEEE Industry Applications Annual Meeting, 2007, pp. 1322-1328.
- [38] G.-J. Su, L. Tang, C. Ayers, and R. Wiles, "An inverter packaging scheme for an integrated segmented traction drive system," in Energy Conversion Congress and Exposition (ECCE), 2013 IEEE, 2013, pp. 2799-2804.
- [39] J. Wang, Y. Li, and Y. Han, "Evaluation and design for an integrated modular motor drive (IMMD) with GaN devices," in 2013 IEEE Energy Conversion Congress and Exposition, 2013, pp. 4318-4325.
- [40] B. Janjic, A. Binder, V. Bischof, and G. Ludwig, "Design of PM integrated motor-drive system for axial pumps," in Power Electronics and Applications, 2007 European Conference on, 2007, pp. 1-10.



- [41] H. A. Mantooth, "Emerging Capabilities in Electronics Technologies for Extreme Environments Part 1-High Temperature Electronics," IEEE Power Electronics Society Newsletter, vol. 18, pp. 9-14, 2006.
- [42] R. Phillips, J. Bultitude, A. Gurav, K. Park, S. Murillo, P. Flores, et al., "High temperature ceramic capacitors for deep well applications," CARTS Int. Proc, 2013.
- [43] T. R. Haller, "Amorphous metal electric motor with integral capacitor," ed: Google Patents, 1980.
- [44] B. Drury, "The Control Techniques Drives and Controls: Handbook, EMERSON," ed: JET, 2009.
- [45] I. S. Association, "519-1992. IEEE Recommended Practices and Requirements for Harmonics Control in Electric Power Systems," New York: IEEE Inc, 1992.
- [46] M. Liserre, F. Blaabjerg, and S. Hansen, "Design and control of an LCL-filter-based three-phase active rectifier," IEEE Transactions on industry applications, vol. 41, pp. 1281-1291, 2005.
- [47] J. Lettl, J. Bauer, and L. Linhart, "Comparison of different filter types for grid connected inverter," in PIERS Proceedings, 2011, pp. 1426-1429.
- [48] A. Chandel, A. Patel, V. Patel, and P. Surti, "Design calculation and simulation verification for 2 kW grid connected transformerless photovoltaic inverter," in Engineering (NUICONE), 2012 Nirma University International Conference on, 2012, pp. 1-6.
- [49] H. R. Karshenas and H. Saghafi, "Basic criteria in designing LCL filters for grid connected converters," in Industrial Electronics, 2006 IEEE International Symposium on, 2006, pp. 1996-2000.
- [50] R. C. Dorf and R. H. Bishop, Modern control systems: Pearson, 2011.
- [51] J. Muhlethaler, M. Schweizer, R. Blattmann, J. W. Kolar, and A. Ecklebe, "Optimal design of LCL harmonic filters for three-phase PFC rectifiers," IEEE Transactions on Power Electronics, vol. 28, pp. 3114-3125, 2013.
- [52] Y. Lang, D. Xu, S. R. Hadianamrei, and H. Ma, "A novel design method of LCL type utility interface for three-phase voltage source rectifier," in Power Electronics Specialists Conference, 2005. PESC'05. IEEE 36th, 2005, pp. 313-317.
- [53] A. Reznik, M. G. Simões, A. Al-Durra, and S. M. Mueen, "LCL Filter Design and Performance Analysis for Grid-Interconnected Systems," IEEE Transactions on Industry Applications, vol. 50, pp. 1225-1232, 2014.
- [54] T. Fan, Q. Li, and X. Wen, "Development of a high power density motor made of amorphous alloy cores," IEEE Transactions on Industrial Electronics, vol. 61, pp. 4510-4518, 2014.
- [55] M.-J. Kim, S.-Y. Cho, K.-D. Lee, J.-J. Lee, J.-H. Han, T.-C. Jeong, et al., "Torque density elevation in concentrated winding interior PM synchronous motor with minimized magnet volume," IEEE Transactions on Magnetics, vol. 49, pp. 3334-3337, 2013.
- [56] D. C. Hanselman, Brushless motors: magnetic design, performance, and control of brushless dc and permanent magnet synchronous motors: E-Man Press LLC, 2012.

- [57] K.-S. Seo, Y.-J. Kim, and S.-Y. Jung, "Stator teeth shape design for torque ripple reduction in surface-mounted permanent magnet synchronous motor," in *Electrical Machines and Systems (ICEMS)*, 2014 17th International Conference on, 2014, pp. 387-390.
- [58] P. Upadhayay and K. R. Rajagopal, "Torque ripple reduction using magnet pole shaping in a surface mounted Permanent Magnet BLDC motor," in *Renewable Energy Research and Applications (ICRERA)*, 2013 International Conference on, 2013, pp. 516-521.
- [59] R. Islam, I. Husain, A. Fardoun, and K. McLaughlin, "Permanent-magnet synchronous motor magnet designs with skewing for torque ripple and cogging torque reduction," *IEEE Transactions on Industry Applications*, vol. 45, pp. 152-160, 2009.
- [60] N. Bianchi and S. Bolognani, "Design techniques for reducing the cogging torque in surface-mounted PM motors," *IEEE Transactions on Industry Applications*, vol. 38, pp. 1259-1265, 2002.
- [61] G. Dajaku and D. Gerling, "New methods for reducing the cogging torque and torque ripples of PMSM," in *Electric Drives Production Conference (EDPC)*, 2014 4th International, 2014, pp. 1-7.
- [62] Y. Yokoi and T. Higuchi, "Stator design of alternate slot winding for reducing torque pulsation with magnet designs in surface-mounted permanent magnet motors," *IEEE Transactions on Magnetics*, vol. 51, pp. 1-11, 2015.
- [63] I. Petrov, P. Ponomarev, Y. Alexandrova, and J. Pyrhönen, "Unequal teeth widths for torque ripple reduction in permanent magnet synchronous machines with fractional-slot non-overlapping windings," *IEEE Transactions on Magnetics*, vol. 51, pp. 1-9, 2015.
- [64] K. Wang, Z. Q. Zhu, G. Ombach, and W. Chlebosz, "Average torque improvement of interior permanent-magnet machine using third harmonic in rotor shape," *IEEE Transactions On Industrial Electronics*, vol. 61, pp. 5047-5057, 2014.
- [65] F. Libert and J. Soulard, "Investigation on pole-slot combinations for permanent-magnet machines with concentrated windings," in *International Conference on Electrical Machines (ICEM 04)*, 2004, pp. 5-8.
- [66] A. M. El-Refaei, "Fractional-slot concentrated-windings synchronous permanent magnet machines: Opportunities and challenges," *IEEE Transactions on industrial Electronics*, vol. 57, pp. 107-121, 2010.
- [67] A. G. Jack, B. C. Mecrow, P. G. Dickinson, D. Stephenson, J. S. Burdett, N. Fawcett, et al., "Permanent-magnet machines with powdered iron cores and prepressed windings," *IEEE Transactions on Industry Applications*, vol. 36, pp. 1077-1084, 2000.
- [68] M. Persson, P. Jansson, A. G. Jack, and B. C. Mecrow, "Soft magnetic composite materials-use for electrical machines," in *1995 Seventh International Conference on Electrical Machines and Drives (Conf. Publ. No. 412)*, 1995, pp. 242-246.
- [69] d. s. JFE Japanese steel company, "Super Core\_Electrical steel sheets for high-frequency application."
- [70] d. s. JFE Japanese steel company, "Magnetic property curves JNEX-Core and JNHf-Core."
- [71] M. M. Personal contact, JFE Steel, Europe, Limited, "Principle of manufacturing process of 6.5% Si steel sheets by chemical vapor deposition (CVD)," ed.

- [72] Data sheet of JFE super core. Electrical steel sheets for high-frequency application. Available: <http://www.jfesteel.co.jp/en/products/electrical/catalog/f1e-002.pdf>
- [73] M. Cossale, A. Krings, J. Soulard, A. Boglietti, and A. Cavagnino, "Practical investigations on cobalt-iron laminations for electrical machines," *IEEE Transactions on Industry Applications*, vol. 51, pp. 2933-2939, 2015.
- [74] A. Krings, M. Cossale, J. Soulard, A. Boglietti, and A. Cavagnino, "Manufacturing influence on the magnetic properties and iron losses in cobalt-iron stator cores for electrical machines," in *2014 IEEE Energy Conversion Congress and Exposition (ECCE)*, 2014, pp. 5595-5601.
- [75] F. Bloch, T. Waeckerle, and H. Fraisse, "The use of iron-nickel and iron-cobalt alloys in electrical engineering, and especially for electrical motors," in *2007 Electrical Insulation Conference and Electrical Manufacturing Expo*, 2007, pp. 394-401.
- [76] D. J. B. Smith, B. C. Mecrow, G. J. Atkinson, A. G. Jack, and A. A. A. Mehna, "Shear stress concentrations in permanent magnet rotor sleeves," in *The XIX International Conference on Electrical Machines - ICEM 2010*, 2010, pp. 1-6.
- [77] Hexcel. (01/05/2017). Product data sheet, HexTow\_AS4C 4000 Carbon Fiber\_industrial. Available: [http://www.hexcel.com/user\\_area/content\\_media/raw/AS4C\\_Industrial\\_HexTow\\_DataSheet.pdf](http://www.hexcel.com/user_area/content_media/raw/AS4C_Industrial_HexTow_DataSheet.pdf)
- [78] J. D. Ede, K. Atallah, G. W. Jewell, J. B. Wang, and D. Howe, "Effect of Axial Segmentation of Permanent Magnets on Rotor Loss in Modular Permanent-Magnet Brushless Machines," *IEEE Transactions on Industry Applications*, vol. 43, pp. 1207-1213, 2007.
- [79] D. M. Saban, C. Bailey, D. Gonzalez-Lopez, and L. Luca, "Experimental evaluation of a high-speed permanent-magnet machine," in *2008 55th IEEE Petroleum and Chemical Industry Technical Conference*, 2008, pp. 1-9.
- [80] H. Polinder and M. J. Hoeijmakers, "Effect of a shielding cylinder on the rotor losses in a rectifier-loaded PM machine," in *Conference Record of the 2000 IEEE Industry Applications Conference. Thirty-Fifth IAS Annual Meeting and World Conference on Industrial Applications of Electrical Energy (Cat. No.00CH37129)*, 2000, pp. 163-170 vol.1.
- [81] P. Beer, J. E. Tessaro, B. Eckels, and P. Gaberson, "High speed motor design for gas compressor applications," presented at the *35th Turbomachinery Symp.*, 2006.
- [82] O. Aglen, "Loss calculation and thermal analysis of a high-speed generator," in *Electric Machines and Drives Conference, 2003. IEMDC'03. IEEE International*, 2003, pp. 1117-1123 vol.2.
- [83] G. Bertotti, "General properties of power losses in soft ferromagnetic materials," *IEEE Transactions on Magnetics*, vol. 24, pp. 621-630, 1988.
- [84] G. Bertotti, A. Boglietti, M. Chiampi, D. Chiarabaglio, F. Fiorillo, and M. Lazzari, "An improved estimation of iron losses in rotating electrical machines," *IEEE Transactions on Magnetics*, vol. 27, pp. 5007-5009, 1991.

- [85] M. Barcaro and N. Bianchi, "Air-Gap Flux Density Distortion and Iron Losses in Anisotropic Synchronous Motors," *IEEE Transactions on Magnetics*, vol. 46, pp. 121-126, 2010.
- [86] G. J. Atkenson, "High power fault tolerant motors for aerospace applications," PhD, Newcastle University, United Kingdom, 2007.
- [87] D. Joo, D. K. Hong, B. C. Woo, Y. H. Jeong, and D. H. Koo, "Iron Loss of 50 W, 100000 rpm Permanent-Magnet Machine in Micro Gas Turbine," in *2012 Sixth International Conference on Electromagnetic Field Problems and Applications*, 2012, pp. 1-4.
- [88] T. J. Juhan Pyrhonen, Valeria Hrabovcova,, *Design of rotating electrical machines*. The United Kingdom: Johan Wiley & Sons Ltd, West Sussex, 2014.
- [89] C. R. Sullivan, "Computationally efficient winding loss calculation with multiple windings, arbitrary waveforms, and two-dimensional or three-dimensional field geometry," *IEEE Transactions on Power Electronics*, vol. 16, pp. 142-150, 2001.
- [90] T. M. J. Patel B. Reddy, Theodore P. Bohn, "Transposition Effects on Bundle Proximity Losses in High-Speed PM Machines," presented at the *IEEE Energy Conversion Congress and Exposition*, San Jose, CA, USA, 2009.
- [91] W. Chen, Y. Liu, J. Islam, and D. Svehkarenko, "Strand-level finite element model of stator AC copper losses in the high speed machines," in *2012 XXth International Conference on Electrical Machines*, 2012, pp. 477-482.
- [92] J. Wang, F. Wang, and X. Kong, "Losses and thermal analysis of high speed PM machine," in *2008 Joint International Conference on Power System Technology and IEEE Power India Conference*, 2008, pp. 1-5.
- [93] D. A. Gonzalez and D. M. Saban, "Study of the copper losses in a high-speed permanent-magnet machine with form-wound windings," *IEEE Transactions on Industrial Electronics*, vol. 61, pp. 3038-3045, 2014.
- [94] H. Hämäläinen, J. Pyrhönen, J. Nerg, and J. Talvitie, "AC resistance factor of litz-wire windings used in low-voltage high-power generators," *IEEE Transactions on Industrial Electronics*, vol. 61, pp. 693-700, 2014.
- [95] P. B. Reddy and T. M. Jahns, "Analysis of bundle losses in high speed machines," in *The 2010 International Power Electronics Conference-ECCE ASIA-*, 2010, pp. 2181-2188.
- [96] J. E. Vrancik, "Prediction of windage power loss in alternators," *United States Patent*, Oct 01, 1968.
- [97] C. Huynh, L. Zheng, and D. Acharya, "Losses in High Speed Permanent Magnet Machines Used in Microturbine Applications," *Journal of Engineering for Gas Turbines and Power*, vol. 131, pp. 022301-022301-6, 2008.
- [98] B. M. Nee and P. L. Chapman, "Integrated Filter Elements in Electric Drives," in *2007 IEEE Vehicle Power and Propulsion Conference*, 2007, pp. 148-153.
- [99] R. M. Tallam, G. L. Skibinski, T. A. Shudarek, and R. A. Lukaszewski, "Integrated Differential-Mode and Common-Mode Filter to Mitigate the Effects of Long Motor Leads on AC Drives," *IEEE Transactions on Industry Applications*, vol. 47, pp. 2075-2083, 2011.

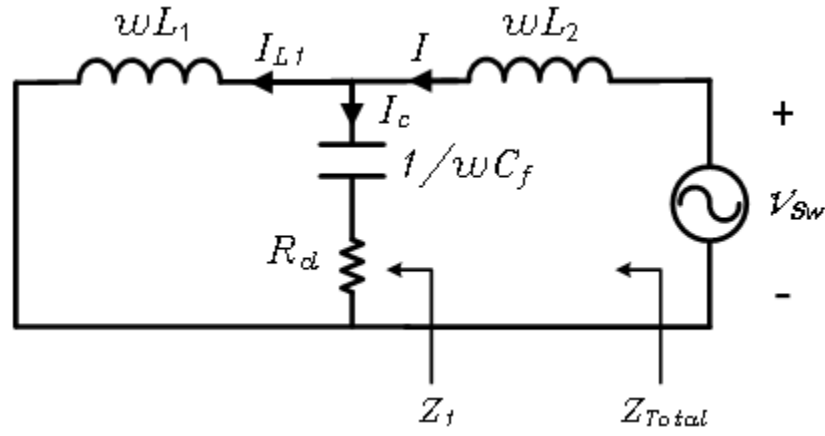
- [100] M. A. Mohamed, S. M. Lambert, B. C. Mecrow, D. J. Atkinson, and A. C. Smith, "An electrical machine with integrated drive LCL filter components," in 8th IET International Conference on Power Electronics, Machines and Drives (PEMD 2016), 2016, pp. 1-6.
- [101] Hylomar. Technical data sheet, Hylomar epoxy putty (ST574). Available: <http://hylomar.com/warrick/wp-content/uploads/2013/10/Hylomar-ST574-TDS-2011.pdf>
- [102] J. D. Widmer, R. Martin, and B. C. Mecrow, "Pre-compressed and stranded aluminium motor windings for traction motors," in 2015 IEEE International Electric Machines & Drives Conference (IEMDC), 2015, pp. 1851-1857.
- [103] A. e. v. company. (2014). Ultimeg Range Technical Guide To Selection. Available: [https://www.aev.co.uk/userfiles/file/Ultimeg\\_Epoxy\\_GTS\\_2014.pdf](https://www.aev.co.uk/userfiles/file/Ultimeg_Epoxy_GTS_2014.pdf)
- [104] M. A. S. Mohamed, S. M. Lambert, B. C. Mecrow, X. Deng, S. Ullah, and A. C. Smith, "Integrating the magnetics of an LCL filter into a high speed machine with pre-compressed coils," in 2017 IEEE International Electric Machines and Drives Conference (IEMDC), 2017, pp. 1-7.
- [105] W. M. Haynes, CRC Handbook of Chemistry and Physics, 2016.
- [106] (2014, 27/03/2017). PCB Creepage calculator. Available: <http://pcbdesign.smeps.us/creepage.html>
- [107] Baker Instrument Company. (2013). User manual, SKF Static Motor Analyzer Available: <http://www.skf.com/binary/30-144871/PUB-CM-I4-71-025-EN-V11-Baker-AWA-IV-User-manual.pdf>

# Appendix A – Analytical calculation and further integration method

## 1. The derivation of the transfer function equation of the LCL filter

- The filter transfer function, including damping branch:

For this analysis, all inductor resistances are ignored. Figure A1 shows a single-phase LCL filter, including the fundamental switch harmonics component, for a short-circuited grid.



**Figure A1** Equivalent circuit of single-phase LCL filter taking into consideration the fundamental component of the switch harmonics

The total filter impedance can be calculated as follows:

$$Z_1 = \omega L_1 / \left( \frac{1}{\omega C_f} + R_d \right)$$

$$Z_1 = \frac{\left( \frac{L_1}{C_f} \right) + \omega L_1 R_d}{\omega L_1 + \frac{1}{\omega C_f} + R_d} = \frac{\omega L_1 + \omega^2 L_1 C_f R_d}{\omega^2 L_1 C_f + \omega C_f R_d + 1}$$

The total impedance of the LCL filter is:

$$Z_{Total} = Z_1 + \omega L_2 = \frac{\omega L_1 + \omega^2 L_1 C_f R_d}{\omega^2 L_1 C_f + \omega C_f R_d + 1} + \omega L_2$$

$$Z_{Total} = \left( \frac{\omega L_1 + \omega^2 L_1 C_f R_d + \omega^3 L_1 L_2 C_f + \omega^2 L_2 C_f R_d + \omega L_2}{\omega^2 L_1 C_f + \omega C_f R_d + 1} \right)$$

Using the formula below, the grid-side current,  $I_{L1}$ , is given by:

$$I_{L1} = I_{L2} \times \frac{\frac{1}{\omega C_f} + R_d}{\frac{1}{\omega C_f} + R_d + \omega L_1} = I_{L2} \times \frac{\omega C_f R_d + 1}{\omega^2 L_1 C_f + \omega C_f R_d + 1}$$

where the drive-side current is:

$$I_{L2} = \frac{V_{sw}}{Z_{Total}}$$

Therefore, the transfer function of the LCL filter with a damping branch in the time domain can be derived as follows:

$$T_{LCL} = \frac{I_{L1}}{V_{sw}} = \frac{1}{Z_{Total}} \times \frac{\omega C_f R_d + 1}{\omega^2 L_1 C_f + \omega C_f R_d + 1}$$

$$T_{LCL} = \frac{\omega^2 L_1 C_f + \omega C_f R_d + 1}{\omega L_1 + \omega^2 L_1 C_f R_d + \omega^3 L_1 L_2 C_f + \omega^2 L_2 C_f R_d + \omega L_2} \times \frac{\omega C_f R_d + 1}{\omega^2 L_1 C_f + \omega C_f R_d + 1}$$

$$T_{LCL} = \left( \frac{\omega C_f R_d + 1}{L_1 L_2 C_f \omega^3 + (L_1 + L_2) C_f R_d \omega^2 + (L_1 + L_2) \omega} \right)$$

The transfer function in the state space is as follow:

$$T_{LCL} = \left( \frac{\omega C_f R_d + 1}{L_1 L_2 C_f S^3 + (L_1 + L_2) C_f R_d S^2 + (L_1 + L_2) S} \right)$$

- **The transfer function without the damping branch is:**

$$T_{LCL} = \left( \frac{1}{L_1 L_2 C_f \omega^3 + (L_1 + L_2) \omega} \right)$$

$$T_{LCL} = \left( \frac{1}{L_1 L_2 C_f S^3 + (L_1 + L_2) S} \right) \rightarrow \text{State space domain}$$

## 2. LCL power filter design for 38 KW and 25000 RPM

The parameters of LCL filter are dictated by the rated power converter and they are derived as shown below:

- The input filter parameters will be derived as a percentage of the base values as shown:

$$\left\{ \begin{array}{l} Z_b = \frac{E_n^2}{P_n} = \frac{415^2}{38 \times 10^3} = 4.53 \Omega \\ C_b = \frac{1}{\omega_g Z_b} = \frac{1}{2\pi f_g \times 4.53} = 702.67 \mu F \\ I_{max} = \frac{P_n}{3 V_{ph}} = \frac{38 \times 10^3}{3 \times 240} = 53 A_{rms} \end{array} \right.$$

- Drive side inductance  $L_{2 min}$  calculation:

$$L_{2 min} = L_{2 min} = \frac{0.01 \times V_{ph(rms)}}{2 \pi f I_{rms}} = \frac{0.01 \times 240}{2 \times \pi \times 50 \times 53} = 0.16 mH$$

- Shunt capacitor calculation  $C_f$ :

$$C_f = 3\% C_b = 0.03 \times 702.67 \mu F \approx 21 \mu F$$

- Grid side inductance  $L_1$  (assuming that the attenuation factor  $K_a$  is 20%):

$$L_1 = \frac{\sqrt{\frac{1}{K_a^2} + 1}}{C_f \omega_{sw}^2} \approx 5 \mu H$$

- The resonant frequency of the desired LCL filter is determined as follows:

$$\omega_{res} = \sqrt{\frac{L_1 + L_2}{L_1 L_2 C_f}} = 104.02 \times 10^3 rad/s$$

$$f_{res} = 16.56 KHZ$$

- Then the effectiveness of the values of  $L_1$  and  $L_2$  must verify the condition of operation of the resonant frequency as follows:

$$10 f_g < f_{res} < 0.5 f_{sw}$$

$$10 \times 50 < f_{res} < 0.5 \times 40 \times 10^3$$

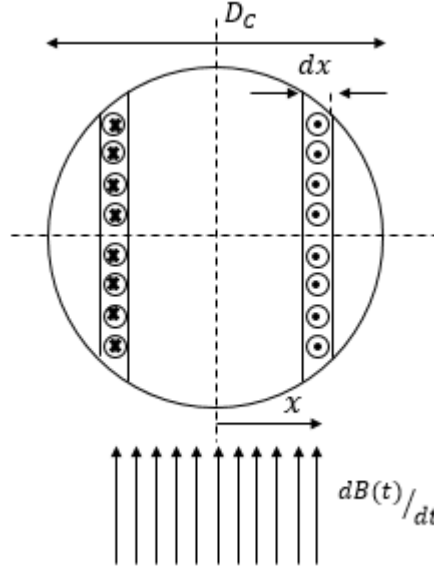
- Damping resistance calculation:

$$R_d = \frac{1}{3\omega_{res} C_f} = 0.4 \Omega$$



### 3. Derivation of the AC loss equation

The derivation of the AC loss equation in the time domain can be conducted based on a conducting cylinder with a uniform flux density,  $B$ , perpendicular to the axis of the cylinder as shown in figure A2. This assumes an eddy current loop at position  $x$  with a thickness of  $dx$ , which is returning in the corresponding path of the cylinder at  $-x$  as shown in figure A2.



**Figure A2 Calculation of eddy current loss in a conducting cylinder with uniform flux density**

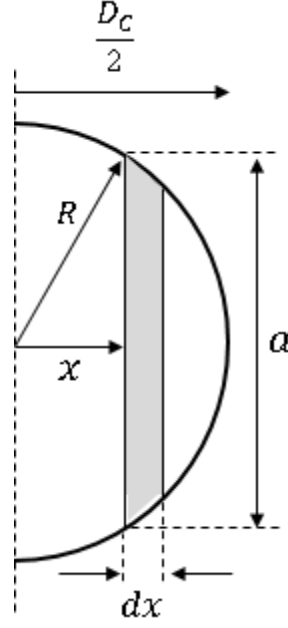
As the EMF induced around the loop in the conductor is caused by the flux perpendicular to the cylinder axis, the derivative of this magnetic flux is:

$$\frac{d\phi}{dt} = 2xl_c \frac{dB(t)}{dt}$$

where  $l_c$  is the length of the cylinder.

The resistance of the specified eddy current path as shown in figure A3 is:

$$R = \frac{\rho l_c}{A_c}$$



**Figure A3 calculation of eddy current area**

The shaded area of the eddy current section can be calculated as follows:

Shaded area ( $A_C$ ) =  $a \times dx$

$$\frac{1}{2}a = \sqrt{R^2 - x^2} \times dx \quad \rightarrow a = 2 \times \sqrt{\frac{D_C^2}{4} - x^2} \times dx$$

As a consequence, the resistance of this path is:

$$R = \frac{\rho \times 2 \times l_c}{2 \sqrt{\frac{D_C^2}{4} - x^2} \times dx}$$

The instantaneous total power dissipated in the cylinder ( $(d\Phi/dt)^2 / R$ ) is approximately integrated with these differential elements, as given in the following equation.

$$P(t) = \int_0^{\frac{d}{2}} \left( 2 \times x \times l_c \times \frac{dB}{dt} \right)^2 \times \frac{\sqrt{\frac{D_C^2}{4} - x^2} \times dx}{\rho l_c}$$

$$P(t) = \frac{\pi l_c D_C^4}{64 \rho} \left( \frac{dB(t)}{dt} \right)^2$$

#### 4. Measurements of the integrated LCL filter

The constructed motorette has been tested by applying a number of AC voltages to the middle tooth and hence an Oscilloscope has been used to calculate the phase shift between the applied voltage and current. As a consequence, the method of calculation middle tooth inductance is as follows:

- $V, I$  and  $\phi$  (phase shift) are known
- $Z_{impedance} = \frac{V}{I} \angle -\phi = x \angle -\phi$  where  $x$  is constant
- $Z_{impedance} = x \cos(-\phi) + jx \sin(-\phi)$

Therefore, the inductance value is in the reactance part of the equation

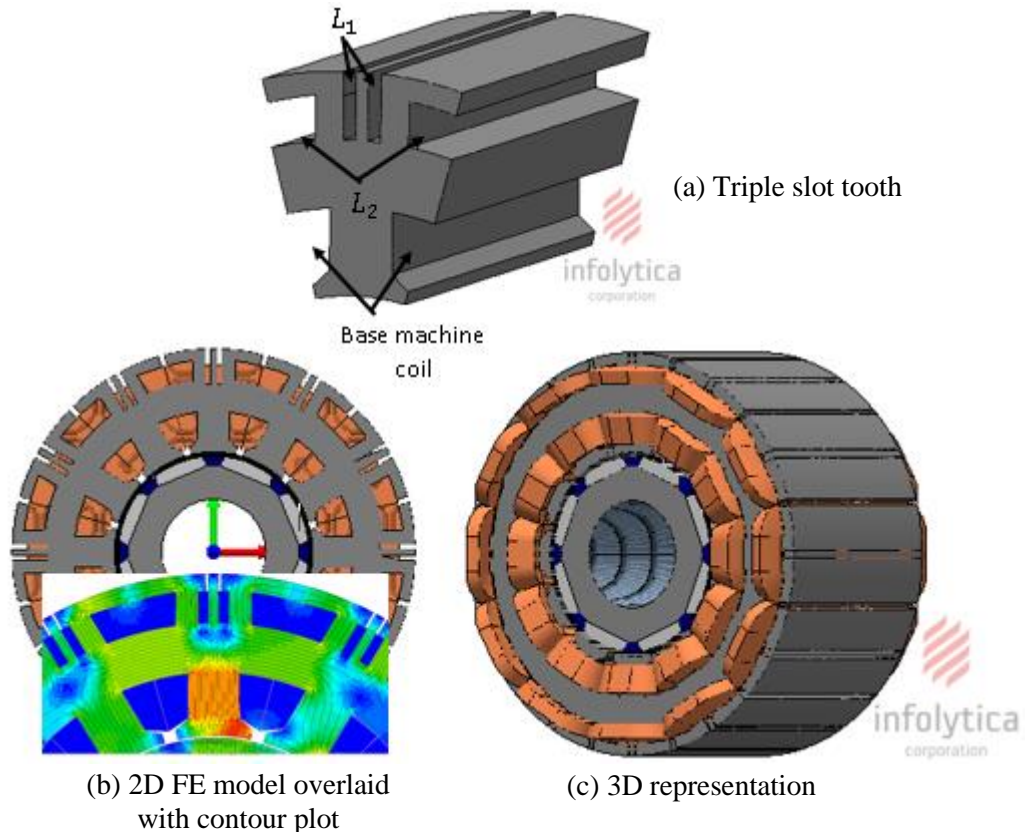
$$Y = x \sin(\phi) = \omega L$$

- The middle tooth inductance is:

$$L = \frac{Y}{\omega}$$

#### 5. Additional methods for integrating grid-side inductors ( $L_1$ ) into the HSHP machine

Triple slot machine method: this approach involves three different coils (for the machine and filter inductors  $L_1$  and  $L_2$ ) with an independent slot for each coil within a stator tooth, as shown in figure A4. The filter inductors have separate air gaps and hence there is a likelihood of independent magnetic paths for each filter inductor along with the independence of the main machine's magnetic circuit.



**Figure A4 Triple slot machine**

However, this approach to integration is might be complicated in terms of the assembly of the filter windings  $L_1$  and  $L_2$  and it is not a cost-effective method compared to the method of the IDS machine.

## 6. Procedures of Mega test

A Meg-Ohm test has been performed using a Megger tester with a test voltage of 500 V based on the operating phase voltage of the machine of 433 V at peak voltage. The dielectric strengths of different components in the constructed IDS machine have been tested, including the ground wall insulation in the double-slot stator, the four-layer busbar boards, the shunt capacitor connections, and the machine housing. Table A-1 shows different cases of the possible testing of end terminals.

**Table A-1 Ground wall insulation test for the IDS machine**

		Expected Meg-Ohm test results												
		$L_{1a}$	$L_{1b}$	$L_{1c}$	$L_{2a}$	$L_{2b}$	$L_{2c}$	$C_a$	$C_b$	$C_c$	$M_a$	$M_b$	$M_c$	Housing
Measured Meg-Ohm test results	$L_{1a}$	S.C	✓	✓	0	✓	✓	0	✓	✓	✓	✓	✓	✓
	$L_{1b}$	✓	S.C	✓	✓	0	✓	✓	0	✓	✓	✓	✓	✓
	$L_{1c}$	✓	✓	S.C	✓	✓	0	✓	✓	0	✓	✓	✓	✓
	$L_{2a}$	0.21 $\Omega$	✓	✓	S.C	✓	✓	0	✓	✓	✓	✓	✓	✓
	$L_{2b}$	✓	0.28 $\Omega$	✓	✓	S.C	✓	✓	0	✓	✓	✓	✓	✓
	$L_{2c}$	✓	✓	0.3 $\Omega$	✓	✓	S.C	✓	✓	0	✓	✓	✓	✓
	$C_a$	0.28 $\Omega$	✓	✓	0.28 $\Omega$	✓	✓	S.C	✓	✓	✓	✓	✓	✓
	$C_b$	✓	0.25 $\Omega$	✓	✓	0.28 $\Omega$	✓	✓	S.C	✓	✓	✓	✓	✓
	$C_c$	✓	✓	0.26 $\Omega$	✓	✓	0.34 $\Omega$	✓	✓	S.C	✓	✓	✓	✓
	$M_a$	✓	✓	✓	✓	✓	✓	✓	✓	✓	S.C	0	0	✓
	$M_b$	✓	✓	✓	✓	✓	✓	✓	✓	✓	0.33 $\Omega$	S.C	0	✓
	$M_c$	✓	✓	✓	✓	✓	✓	✓	✓	✓	0.35 $\Omega$	0.28 $\Omega$	S.C	✓
	Housing	✓	✓	✓	✓	✓	✓	✓	✓	✓	✓	✓	✓	S.C
Symbols: $L_{1(a,b,c)}$ : grid-side phase inductor, $L_{2(a,b,c)}$ : drive-side phase inductor, $C_{(a,b,c)}$ : phase filter capacitor, $M_{(a,b,c)}$ : phase machine coils, S.C: short circuit, ✓: successful insulation test (no fault).														

According to the results obtained in the strength of the insulation test shown in table A-1, the IDS machine has an adequate dielectric strength to withstand the maximum operating voltage.

## 7. Procedures of surge test

The principle of the surge test is that it applies a high current impulse to a coil using a fast rise time in order to create a potential voltage across the wire of the winding. These short high-current pulses produce a momentary voltage stress between adjacent conductors. In this case, the coil becomes one of the two elements in an LC circuit which is made up of the coil's inductance (L) and the internal capacitor of the surge tester (C). The voltage present across the test leads of the tester is a representation of the surge waveform. The coil inductance is basically dictated by the number of copper turns and the type of iron core in which it rests. In the case of turn-to-turn fault the voltage

potential is greater than the dielectric strength of insulation of turn and thereby one or more turns might short out of the circuit. The inductance of coil will be reduced with fewer working turns. Therefore, the indication of a turn-to-turn fault is a jump to the left of the surge waveform pattern, which can be seen on the screen display of the Baker instrument.

The wave pattern frequency which decays with time is determined by the following equation.

$$Frequency = \frac{1}{2\pi \sqrt{LC}}$$

The surge test process for the IDS machine has been conducted using a test voltage of 1000 V, which is more than double the operating machine voltage and is based on the appropriate standards and company guidelines [107]. A preliminary surge test was performed on a master coil which is likely to be in a fully healthy state, where the surge waveform was stored as a reference master waveform for all other coils tested.

Figure 6-15 shows a series of tests which can be carried out on the coil, including the waveform of the surge test for a healthy coil. The method of determining the pulse-to-pulse error area ratio (PP-EAR) is applied in the coil testing to be compared to the saved waveform of the master coil, indicating a healthy or failed coil. The PP-EAR method applies a voltage impulse to the coil and measures the differences between pulses. An acceptable error (PP-EAR %) should be less than 10% of the saved master coil waveform [107]. Furthermore, the measurement of coil resistance and Meg-Ohm and HiPt tests have all been carried out with different levels of voltages, as shown in figure 6-15. The 24 coils (of the base machine and filter inductors) of the IDS machine were tested and they all passed the surge test successfully.

Results Summary		Test Date/Time 8/8/2017 4:34:25 PM	
Test ID:Default		Repair/Job #	
Tested By		Tested For	
Room#		MCC	
Location:Default		Building:Default	
Temp Status	No Test Performed	PI Status	No Test Performed
Temp		Volts (V)	0
Resist Status	PASS	DA Ratio	0.0
L1-L2 (Ohms)	0.170	PI Ratio	0.0
L2-L3 (Ohms)	0.170	HiPot	PASS
L3-L1 (Ohms)	0.169	Volts (V)	1000
Max Delta R %	0.167	I(μA)	0.01
Coil 1 (Ohms)	0.085	Resist (Mohm)	111682
Coil 2 (Ohms)	0.085	Surge Status	PASS
Coil 3 (Ohms)	0.085	Peak Volt(V) L1	1010
Megohm Status	PASS	Peak Volt(V) L2	1010
Volts (V)	500	Peak Volt(V) L3	0
I(μA)	0.01	Max P-P EAR(%)	1.6/1.5/--
Resist (Mohm)	89831	EAR 1-2/2-3/3-1(%)	No Test

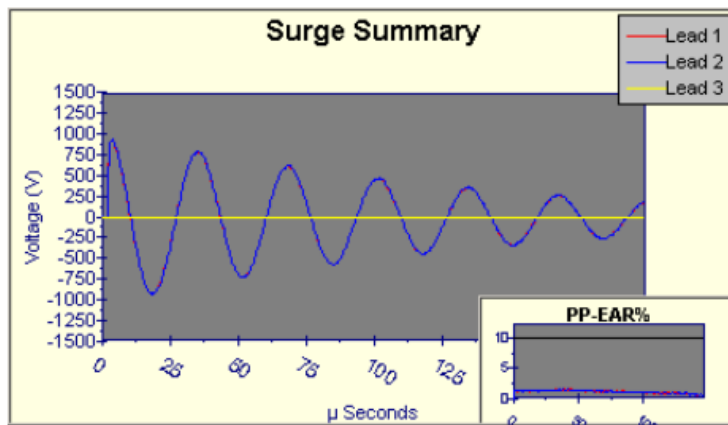


Figure A5 Complete test of coil with the surge test waveform compared to the master coil

## 8. Demagnetisation curves of the utilised magnet material

The following figure A5 illustrates the B-H curve of the PM material grade N42UH which is used for the rotor magnets.

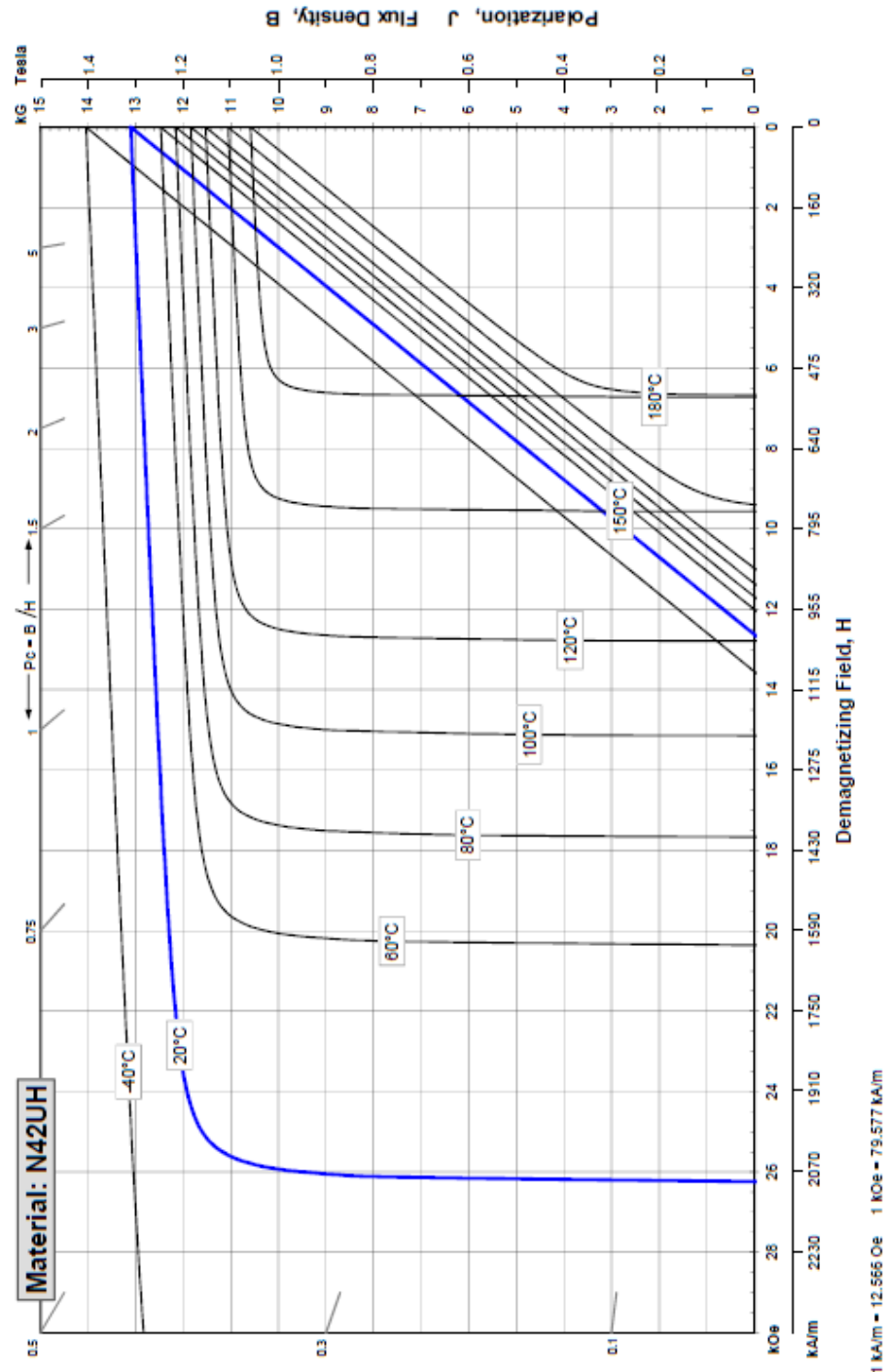


Figure A6 Demagnetisation curves of the magnet material used of N42UH



# Appendix B – 34kW/25000 RPM machine drawings

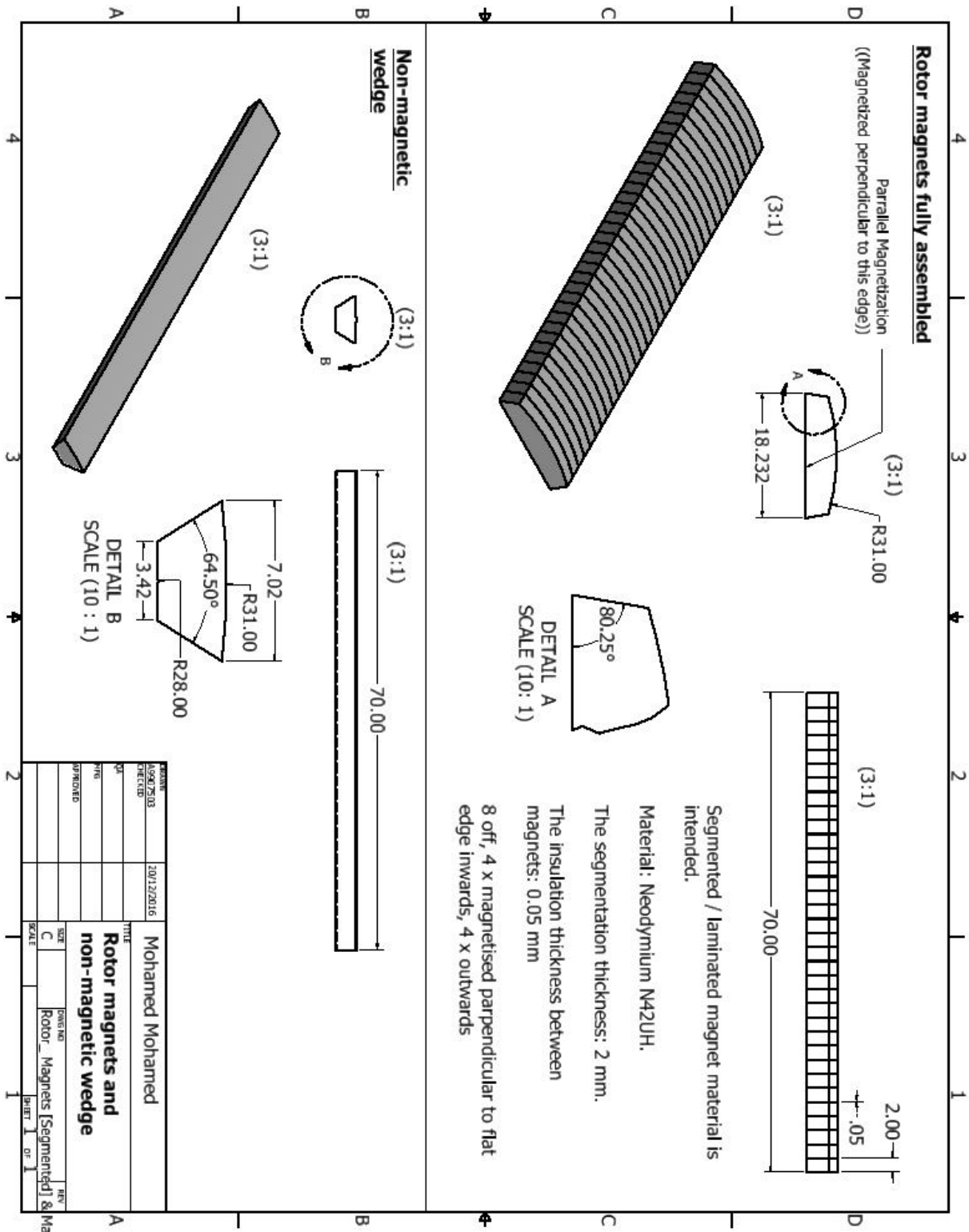


Figure B1 Drawings of rotor magnets and non-magnetic wedge

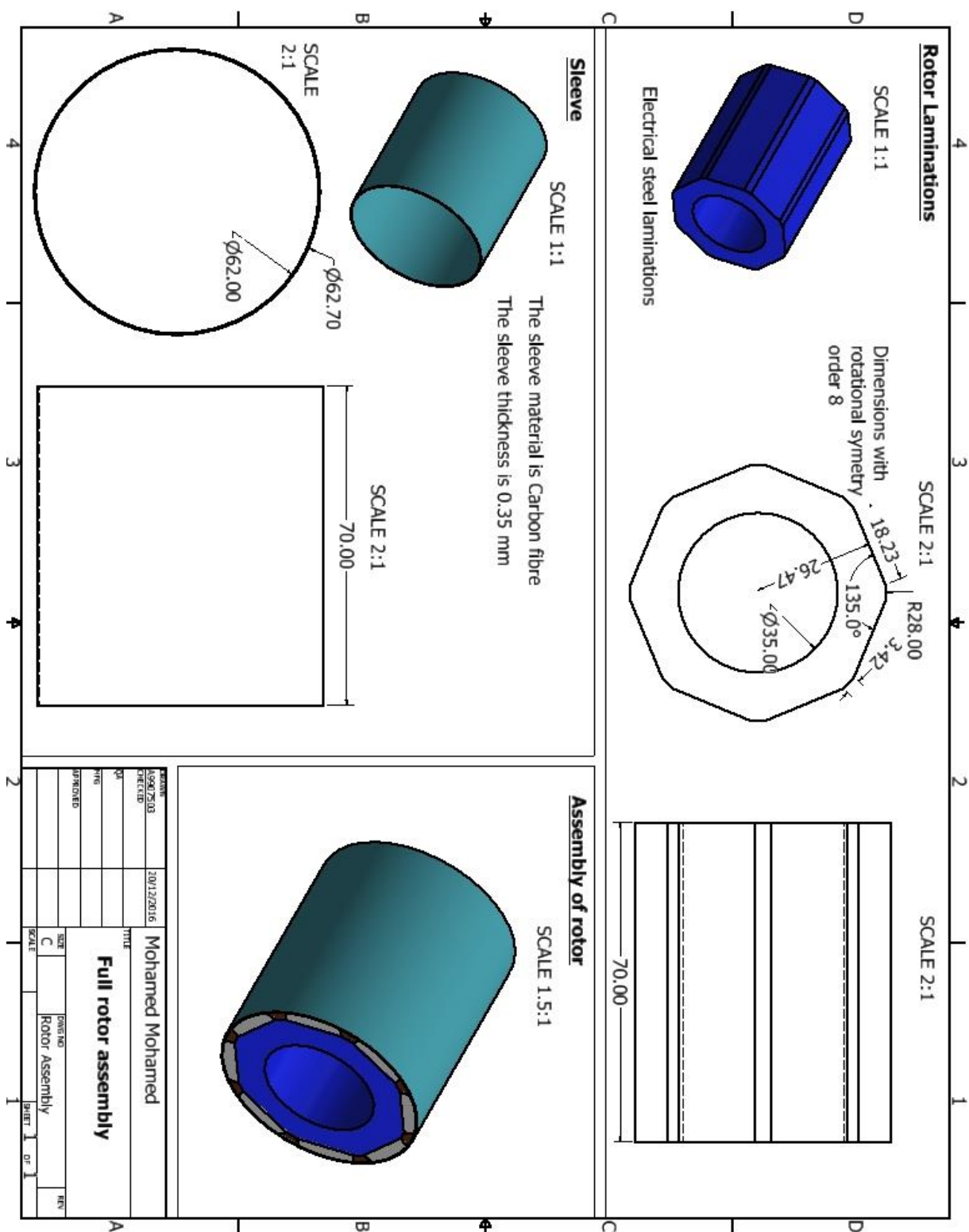


Figure B2 Drawings of full rotor assembly

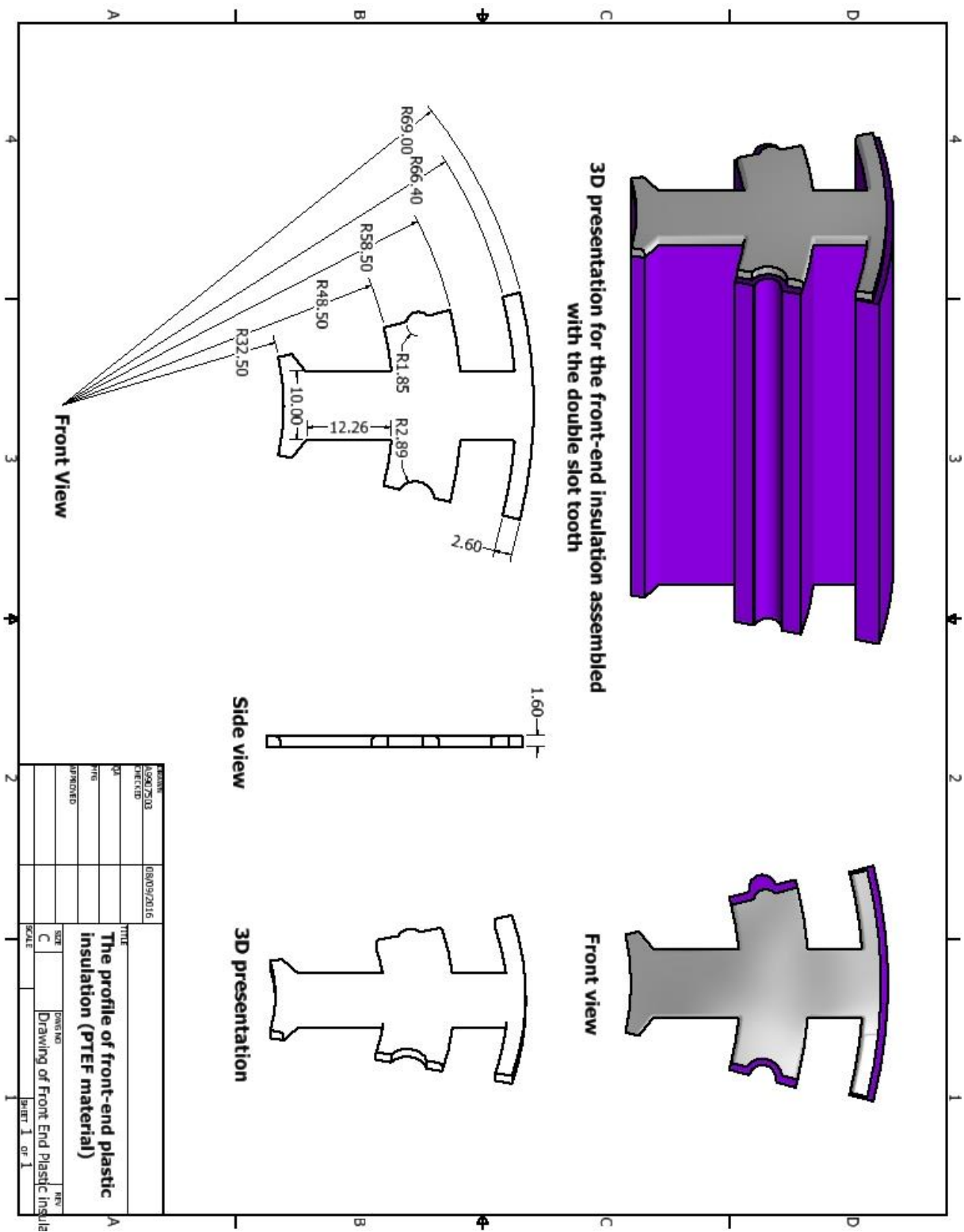


Figure B3 Drawings of front-end plastic insulation for the stator teeth

# Appendix C – Drawings of pressing tools

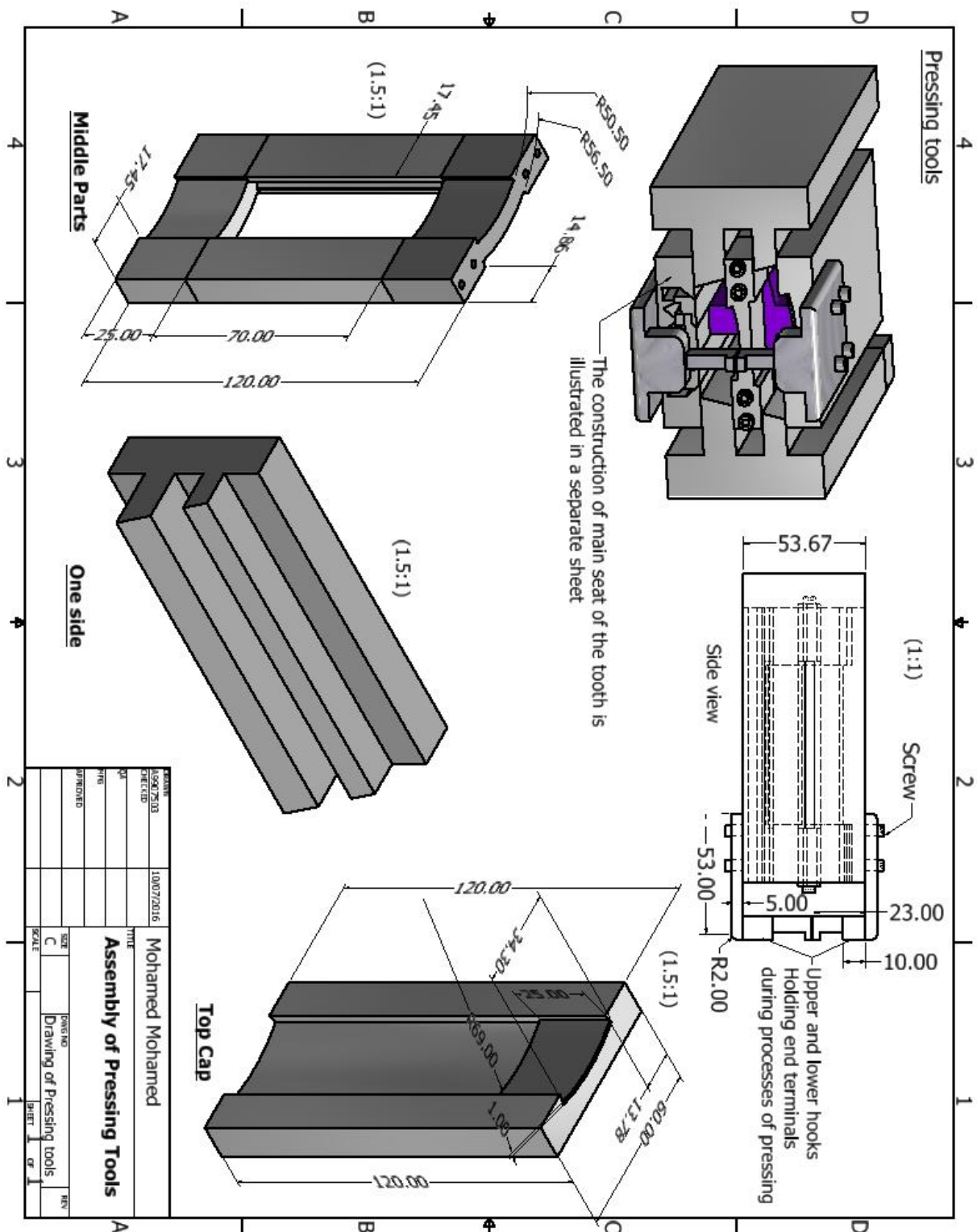
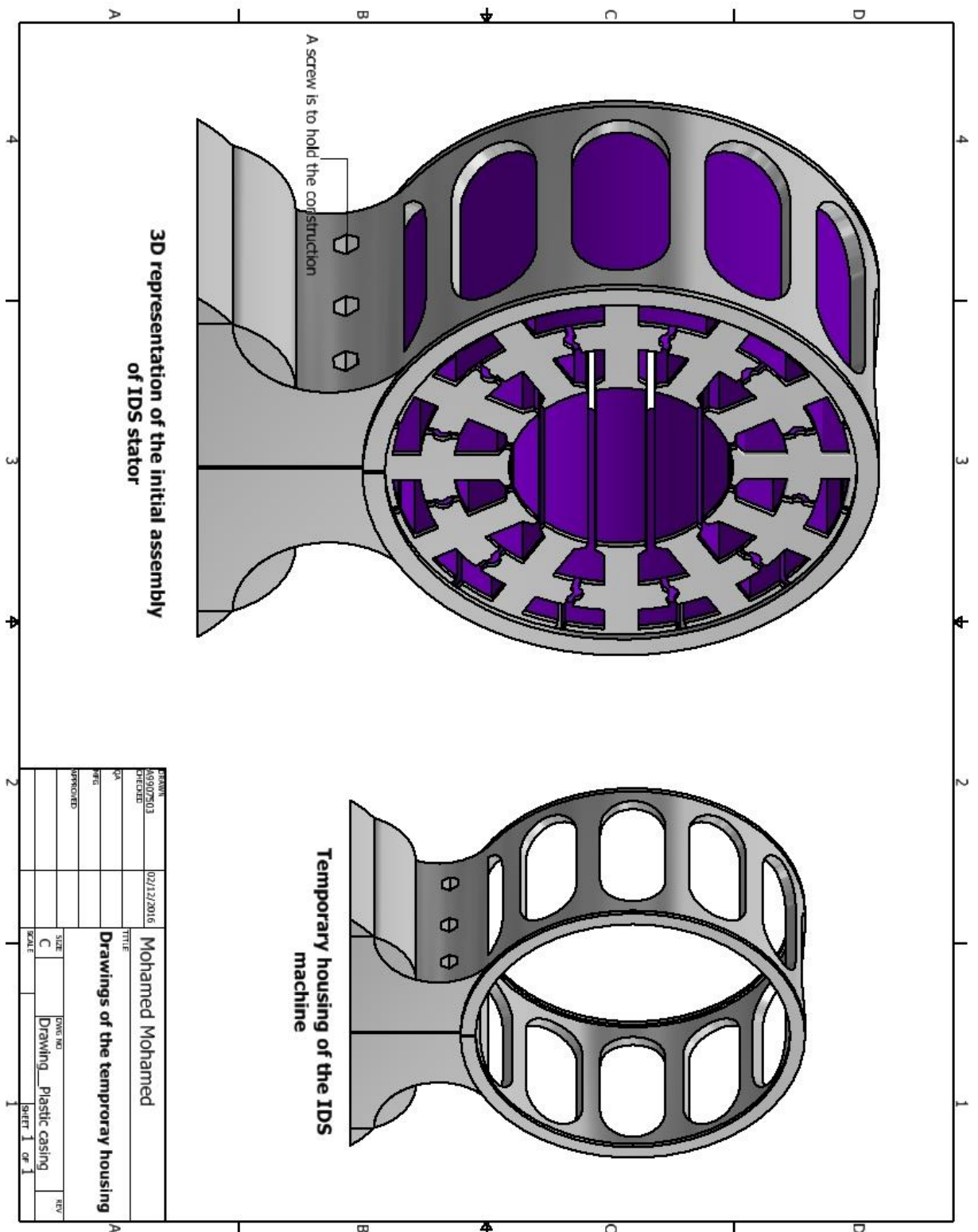


Figure C1 Drawings of parts of pressing tools

196

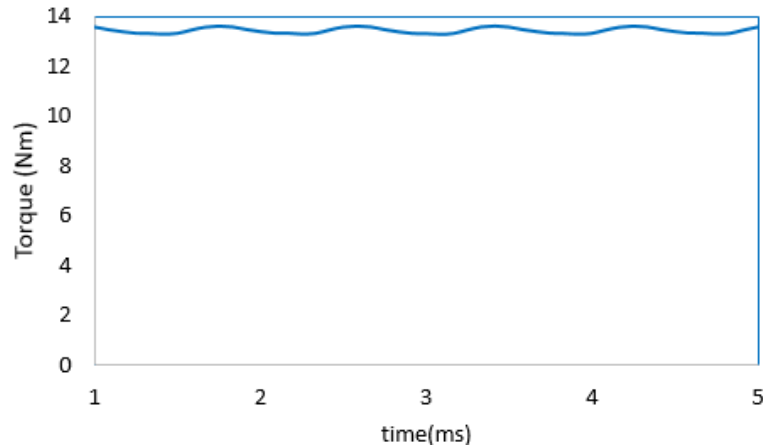


### Figure C3 Drawings of temporary housing

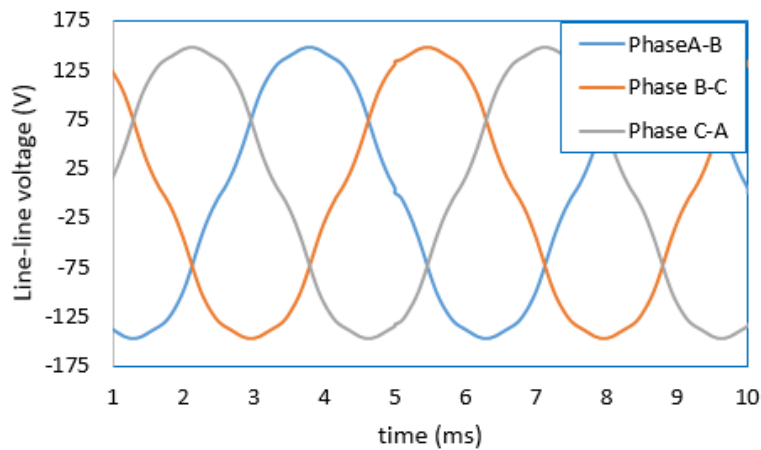


## Appendix D – 4.56kW/3000 RPM - FE results

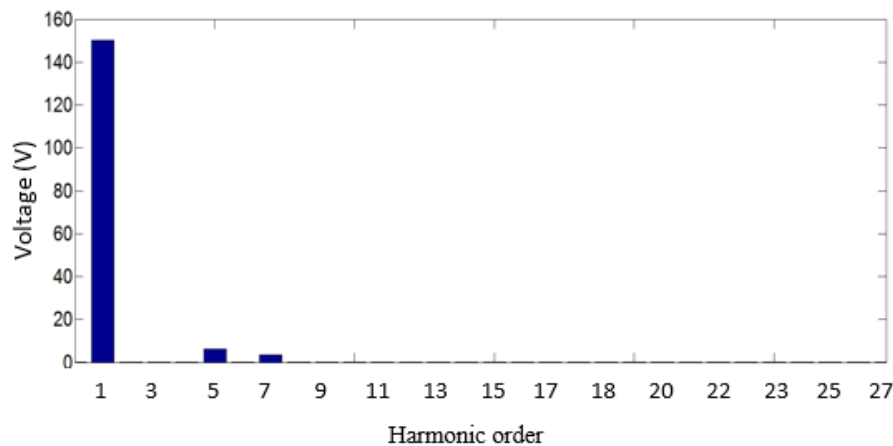
**FEA Results for the low-speed machine at 3000 RPM:**



**Figure D1 2D torque performance prediction at 3000 RPM**



**Figure D2 2D line back-EMF voltages at 3000 RPM**



**Figure D3 Harmonic spectrum of line-to-line back-EMF**